Highly Transparent and Highly Passivating Silicon Nitride for Solar Cells

Yimao Wan

March 2014

A thesis submitted for the degree of Doctor of Philosophy
of the Australian National University

Australian
National
University

I dedicate this thesis to

my family, my wife, Annie, and my beloved children, Paul and Sophia,

for their constant support and unconditional love.

I love you all dearly.

Declaration

I certify that this thesis does not incorporate without acknowledgement any material submitted for a degree or diploma in any university and that, to the best of my knowledge, it does not contain any material previously published or written by another person except where due reference is made in the text. The work in this thesis is my own, except for the contributions made by others as described in the Acknowledgements.

Yimao Wan

March 2014

Acknowledgements

The pursuit of this PhD has been a truly lifetime-changing experience for me. It is a pleasure to gratefully acknowledge all those people who made this thesis possible.

I owe my deepest gratitude to my principle supervisor Dr. Keith McIntosh. I appreciate all his contributions of time, ideas, and funding to make my PhD experience productive and stimulating. I am also thankful to him for being accessible and enabling me to draw on his knowledge and experience whilst allowing me space for ingenuity. His regard for intricate details and constructive criticism drove me forward and steered my efforts into the present form that I now humbly put forward. His enthusiasm was contagious and inspirational, and his commitment to this work beyond his time at the ANU was a class act.

I would also like to express my special thanks to my supervisors: Prof. Andres Cuevas and Dr. Andrew Thomson for their generous mentorship, advice and assistance. Their enthusiasm to do frequent discussions has been essential to advance this study. Their intensity and willingness in reading and reviewing undoubtedly improved the quality of this thesis.

The members at the Centre for Sustainable Energy Systems (CSES) and Research School of Engineering have contributed immensely to my personal and professional time at the ANU. The group has been a source of friendships as well as good advice and collaboration. I am grateful to my fellows for making this journey exciting and enjoyable. Specific acknowledgement is made to Dr. Simeon Baker-Finch for assistance in reviewing Chapter 6, Lachlan Black for fruitful discussions on surface recombination and C–V analysis, and Di Yan for furnace diffusions. I am also grateful to Dr. Daniel Macdonald for his generosity in offering me a part-time research assistantship.

I am indebted to the staff at the CSES for their assistance in the maintenance of equipment that was central to experimental work presented in this thesis. I would particularly like to thank Nina DeCaritat, Chris Samundsett, James Cotsell and Bruce Condon for invaluable support.

I wish to thank my family and friends for their unconditional support, love and inspiration. I am forever grateful to my parents who raised me with a love of life and supported me in all my pursuits. I cannot be grateful enough to my mother for giving me life, for sparking my inquisitiveness and for always answering all my queries patiently.

Finally, I would like to express my deepest and most heartfelt thanks to my loving, supportive, encouraging, and patient wife Annie for her faithful support and sharing of this entire journey. I truly thank Annie for sticking by my side, even when I was irritable and depressed. Thank you, Annie. I am deeply indebted to you and I feel that what we both learned tremendously about life and strengthened our commitment and determination to each other and to live life to the fullest. Another huge thanks goes to our son, Paul, who witnessed all my efforts; and to our daughter Sophia, a surprising gift at the last stage of this journey. Thank you both for providing me the much needed lighter moments and love, and apologies for depriving you of your daddy time.

Abstract

This thesis concerns the optimisation and application of silicon nitride (SiN_x) films for silicon solar cells. Systematic and comprehensive studies of SiN_x properties are undertaken to advance *(i)* the technology of SiN_x synthesised by plasma enhanced chemical vapour deposition (PECVD), and *(ii)* the understanding of recombination at SiN_x-passivated silicon surfaces.

We examine the film properties of SiN_x prepared by a microwave/radio-frequency dual-mode PECVD reactor. It is shown that there is no universal correlation between surface recombination and *(i)* bulk structural properties such as chemical bond densities, and *(ii)* bulk optical properties such as refractive index and extinction coefficient. Results of this study repudiate the common perception that surface recombination decreases as SiN_x becomes Si-rich. The finding introduces the potential to independently control the optical and surface recombination properties of SiN_x. This is of great importance for the industrial application of SiN_x films to photovoltaic cells, as it allows the front surface transmission to be maximised while still attaining outstanding surface passivation.

We attain a low and relatively constant surface recombination over a wide range of SiN_x refractive indices. Notably, the behaviour is observed on several types of silicon surface surfaces—planar, textured, *p*-type, *n*-type, diffused and undiffused—with direct relevance to most silicon solar cell structures. The results confirm that the trade-off between the optical transmission and surface recombination is circumvented. In specific, we attain a highly transparent and highly passivating SiN_x film. The value of this film is demonstrated on an *n*-type interdigitated back contact solar cell with no front surface diffusion, which makes the cell highly susceptible to the front surface passivation. On such a cell, the optimum SiN_x

developed in this thesis enables a conversion efficiency of $24.4 \pm 0.5\%$ under standard testing conditions (25°C, AM1.5G spectrum).

Besides the significant improvement in optical transmission and surface passivation, the results of this thesis also advance the current understanding of recombination at SiN_x-passivated silicon surfaces. It is found that an increase in recombination of the textured surfaces is related to the presence of vertices and/or edges of the pyramids rather than to the presence of {111}-orientated facets. Furthermore, this thesis demonstrates that the increase in recombination introduced by *(i)* a lower pressure, leading to a higher refractive index, *(ii)* a higher NH_3:SiH_4 ratio, leading to a lower refractive index, and *(iii)* the vertices and/or edges of the pyramids, is primarily attributable to an increase in interface defect density rather than a decrease in SiN_x charge density. In addition, we hypothesise that the increase in interface defect density is caused by an ion bombardment of the silicon surface at a lower pressure, and by an excessive incorporation of NH_b radicals into the SiN_x film network at a higher NH_3:SiH_4 ratio.

The satisfactory resolution of the trade-off between optical transmission and surface passivation, and the improved understanding of recombination at SiN_x-passivated silicon surfaces, represent significant contributions to the science and technology of silicon solar cells.

Contents

Declaration v

Acknowledgements vii

Abstract ix

1 Introduction 1

1.1 Motivation 1

1.2 Outline 4

2 Review of SiN_x properties 7

2.1 Introduction 7

2.2 Optical properties 7

2.2.1 Refractive index versus N/Si ratio 8

2.2.2 Extinction coefficient versus N/Si ratio 9

2.2.3 Reflectance spectrophotometry 10

2.3 Chemical bond structure 10

2.3.1 [Si–N] versus N/Si ratio 10

2.3.2 [Si–H] and [N–H] versus N/Si ratio 12

2.3.3 Si–H peak wavenumber versus N/Si ratio 13

2.3.4 Fourier transform infrared spectroscopy 13

2.4 Electronic properties 14

2.4.1 Insulator charge density versus N/Si ratio 14

2.4.2 Interface defect density versus N/Si ratio 16

2.4.3 Capacitance–voltage 18

2.4.4 Corona–lifetime 18

2.5 Surface recombination 19

2.5.1 Theory 19

2.5.2 Surface recombination velocity versus N/Si ratio 20

2.5.3 Photoconductance 22

2.6 Chapter summary 23

3 PECVD reactor configuration and preparation **25**

3.1 Introduction 25

3.2 Plasma reactors for SiN_x deposition in PV industry 26

3.2.1 Types of PECVD reactor 26

A. Direct PECVD 27

B. Remote PECVD 28

C. Dual-mode PECVD 29

3.2.2 Impact of reactors on surface passivation 31

3.3 SiN_x deposition cycle and chemical reaction scheme 32

3.3.1 SiN_x deposition cycle 32

3.3.2 Chemical reactions for SiN_x growth 35

3.4 Reactor and sample preparation prior to SiN_x deposition 37

3.4.1 Reactor outgassing before plasma ignition 37

3.4.2 Silicon surface treatment before loading 39

3.4.3 Post-cleaning chamber coating 41

3.5 Chapter summary 43

4 Effect of deposition conditions on SiN_x properties 45

4.1 Introduction 45

4.2 Experimental details 46

4.3 Central composition experiment 49

4.3.1 Dependence of SiN_x properties on deposition conditions 49

A. Results 49

B. Discussion 53

4.3.2 Correlations between SiN_x properties 55

A. n_{632} versus [Si–H]/[N–H] ratio 56

B. $S_{eff,UL}$ versus chemical bond density 57

C. $S_{eff,UL}$ versus n_{632} 59

D. $S_{eff,UL}$ versus D_{it} and Q_{eff} 60

4.3.3 Conclusions 61

4.4 Varying pressure at optimum temperature 62

4.5 Characterising the optimum SiN_x properties 65

4.5.1 Measured injection-dependent effective minority carrier lifetime 65

4.5.2 Extraction and modelling of $S_{eff,UL}(\Delta n)$ 66

4.5.3 Simulation of optical performance 69

4.6 Chapter summary 70

5 Influence of NH_3:SiH_4 ratio and NH_3 plasma exposure on SiN_x properties 73

5.1 Introduction 73

5.2 Experimental details 74

5.3 Experiment 1—varying the NH_3:SiH_4 ratio 75

5.3.1 Background 76

5.3.2 Results and discussion 76

5.4 Experiment 2—NH_3 plasma exposure 79

5.4.1 Background ... 79

5.4.2 Results and discussion ... 79

A. Lifetime measurements ... 79

B. FTIR measurements ... 81

C. Optical measurements ... 83

D. C–V measurements ... 84

5.5 Discussion ... 85

5.6 Chapter summary ... 86

6 Recombination at SiN_x-passivated undiffused textured silicon 89

6.1 Introduction ... 89

6.2 Literature review ... 91

6.3 Experimental details ... 93

6.4 Dependence of S_{eff} on substrate orientation, morphology, and SiN_x stoichiometry 96

6.4.1 Rantex ... 96

A. Varying the NH_3:SiH_4 ratio ... 97

B. Varying the deoposition pressure ... 98

C. Varying the substrate temperature ... 98

D. Summary ... 99

6.4.2 Intex ... 100

6.4.3 Isotex ... 103

6.4.4 Conclusions ... 104

6.5 Probing SiN_x electronic properties at textured surfaces ... 105

6.5.1 Dependence of S_{eff} on surface charge density Q_s ... 106

6.5.2 Depositing corona charge at planar {100}, planar {111} and rantex surfaces ... 108

6.5.3 Depositing corona charge at intex surfaces ... 110

6.5.4 Depositing corona charge at isotex surfaces ... 111

6.5.5 Conclusions ... 112

6.6 Exposing SiN_x-passivated textured surfaces to NH_3 plasma ... 113

6.7 Chapter summary ... 115

7 Applicability to phosphorus-diffused surfaces and to silicon solar cells 119

7.1 Introduction ... 119

7.2 Passivating phosphorus-diffused Si surfaces ... 120

7.2.1 Experimental details ... 121

7.2.2 Results and discussion ... 123

A. J_0 on planar phosphorus-diffused surfaces ... 123

B. J_0 on textured phosphorus-diffused surfaces ... 125

C. Textured-to-planar J_0 ratio at phosphorus-diffused surfaces ... 125

7.2.3 Conclusions ... 128

7.3 Simulating the impact of SiN_x on IBC and PERC cell performance ... 129

7.3.1 Antireflection coating of textured Si surfaces ... 130

7.3.2 Cell performance: V_{OC}, J_{SC}, FF and η ... 132

7.4 Applying the optimum SiN_x on IBC Si solar cells ... 133

7.4.1 Cell structure and fabrication ... 134

7.4.2 Cell results & discussion ... 135

7.4.3 Conclusions ... 136

7.5 Chapter summary ... 137

8 Conclusions 139

8.1 Summary ... 139

8.2 Specific conclusions by chapter ... 142

8.3 Suggestions for further work ... 147

A Cell parameters used in Quokka simulation 149

B Calibration of silicon substrate temperature in the PECVD reactor 155

B.1 Measurement of silicon wafer temperature using thermocouple 155

B.2 Installation and calibration of infrared thermometer 157

B.3 Summary 158

C Characterisation of stress in SiN_x and its effect on surface passivation 159

C.1 Introduction 159

C.2 Experimental details 160

C.3 Results and discussion 160

C.3.1 Front and rear radius of curvature measurements 160

C.3.2 Effect of SiN_x stoichiometry and chemical bond density on stress 161

C.3.3 Relationship between surface recombination and stress 164

C.4 Conclusion 165

List of Publications 167

Bibliography 171

Introduction

1.1 Motivation

Photovoltaic solar energy has grown exponentially for the past 25 years, reaching a cumulative installation above 100 GW in 2012 [1]. In parallel, the prices of crystalline silicon solar cells, which comprises 85–90% of the total photovoltaic market, have fallen from $76.67/Watt in 1977 to an estimated $0.74/Watt in 2013 [2]. This development has corresponded to a reduction in module prices of 20% for every doubling of industry capacity. To sustain the continued development, it is vital to further reduce the cost of PV electricity, which can be realised by reducing the manufacturing cost and increasing solar cell efficiency.

With the cost-driven reductions in the silicon substrate thickness, and improvements in their electronic quality, surface recombination losses have become more significant and can indeed be the largest losses in a high efficiency cell [3-5]. Therefore by reducing surface recombination, large improvements in solar cell efficiencies can be gained. The suppression of surface recombination, known as surface passivation, is a core focus of this thesis.

Amorphous silicon nitride (SiN_x) prepared using plasma enhanced chemical vapour deposition (PECVD) is an indispensable element in virtually every commercial solar cell [6, 7]. The reason for its importance is that the film performs three crucial functions: (*i*) it comprises the antireflection coating [6]; (*ii*) it provides surface and bulk passivation [8-10]; and (*iii*) it forms a chemical barrier to protect underlying interfaces from the degrading effects of moisture, humidity [11, 12] and sodium ions [13, 14].

In this thesis, we focus on the antireflection and surface passivation properties of SiN_x. To elucidate the impact of the two properties on cell performance and delineate the space in the improvement of SiN_x properties, Figure 1.1 depicts the relationship between SiN_x refractive index n at 632 nm (n_{632}) and (a) the optimum photogenerated current density J_{Gen}, (b) surface recombination velocity S_{eff}, and (c) the simulated conversion efficiency of an interdigitated back contact (IBC) silicon solar cell developed at the ANU [15, 16]. The blue lines in Figure 1.1(b) and (c) represent the state of the art SiN_x from prior works [17-21], as summarised in Chapter 2; and the red lines represent the improved SiN_x developed in this thesis.

As shown in Figure 1.1(a), J_{Gen} stays relatively constant when n_{632} ranges from 1.83 to 2.0, and then decreases markedly as n_{632} increases above 2.0. This decrease stems from an increase in light absorption in SiN_x. Counteracting this behaviour, the blue line in Figure 1.1(b) shows an apparent trend in which S_{eff} decreases as n_{632} increases. The counteractive behaviour of J_{Gen} and S_{eff} leads to a trade-off between surface passivation and optical transmission, and in consequence, it results in an optimum cell efficiency, as depicted in Figure 1.1(c).

The efficiency of the simulated cell peaks at 22.0% when $n_{632} = 2.3$, as depicted by the blue line. This optimum is attributable to *(i)* a high surface recombination when $n_{632} < 2.3$, and *(ii)* a high light absorption when $n_{632} > 2.3$. It is therefore desirable to decouple the optical and surface recombination properties of SiN_x because it allows independent control of the two properties, and as a consequence S_{eff} could be reduced further without sacrificing J_{Gen}. Moreover, an improved understanding of *(i)* the root cause for the increase of S_{eff} as the NH_3:SiH_4 ratio increases (and so n decreases), and *(ii)* the recombination behaviour at textured surfaces, are of great benefit in minimising the surface recombination and so improving cell efficiency. Thus, despite SiN_x being used on almost all industrial silicon solar cells, there remains ways that it can be improved and better understood.

In this thesis, we endeavour to circumvent the trade-off between J_{Gen} and S_{eff} through an extensive examination of the SiN_x properties. By correlating the relationship between SiN_x properties, it is found that the recombination does not correlate universally with the bulk structural and optical properties, suggesting an

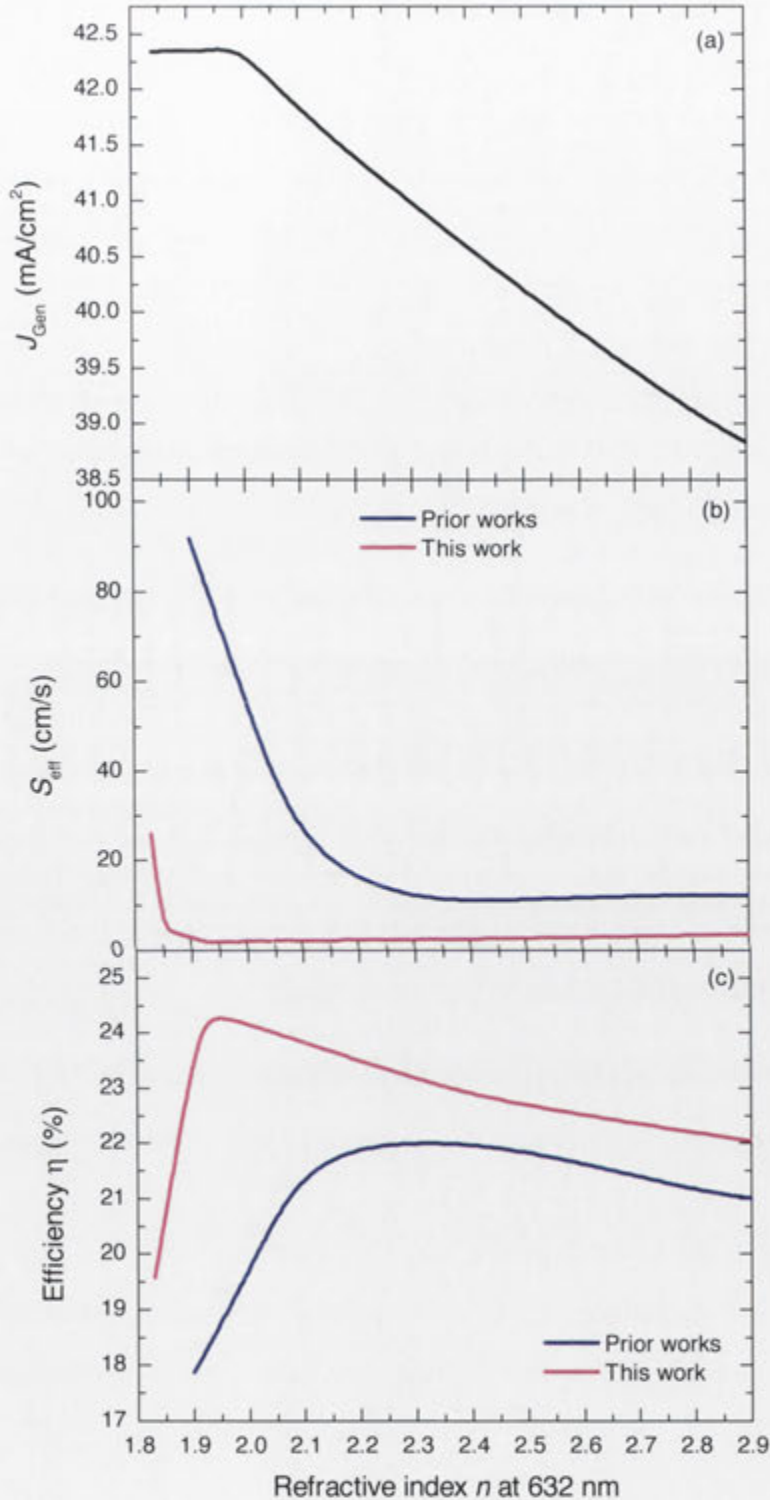

Figure 1.1: The relationship between SiN_x refractive index *n* at 632 nm (n_{632}) and **(a)** the optimum photogenerated current density J_{Gen}, **(b)** surface recombination velocity S_{eff}, extracted from prior works that represent the current state of the art surface passivation by SiN_x [17-21], and **(c)** the simulated conversion efficiency of an IBC silicon solar cell developed at the ANU [15, 16]. The simulations were performed with OPAL 2 and Quokka as described in Appendix A. In Chapter 7, the figures are populated with experimental data points.

opportunity to independently optimise the performance of antireflection coating and surface passivation by SiN_x. We attain a low recombination over a broad range of n_{632} (1.9–2.9), as demonstrated in Figure 1.1(b) by the red line. Notably, this finding applies on several types of Si surface conditions that are planar, textured, *p*-type, *n*-type, diffused and undiffused, with direct relevance to most silicon solar cell structures. In specific, we attain a highly transparent and highly passivating SiN_x film, of which the application on the *n*-type IBC solar cell developed at the ANU enables conversion efficiency of $24.4 \pm 0.5\%$. This thesis demonstrates that, with careful optimisation of SiN_x properties, the optical advantages of SiN_x can be enjoyed without penalty in recombination.

In this thesis, we also provide new insights into the recombination at SiN_x-passivated surfaces. We find that an increase in recombination of the textured surfaces is related to the presence of vertices and/or edges of the pyramids rather than to the presence of {111}-orientated facets. Furthermore, this thesis demonstrates that the increase in recombination introduced by *(i)* a lower pressure, *(ii)* a higher NH_3:SiH_4 ratio, and *(iii)* the vertices and edges of the pyramids, is primarily due to an increase in interface defect density (D_{it}) rather than a decrease in SiN_x charge density (Q_{eff}).

1.2 Outline

This thesis explores the physical properties of PECVD SiN_x and its application in silicon photovoltaic devices with an emphasis on the antireflection coating and surface passivation. It improves the understanding of the recombination incurred at the silicon solar cell surfaces that are planar, textured, *p*-type, *n*-type, diffused and undiffused.

Chapter 2 reviews SiN_x film properties and relevant characterisation techniques used in this thesis. We demonstrate that (*i*) irrespective of deposition techniques and conditions, the bulk structural and optical properties are correlated universally to the N/Si ratio; and (*ii*) the electronic properties including Q_{eff}, D_{it}, and S_{eff}, appear independent of the N/Si ratio.

Chapter 3 presents the reactor configurations for laboratory and inline PECVD, and follows with their impacts on surface passivation by SiN_x. The chemical reactions that occur during SiN_x deposition are discussed, and the procedures in the preparation of PECVD reactor and silicon samples are evaluated with a focus on surface passivation.

Chapter 4 presents an extensive study into SiN_x prepared by the microwave/radio-frequency (μW/RF) dual-mode PECVD reactor. The dependence of SiN_x properties on deposition conditions is systematically investigated, with the NH_3:SiH_4 ratio, deposition pressure and substrate temperature identified as the most sensitive parameters to SiN_x optical and passivation properties. By correlating the relationship between SiN_x properties, it is found that *(i)* S_{eff} does not correlate universally with the bulk structural and optical properties; and *(ii)* S_{eff} depends primarily on D_{it} rather than Q_{eff}. Based on these fundamental studies, we identify an optimum deposition condition and attain a highly transparent and highly passivating SiN_x. The optimum film has a nearly stoichiometric composition and negligible absorption of short-wavelength light. Meanwhile, the film provides a low S_{eff} (1.6 cm/s) on 0.85-Ω·cm *p*-type and immeasurably low S_{eff} on 0.45-Ω·cm *n*-type silicon substrates. Finally, a brief characterisation of the optimum SiN_x is presented.

Chapter 5 employs the optimum deposition condition developed in Chapter 4 and examines *(i)* the surface recombination properties over a wide range of n_{632} by varying the NH_3:SiH_4 ratio, and *(ii)* the cause of the increase in S_{eff} with the increase in the NH_3:SiH_4 ratio using NH_3 plasma exposure. It is found that *(i)* S_{eff} remains low and relatively constant when the NH_3:SiH_4 ratio increases from 0 to 1.9 (n_{632} decreases from 4.1 to 1.87), resulting in a low S_{eff} over a broad range of n_{632} (1.87–4.1) on low-resistivity (≤ 1.1 Ω·cm) *p*-Si and *n*-Si substrates; and *(ii)* S_{eff} increases strongly as the NH_3:SiH_4 ratio increases from 1.9 to 4.7 (n_{632} decreases from 1.87 to 1.83). The physical cause underlying the increase in S_{eff} with the increase in the NH_3:SiH_4 ratio is postulated to be an excessive incorporation of NH_b radicals into SiN_x bulk and SiN_x/Si interface. This hypothesis is evaluated by introducing NH_b radicals into the SiN_x–Si system through exposing the samples to an NH_3 plasma.

Chapter 6 investigates the recombination at the textured undiffused Si surfaces. We achieve a low S_{eff} on textured samples (< 10 cm/s) over a wide range of n_{632} (1.9–

4.1). We also find that as the NH_3:SiH_4 ratio decreases, and so n increases, recombination at the textured surfaces (after area-correction) decreases rapidly and approaches the same S_{eff} as the planar surfaces. By contrast, we find that irrespective of the NH_3:SiH_4 ratio, and therefore n, S_{eff} is equivalent on {100} and {111} planar surfaces, indicating that the increase in S_{eff} of the textured surfaces is related to the presence of vertices and/or edges of the pyramids rather than to the presence of {111}-orientated facets.

By depositing varying degrees of corona charge on the samples, it is found that the increase in recombination introduced by *(i)* a higher NH_3:SiH_4 ratio, and *(ii)* the vertices and edges of the pyramids, is primarily due to an increase in D_{it} rather than a decrease in Q_{eff}. Finally, the exposure of SiN_x-passivated textured samples to NH_3 plasma reveals that the incorporation of NH_b radicals are likely to cause more degradation in the recombination at textured surfaces than at their planar equivalents.

Chapter 7 extends the recombination studies to phosphorus-diffused surfaces with a wide range of sheet resistances (16–700 Ω/□), demonstrating a low and constant recombination rate over a range of n_{632} (1.9–2.9). Compared to a planar diffused surface, it is shown that, *(i)* additional recombination (after area-correction) at a lightly diffused textured surface relates significantly to the NH_3:SiH_4 ratio (and therefore correlates inversely with n), in accordance with the results on undiffused surfaces; and *(ii)* regardless of the NH_3:SiH_4 ratio, a negligible increase in recombination (after area-correction) is incurred at a heavily diffused textured surface.

Furthermore, combining the experimental optical and recombination results, we evaluate the impact of SiN_x on cell performances of an n-type IBC and a p-type passivated emitter and rear cell (PERC). Finally, the optimum SiN_x is applied to the n-type IBC cell developed at the ANU, yielding a cell efficiency of 24.4 ± 0.5%, an open-circuit voltage of 705 mV, a short-circuit current of 41.9 ± 0.7 mA/cm^2 and a fill-factor of 82.7%.

Chapter 8 summarises the key findings and offers suggestions for further work.

Review of SiN_x properties

2.1 Introduction

The first demonstration of SiN_x on silicon solar cells was presented by Hezel and Schorner in 1981, achieving cell efficiencies in the range of 15.0–18.5% on float-zoned silicon [9]. Nowadays, PECVD SiN_x is incorporated into most laboratory and industrial silicon solar cells [22, 23], fulfilling three functions: (*i*) it constitutes the antireflection coating (ARC) [6]; (*ii*) it provides surface and bulk passivation [8-10]; and (*iii*) it forms a chemical barrier to protect underlying interfaces from the degrading effects of moisture, humidity [11, 12] and sodium ions [13, 14].

In this chapter, the film properties and characterisation techniques are reviewed and discussed, creating a foundation for analysing the experimental data presented in the subsequent chapters. Since the N/Si ratio within the film (i.e., the stoichiometry) is a fundamental physical property, the following sections present the optical, structural, and electronic properties as a function of the N/Si ratio. Note that most data points presented in this chapter were reproduced from literature data that did not include experimental uncertainty; consequently error bars are omitted from figures presented in this chapter.

2.2 Optical properties

The refractive index and extinction coefficient are two key properties that dictate how well a SiN_x film performs as an ARC layer in silicon solar cells. This section first reviews the relationship between the optical properties and film stoichiometry,

and then follows with a brief description of the characterisation techniques used in this thesis.

2.2.1 Refractive index versus N/Si ratio

Figure 2.1 shows the n_{632} versus the N/Si ratio from several works [24-26]. The N/Si ratio presented in the literature was experimentally determined by either Rutherford backscattering (RBS) or elastic recoil detection (ERD). It is shown that, irrespective of deposition techniques, n_{632} decreases as the N/Si ratio increases.

It has been proposed that n_{632} of SiN_x could be represented as the atomic density-weighted linear combination of a reference n_{632} taken at N/Si = 0 (i.e., amorphous Si) and at N/Si = 4/3 (i.e., Si_3N_4) [27]. By setting n_{632} of Si at 3.3 and n_{632} of Si_3N_4 at 1.9, Bustarret *et al.* [28] proposed an equation to relate the n_{632} to the N/Si ratio

$$\frac{\mathrm{N}}{\mathrm{Si}} = \frac{4}{3}\frac{3.3 - n_{632}}{n_{632} - 0.5}. \tag{2.1}$$

As evident in Figure 2.1, the relationship between n_{632} and the N/Si ratio depicted by Eq. 2.1 is in fair agreement with the experimental results presented in the literature. Eq. 2.1 is therefore used to determine the N/Si ratio of our SiN_x films.

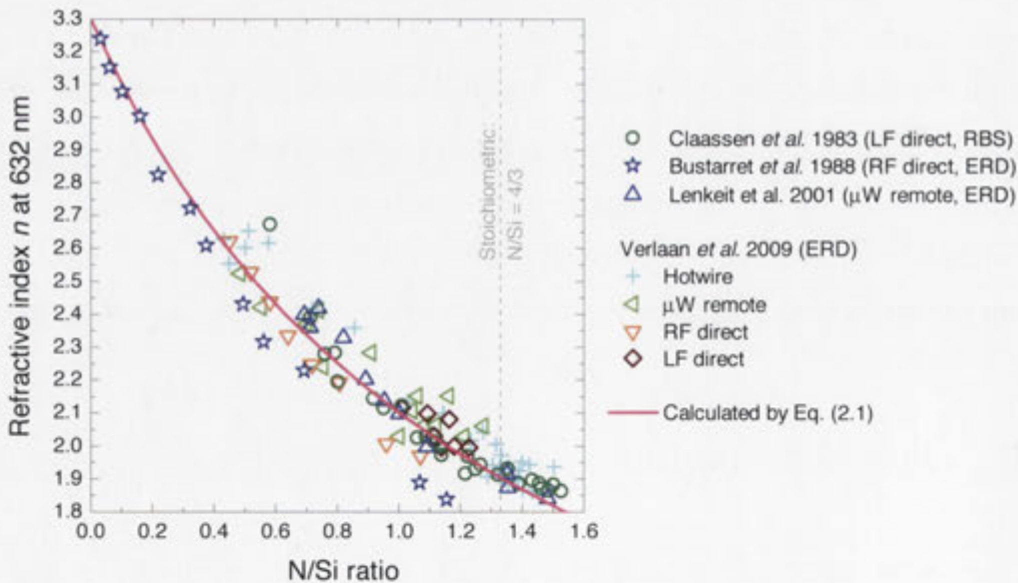

Figure 2.1: Correlation between n_{632} and the N/Si ratio for SiN_x films deposited by several deposition techniques: LF direct by Claassen *et al.* [25], RF direct by Bustarret *et al.* [28], and μW remote by Lenkeit *et al.* [26].

2.2.2 Extinction coefficient versus N/Si ratio

For implementation in silicon solar cells, it is important for the SiN_x films to be transparent over a wide range of wavelengths. Characterisation of the extinction coefficient is therefore crucial when optimising SiN_x films for use in silicon solar cells. The extinction coefficient k plays an attenuating role in the film. When the attenuation is solely due to absorption (i.e., no scattering), it is termed the absorption coefficient α, and relates directly to k, where $\alpha = \frac{4\pi k}{\lambda}$.

Figure 2.2 plots the extinction coefficient and absorption coefficient at 360 nm (k_{360} and α_{360}) as a function of the N/Si ratio for three previous studies as well as from this thesis (see Chapters 4 and 5). It is shown that k_{360} (and α_{360}) exhibits a decreasing trend with an increase in N/Si ratio. This trend is reasonably similar to that of n_{632}, implying that k generally increases as n_{632} increases, as discussed in Section 4.3.1–A. Note that k_{360} remains negligible for our SiN_x films when the N/Si ratio exceeds 1.2.

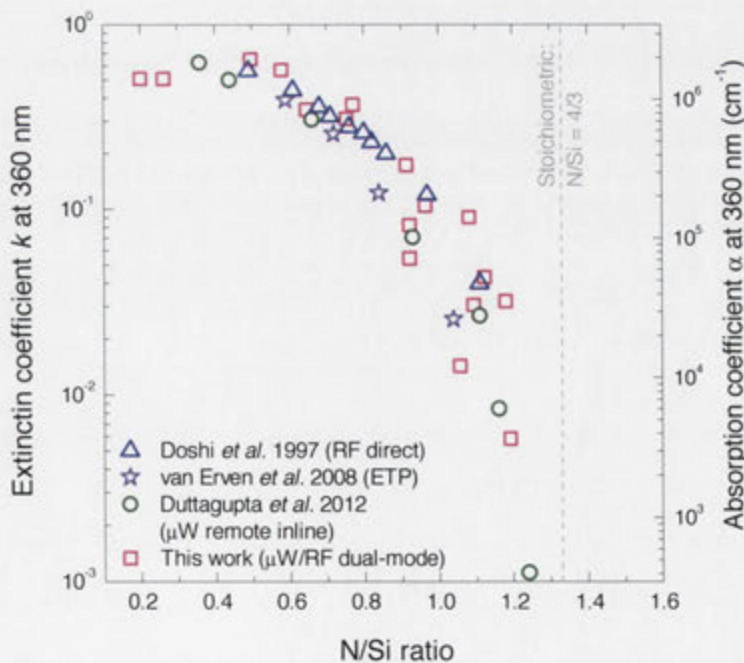

Figure 2.2: Correlation between the extinction coefficient (and absorption coefficient) at 360 nm and the N/Si ratio for SiN_x films deposited by several deposition techniques: RF direct by Doshi *et al.* [29], ETP by van Erven *et al.* [30], and µW remote inline by Duttagupta *et al.* [17].

2.2.3 Reflectance spectrophotometry

Two types of reflectance spectrophotometry are used in this thesis to determine the thickness and optical constants of the SiN_x films. The first is variable angle spectrophotometry. A PerkinElmer Lambda 1050 UV/Vis/NIR Spectrophotometer equipped with an automated reflectance transmittance analyser accessory was used to measure the directional reflectance at 10°, 40° and 70° over the wavelength range 250–1300 nm. A commercial software (CODE version 2.95) adapting the O'Leary–Johnson–Lim (OJL) intraband transition model [31] was employed for optical analysis. The second type of spectrophotometry is dual-angle 'reflectometer' (FilmTek 4000) that measures the directional reflectance at incident angles of 0° and 70°, using the Tauc–Lorentz model for the optical analysis [32].

2.3 Chemical bond structure

The chemical bond structure defines the internal structure of SiN_x films. This section first reviews the structural properties by examining its correlation to the N/Si ratio, where SiN_x films were prepared by several deposition techniques. Fourier transform infrared (FTIR) spectroscopy is used in this thesis to characterise the bond structure, and the basic principles for characterisation and analysis are then described in Section 2.3.4.

2.3.1 [Si–N] versus N/Si ratio

Several publications have concluded that the Si–N bond density (i.e., [Si–N]) of SiN_x affects bulk passivation in the underlying silicon wafer [10, 33-36]. Hong *et al.* showed that higher densities of SiN_x improves the bulk passivation [35], whereas Romijn *et al.* found an optimum [Si–N] of 1.3×10^{23} cm^{-3} for bulk passivation [36]. Since the [Si–N] is related to the mass density [30], Romijn *et al.* explained that films with lower [Si–N] are insufficiently dense to prevent H_2 formed in the film from effusing into the ambient. On the other hand, in films with higher [Si–N] (i.e., denser films), the diffusivity of atomic hydrogen is too low for a good bulk passivation during short firing. Even though no direct proof of this hypothesis has

been established, it remains the most plausible explanation for the relationship between film density and bulk passivation by SiN_x.

The [Si–N] also appears to be crucial for the thermal stability of surface passivation [37]. Weeber *et al.* [37] showed that good surface passivation by as-deposited SiN_x can be obtained for films with lower [Si–N], but that the surface passivation is not stable after long thermal annealing, presumably due to a substantial loss of hydrogen. On the contrary, for the SiN_x films with higher [Si–N], the surface passivation is significantly improved upon thermal annealing, even though the as-deposited surface passivation is low. Similar behaviour is also observed in this thesis, as presented in Section 4.3.2–B. Interestingly, Weeber *et al.* [37] found that the most thermally stable SiN_x had [Si–N] = 1.1×10^{23} cm^{-3}, which is approximately comparable to the optimum [Si–N] for bulk passivation.

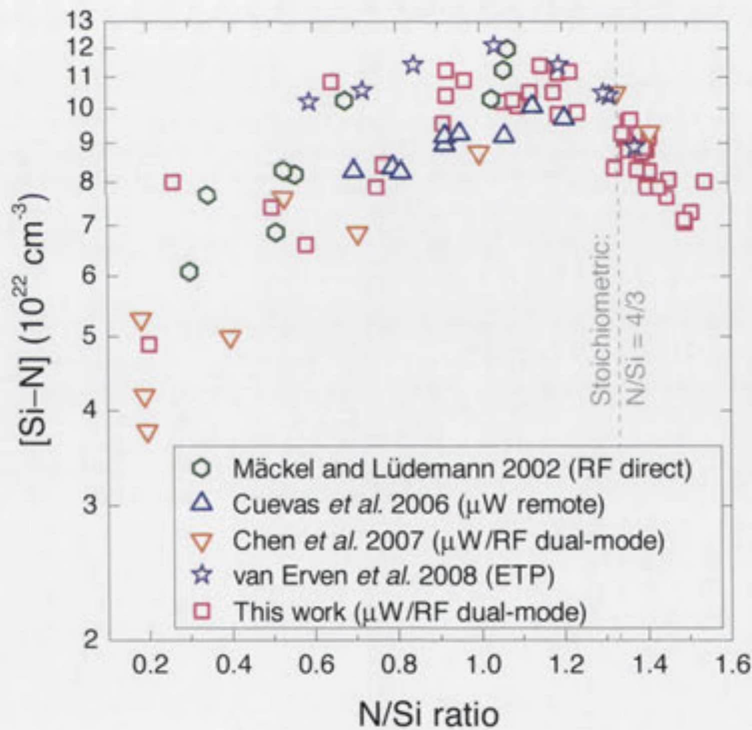

Figure 2.3: Correlation between the [Si–N] and the N/Si ratio for SiN_x films deposited by different deposition techniques: RF direct by Mäckel and Lüdemann [20], µW remote by Cuevas *et al.* [38], µW/RF dual-mode by Chen *et al.* [39], and ETP by van Erven *et al.* [30].

Figure 2.3 shows the relationship between [Si–N] and the N/Si ratio. We find that, irrespective of the deposition techniques and varied deposition conditions, [Si–N]

exhibits a universal relationship to the N/Si ratio, where the [Si–N] exhibits a peak of 1.0×10^{23}–1.2×10^{23} cm^{-3} at N/Si = 1.1 ± 0.1, corresponding to n_{632} = 2.0 ± 0.02 (calculated using Eq. 2.1). Notably, this would be the reason that industrial firing stable SiN_x commonly has n_{632} ~2.0 [40].

2.3.2 [Si–H] and [N–H] versus N/Si ratio

As discussed previously, hydrogen incorporated in SiN_x plays an important role in bulk passivation. Numerous efforts have therefore been devoted to gain knowledge on the behaviour of hydrogen within SiN_x [10, 33-37, 41-43]. Hydrogen in SiN_x is mainly bonded as Si–H and N–H. Figure 2.4 plots [Si–H] and [N–H] as a function of the N/Si ratio. It is shown that both [Si–H] and [N–H] possess a universal relationship to the N/Si ratio, whereby [Si–H] decreases and [N–H] increases strongly as the N/Si ratio increases. This comes as no surprise: it states that the concentration of N-H bonds increases as the concentration of N increases; and similarly, the concentration of Si-H bonds increases as the concentration of Si increases. Note that the trend is observed for a wide variety of deposition techniques and deposition conditions, in accordance with the behaviour of [Si–N].

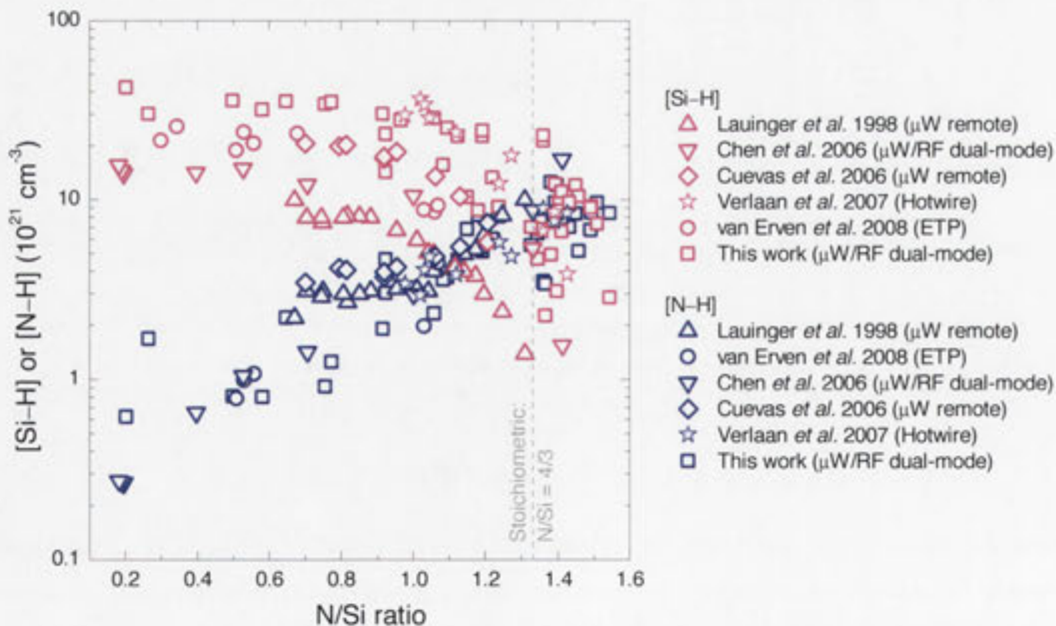

Figure 2.4: Correlation between the [Si–H], [N–H] and the N/Si ratio for SiN_x films deposited by a variety of deposition techniques: μW remote by Lauinger *et al.* [18] and Cuevas *et al.* [38], μW/RF dual-mode by Chen *et al.* [39], hotwire by Verlaan *et al.* [44], and ETP by van Erven *et al.* [30].

2.3.3 Si–H peak wavenumber versus N/Si ratio

The peak wavenumber of the Si–H stretching mode depends strongly on the back bonding of Si–H [45, 46] and is therefore a good indicator of SiN_x internal structure. Figure 2.5 plots the relationship between the Si–H peak wavenumber and the N/Si ratio, showing a universally increasing trend. The results indicate that as the N/Si ratio increases, the back bonding of N atoms to Si–H increases, as represented by the right Y-axis using the corresponding peak wavenumbers for different Si–H stretching modes presented in [46].

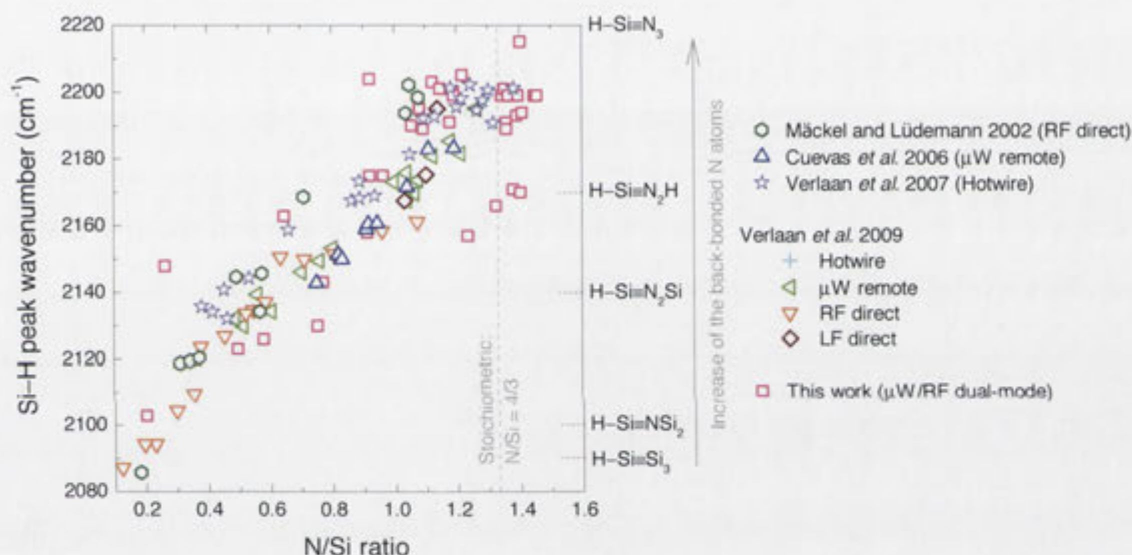

Figure 2.5: Correlation between the [Si–H] peak wavenumber and the N/Si ratio for SiN_x films deposited by different deposition techniques: RF direct by Mäckel and Lüdemann [20], µW remote by Cuevas *et al.* [38], and hotwire by Verlaan *et al.* [44]. The corresponding peak wavenumber for different Si–H stretching modes presented in [46] are presented at the right Y-axis.

2.3.4 Fourier transform infrared spectroscopy

Fourier transform infrared spectroscopy (FTIR) is applied to analyse the chemical bonds in SiN_x films. Infrared photons can be absorbed by an oscillating electrical dipole which is caused by an asymmetrical electron distribution of a chemical bond [47]. The absorbed IR energy corresponds to particular molecular vibration energy, thus allowing an identification of the bonding configuration.

In SiN_x films, there are three distinct absorption peaks associated with Si–N, Si–H and N–H vibrational modes at about 850, 2140 and 3340 cm^{-1}, respectively [46]. The bond density [A–B], defined as the number of bonds per unit volume, can be determined by $[\text{A–B}] = 2.303 \cdot d \cdot k_{\text{A–B}} \cdot \int \frac{\alpha(\omega)}{\omega}$ [48], where d is the thickness of SiN_x, $\alpha(\omega)$ is the absorption coefficient at wavenumber ω, $k_{\text{A-B}}$ is the proportionality constant in cm^{-2}, which is determined by calibrating the bond density by FTIR measurements to the density by ERD analysis. Several sets of proportionality constant have been proposed in previous works [28, 46, 49-51], and in this thesis, $k_{\text{A-B}}$ for Si–N, Si–H and N–H is taken from Ref. [46], which is the most commonly employed in the literature.

A Bruker Vertex 80V FTIR spectrometer was used to obtain the spectra over the wavenumber range of 400–4000 cm^{-1} with a resolution of 6 cm^{-1}. Correction for substrate absorption was achieved by subtraction of a measured spectrum from a bare control Si substrate. Contributions caused by ambient moisture and carbon dioxide were minimised by performing measurements in a vacuum.

2.4 Electronic properties

The surface passivation by SiN_x depends on the electronic properties, including the effective insulator charge and the interface defect states. This section reviews SiN_x electronic properties by correlating insulator charge density Q_{eff} and interface defects density D_{it} to the N/Si ratio. Capacitance–voltage (C–V) which is widely used to characterise Q_{eff} and D_{it} on planar Si surfaces is then briefly described in Section 2.4.3. In addition, the deposition of corona charge onto a passivating dielectric surface alters surface carriers concentration at the underlying silicon surface and consequently alters the surface recombination velocity. Corona–lifetime measurement, which determines Q_{eff} and provides qualitative evaluation to the D_{it}, is presented in Section 2.4.4.

2.4.1 Insulator charge density versus N/Si ratio

The presence of charge in SiN_x affects significantly the surface passivation [6]. The

host site for the charge is well-known to be the 'K-center', at which three N atoms are back-bonded to a Si atom [52, 53]. The K-center is amphoteric, inferring it can be either positively or negatively charged. In addition to any charge stored in K-centres, it is also suggested that there can be an additional positive charge stored in the bulk of the film due to oxygen-related states [54]. Furthermore, the interface defects can also contribute to the measured charge density [55-57]. The total effective insulator charge Q_{eff} determined from the flat-band voltage therefore probably consists of three parts: charge stored at K-centres, charge stored at other sites within the film, and charge stored at interface defects.

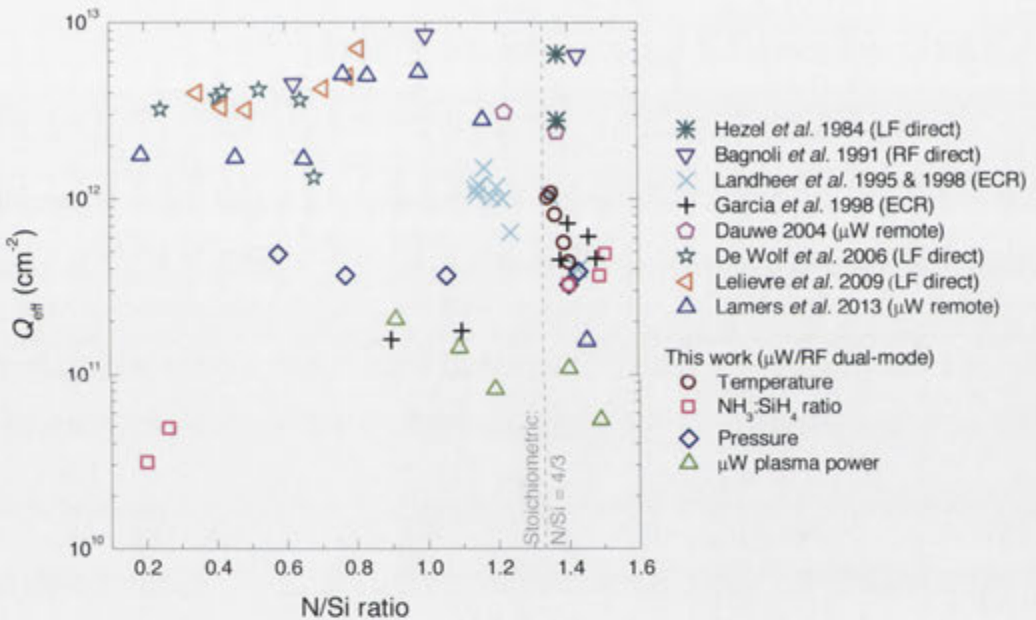

Figure 2.6: Relationship between the density of effective insulator charge Q_{eff} and the N/Si ratio for SiN_x films deposited by different deposition techniques: LF direct by Hezel *et al.* [58], De Wolf *et al.* [59], and Lelièvre *et al.* [19], RF direct by Bagnoli *et al.* [60], ECR by Landheer *et al.* [61] and Garcia *et al.* [62], μW remote by Dauwe [63] and Lamers *et al.* [64].

Even though SiN_x has been used in semiconductor devices for more than five decades, the formation of K-centres is still not established. Mäckel and Lüdemann [20] proposed the N–H to be the precursor sites for forming the K-center, and therefore predicted that Q_{eff} increases as the SiN_x becomes more N-rich. However, a thorough literature review, as summarised in Figure 2.6, reveals that there exists no universal correlation between Q_{eff} and film stoichiometry. Depending

on the deposition technique and deposition condition, for a given N/Si ratio, Q_{eff} indeed varies in a wide range by more than an order of magnitude. These large differences in Q_{eff} reported by different authors may be partly attributtable to systematic error in the quantitative determination of Q_{eff}. The experimental results for SiN_x films obtained in this thesis are also included in Figure 2.6, supporting the conclusion that Q_{eff} in SiN_x depends weakly on the N/Si ratio, but strongly on the deposition conditions. For example, when the deposition temperature was varied, no significant change in film stoichiometry was observed, whereas Q_{eff} was altered by approximately one order of magnitude. The microscopic origin of the charge centers associated with our SiN_x is discussed in Section 4.3.1–A.

2.4.2 Interface defect density versus N/Si ratio

At the SiN_x/Si interface, the Si dangling bond is considered to be the dominant defect [65-67]. This dangling bond has a three-folded configuration where the Si atom is back bonded with the three nearest neighbours either Si or N (i.e., •Si≡). Combining the electron elastic resonance (ESR) and C–V measurements on metal–SiN_x–*p*-Si structure, Jousse *et al.* [68] observed four distinct defects with different *g* values and energy levels. They also suggested that the physical origin of the observed interface defects were Si dangling bond with different back bond configurations. While the Si dangling bond with three N back bond (i.e., the K-center) lies slightly below the conduction band (E_c), the remaining three defects are located in the lower half of the silicon band gap. Using small-pulse deep-level transient spectroscopy, Schmidt *et al.* [54, 69] also observed four types of defects at the SiN_x/Si interface with different energy levels and capture cross sections of electrons to holes. Interestingly, they presented similar energy levels of the four defects to that observed by Jousse *et al.* [68]. We therefore tentatively speculate the four defects observed by the two groups are Si dangling bonds with different back bond configurations. A schematic summary of these findings is depicted in Table 2.1.

The relationship between D_{it} at midgap and the N/Si ratio is rarely found in the literature. Only three studies, the results of which are summarised in Figure 2.7, were uncovered. The experimental results for SiN_x films obtained in this thesis are

Table 2.1: Summary of four types of defects presented in [54, 69] and [68].

$E_T - E_{mid\text{-}gap}$ (eV)

−0.56 | −0.16 | −0.08 | −0.04 | 0 | 0.46 | 0.56

E_V | C | B | A | $E_{mid\text{-}gap}$ | D | E_C

	C	B	A	D
Bonding configuration	•Si≡N_2Si	•Si≡NSi_2	•Si≡Si_3	•Si≡N_3
ESR g-value	2.0044	2.0044	2.0052	2.0028
Energy level, $E_T - E_{mid\text{-}gap}$ (eV)	-0.16	-0.08	-0.04	0.46
capture cross section for electrons σ_n (cm^2)[a]	8.3×10^{-15}	3.6×10^{-14}	2.2×10^{-12}	–
capture cross section for holes σ_p (cm^2)[a]	1.3×10^{-13}	2.3×10^{-16}	1.5×10^{-17}	–

[a]The capture cross section for electrons and holes (i.e., σ_n and σ_p) contained in [69] exhibit a strong dependence on the trap energy and do not saturate. The values presented in this figure are the peaks near midgap.

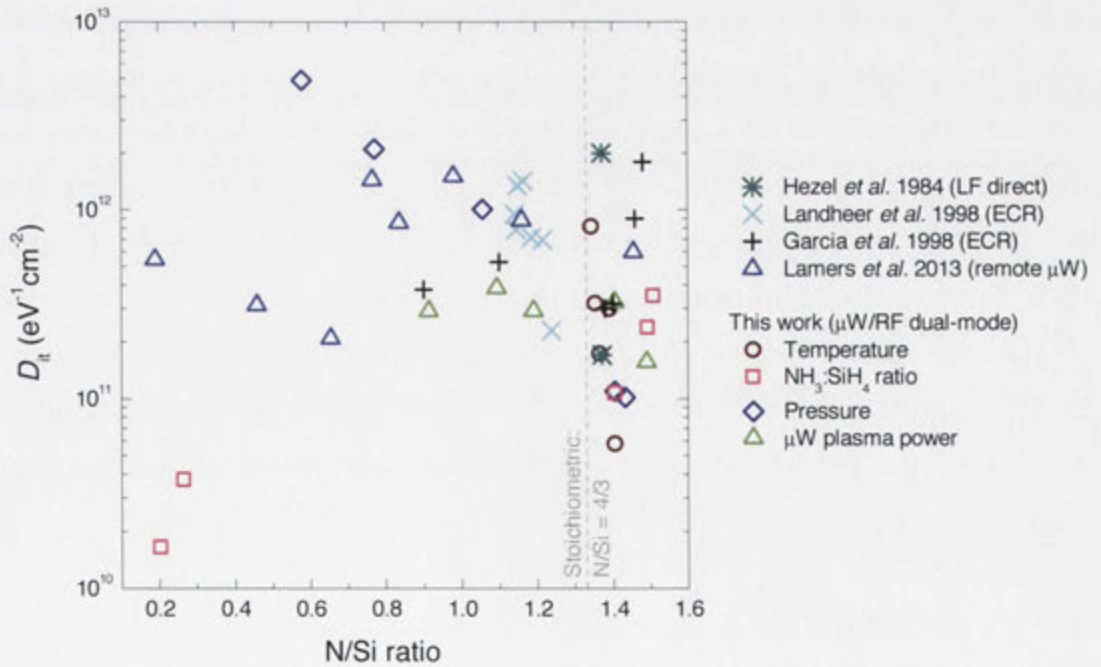

Figure 2.7: Correlation between the density of interface defects D_{it} at midgap and the N/Si ratio for SiN_x films deposited by different deposition techniques: LF direct by Hezel *et al.* [58], ECR by Landheer *et al.* [61] and Garcia *et al.* [62], µW remote by Lamers *et al.* [64].

also included. Similar to the trend of Q_{eff}, D_{it} has no universal correlation to the N/Si ratio, and instead depends strongly on the deposition conditions. The results are not surprising, given the fact that the interface defects relate presumably to the interfacial structural properties rather than to the bulk properties. Even though both the interfacial and bulk structural properties depend on the plasma conditions, the two structural properties are not necessarily correlated. This is an important observation, as it suggests an opportunity to independently optimise the performance of surface passivation and antireflection coating by SiN_x.

2.4.3 Capacitance–voltage

Capacitance–voltage (C–V) measurements of metal–insulator–semiconductor (MIS) capacitor are widely used to characterise the interface and bulk electronic properties of dielectric films [70]. In this thesis, the front metal contact was formed by evaporating aluminium through a shadow mask to create circular dots of diameter ~ 700 μm and thickness ~ 100 nm. The rear contact was formed with a GaIn eutectic. High frequency and quasistatic C–V measurements were performed using an HP 4284A Precision LCR Meter and HP 4140B Picoammeter/DC Voltage Source. Q_{eff} was calculated from the flat-band voltage, assuming that all charge was located at the SiN_x/Si interface. When films were not leaky, D_{it} at midgap was determined by applying the Castagné–Vapaille method [71] to high frequency and quasistatic C–V measurements. When films were too leaky such as Si-rich SiN_x, quasistatic C–V measurements could not be performed and therefore in this case, D_{it} was solely determined by applying the Terman method [72] to high frequency C–V measurements, typically leading to a higher measurement error. We hence treat the absolute value of D_{it} for Si-rich films in our work with caution. Nevertheless, we remain confident in the conclusions derived from this study because they rely on trends rather than absolute values of D_{it}

2.4.4 Corona–lifetime

Typically, C–V analysis is employed to probe interface electronic properties such as D_{it} and Q_{eff} on planar silicon surfaces. This method however is not suited to the

analysis of textured surfaces, mainly due to high leakage that films incur when deposited on textured silicon [56]. One alternative means to probe interface electronic properties is depositing corona charge on dielectric passivated samples and monitoring the change in surface recombination. Deposition of corona charge onto a passivating dielectric surface alters surface carriers concentration at the underlying silicon surface and consequently alters the surface recombination velocity. This method determines an effective insulator charge density Q_{eff} and provides qualitative access to the interface defect density D_{it}. The analysis procedure for the determination of D_{it} and Q_{eff} using this method on SiN_x films are described and discussed in Section 6.5.1.

2.5 Surface recombination

The silicon surface represents an abrupt disturbance of the crystal lattice. A large amount of silicon bonds remain unsaturated ('dangling'), leading to a large density of defects (surface states) within the silicon band gap [4]. The recombination of light-generated or injected carriers via defects at the silicon surface is described as surface recombination [4]. This section first presents the theory of surface recombination (Section 2.5.1), and follows with an extensive review on the relationship between surface recombination and the N/Si ratio (Section 2.5.2). Finally, the photoconductance measurement used to characterise the surface recombination is briefly introduced in Section 2.5.3.

2.5.1 Theory

Recombination of electron-hole pairs via a single defect is described by the Shockley–Read–Hall (SRH) formalism, defining the surface recombination rate U_s of carriers at a single trap energy level E_T by

$$U_s = N_{it} \cdot \frac{n_s p_s - n_i^2}{\frac{n_s + n_1}{\sigma_p v_p} + \frac{p_s + p_1}{\sigma_n v_n}}, \tag{2.3}$$

where n_s and p_s are the electron and hole concentrations at the surface, n_i is the effective intrinsic carrier concentration, n_1 and p_1 are the electron and hole concentrations that would be present if the Fermi level E_F were equal to E_T, given by $n_1 = n_i \exp((E_T - E_i)q/kT)$ and $p_1 = n_i \exp((E_i - E_T)q/kT)$, E_i is the intrinsic Fermi energy, N_{it} is the density of surface states per unit area, σ_n and σ_p are the capture cross sections for electrons and holes, v_n and v_p are the thermal velocity for electrons and holes, k is the Boltzmann constant, and T is the absolute temperature.

It is worth mentioning that, at a real silicon surface, the defects do not have exactly the same energy at all locations; instead there is a distribution of defect energies. To account for this distribution, the total recombination rate is calculated by an integration of the single-level recombination rates over all energies within the bandgap [73]. Moreover, at a real silicon surface, there usually exists electrical charges in an intrinsic overlying insulator or extrinsic applied biasing, leading to a bending of energy bands at the surface and therefore a surface space charge region. In this case, the excess carrier concentration of electrons and holes are generally not equal at the surface. The surface carrier concentrations n_s and p_s therefore have to be determined by means of numerical methods. A simplified approach, namely the extended SRH formalism firstly introduced by Grove and Fitzgerald [74] and later improved by Girisch *et al.* [75] and Aberle *et al.* [76], can be used to determine n_s and p_s.

The recombination at SiN_x-passivated Si surfaces therefore depends not only on the density and nature of the interface defects but also on the density of electrical charge in the SiN_x. As discussed in Sections 2.4.1 and 2.4.2, both Q_{eff} and D_{it} exhibit no universal correlation to the N/Si ratio. It is therefore expected that the surface recombination should not correlate to the N/Si ratio.

2.5.2 Surface recombination velocity versus N/Si ratio

In the last few decades, numerous recombination studies at SiN_x-passivated Si surfaces have been published [17-21, 77]. Figure 2.8 summarises the results by plotting the S_{eff} as a function of the N/Si ratio. Note that all S_{eff} values presented here are by as-deposited SiN_x.

As evident in Figure 2.8(a), before the presentation of our work, an apparent trend between S_{eff} and the N/Si ratio is observed: i.e., S_{eff} increases as the N/Si ratio increases. Notably, this trend occurred for several deposition techniques, as described in Refs. [17] and [19, 20]. More complicated trends can be observed for the results in Refs. [18] and [21], whereby S_{eff} first decreases with decreasing N/Si ratio and saturates for N/Si < 0.7. Nevertheless, it might be inferred from the previous results that S_{eff} decreases as the SiN_x film becomes Si-rich. In fact, this conclusion is a generally perceived misconception in the PV industry. We do not wish to reinforce this correlation, however, since it will be shown in Chapter 4 that S_{eff} does not depend on the N/Si ratio, instead it depends strongly on the choice of the deposition conditions.

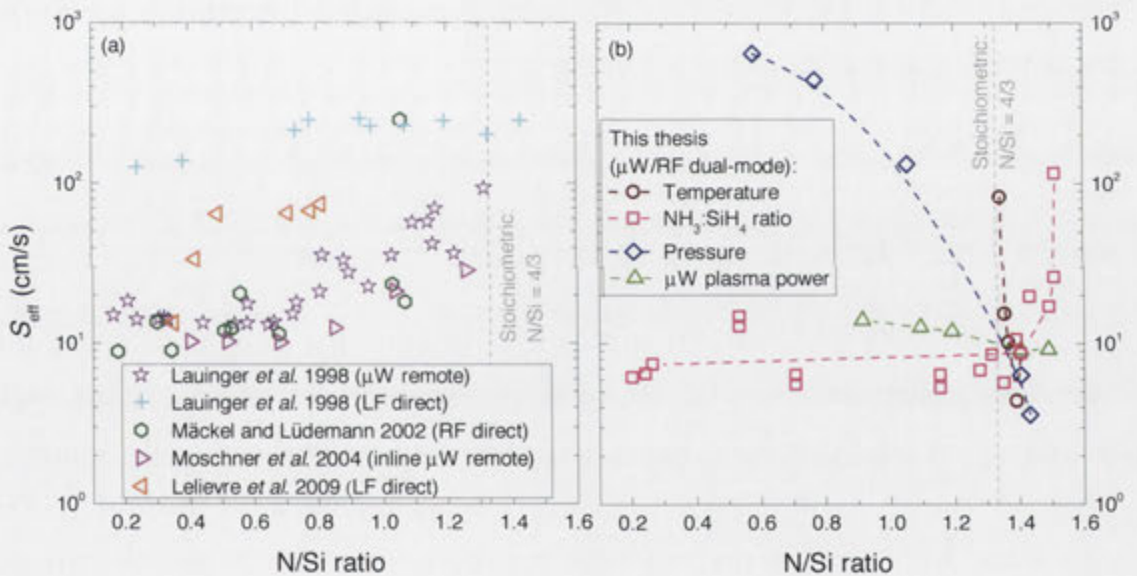

Figure 2.8: Relationship between the S_{eff} at Δn = 10^{15} cm^{-3} and the N/Si ratio for SiN_x films presented in **(a)** previous studies, and **(b)** this thesis, using different deposition techniques: μW remote by Lauinger *et al.* [18], RF direct by Mäckel and Lüdemann [20], inline μW remote by Moschner *et al.* [21], and LF direct by Lelièvre *et al.* [19].

Importantly, the varied deposition parameter in all these prior works was the reactant gas ratio. We obtain similar trend when the NH_3:SiH_4 ratio is solely varied to alter SiN_x properties. However, by varying pressure and μW plasma power, S_{eff} decreases as the N/Si ratio increases. To highlight such complicated relationships, we include our own results in Figure 2.8(b). The trends in S_{eff} and and N/Si ratio by

varying deposition parameters are discussed in more details in Secton 4.3.1 by relating them to plasma physics.

2.5.3 Photoconductance lifetime

The photoconductance (PC) lifetime measurements are extensively employed in this thesis to determine recombination properties. A Sinton WCT-120 PC tool is employed to measure the effective lifetime τ_{eff} as a function of excess carrier density Δn. The details on the tool configurations as well as on the measurement procedures, can be found in [78].

For a high quality undiffused silicon substrate such as FZ Si with the same surface passivation on each side, the effective surface recombination velocity S_{eff} can be extracted from the PC lifetime measurement. Assuming a uniform Δn across the test sample, S_{eff} can be extracted according to

$$S_{eff} = \frac{w}{2}\left(\frac{1}{\tau_{eff}} - \frac{1}{\tau_{bulk}}\right), \tag{2.4}$$

where w is the thickness of silicon substrate, τ_{bulk} is the bulk lifetime in Si.

The bulk lifetime in Si is usually unknown and assumed to be infinite, giving the theoretical upper limit of S_{eff}. A more precise approach is to assume bulk recombination only constitutes intrinsic recombination—radiative and Coulomb-enhanced Auger recombination, ignoring the contribution of extrinsic SRH recombination. Several parameterisations have been reported to model the intrinsic recombination rate in Si [79-81]. However, as the Si substrate quality and passivation techniques have been improved, it is clear these parameterisations have led to the intrinsic recombination being overestimated. Based on the literature and their own experimental lifetime measurements, Richter *et al.* [82] have recently proposed an improved parameterisation for the intrinsic recombination rate in Si. We employ this most recent parameterisation throughout this thesis to determine the upper limit to surface recombination velocity $S_{eff,UL}$.

When the silicon surface is heavily doped (diffused), the saturation current density J_0 can be extracted from the PC lifetime measurement by employing the technique developed by Kane and Swanson [83]:

$$\frac{1}{\tau_{\mathrm{eff}}} - \frac{1}{\tau_{\mathrm{bulk}}} = \left(\frac{2J_0}{qn_i^2 w}\right)\left(\Delta n + N_{dop}\right), \tag{2.5}$$

where N_{dop} is the bulk dopant concentration of an identically diffused and passivated silicon sample. The J_0 can hence be determined from the slope of the relationship between $\frac{1}{\tau_{\mathrm{eff}}} - \frac{1}{\tau_{\mathrm{bulk}}}$ and $\Delta n + N_{\mathrm{dop}}$.

2.6 Chapter summary

In this chapter, the SiN_x properties and characterisation techniques were reviewed and discussed, providing a background for understanding and analysing the experimental data presented in the subsequent chapters. By correlating SiN_x properties to the N/Si ratio, it was shown that (*i*) irrespective of deposition techniques and deposition conditions, the bulk structural and optical properties are universally correlated to the N/Si ratio; and (*ii*) the bulk and interface electronic properties including Q_{eff}, D_{it} and $S_{\mathrm{eff,UL}}$ appear independent of the N/Si ratio. The film properties of SiN_x prepared by a μW/RF dual-mode PECVD are investigated extensively in this thesis, with an emphasis on the optical and recombination properties.

PECVD reactor configuration and preparation

3.1 Introduction

Silicon nitride film properties vary enormously depending on the deposition conditions, which themselves depend strongly on the reactor configuration and preparation procedures [6, 7]. In the PV industry, several types of reactor configurations are employed and they exhibit a strong impact on surface passivation by SiN_x. Moreover, the preparation of a PECVD reactor and the silicon samples is an important component of the deposition of SiN_x. For example, cleaning and outgassing of the reactor can reduce the concentration of impurities that are likely to induce recombination centres [84]. It is therefore important to examine the impact of *(i)* the reactor configuration and preparation, and *(ii)* the silicon sample preparation, on surface passivation by SiN_x.

In this chapter, a review of PECVD reactors for the deposition of SiN_x is presented. The reactor configurations for laboratory and inline PECVD reactors are introduced, and followed by a comparative study on the impact of reactor configurations on surface passivation. After describing a deposition cycle for SiN_x and the associated chemical reactions, the impact of preparation procedures for the reactor and silicon sample on the surface passivation quality are evaluated, resulting in a robust procedure to enable good surface passivation. The improved preparation procedures resulting from these preliminary studies are used extensively for all subsequent experiments in this thesis.

3.2 Plasma reactors for SiN_x deposition in the PV industry

PECVD was invented by Stirling and Swann in 1965 [85]. Since then, it has been widely employed for the fabrication of dielectric films and optical coatings. This includes single-layer, multilayer, and gradient-index thin-film systems for applications such as optical filters, antireflective coatings and optical waveguides. Besides their basic optical properties, dielectric films synthesised by PECVD also offers other desirable characteristics. These include good adhesion to technologically important substrate materials such as silicon, and long-term thermal and environmental stability for the application of a barrier capping layer [11-14].

In this section, the PECVD reactor configurations used to deposit SiN_x films in the PV industry are described in Section 3.2.1 and the impact of the plasma source and reactor configuration on the surface passivation is discussed in Section 3.2.2.

3.2.1 Types of PECVD reactor

PECVD is a material synthesis process in which gas-phase constituents react with a surface to form a thin film [86]. An electromagnetic glow discharge is employed to transfer energy into the reactant gases promoting chemical reactions. The reactant gases employed in this technique are typically silane (SiH_4) and either ammonia (NH_3) or nitrogen (N_2). Sometimes, noble gas diluents such as Ar or He are also added to enhance the dissociation and ionisation of reactant gases.

Deposition parameters such as the reactant gas flow, pressure, plasma power and excitation frequency can be varied to alter the plasma chemistry. Typical excitation frequencies employed in PECVD processes are 10–500 KHz (low frequency: LF), 13.56 MHz (radio frequency: RF) and 2.45 GHz (microwave frequency: μW). Regarding the plasma reactor configuration, there are two distinctive designs: direct and remote. Recently, a μW/RF dual-mode PECVD reactor has been employed in PV research [84].

Table 3.1 classifies PECVD reactors into four categories based on the reactor configuration and plasma source. In the next section, we review and discuss the impact of these types of PECVD reactors on the surface passivation by SiN_x.

A. Direct PECVD

In a direct PECVD reactor, the reactant gases are excited by an electromagnetic field between two parallel plates. The wafer is placed onto one of the plates and is in direct contact with the plasma. Figure 3.1 presents a schematic cross section of a direct PECVD reactor designed by Oxford Plasmalab [87].

Table 3.1: Types of PECVD reactors employed by the PV industry

Category	Reactor configuration	Plasma frequency
1	Direct	Low (50–100 kHz)
2	Direct	Radio (13.56 MHz)
3	Remote	Microwave (2.45 GHz)
4	Dual mode	Microwave (2.45 GHz) and radio (13.56 MHz)

The process can be divided into three steps: *(i)* the delivery of reactant gases, e.g. SiH_4, NH_3 into process chamber, *(ii)* the excitation of reactant gases and generation of chemically active species (SiH_a and NH_b) in the plasma region and simultaneously forming precursors molecules that contain the bonding groups of the desired SiN_x films, and *(iii)* the deposition of a SiN_x thin film onto Si substrate, which is located at a heated substrate holder. The reactor shown in Figure 3.1 is one in which the ion energy is supplied via inductive coupling. The plasma excitation frequency employed in this reactor is LF at 50–100 kHz, RF at 13.56 MHz, or a combination of both frequencies. The direct PECVD configuration was first employed to deposit SiN_x on solar cells by Hezel and Schorner in 1981 [9]. It was then found by Kyocera to improve mc-Si wafer quality due to a hydrogenation of bulk defects such as some of the grain boundaries [88]. The first investigation of surface passivation by direct PECVD SiN_x was performed by Lauinger *et al.* [89]. As will be summarised in Section 3.2.2, they demonstrated that SiN_x deposited at RF provides significantly better surface passivation than when deposited at LF.

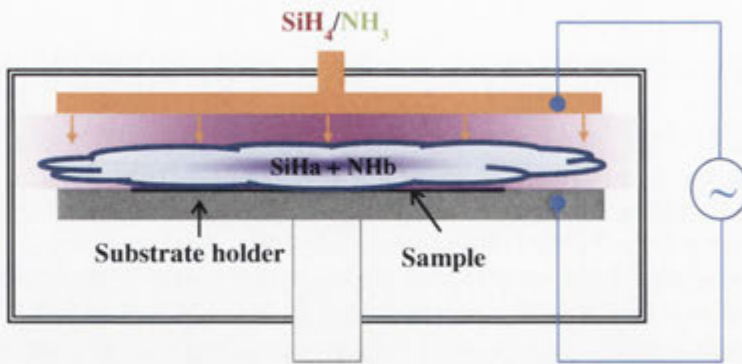

Figure 3.1: schematic cross section of a direct PECVD reactor designed by Oxford Plasmalab.

B. Remote PECVD

Figure 3.2 presents a schematic cross section of a remote PECVD reactor employed in [18]. In the remote-plasma reactor, excitation of the plasma is spatially separated from the substrate. The process can be divided into four steps: *(i)* the excitation of reactant gases (NH_3) and generation of chemically active species (NH_b), in the plasma region/cavity at a μW frequency, *(ii)* the extraction of active species (NH_b) into the process chamber due to the pressure difference at the plasma cavity and process chamber, *(iii)* the dissociation of SiH_4 to SiH_b by energetic NH_b and simultaneously mixing with NH_b to form precursors molecules that contain the bonding groups of the desired SiN_x films, and *(iv)* the deposition of a SiN_x thin film onto Si substrate, which is located at a heated substrate holder. Since the substrate is not in direct contact with the plasma in this design, the substrate is not bombarded with ions and surface damage is avoided. Other benefits of the remote reactor include the ability to generate a higher plasma density, a faster growth rate, and superior uniformity [90].

Remote PECVD reactors have been extended to permit in-line processing, where all depositions are carried out dynamically (i.e., onto the continuously moving carrier) [21]. A linear microwave plasma source consists of two parallel quartz tubes with a copper antenna inside [91]. The source is operated at a μW frequency of 2.45 GHz. One advantage of an in-line reactor is that the plasma excitation and wafer

transportation are decoupled, enabling high throughput. More details on this type of reactor can be found in Refs [17, 21, 91].

The first study into the surface passivation by remote PECVD SiN_x was undertaken by Lauinger *et al.* [8]. They attained $S_{eff,UL}$ = 13.1 cm/s on 1.5 Ω·cm *p*-Si substrates for SiN_x with n_{632} = 2.3. A comparable surface passivation level was demonstrated by Moschner *et al.* and Duttagupta *et al.* [17, 21], as to be discussed in Section 3.2.2.

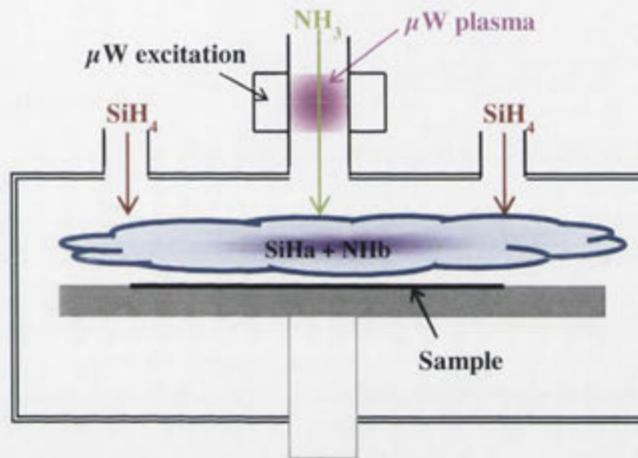

Figure 3.2: Schematic cross section of a lab-scale remote PECVD reactor employed in [18].

C. Dual-mode PECVD

In addition to the two abovementioned PECVD reactors, there is another reactor that combines the two, called a dual-mode PECVD reactor. This reactor is featured in a lab-scale PECVD reactor from Roth & Rau, namely the AK-400, which is used for all the experiments in this study. Figure 3.3 contains a schematic cross section of this system. The reactor consists of two gas inlets: *(i)* a gas shower at the top for the injection of NH_3 and/or Ar, and *(ii)* a gas ring at the bottom for the injection of SiH_4. The plasma is excited around the quartz tubes by means of two continuous-wave magnetron microwave generators with a frequency of 2.45 GHz, introducing up to 2000 W of microwave power into the process chamber. The RF plasma is excited near the graphite substrate by means of a generator with a frequency of 13.56 MHz, creating a bias voltage of up to 300 V between the substrate and the ground. Since the plasma excitation occurs inside the deposition chamber, it is not

a purely remote reactor, and since the substrate is not in direct contact with the microwave plasma, it is not a purely direct reactor. Instead, this reactor is classified as a dual-mode PECVD reactor.

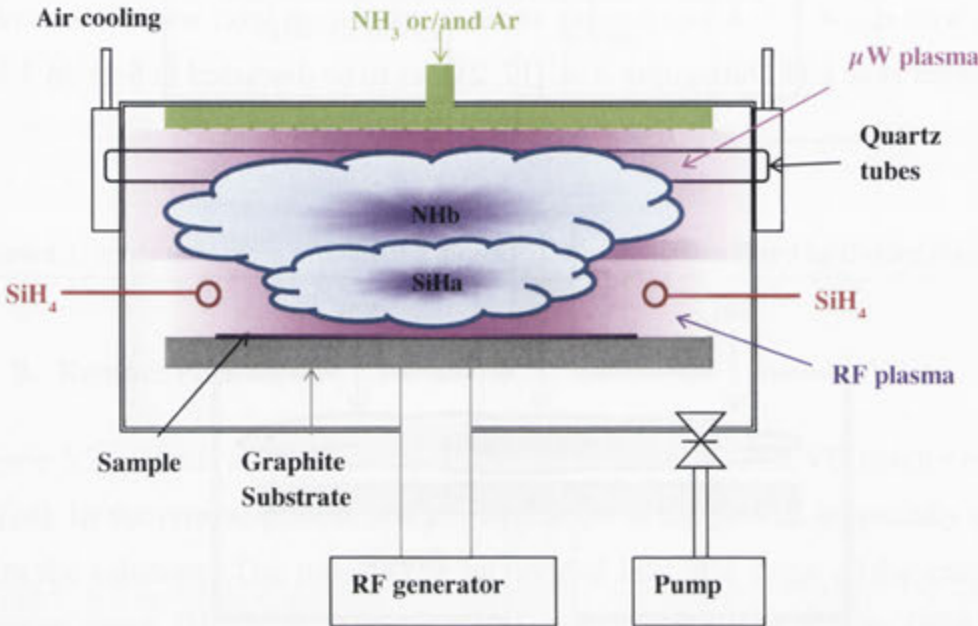

Figure 3.3: Schematic representation of a μW/RF dual-mode PECVD reactor employed in this thesis.

The process can be divided into three steps:

(i) Excitation of reactant gases and generation of chemically active species:

- NH_3/Ar are injected from the top shower head and dissociated into NH_b radicals,
- SiH_4 is injected from the gas ring and dissociated into SiH_a radicals;

(ii) Formation of an a-Si-like layer on the silicon wafer by SiH_a radicals and simultaneous insertion with NH_b radicals;

(iii) Deposition of SiN_x film by surface reactions at the sample located on a heated substrate holder.

Before this thesis, the best passivation on undiffused Si attained by a dual-mode reactor had a $S_{eff,UL}$ of 3.5 cm/s on 1.0-Ω·cm *n*-Si for SiN_x with a high n_{632} of 2.8 [92].

We achieved a comparable surface passivation on both *p*-Si and *n*-Si with SiN_x films of a broad range of n_{632} = 1.87–4.1, as to be presented in Chapter 5.

3.2.2 Impact of reactors on surface passivation

In the last two decades, an enormous effort has been devoted to improving the surface passivation by SiN_x. Figure 3.4 summarises the results that have been achieved by various reactors, with an adaption of the results plotted in Figure 2.8 according to the reactor classification. All the samples are {100}-oriented FZ *p*-Si wafers with a range of resistivity (0.85–5.0 Ω·cm). Details of the bulk resistivity are also included in Figure 3.4. To fairly compare the surface passivation quality among these works, we recalculated $S_{eff,UL}$ using the latest Auger parameterisation given in Richter *et al.* [82]. Note that in all of the experiments contained in Figure 3.4, the range of SiN_x refractive indices was attained by varying the reactant gas ratio.

We first observe that films deposited by LF direct reactor have a higher $S_{eff,UL}$ than the films deposited by the other three types of reactors. This has been attributed to the silicon surface damage caused by ion bombardment at low plasma excitation frequency [54, 93]. The reason is that below the plasma frequency (~ 4 MHz), ions are able to follow the plasma excitation frequency and therefore produce a strong surface bombardment. On the contrary, the acceleration periods for the ions generated by the excitation frequencies above 4 MHz are too short to absorb a significant amount of energy, mitigating the direct surface bombardment.

We next observe that SiN_x deposited by lab-scale RF direct and μW remote reactors provide similar surface passivation on low-resistivity *p*-Si wafers. This behaviour is consistent for SiN_x deposited by inline μW remote reactor. For the SiN_x deposited by a dual-mode reactor employed in this thesis, $S_{eff,UL}$ on the very low resistivity *p*-Si samples is slightly lower than $S_{eff,UL}$ obtained by SiN_x deposited by RF direct or μW remote reactors. As will be demonstrated in Chapter 4, the key reason that superior SiN_x films have been attained with the dual-mode reactor is that the deposition pressure has been optimised.

Finally, we observe that $S_{eff,UL}$ decreases as n_{632} increases (or more specifically, as the NH_3:SiH_4 ratio decreases), irrespective of the reactors. In Chapter 5 we attribute this behaviour to a reduced incorporation of NH_b radicals into SiN_x network.

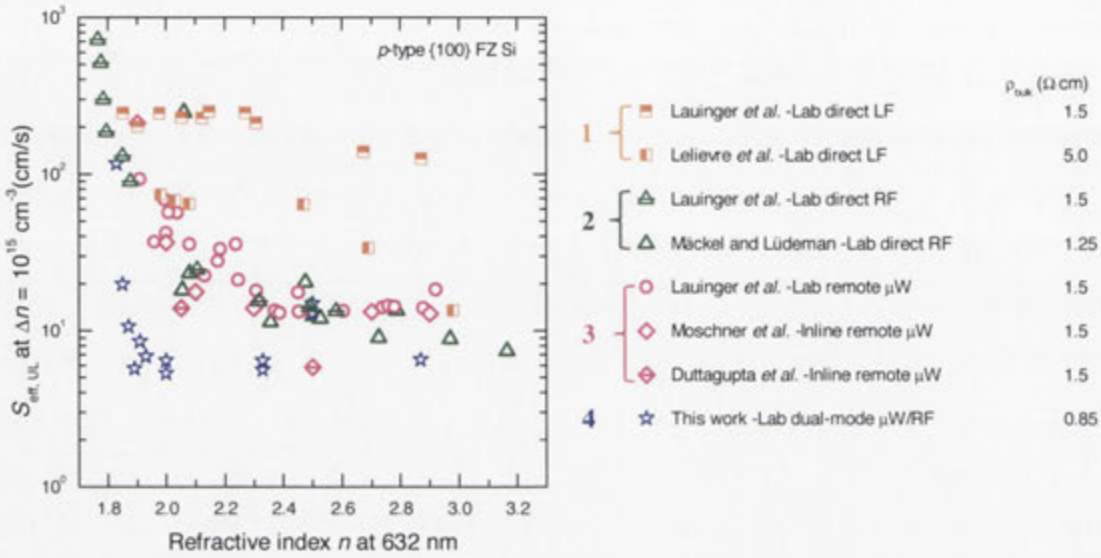

Figure 3.4: The impact of reactors on the surface passivation by SiN_x films via examining the relationship between $S_{eff,UL}$ and n_{632}. Note that all the SiN_x refractive indices shown in this figure were altered by varying reactant gas ratio.

3.3 SiN_x deposition cycle and chemical reaction scheme

3.3.1 SiN_x deposition cycle

The deposition cycle using the μW/RF dual-mode PECVD (AK-400) consists of eight steps: loading, heat-up, outgassing, gas injection, plasma ignition, film deposition, cool-down and unloading. Figure 3.5 shows how the environmental conditions change during each step, and Table 3.2 gives the value of hardware specifications and conditions at the film deposition step that was used at the commencement of this thesis (the inherited settings). The eight steps of the deposition cycle are described as follows:

1) **Loading:** During loading, the chamber door is open hence the chamber is at atmospheric pressure.

2) **Heat-up:** After sample loading, the chamber is evacuated and the heating element is switched on.

3) **Outgassing:** When the setpoint temperature is reached, the reactor is maintained at that temperature and pressure to outgas the adsorbed molecules in the chamber walls. As will be discussed in Section 3.4.1, this outgassing step is crucial to enable a good surface passivation by SiN_x.

4) **Gas injection:** Prior to the film deposition, the system takes 10 seconds to switch on all required gases until reaching the pressure setpoint.

5) **Plasma ignition:** It takes 15 seconds to ignite the RF plasma and another 10 seconds to ignite the μW plasma. Notably, during the plasma ignition step, a very thin layer of SiN_x is speculated to grow on silicon substrate. This film is too thin to be analysed by FTIR. A detailed analysis on this thin film appears warranted since the first few nanometres of the layer are of great influence on the surface passivation.

6) **Film deposition:** SiN_x is deposited through the chemical reactions presented in Section 3.3.2.

7) **Cool-down:** After the deposition of the SiN_x film, Ar gas is injected into the chamber at its maximum flow rate. The Ar gas is used not only to purge the residue NH_3 and SiH_4 gases in the chamber but also to accelerate the cool-down.

8) **Unloading:** Finally, the system is idle and at atmospheric pressure for unloading the processed samples.

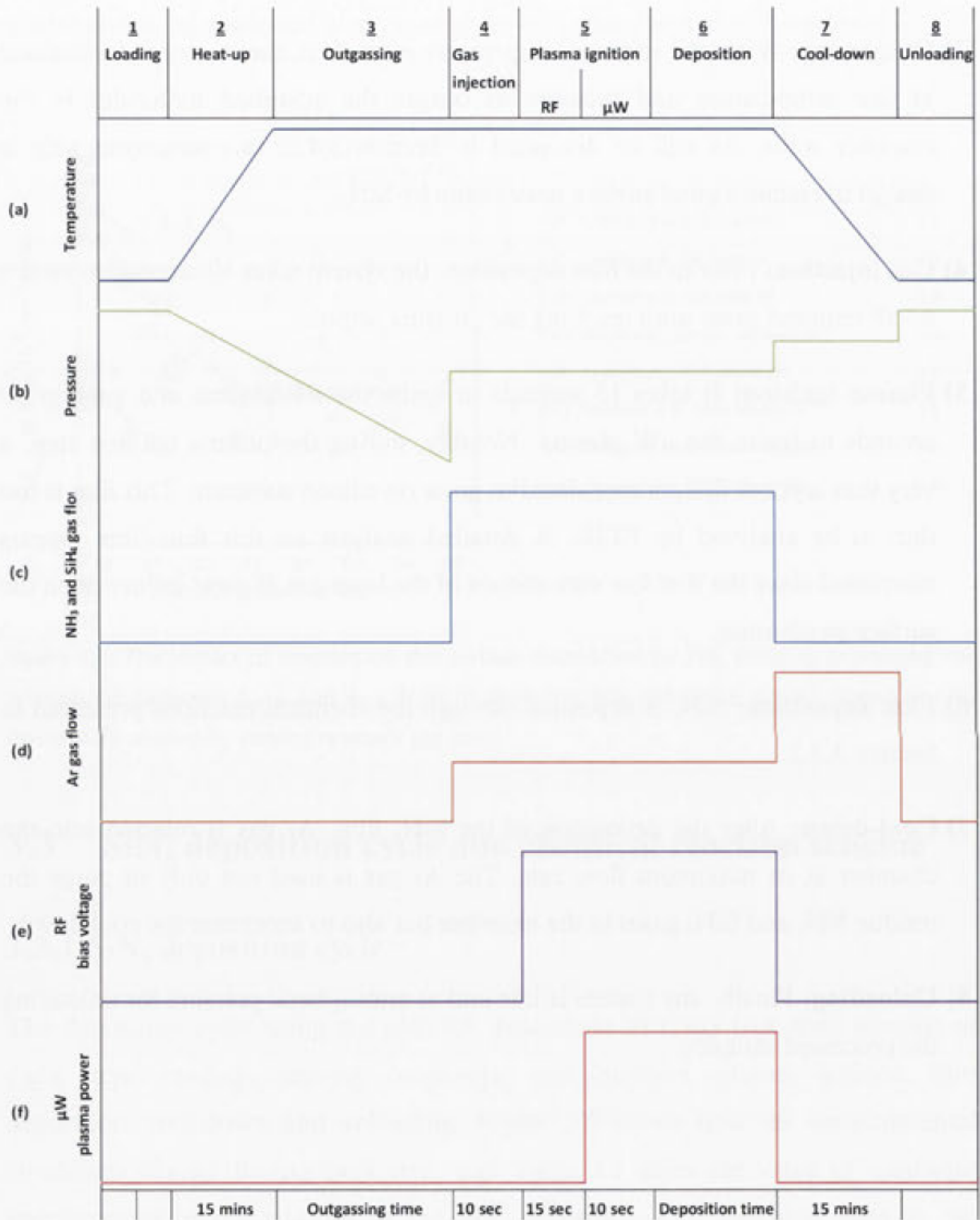

Figure 3.5: Schematic of the SiN_x deposition cycle and the deposition parameters at each step: **(a)** temperature, **(b)** pressure, **(c)** reactant gas flow, **(d)** Ar gas flow, **(e)** radio-frequency bias voltage and **(f)** microwave plasma power. Note that the width of the steps depicting process time is not drawn to scale.

Table 3.2: Manufacture specified operational range and inherited settings at the film deposition step (Step 6).

	Operational range	Inherited setting at Step 6
Temperature (°C)	25–485	235
Pressure (mbar)	0.02–1.0	0.2
NH_3 gas flow (sccm)[a]	0–140	20
SiH_4 gas flow (sccm)[a]	0–140	20
Ar gas flow (sccm)[a]	0–140	20
Total gas flow (sccm)[a]	N.A.[b]	60
μW plasma power (W)	0–1000	500
RF bias voltage (V)	0–600	150
Deposition time (min)	N.A.	3

[a]sccm denotes cubic centimetre per minute at standard temperature and pressure.

[b]The rate of total gas flow sums up the total flow rate of NH_3, SiH_4 and Ar gases.

3.3.2 Chemical reactions for SiN_x growth

In this section, we adapt the SiN_x growth model proposed by Smith *et al.* [94], Kessels *et al.* [95] and van de Oever *et al.* [96] to discuss possible chemical reactions for SiN_x growth in this thesis.

For depositions with the gas mixture of N_2 and SiH_4, Smith *et al.* [94] and Kessels *et al.* [95] proposed that an a-Si-like surface layer is created by SiH_a radicals and the a-Si-like surface is simultaneously reacted with N radicals, leading to the formation of SiN_x. van de Oever *et al.* [96] studied the plasma chemistry for the gas mixture of NH_3, SiH_4 and Ar and refined the growth model, concluding that SiN_x is formed by the direct surface reaction between the a-Si-like layer and NH_b radicals. We adapt the abovementioned models and refine a simple reaction scheme for SiN_x growth with the dual-mode PECVD reactor used in this thesis:

(I) Gas phase dissociation:

- NH_3 is introduced into the system through the shower-head which forms part of the ceiling of the deposition chamber above the μW quartz tubes and is dissociated:

$$NH_3 + e \rightarrow NH_b + (3 - b)H + e \quad \text{(a)}$$

- SiH_4 is fed from the gas ring that is between the quartz tube and RF-biased graphite substrate and is dissociated:

$$SiH_4 + e \rightarrow SiH_a + (4 - a)H + e \quad \text{(b)}$$

(II) Formation and insertion:

An a-Si-like layer is formed on the silicon wafer by SiH_a radicals and simultaneously inserted with NH_b radicals, forming precursor molecules that contain the bonding groups of the desired SiN_x films.

(III) Film densification by cross-linking:

The SiN_x precursor molecules are densified at elevated substrate temperature to break Si–H and N–H and form Si–N:

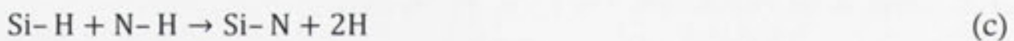

$$Si\text{-}H + N\text{-}H \rightarrow Si\text{-}N + 2H \quad \text{(c)}$$

Concurrently, the excessive incorporation of NH_b radicals breaks and replaces the existing Si–H bonds at elevated substrate temperature, forming Si–N:

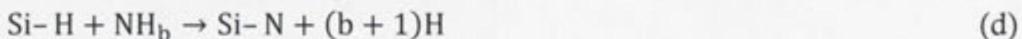

$$Si\text{-}H + NH_b \rightarrow Si\text{-}N + (b + 1)H \quad \text{(d)}$$

or otherwise, the excessive incorporation of SiH_a radicals breaks and replaces the existing N–H bonds, forming Si–N:

$$N\text{-}H + SiH_a \rightarrow Si\text{-}N + (a + 1)H \quad \text{(e)}$$

As will be presented in Section 4.3.1–B, these chemical reactions will be employed to understand the effects of deposition parameters on the film properties.

3.4 Reactor and sample preparation prior to SiN_x deposition

The preparation of the reactor and silicon samples is important for obtaining a good surface passivation. For example, cleaning and outgassing the reactor can reduce the concentration of impurities that are likely to induce recombination centres [84]. In addition, silicon surface cleaning affects significantly the surface passivation quality of the films [84]. In this section, three types of preparation procedures are evaluated in terms of the surface passivation.

The lifetime samples in this experiment were *p*-type {100} FZ-Si wafers with a resistivity of 0.85 Ω·cm and a thickness of 300 μm. All samples were etched in tetramethylammonium hydroxide (TMAH) at ~85 °C to remove saw damage. The *p*-Si samples were cleaned by the RCA procedure and diffused with phosphorus to getter iron and other metallic impurities [97]. The phosphorus glass was then removed in HF acid and the phosphorus-doped silicon layer was removed by etching in a 1:10 HF:HNO_3 solution. Next, all wafers were cleaned by the RCA procedure, dipped in HF to remove the native oxide, and then coated with the passivating SiN_x on both surfaces by two sequential depositions. Note that the passivating SiN_x is prepared using the inherited setting presented in Table 3.2. The deposition time was 3 minutes, resulting in a film thickness of 85 nm.

The effective lifetime of the samples was measured by photoconductance in the transient mode, and $S_{eff,UL}$ was calculated in accordance with Section 2.5.3. The surface passivation is quantified by plotting (a) the effective minority carrier lifetime τ_{eff} as a function of minority carrier density Δn, and (b) the extracted $S_{eff,UL}$ at $\Delta n = 10^{15}$ cm^{-3} for the samples with different process conditions.

3.4.1 Reactor outgassing before plasma ignition

As described in Section 3.3.1, no loading dock is installed in our system. The door of the plasma chamber therefore has to be kept open during loading and unloading, which exposes the interior reactor surfaces to the air. The interior surfaces adsorb

gases and vapours from the air to reduce the unfulfilled bonding forces of the surface atoms. Hence the surfaces will outgas when under vacuum and at elevated temperature. The most common outgassing molecules are water vapour and oxygen.

Outgassed molecules are a source of impurities in a vacuum chamber. The impurities might be incorporated into the SiN_x film as well as the SiN_x/Si interface, which is detrimental to the passivation quality. Before igniting the plasma sources for film deposition, a vacuum chamber has to be heated up for certain duration to remove the adsorbed molecules.

In this section, we set the outgassing temperature to 235 °C (the same as the deposition temperature) and vary the duration of the Outgassing Step (i.e., Step 3 in Section 3.3.1) to study its impact on surface passivation. Note that outgassing must also occur during ramping up and afterward at elevated temperature. The outgassing time was varied (0, 10, 20 and 40 minutes) in this experiment. Figure 3.6 presents the surface passivation results. It shows that as the outgassing time increases, the level of surface passivation provided by the SiN_x increases significantly.

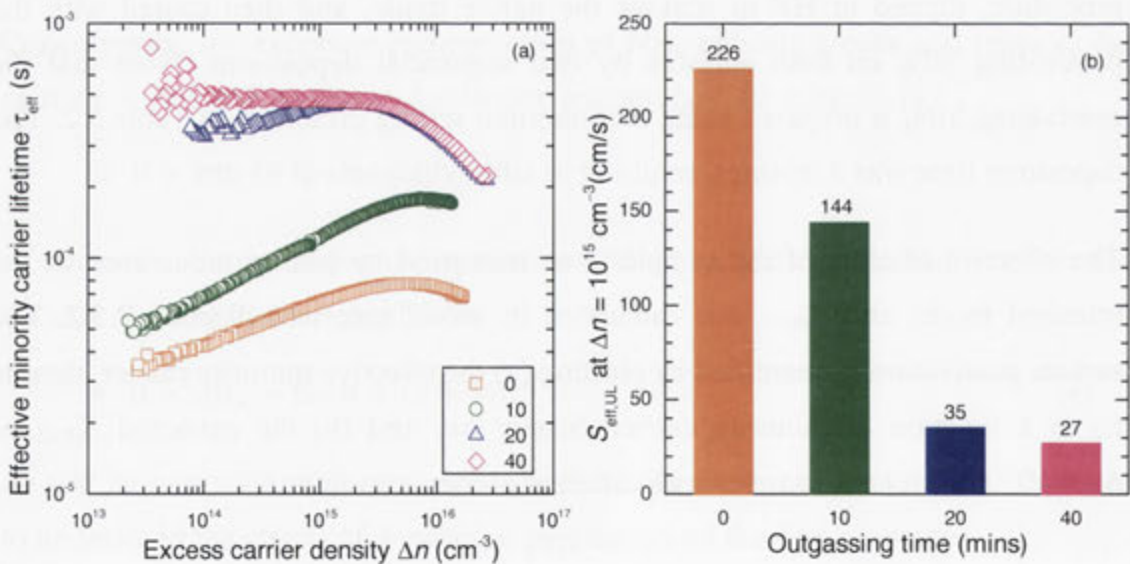

Figure 3.6: The impact of reactor outgassing before plasma ignition on the surface passivation by SiN_x by plotting **(a)** the τ_{eff} as a function of Δn, and **(b)** the extracted $S_{eff,UL}$ at $\Delta n = 10^{15}$ cm^{-3} against the time of outgassing. Note that the passivating SiN_x is prepared using the inherited settings presented in Table 3.2.

Without the Outgassing Step, the sample possesses a high $S_{eff,UL}$ of 226 cm/s at $\Delta n = 10^{15}$ cm^{-3}. Additionally, we also visually observe yellow powder on both sides of the sample, implying that the outgassed molecules affect strongly the composition of the deposited SiN_x films. When the duration of the Outgassing Step was 10 minutes, the level of surface passivation is improved significantly with $S_{eff,UL}$ = 144 cm/s. Meanwhile, the amount of yellow powder is markedly reduced. This is a strong indication of the importance of chamber outgassing on the surface passivation by SiN_x. Moreover, when the Outgassing Step was 20 minutes, further improvement in surface passivation is achieved with $S_{eff,UL}$ = 35 cm/s. Notably, in this case, no yellow powder is observed on the sample. Finally, when the Outgassing Step was further increased to 40 minutes, a slight enhancement in surface passivation is observed with $S_{eff,UL}$ = 27 cm/s.

The results suggest that the impurities resulting from insufficient outgassing before plasma ignition are detrimental to the surface passivation. The results also indicate that an outgassing time of at least 20 minutes is necessary to remove most of the adsorbed molecules, yielding a reasonably good surface passivation. The duration used for the Outgassing Step in all the subsequent experiments of this thesis is 20 minutes.

3.4.2 Silicon surface treatment before loading

Prior to SiN_x deposition, the silicon samples are commonly cleaned with RCA 1 and RCA 2 to remove particulates and metal contamination [98]. However, a thin layer of chemical oxide typically forms during this cleaning procedure [98]. The chemical oxide consequently causes poor surface passivation [99, 100]. A short dip in HF acid (< 5 seconds) is therefore employed to strip off the remaining oxide. Recent works by Angermann's group also revealed that the interface defect density on initially H-terminated {100} c-Si surfaces increased strongly after 60 minutes storage time in air [99, 100], attributable to the growth of native oxide.

In addition to the chemical oxide formed in RCA solutions, the silicon surfaces are also oxidised when the bare samples are exposed to air, forming a thin native oxide. The exposure of samples to air occurs when *(i)* transferring samples from the chemical bench to the PECVD loading bench, and *(ii)* waiting for the reactor to

vent to atmosphere pressure. The estimated time for the two actions is about 2 minutes.

In this section, the effect of silicon surface treatment on the surface passivation from SiN_x is evaluated. The growth of native oxide in air was controlled by exposing the samples to the air for different durations. The impact of the chemical oxide that is formed during the RCA cleans is also included for comparison. Figure 3.7 shows the results. After RCA cleaning of all samples, Sample 1 was loaded into chamber immediately after a short dip in HF. Note that there remained a short period (~ 2 minutes for venting chamber) when a native oxide could grow. This sample exhibits the best surface passivation, yielding $S_{eff,UL}$ = 17 cm/s. Sample 2 and 3 received a short dip in HF and then were exposed to the air for 1 hour and 3 hours, respectively, leading to the formation of a thin oxide layer on samples. Whereas Sample 2 exhibits slight degradation in surface passivation, the passivation degrades further for Sample 3. Finally, When Sample 4 was loaded into PECVD chamber without dipping in HF, leaving a chemical oxide on silicon substrate, the highest $S_{eff,UL}$ among the samples in this experiment is observed.

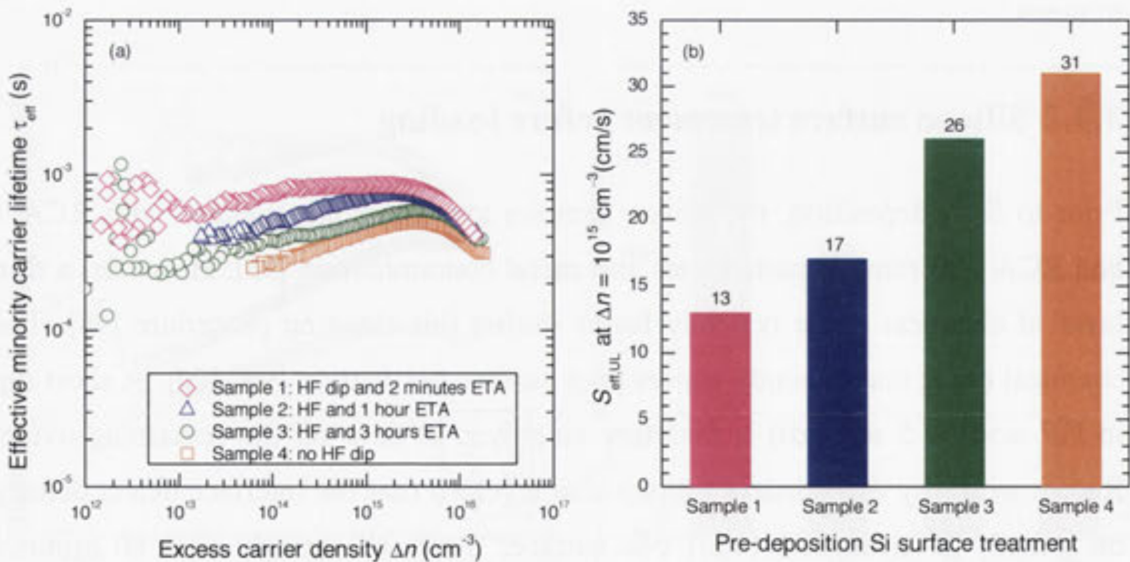

Figure 3.7: The impact of silicon surface treatment on the surface passivation by SiN_x by plotting **(a)** the τ_{eff} as a function of Δn, and **(b)** the extracted $S_{eff,UL}$ at $\Delta n = 10^{15}$ cm^{-3} against Si surface treatment procedures. "ETA" in the legend stands for "exposure to air".

The results indicate that both the native oxide grown in air and the chemical oxide grown in RCA solutions have deleterious effect on the surface passivation by SiN_x, consistent with the results presented in [100]. The avoidance of the growth of chemical and native oxide is therefore crucial for a good surface passivation. Samples used in all subsequent experiments in this thesis are treated with a short HF dip and ~2 minutes unavoidable exposure to air.

It is worth noting that $S_{eff,UL}$ for the stack of PECVD SiN_x/RCA SiO_2 is still reasonably low (31 cm/s), which is sufficient for the passivation of most the industrial silicon solar cells. Indeed, Mihailetchi *et al.* [101] has found that the stack of SiN_x and chemical SiO_2 grown in nitric acid is able to provide good passivation of boron diffused surfaces. Based on the reasonably good passivation of *p*-type undiffused surfaces, the stack of SiN_x/RCA SiO_2 may also suitable for the passivation of boron-diffused surfaces.

3.4.3 Post-cleaning chamber coating

Subsequent film depositions cause an accumulation of deposited films on the interior reactor surfaces, leading to a peeling-off of the film residue or powder from the chamber wall, quartz tube, gas shower and ring, surrounding ceramic insulator and shielding metal plates. This film residue or powder might introduce impurities into the SiN_x/Si interface and hence recombination centres. In order to attain good surface passivation by SiN_x, it is necessary to remove the accumulated films. The cleaning procedures include scrubbing, outgassing and coating of the interior chamber surfaces. It has been found that after cleaning and outgassing, the chamber should be coated with a SiN_x that is known to provide good surface passivation [84]. In this experiment, we re-examine the post-cleaning chamber coating procedure. It is found that the best surface passivation is given by SiN_x that is deposited after coating with six layers of passivating SiN_x followed by a gradient-index film.

Four *p*-Si samples were used in this experiment to examine the impact of chamber coating on the surface passivation. Before each passivation test, the abovementioned parts in the chamber were manually scrubbed using abrasive pads. The graphite substrate was soaked in diluted HF acid to remove SiN_x residue and

powder. All parts were then reassembled and outgassed at 235 °C until the base pressure reached 10^{-4} mbar. Figure 3.8 presents the results.

Sample 1, for which no layer was coated on the chamber walls, exhibits the highest $S_{eff,UL}$ of 259 cm/s. When the chamber was coated with a single layer of passivating SiN_x, the surface passivation for Sample 2 is improved greatly, showing one order of magnitude reduction in $S_{eff,UL}$ with a value of 22 cm/s. The result clearly implies that coating of chamber has a strong impact on surface passivation. Moreover, when the chamber was coated with six layers of passivating SiN_x (i.e., Sample 3), further improvement in surface passivation is achieved, yielding an $S_{eff,UL}$ = 10 cm/s. For Sample 4, we coated the chamber with six layers of passivating SiN_x, followed by a gradient-index film that consists of a range of refractive indices. The n_{632} are 1.9, 2.3, 2.9 and 4.1. It is found that the surface passivation is further improved, yielding an $S_{eff,UL}$ of 3 cm/s.

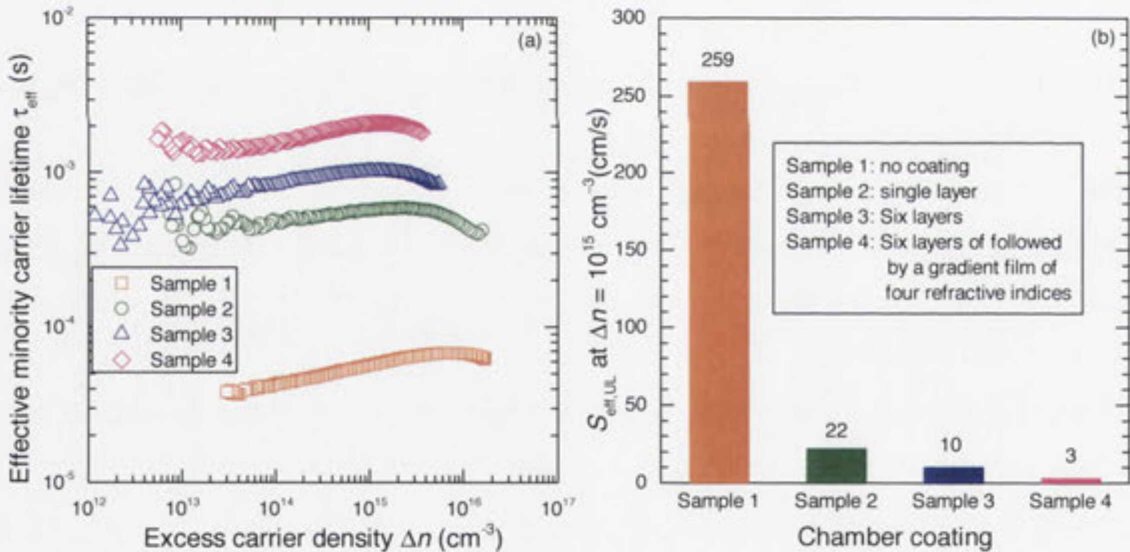

Figure 3.8: The impact of chamber coating on the surface passivation by SiN_x by plotting **(a)** the τ_{eff} as a function of Δn, and **(b)** the extracted $S_{eff,UL}$ at $\Delta n = 10^{15}$ cm^{-3} against chamber coating conditions.

In summary, we find that the post-cleaning chamber coating affects significantly the surface passivation. After manually cleaning and thermally outgassing of the interior chamber surfaces, chamber coating with six layers of passivating SiN_x and a

gradient-index film provides the best reactor condition for surface passivation by SiN_x. This procedure was followed for all subsequent experiments in this thesis.

3.5 Chapter summary

In this chapter, we reviewed the literature in the area of PECVD of SiN_x with an emphasis on surface passivation of Si solar cells. Section 3.2 presented the reactors for laboratory and inline PECVD and their impacts on surface passivation. It is found that, on low resistivity *p*-Si wafers, SiN_x deposited by RF direct and μW remote reactors provide similar surface passivation, and better than the films deposited by LF direct reactor.

Section 3.3 focused on the description of a dual-mode PECVD reactor that will be used extensively in this thesis. After describing details of deposition cycle, the chemical reactions for SiN_x deposition were discussed.

Section 3.4 examined the impact of three procedures in the preparation of the reactor and silicon sample on surface passivation. The improved procedures resulting from the preliminary experiments are summarised in Table 3.3 and are to be used in all subsequent experiments in this thesis. The procedures are reasonably reproducible as confirmed by the experimental results presented in next three chapters. Note that the three experiments presented below were preliminary investigations with a focus on optimising surface passivation quality by SiN_x, and therefore the impact of the three preparation procedures on optical, structural, or electronic properties of SiN_x was not undertaken in details. As summarised in Section 8.3, these detailed characterisations warrants further investigation.

Table 3.3: Summary of the optimised procedures for the preparation of the chamber and Si samples.

Preparation	Improved procedure for surface passivation	Section
Outgassing Step	The duration at Outgassing Step is 20 minutes.	3.4.1
Silicon surface treatment	The RCA-cleaned samples receive a short dip in HF and an immediate loading into chamber.	3.4.2
Post-cleaning chamber coating	A chamber coating with six layers of passivating SiN_x and a gradient-index film provides the best condition for surface passivation by SiN_x.	3.4.3

Chapter 4

Effect of deposition conditions on SiN_x properties

4.1 Introduction

Armed with the robust preparation procedures developed in Chapter 3, the focus of this chapter is to examine the effect of the deposition conditions on SiN_x film properties. In particular, we emphasise the optical and surface passivation properties, both of which are of primary importance to silicon solar cells.

A systematic study of the dependence of SiN_x properties on deposition conditions is presented in Section 4.3. It is shown that *(i)* S_{eff} does not correlate universally to the chemical bond density and refractive index; and *(ii)* S_{eff} depends primarily on the defect density at the SiN_x/Si interface rather than the insulator charge. The most important implication of this finding is the opportunity of decoupling SiN_x surface recombination and optical transmission properties and therefore circumventing the trade-off between the two properties.

We demonstrate a low $S_{eff,UL}$ of 1.6 cm/s on 0.85-Ω·cm *p*-type and immeasurably low $S_{eff,UL}$ on 0.45-Ω·cm *n*-type silicon substrates through an extensive optimisation of the deposition conditions. The effective carrier lifetime of *n*-type samples exceeds the recently proposed intrinsic upper limit over a wide range of excess carrier densities [82]. Importantly, the highly passivating SiN_x has a stoichiometric composition (i.e., n_{632} = 1.93) and a negligible absorption of sunlight spectrum above 360 nm.

A brief characterisation of the optimum SiN_x is also presented, where *(i)* C–V measurements reveal that $D_{it} = 3.0 \times 10^{11}$ $eV^{-1}cm^{-2}$ at midgap and $Q_{eff} = 5.6 \times 10^{11}$ cm^{-2}; *(ii)* either Defect A or B (or both) observed by Schmidt *et al.* [69] is likely to dominate the surface recombination rate at the SiN_x/Si interface; and *(iii)* compared to the Si-rich SiN_x (n_{632} = 2.5) with equivalent passivation, the optimised SiN_x would enhance the photo-generated current density by more than 0.66 mA/cm^2 or 1.40 mA/cm^2 for solar cells encapsulated in glass/EVA or operating in air, respectively. The SiN_x described here is ideally suited for high-efficiency solar cells, which require good surface passivation and low absorption from their front surface coatings.

4.2 Experimental details

For the optimisation of six deposition parameters, we performed a fractional factorial design-of-experiment method called a central composition experiment (CCE). The use of a CCE greatly reduces the number of samples required while still allowing all the main effects to be investigated [102]. The experiment consisted of 28 different deposition conditions (parameter sets) and four additional replications of the baseline. Each set of experiments involved varying one deposition parameter while keeping the other parameters constant and at their baseline value. Table 4.1 presents the baseline and range of the deposition parameters varied in this section. It is common to have an offset between the set-point of the substrate table temperature and the actual silicon sample temperature [18, 21], so all deposition temperatures reported here refer to the actual wafer temperature measured by an external calibrated thermocouple, and not to the reactor's set-point temperature (see Appendix B).

The lifetime samples in this experiment were *p*-type {100} FZ-Si wafers with a resistivity of 0.85 Ω·cm and a thickness of 300 μm. All samples were etched in tetramethylammonium hydroxide (TMAH) at ~85 °C to remove saw damage. The *p*-Si samples were cleaned by the RCA procedure and diffused with phosphorus to getter iron and other metallic impurities [97]. The phosphorus glass was then removed in HF acid and the phosphorus-doped silicon layer was removed by

Table 4.1: Baseline and tested range of PECVD deposition parameter.

	Baseline	Range
Temperature (°C)	235	165–405
Pressure (mbar)	0.2	0.02–0.50
NH_3/SiH_4 gas flow ratio[a]	1.0	0.3–3.0
Total gas flow (sccm)[b, c]	60	30–240
μW plasma power (W)	500	50–1000
RF Bias voltage (V)	150	75–250

[a] Ar gas flow is constant at 20 sccm.

[b] Total gas flow includes NH_3, SiH_4 and Ar.

[c] sccm denotes cubic centimetre per minute at standard temperature and pressure.

etching in a 1:10 HF:HNO_3 solution. For experiments in Section 4.4, in addition to the *p*-Si wafers, *n*-type {100} FZ-Si substrates with a resistivity of 0.45 Ω·cm and a thickness of 235 μm are also included. Note that no phosphorus diffusion step was applied on *n*-Si samples, since *n*-Si has a lower sensitivity to metal contaminants than *p*-Si [103]. Next, all wafers were cleaned by the RCA procedure, dipped in HF to remove the native oxide, and then coated with SiN_x on both surfaces by two sequential depositions. Note that before the deposition of the SiN_x films, the PECVD reactor and silicon samples were prepared in accordance with Section 3.4. The effective lifetime of the samples was then measured by photoconductance in the transient mode, and the $S_{eff,UL}$ was calculated in accordance with Section 2.5.3.

Reflectance, FTIR, and C–V measurements were performed on double-sided polished *n*-type {100} FZ-Si with a resistivity of 1.0 Ω·cm and a thickness of 290 μm. The sample preparation, characterisation and analysis of the three measurements were undertaken in accordance with Sections 2.2.3, 2.3.4 and 2.4.3, respectively.

The diagrams in Figure 4.1 and 4.2 summarise respectively the testing structures and processing flow of the samples used in this chapter.

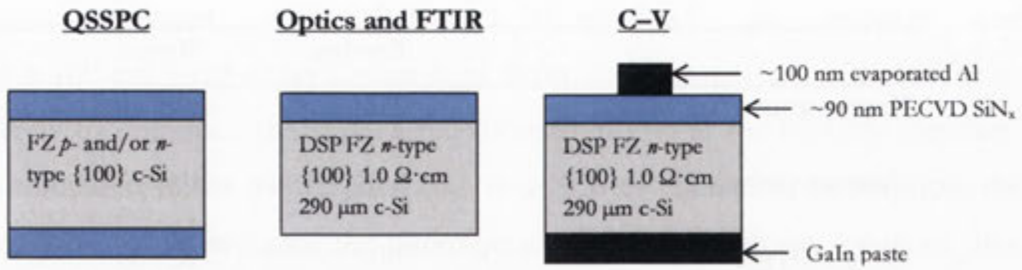

Figure 4.1: Diagram of silicon substrates and test structures used in this chapter.

FZ {100}, 0.8 Ω·cm, 300 μm *p*-Si

FZ {100}, 0.45 Ω·cm, 235 μm *n*-Si

FZ {100}, 1.0 Ω·cm, 290 μm DSP *n*-Si

Bulk gettering

RCA1, RCA 2 & HF dip

Front SiN_x

Spectrophotometer (n, k & t); and FTIR (chemical bond density)

Rear SiN_x

Front Al evaporation

Rear GaIn paste

QSSPC (τ_{eff})

C–V (D_{it}, Q_{eff})

Figure 4.2: Flow diagram of sample preparations used in this chapter.

4.3 Central composition experiment

It is well-known that SiN_x properties depend strongly on the deposition conditions [93]. For example, the refractive index of SiN_x can be altered over a wide range by varying reactant gas flow ratio [18, 20]. Extensive characterisation of a μW remote PECVD was undertaken by Lauinger *et al.*, where the deposition temperatures, pressure, plasma power, total gas flow and NH_3:SiH_4 ratio were varied to examine their effect on SiN_x properties such as deposition rate, refractive index and surface passivation. Similar studies on a RF direct PECVD were performed by Kerr [78] with the focus on surface passivation and optical properties for the application in silicon solar cells. Systematic characterisation of a μW/RF dual-mode PECVD has not been published. This gap is filled by the experimental work presented in this section, including further insights on the SiN_x/Si interface and bulk electronic properties.

4.3.1 Dependence of SiN_x properties on deposition conditions

This section presents the dependence of SiN_x film properties on deposition conditions. The experimental results are described in Section 4.3.1–A, while the underlying causes for these dependences are discussed in Section 4.3.1–B.

A. Results

Figure 4.3 plots the dependence of the deposition rate, bond densities, optical and surface recombination properties of plasma SiN_x on the various deposition parameters. The experimental results are now described.

Deposition rate—For throughput considerations, the deposition rate by PECVD should be high. Figure 4.3(a) shows the effect of deposition parameters on the deposition rate. The deposition time for all conditions was 3 min, and the resulting film thickness ranged from 50 to 200 nm. We find that increasing the total gas flow, within the range tested, causes a threefold increase in the deposition rate. The factor increase is ~2 for the decrease of NH_3:SiH_4 ratio and smaller (~1.2) for the variation of other parameters.

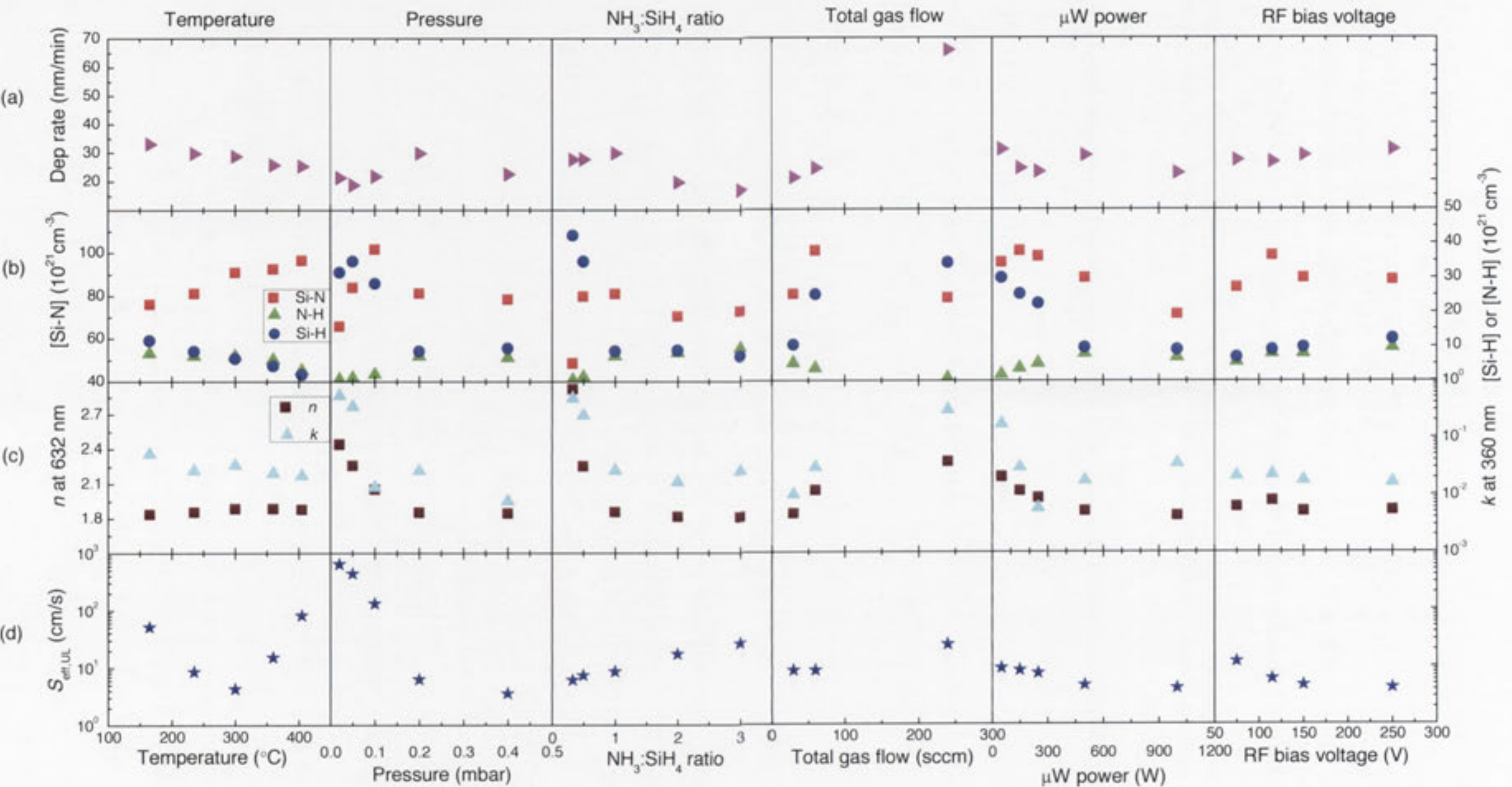

Figure 4.3: The effect of deposition conditions on SiN_x **(a)** deposition rate, **(b)** chemical bond densities, **(c)** n_{632} and k_{360}, and **(d)** extracted surface recombination velocity $S_{eff,UL}$ at $\Delta n = 10^{15}$ cm^{-3} on FZ, 0.85 Ω·cm, {100} 300 µm *p*-Si.

Bond densities—Figure 4.3(b) shows the influence of deposition parameters on the SiN_x chemical bond densities, namely [Si–N], [N–H] and [Si–H]. [Si–N] exhibits a peak within the tested range of all the parameters, except for temperature, for which [Si–N] increases as temperature increases. When deposition pressure, NH_3:SiH_4 ratio, and plasma power are increased, and when total gas flow is decreased, the hydrogen-bond concentrations, [N–H] and [Si–H] tend to exhibit inverse relationships, where [N–H] increases moderately and [Si–H] decreases strongly. This trend is consistent with the films becoming less Si-rich. Exceptions to this inverse correlation is that both [N–H] and [Si–H] decrease moderately as temperature increases and RF bias decreases.

Optical properties—Figure 4.3(c) depicts the responses of n_{632} and k_{360} to the deposition parameters. As we can see, n_{632} decreases strongly with increasing NH_3:SiH_4 ratio, μW plasma power, pressure, and total gas flow, whereas it is hardly affected by the variation of deposition temperature and RF bias voltage. Moreover, Figure 4.4(a) and (b) show the wavelength-dependent refractive index n and extinction coefficient k. The results are consistent with those reported in other studies [29, 104, 105], showing a decrease of n and k with increasing wavelength. As expected, SiN_x of low n_{632} (≤ 2.0) exhibits low absorption of short-wavelength light and almost negligible absorption at wavelengths above 360 nm, implying it is better suited as the ARC in solar cells. In addition, we find that, irrespective of the variation of deposition parameters, an increase of k_{360} is generally accompanied by an increase of n_{632} as made clearer with Figure 4.4(c).

Surface recombination—Figure 4.3(d) plots $S_{eff,UL}$ of the as-deposited SiN_x. It indicates that $S_{eff,UL}$ depends strongly on deposition temperature, pressure, and NH_3:SiH_4 ratio, and slightly on total gas flow, μW plasma power, and RF bias voltage. Whereas $S_{eff,UL}$ increases with increasing NH_3:SiH_4 ratio, $S_{eff,UL}$ decreases significantly as pressure increases. An optimum deposition temperature is observed at 300 °C, leading to a minimum $S_{eff,UL}$.

Figure 4.5 shows the injection-dependent effective lifetime $\tau_{eff}(\Delta n)$ for SiN_x-passivated p-type silicon samples. We briefly comment on how $\tau_{eff}(\Delta n)$ is affected by temperature and pressure since passivation is the most sensitive to these parameters.

For reference, the Auger limit parameterised by Richter *et al.* is also plotted [82]. We note that none of the $\tau_{\mathrm{eff}}(\Delta n)$ curves cross over except for SiN_x deposited at 405 °C, which has a maximum τ_{eff} at $\Delta n = 5 \times 10^{15}$ cm^{-3}. This means that we can meaningfully compare τ_{eff} (and hence $S_{\mathrm{eff,UL}}$ as presented in Figure 4.3(d)) at a particular Δn, such as 1×10^{15} cm^{-3}.

Figure 4.5(a) shows that the shape of the $\tau_{\mathrm{eff}}(\Delta n)$ curves diverges from the shape of the intrinsic lifetime curve as temperature increases. More specifically, there is an increasing injection dependence at low Δn, whereby τ_{eff} increases with Δn, consistent with the silicon surface being in inversion due to positive insulator charges [106, 107]. With C–V measurements, we confirm this speculation. As evident in the inset of Figure 4.5(a), Q_{eff} increases with an increase in deposition temperature. In contrast to the temperature variation, Figure 4.5(b) shows that there is no change to the injection dependence of $\tau_{\mathrm{eff}}(\Delta n)$ when pressure is varied, which correlates to a relatively constant Q_{eff}. The dependence of Q_{eff} on deposition temperature but not on pressure is in accordance with the insulator charge originating from thermal-assisted charge injection from the silicon substrate [108].

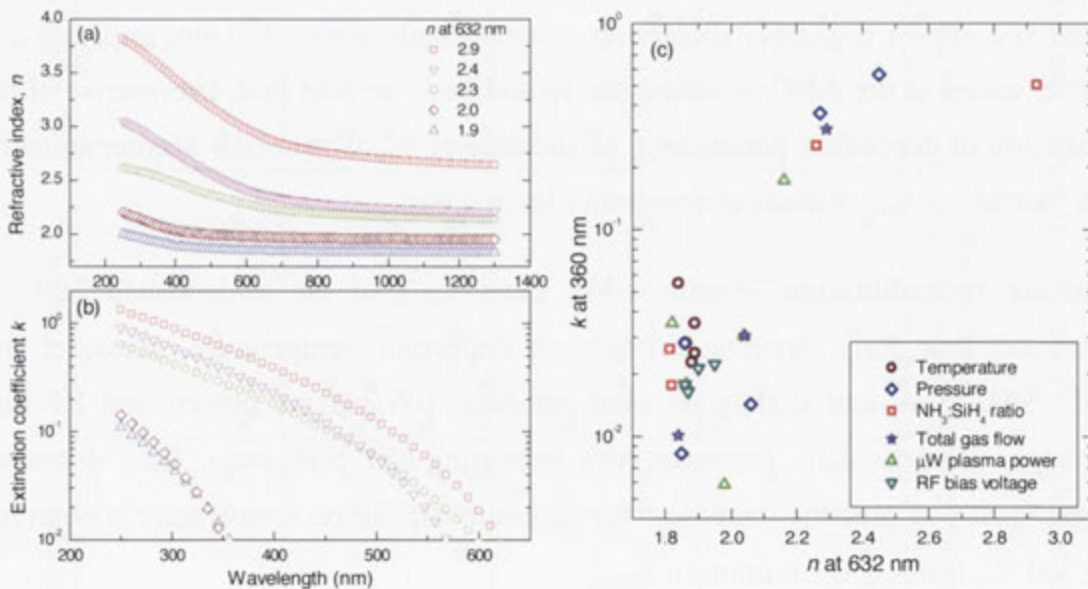

Figure 4.4: Wavelength-dependent **(a)** refractive index, and **(b)** extinction coefficient, for representative SiN_x films determined from spectrophotometry measurements. The correlation between n_{632} and k_{360} is illustrated in **(c)**.

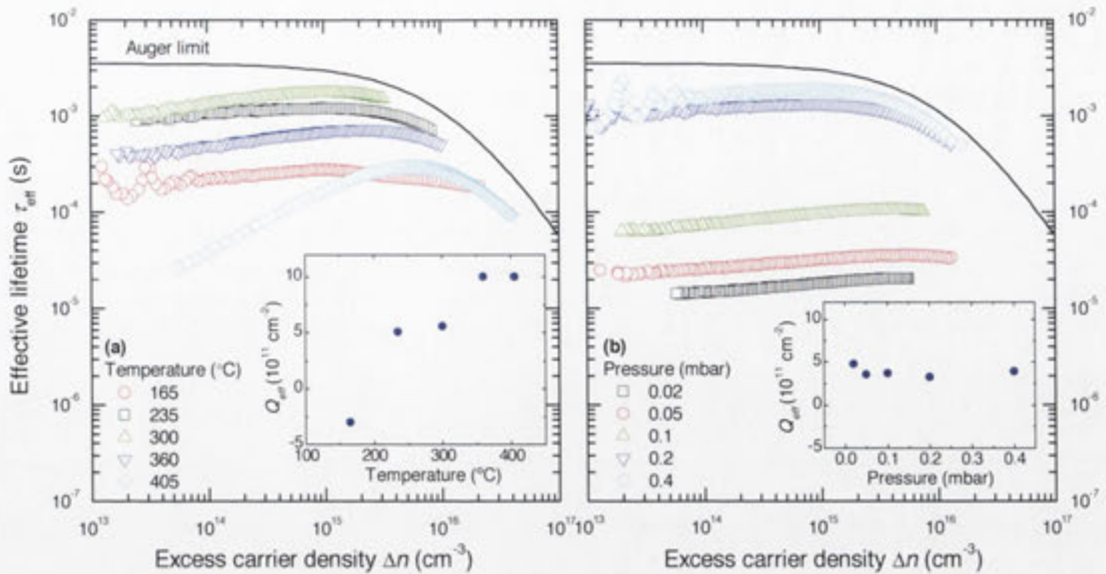

Figure 4.5: Measured τ_{eff} as a function of Δn for low resistivity *p*-type silicon (FZ, 0.85 Ω cm, {100} 300 µm). SiN_x was altered by varying **(a)** substrate temperature, and **(b)** deposition pressure. The insets demonstrate the impact of temperature and pressure on the effective insulator charge Q_{eff} in the SiN_x.

B. Discussion

We now discuss the effect of process parameters on the deposition rate and chemical bond density in relation to the chemical reactions described in Section 3.3.2. Table 4.2 summarises how deposition conditions affect the reactions and consequently the SiN_x film properties.

The **reactant gas flow ratio** is commonly varied to alter SiN_x film properties as it tailors directly the partial pressure of the resultant radicals, affecting strongly the reaction Steps I and II. As the NH_3:SiH_4 ratio increases, the proportion of NH_b radicals in the reactor increases while the proportion of SiH_a radicals decreases, leading to a higher insertion of NH_b radicals and a lower formation of a-Si-like layer. These changes are consistent with the observations in Figure 4.3, which shows that as NH_3:SiH_4 increases, *(i)* the deposition rate decreases; and *(ii)* [Si–H] decreases and [N–H] increases.

The **deposition temperature** has little effect on reaction Steps I and II but causes significant change in film densification (Step III). According to Figure 4.3(b), both [Si–H] and [N–H] decrease as the deposition temperature increases. This behaviour

Table 4.2: The effect of deposition conditions on chemical reactions and consequently the SiN_x film properties. Symbol ↑ (↓) represents enhancing (depressing) the reaction or film properties, while symbols '—' and '?' represent respectively 'little' and 'unknown' effect on the reaction or film properties.

Reaction schemes	Varying deposition condition—an increase of					
	NH_3:SiH_4	Temperature	Pressure	μW power	RF bias	Total gas flow
Step I: Gas phase dissociation						
(a) $NH_3 + e \rightarrow NH_b + (3-b)H + e$	↑	—	↑	↑	—	?
(b) $SiH_4 + e \rightarrow SiH_a + (4-a)H + e$	↓	—	—	—	—	?
Step II: Formation of SiN_x precursor molecular						
Forming an a-Si-like layer, and	↓	—	—	—	↑	↑
inserting NH_b radicals	↑	—	↑	↑	↑	?
Step III: Film densification by cross-linking						
(c) $Si{-}H + N{-}H \rightarrow Si{-}N + 2H$	—	↑	—	—	—	—
(d) $Si{-}H + NH_b \rightarrow Si{-}N + (b+1)H$	—	—	↑	↑	—	?
(e) $N{-}H + SiH_a \rightarrow Si{-}N + (a+1)H$	—	—	—	—	—	?
Changing film properties						
Deposition rate	↓	↓	—	—	↑	↑
[Si–N]	—	↑	—	—	—	—
[Si–H]	↓	↓	↓	↓	↑	↑
[N–H]	↑	↓	↑	↑	↑	↓
n & k	↓	—	↓	↓	—	↑

is attributed to the film densification through reaction (c). As temperature increases, the film is densified through the restructuring of Si–H and N–H to form Si–N. Film densification by cross-linking at elevated temperature would also result in a decrease in film thickness, as evident in Figure 4.3(a).

The influence of **deposition pressure and μW plasma power** on the hydrogen bond densities can also be elucidated from the reactions described in Section 3.3.2 and restated in Table 4.2. Changing the deposition pressure and plasma power has a strong effect on the gas phase dissociation rate and the shape of the electron distribution function [109, 110]. As pressure increases, the μW plasma becomes more confined near the quartz tubes and departs further from the downstream SiH_4 gas injection region [21]. The increase of pressure therefore enhances the dissociation of NH_3, leading to an increase in [N–H] and a decrease in [Si–H]. Moreover, the excessive incorporation of NH_b radicals (at high pressure) further reduces [Si–H] through reaction (d). We noted that Moschner *et al.* [21] observed an opposite effect of pressure on hydrogen bonds, where an increase in pressure resulted in a decrease in [N–H] and an increase in [Si–H]. This can be attributable to the dual-mode plasma sources used in this work, where the RF plasma creates a bias voltage and enhances the flux of radicals onto the substrate surface.

Next, note that NH_3 in our reactor is injected from the top shower head and is mainly dissociated by the μW plasma power through reaction (a). This geometrical setup causes an increase in μW plasma power to enhance more dissociation of NH_3 than of SiH_4. We therefore observe that [N–H] increases with the increase of μW plasma power. Again, the excessive flux of impinging NH_b radicals (at high μW plasma power) further breaks Si–H bonds through reaction (d). These conclusions are consistent with Figure 4.3(b), which shows that [N–H] increases and [Si–H] decreases when either pressure or μW plasma power is increased.

Plasma power is primarily dominated by μW plasma rather than by RF plasma in the μW/RF dual-mode reactor because the ion density in a μW plasma is more than an order of magnitude higher than in an RF plasma [110]. The main purpose of the RF plasma in our system is to create a **RF bias voltage** between the plasma and the substrate, thereby enhancing the flux of radicals onto the substrate surface

(Step II), improving the uniformity across the substrate. Based on this discussion, we are not surprised to see in Figure 4.3 that an increase in the RF bias voltage is accompanied by a slight increase in the deposition rate, [Si–H], and [N–H].

Without sufficient information on the relative amount of gas phase consumption of a precursor, also called depletion, we cannot postulate how an increase of **total gas flow** causes an increase of [Si–H] and a decrease of [N–H]. Nevertheless, the strong increase of deposition rate as well as the increase of [Si–H] with increasing total gas flow suggests that SiN_x deposition rate in our system is primarily limited by the supply of SiH_4 reactant gas, and consequently by the incorporation of SiH_a radicals.

4.3.2 Correlations between SiN_x properties

The extensive literature review on SiN_x properties presented in Chapter 2 has shown that (*i*) irrespective of deposition techniques and deposition conditions, the SiN_x structural and optical properties exhibit a universal correlation to the atomic N/Si ratio; and (*ii*) no universal relationship exists between SiN_x electronic properties including Q_{eff}, D_{it} and $S_{eff,UL}$ and the N/Si ratio. In this section, we study the correlations between SiN_x properties reported in Section 4.3.1, with an emphasis on finding any fundamental dependence of $S_{eff,UL}$ on SiN_x interface and bulk properties.

A. n_{632} versus [Si–H]/[N–H] ratio

Since an increase in n_{632} is believed to correlate to a shift in the chemical composition toward being more Si rich (see [111] and Section 2.2.1), we plot n_{632} as a function of [Si–H]/[N–H] ratio in Figure 4.6 for all deposition conditions. We can then express the results by the linear relationship

$$n_{632} = 0.0151(\pm 0.0006)\frac{[\text{Si-H}]}{[\text{N-H}]} + 1.86(\pm 0.01),$$

where the uncertainty represents the 95% confidence interval, of the linear fit. This empirical relation indicates that, over a wide range of deposition conditions, the optical properties depend primarily on the ratio of [Si–H] to [N–H] rather than

being independently correlated to [Si–N], [Si–H] and [N–H], consistent to the linear relationship presented in [25].

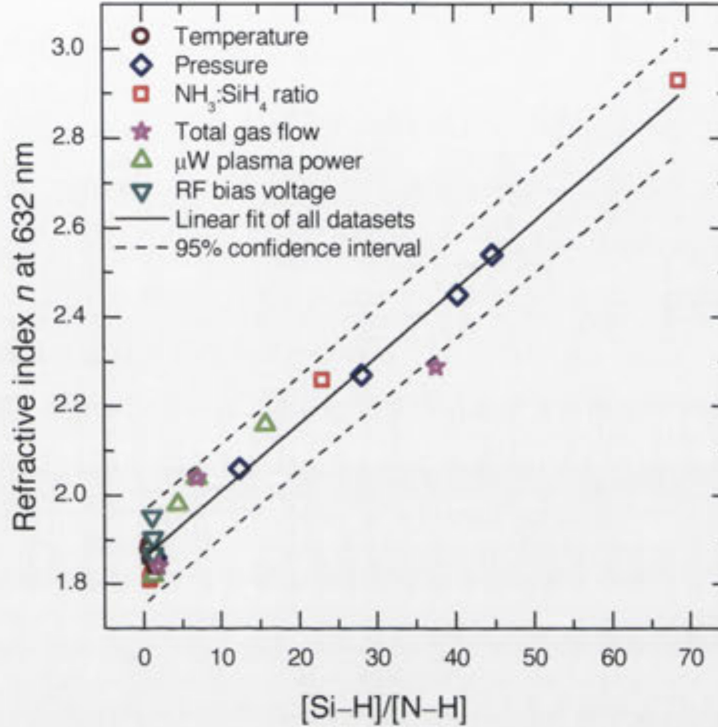

Figure 4.6: Relationship between measured n_{632} and [Si–H]/[N–H] ratio. The solid line is a linear best fit and the dashed lines are its 95% confidence intervals.

B. $S_{\mathrm{eff,UL}}$ versus chemical bond density

The [Si–H] is regularly considered as a measure of surface passivation quality, owing to the hypothesis that higher [Si–H] implies a higher probability that hydrogen terminates the Si dangling bonds at the SiN_x/Si interface [18, 20]. Lauinger *et al.* found a clear increase in τ_{eff} with an increase in n_{632}, where the increase in n_{632} corresponded to an increase of [Si–H] and a simultaneous decrease of [N–H]. This was observed both for direct and remote reactors [18, 20].

Figure 4.7 plots $S_{\mathrm{eff,UL}}$ against [Si–H] for the films in this thesis. It shows that when the NH_3:SiH_4 ratio or RF bias voltage is varied, surface passivation improves as [Si–H] increases. These results are consistent with [18, 20]. However, contrary to the trend, when other deposition parameters are varied, no consistent correlation can

be established between $S_{eff,UL}$ and [Si–H]. As evident in Figure 4.7, $S_{eff,UL}$ increases with an increase in [Si–H] when pressure and μW plasma power are varied. More complicated behaviour is induced by varying deposition temperature whereby $S_{eff,UL}$ exhibits a minimum at [Si–H] = 7×10^{21} cm^{-3}. Clearly there is no universal dependence of $S_{eff,UL}$ on [Si–H].

Similarly, no universal correlation is found between $S_{eff,UL}$ and [Si–N] for our as-deposited films. The blue squares in Figure 4.8 indicate that [Si–N] has little influence on the as-deposited SiN_x passivation. Figure 4.8 also plots $S_{eff,UL}$ against [Si–N] for the same samples after a rapid-thermal anneal (RTA) at 800 °C for 5 seconds. The results show that [Si–N] affects strongly the passivation of post-RTA SiN_x, consistent with several studies which concluded that [Si–N] has a strong influence on the surface passivation after a thermal annealing [37-39, 43]. Higher [Si–N] improves the thermal stability of SiN_x passivation, attributing to lower effusion of H_2 molecules from the denser SiN_x film into the ambient during short annealing step [33].

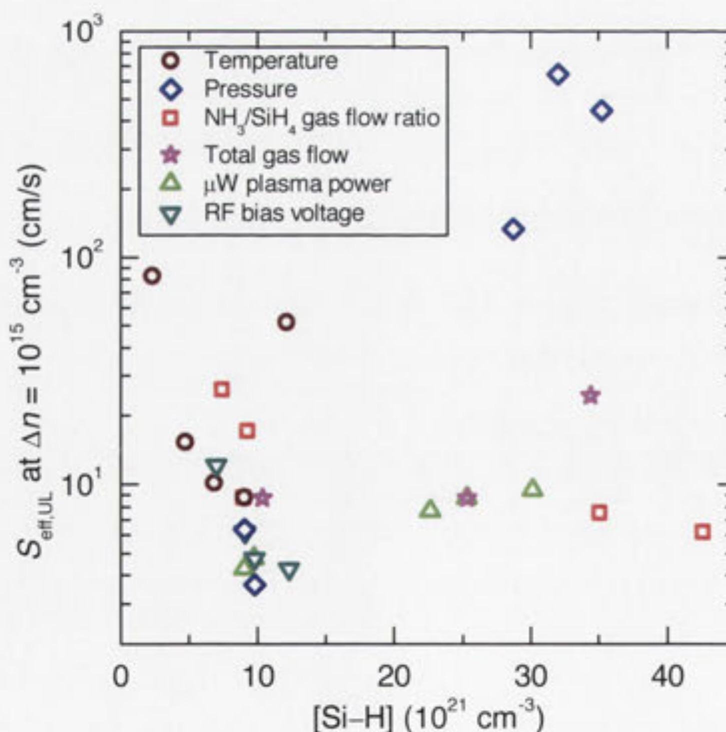

Figure 4.7: $S_{eff,UL}$ as a function of [Si–H] for SiN_x deposited at a variety of conditions.

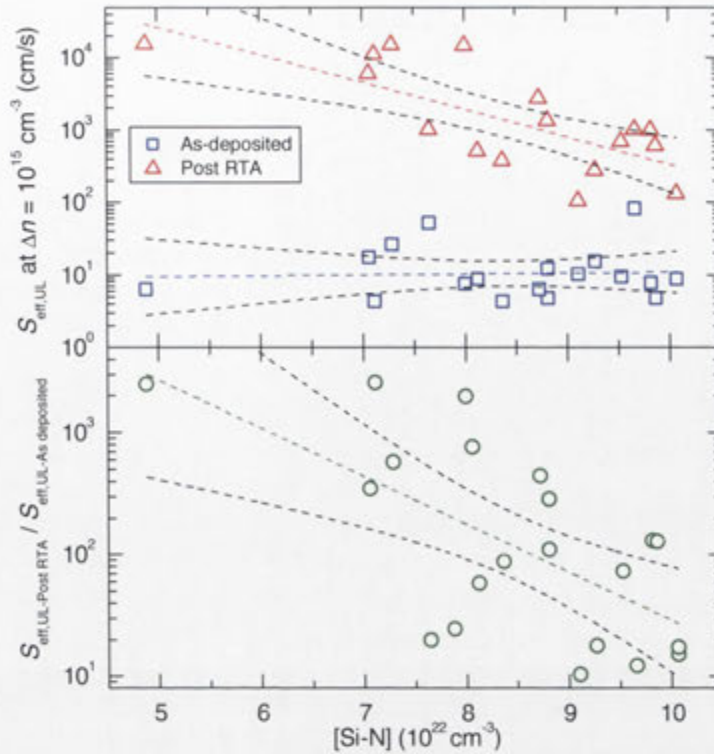

Figure 4.8: (a) $S_{eff,UL}$ for as-deposited and post-RTA SiN_x, and **(b)** the ratio between $S_{eff,UL}$ for as-deposited and post RTA SiN_x are plotted against [Si–N]. The solid line is a linear best fit and the dashed lines are its 95% confidence intervals.

C. $S_{eff,UL}$ versus n_{632}

Figure 4.9 plots $S_{eff,UL}$ against n_{632} for SiN_x films. It shows that when the NH_3:SiH_4 ratio is varied, surface passivation improves as n_{632} increases, in accordance with the results in Refs. [18] and [20]. However, contrary to the trend, when other deposition parameters are varied, no consistent correlation can be established between $S_{eff,UL}$ and n_{632}. As evident in Figure 4.9, $S_{eff,UL}$ increases with an increase in n_{632} when pressure and μW plasma power are varied. Clearly, there is no universal dependence of $S_{eff,UL}$ on n_{632}.

As illustrated in Figure 4.9, the responses of n_{632} and $S_{eff,UL}$ to various deposition conditions vary vastly, particularly to the NH_3:SiH_4 ratio, deposition pressure and silicon substrate temperature. The results indicate a chance to decouple the optical transmission and surface passivation properties of SiN_x. Section 4.4 examines the challenge of developing a single SiN_x layer that circumvents the trade-off between the two aforementioned properties.

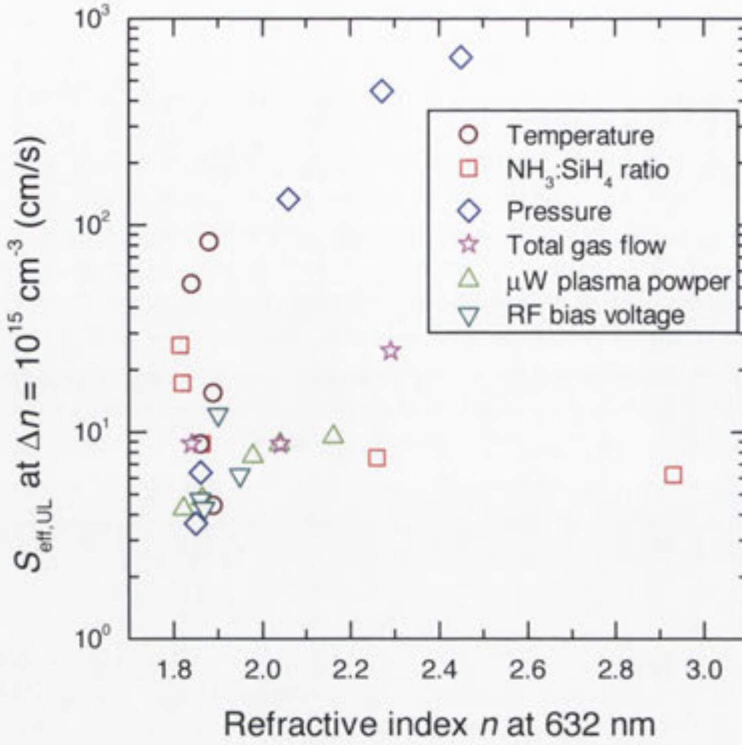

Figure 4.9: $S_{eff,UL}$ as a function of n_{632} of SiN_x deposited with a variety of conditions.

D. $S_{eff,UL}$ versus D_{it} and Q_{eff}

C–V measurements were performed on selected samples to determine D_{it} at midgap and Q_{eff} at flat-band. Quasi-static C–V measurements on typical Si-rich SiN_x could not be performed because of high leakage current. Hence, we treat the absolute value of D_{it} in our work with caution since D_{it} was solely determined by applying the Terman method [72] to high frequency C–V measurements. Nevertheless, we remain confident in the conclusions derived from this study because they rely on trends, rather than absolute values of D_{it}. As shown in Figure 4.10(a), we find that $S_{eff,UL}$ depends strongly on D_{it}, irrespective of the varied process parameters. As D_{it} increases over three orders of magnitude, $S_{eff,UL}$ increases by two orders of magnitude. However, $S_{eff,UL}$ shows different relationships with Q_{eff} when the SiN_x is altered by varying different deposition parameters. As evident in Figure 4.10(b), $S_{eff,UL}$ is almost constant as Q_{eff} increases from 3×10^9 cm^{-2} to 3×10^{11} cm^{-2}, and then exhibits two orders of magnitude variation when $Q_{eff} = 4 \times 10^{11}$ cm^{-2}. Figure 4.10 shows that recombination at SiN_x-passivated silicon surface in this work depends primarily on interface defect density rather than insulator charge.

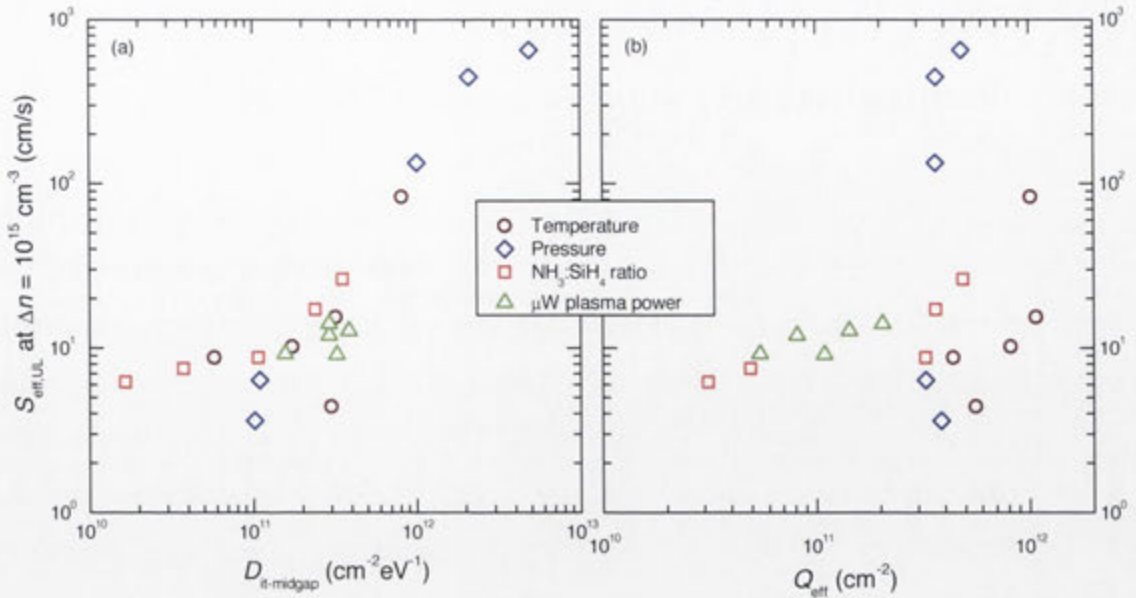

Figure 4.10: Extracted $S_{eff,UL}$ as a function of **(a)** interface defects density D_{it} at midgap, and **(b)** effective insulator charge Q_{eff} for the variation of deposition temperature, pressure, NH_3:SiH_4 ratio and µW plasma power.

4.3.3 Conclusions

This section presented an extensive characterisation of SiN_x films prepared using the dual-mode PECVD reactor, showing that the NH_3:SiH_4 ratio, deposition pressure and substrate temperature are the three key parameters in altering SiN_x optical and surface passivation properties. By studying the correlations between the structural, optical and electrical properties, it was found that for the SiN_x prepared in this work *(i)* $S_{eff,UL}$ does not display a universal correlation with the bulk structural and optical properties such as chemical bond densities and refractive index; and *(ii)* $S_{eff,UL}$ depends primarily on the defect density at the SiN_x/Si interface rather than the insulator charge. The former finding promotes an opportunity to decouple the two SiN_x properties that are of great interest to silicon solar cells: optical transmission and surface passivation. It is therefore possible to develop a SiN_x film that can provide low surface recombination as well as low optical absorption, which is the focus of the next section.

4.4 Varying pressure at optimum temperature

As presented in Section 2.5.2, low surface recombination has been achieved by various plasma techniques [8, 17, 19-21, 92]. These studies demonstrated an apparent trend: surface passivation increases as n_{632} increases. One exception to this trend was presented by Schmidt and Kerr [77, 112] who achieved $S_{eff,UL}$ of 15.2 cm/s by a stoichiometric SiN_x of n_{632} = 1.9. A key process to fabricate this SiN_x was reported to be the inclusion of N_2 with SiH_4 and NH_3 as a reactant gas. As illustrated in Figure 4.9, when the deposition pressure was varied, $S_{eff,UL}$ decreases monotonically with a decrease in n_{632}, promoting an opportunity to develop an alternative in obtaining a SiN_x film which provides low surface recombination and low optical absorption. This section therefore focuses on varying the deposition pressure at the optimum substrate temperature identified in Section 4.3.

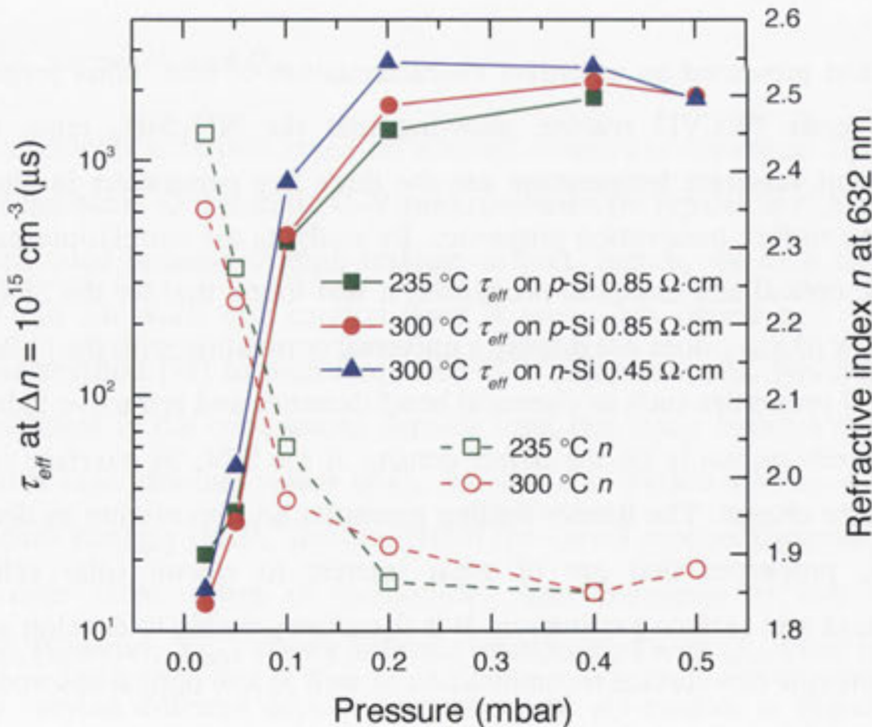

Figure 4.11: Measured τ_{eff} of FZ {100} c-Si (0.85-Ω·cm 300-µm-thick *p*-type and 0.45-Ω·cm 235-µm-thick *n*-type) passivated with SiN_x as a function of the pressure at two deposition temperatures. The n_{632} versus the pressure is also included.

Figure 4.11 depicts the impact of the pressure on τ_{eff} and n_{632} at two temperatures: 235 °C and 300 °C, where the NH_3:SiH_4 ratio is constant at 1. Note that we present τ_{eff} rather than $S_{eff,UL}$ and the reason is the highest lifetime obtained in this section exceeds the recently proposed Auger limit [82], as to be discussed in Section 4.5.1. As can be seen, τ_{eff} on *p*-Si increases as the pressure increases up to 0.4 mbar, irrespective of deposition temperature. While τ_{eff} of SiN_x deposited at 300 °C peaks at a pressure of 0.4 mbar and decreases at 0.5 mbar, τ_{eff} of 235 °C deposited SiN_x was limited to 0.4 mbar pressure, as depositions at higher pressures were found to produce excessive particulates. Interestingly, depositions at pressure higher than 0.5 mbar at 300 °C produced particulates as well. It seems this behaviour is due to the interaction of the substrate temperature and the deposition pressure. Moreover, we noticed that the spatial uniformity of the film across the graphite substrate holder (25 × 12.5 cm^2) was poor when deposited at pressure higher than 0.2 mbar. In addition, τ_{eff} on *n*-type Si passivated by 300 °C deposited SiN_x shows similar trend to that on its *p*-type counterpart but peaks at a pressure of 0.2 mbar. We therefore select an optimum deposition pressure of 0.2 mbar instead of 0.4 mbar, even though the film deposited at 0.4 mbar provides lower $S_{eff,UL}$ on *p*-Si than that at 0.2 mbar.

While surface passivation generally improves as the pressure increases, n_{632} of the SiN_x decreases. This trend gives a great opportunity to achieve an optimum SiN_x of high surface passivation and low optical absorption. Figure 4.12 plots τ_{eff} at $\Delta n = 10^{15}$ cm^{-3} versus n_{632} for the above-presented variation of pressure and the variation of NH_3:SiH_4 ratio presented in Section 4.3.1. For clarity, lifetime on *p*-Si samples is only included. A markedly different behaviour is observed from changing the two parameters. By varying the NH_3:SiH_4 ratio, τ_{eff} is observed to increase as n_{632} increases, achieving a comparable degree of surface passivation to the state-of-the-art SiN_x passivation reported to date [8, 17, 18, 77, 92]. This behaviour is consistent with the apparent trend presented in Figure 2.8(a), as is also evident in Figure 4.12. However, as mentioned previously, when the pressure is varied to alter the SiN_x properties, we observe the opposite trend: surface passivation increases with decreasing n_{632}. The trends, illustrated in Figure 4.11 and 4.12, indicate that surface passivation by SiN_x does not necessarily increase when

n_{632} increases, consistent with the finding presented in Section 4.3. In fact, these two SiN_x properties are physically independent. Whereas n_{632} depends on the SiN_x bulk properties, surface passivation depends partly on film properties near or at the SiN_x/Si interface such as D_{it} and capture cross sections [4] (also see Figure 4.10), although it also depends on Q_{eff}, which is usually a bulk property of SiN_x.

Finally, the optimum deposition condition is concluded to be 300 °C, 0.2 mbar, NH_3/SiH_4/Ar gas flow at 20/20/20 sccm, μW plasma power at 500 W and RF bias voltage at 150 V. The resultant SiN_x film has a nearly stoichiometric composition with n_{632} = 1.93 and provides high surface passivation with τ_{eff} = 1.9 ms and 2.5 ms at $\Delta n = 10^{15}$ cm^{-3} on *p*-Si and *n*-Si, respectively. The optimum deposition condition are utilised to examine the surface passivation by SiN_x on planar undiffused Si (see Chapter 5), textured undiffused Si (see Chapter 6), phosphorus-diffused planar/textured Si and IBC solar cells (see Chapter 7).

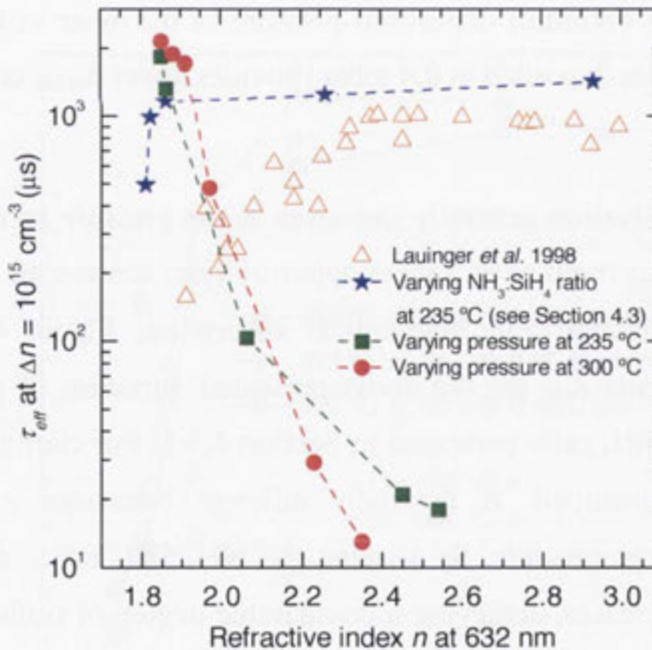

Figure 4.12: Measured τ_{eff} at $\Delta n = 10^{15}$ cm^{-3} versus n_{632} on FZ 0.85-Ω·cm *p*-type {100} silicon substrates. The variation of deposition parameters are indicated by legends. Result from Lauinger *et al.* [18] is also included.

4.5 Characterising the optimum SiN_x properties

The excellent surface passivation and optical properties reported in the previous section for the nearly stoichiometric SiN_x film make it promising for the application in high-efficiency silicon solar cells. The focus of this section is to characterise the optimum SiN_x properties in more details including *(i)* injection-dependent τ_{eff} on *p*- and *n*-Si, *(ii)* extraction and modelling of $S_{eff,UL}$, and *(iii)* simulation of optical performance.

4.5.1 Measured injection-dependent effective minority carrier lifetime

Figure 4.13 plots the injection-dependent effective lifetime of both *p*-Si and *n*-Si passivated by the SiN_x deposited at two temperatures. For reference, τ_{bulk} calculated by the parameterisations given in [80] and [82] are plotted. As can be seen, the measured τ_{eff} on both types of Si is higher than that calculated by the Kerr and Cuevas model [80] over a broad range of excess carrier densities. This deviation suggests that the model overestimates intrinsic recombination in c-Si.

Richter *et al.* [82] have recently introduced a new parameterisation for intrinsic recombination in c-Si at 300 K, where the limit is derived by experimental measurements of surface passivation provided by plasma-assisted atomic-layer-deposition Al_2O_3. The calculated τ_{bulk} using this improved model is included in Figure 4.13. By applying the new parameterisation, we are able to calculate $S_{eff,UL}(\Delta n)$ of SiN_x-passivated *p*-Si to extract the contribution of silicon wafer thickness and doping in the various studies. However, the measured τ_{eff} on *n*-Si still significantly exceeds the modelled τ_{bulk} using Richter *et al.* parameterisation and we thus limited the extraction and modelling of the $S_{eff,UL}(\Delta n)$ solely to *p*-Si, as presented in the Section 4.5.2.

As commonly presented in the literature [89, 107], strong injection-dependence of the *p*-Si passivated by the optimised SiN_x can be observed at Δn below 10^{15} cm^{-3}. This behaviour is likely attributable to an inversion layer or space charge region

[113] induced by the positive Q_{eff} associated with SiN_x on *p*-Si [114]. Steingrube *et al.* [115] proposed this behaviour might be due to a surface damage layer in Si bulk near the SiN_x/Si interface. Recent paper published by Veith *et al.* [116] has found this behaviour to be related to shunting of the inversion layer at the edges of the lifetime sample. The $\tau_{eff}(\Delta n)$ dependence of SiN_x-passivated *n*-Si in this work is shown to be constant under low injection conditions, which is similar to that presented in [107].

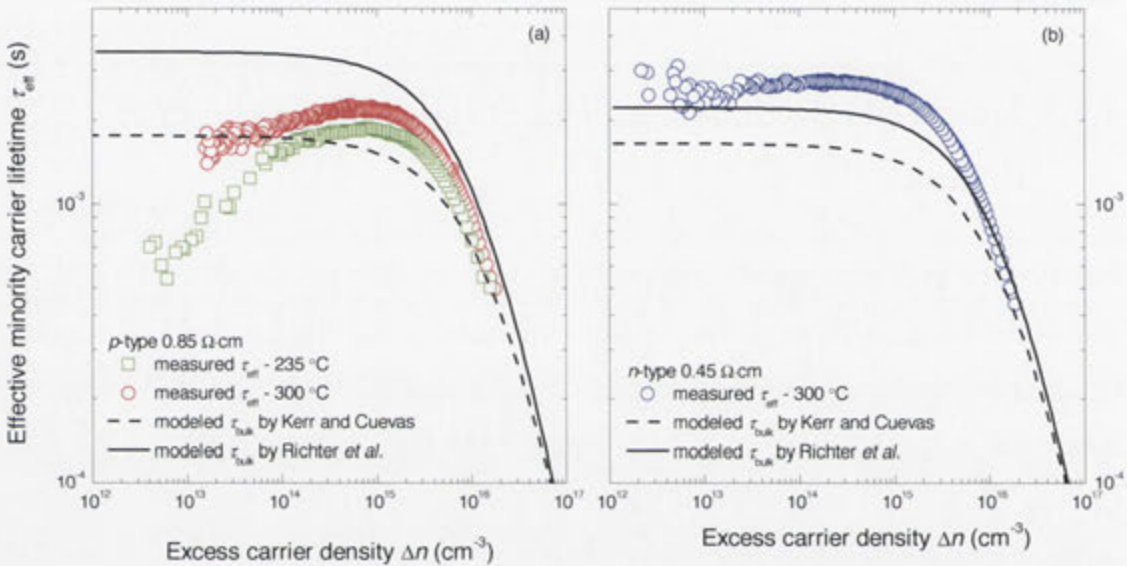

Figure 4.13: Measured τ_{eff} as a function of Δn for **(a)** 0.85-Ω·cm *p*-type, and **(b)** 0.45-Ω·cm *n*-type, FZ {100} silicon passivated by our nearly stoichiometric SiN_x. The modelled τ_{bulk} using parameterisations given by Refs. [80] and [82] are plotted.

4.5.2 Extraction and modelling of $S_{eff,UL}(\Delta n)$

To fairly compare our results to those mentioned previously, we recalculate $S_{eff,UL}(\Delta n)$ presented in [8, 17, 77, 107] using the latest Auger parameterisation given in [82]. Figure 4.14 plots and compares the results. As can be seen, the SiN_x presented here has the lowest $S_{eff,UL}$ of 3.1 cm/s and 1.6 cm/s at $\Delta n = 10^{15}$ cm^{-3} for the SiN_x deposited at 235 °C and 300 °C, respectively. Interestingly, the general dependence of $S_{eff,UL}$ on Δn for *p*-Si in all six works is reasonably comparable. This suggests that the underlying dominant defects at these SiN_x/*p*-Si interfaces are similar.

It is worth noting here that the $S_{eff,UL}$ shown in Figure 4.14 is for the as-deposited SiN_x. The *p*-Si sample (235 °C deposition) was also submitted to a rapid thermal anneal at 800 °C for 5 seconds to simulate the screen-printed metal-contacts firing process. The τ_{eff} at $\Delta n = 10^{15}$ cm^{-3} degraded from 1.8 ms to 2.2 µs upon firing, indicated a substantially degraded surface passivation. Preliminary study showed the increase in S_{eff} after firing is primarily due to an increase in D_{it}. While there is no passivation results for fired SiN_x in [18, 112], τ_{eff} of SiN_x in Refs [18, 112] degraded substantially after a forming gas annealing at 500 °C for 40 minutes.

By comparing the calculated $S_{eff,UL}(\Delta n)$ to the measured results, we gain more insight into the SiN_x/Si interfacial properties. This model was calculated using the D_{it} at midgap and Q_{eff} extracted from C–V measurements, as listed in Table 4.3. It is worth mentioning that quasistatic C–V measurements on the SiN_x deposited at 235 °C could not be performed as the MIS leakage current during quasistatic measurements was large. We hence restricted the modelling of $S_{eff,UL}(\Delta n)$ for the *p*-type sample passivated by the 300-°C-deposited SiN_x. For simplicity, we used a single defect at a single energy level (midgap) to model the $S_{eff,UL}(\Delta n)$. The capture cross section for holes σ_p, and electrons σ_n are taken from [69], as presented in Table 4.3. Using small-pulse deep-level transient spectroscopy, Schmidt *et al.* [69] observed three different types of defect (labeled defect A, B and C) at the SiN_x/Si interface prepared by low-frequency (at 100 KHz) direct PECVD. Moreover, they demonstrated that all three defects exhibited similar density but distinctly different σ_n and σ_p, near midgap. We hence assign the same density to the three defects in modelling.

Table 4.3: Summary of D_{it} at midgap and Q_{eff} obtained by C–V measurements of the SiN_x deposited at 300 °C. The capture cross section for holes σ_p, and electrons σ_n of three types of defect are given by [69].

	A	B	C
D_{it} (cm^{-2} eV^{-1})		3.0×10^{11}	
Q_{eff} (cm^{-2})		5.6×10^{11}	
σ_n (cm^2)	2.2×10^{-12}	3.6×10^{-14}	8.3×10^{-15}
σ_p (cm^2)	1.5×10^{-17}	2.3×10^{-16}	1.3×10^{-13}

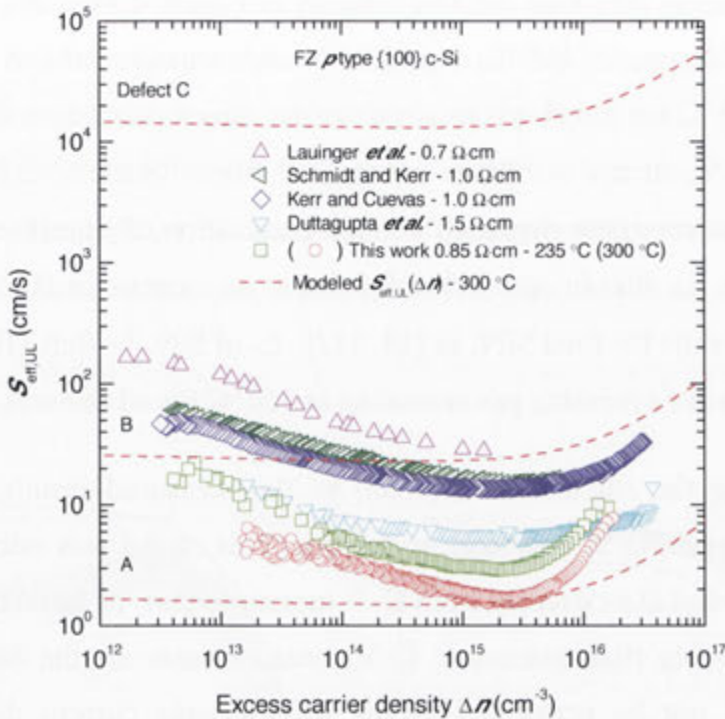

Figure 4.14: Extracted $S_{eff,UL}$ as a function of Δn for *p*-Si passivated with PECVD SiN_x. Several previous works depicted by legends are included for comparisons. The modelled $S_{eff,UL}(\Delta n)$ based on the three types of defect (labelled A, B and C) given in [69] is also plotted.

In order to investigate which of the three defects dominates $S_{eff,UL}(\Delta n)$ at our SiN_x/Si interface, we calculated $S_{eff,UL}(\Delta n)$ based on the three unique pairs of σ_n and σ_p. The modelled results are plotted as dashed-red lines in Figure 4.14 and labelled Defect A, B and C.

The results of this modelling should be considered rather tentative because *(i)* the interface is modelled as a single defect at midgap; and *(ii)* the σ_n and σ_p contained in [69] exhibit a doubtfully strong dependence on the trap energy and do not saturate. Nevertheless, it is the most recent data on the subject and the best that can be achieved with our SiN_x samples. Our modelling therefore simply suggests that rather than Defect C, which is more recombination active, Defect A or B is more likely to dominate the surface recombination at our SiN_x/Si interface. This is consistent with Refs [54, 69], who concluded that Defect C is caused by ion bombardment of the Si surface during SiN_x deposition. Since the deposition system employed in this work features microwave (at 2.45 GHz) and radio-frequency (at 13.56 MHz) plasma source, the ion bombardment is not likely to be significant.

Further characterisations on the fundamental properties for our SiN_x/Si interface such as a reliable σ_n and σ_p are necessary.

4.5.3 Simulation of optical performance

The absorption coefficient α of the SiN_x films presented in Figure 4.14 is plotted as a function of wavelength. Figure 4.15 compares the results. Since the same SiN_x was used in [77] and [107], we only plot one set of $\alpha(\lambda)$ for representation. Whereas both Si-rich SiN_x in [8, 18] and [17, 117] exhibit pronounced absorption at short wavelengths, the nearly stoichiometric SiN_x in [77, 107] and this work show low absorption of photons at wavelengths above 360 nm.

The photogenerated current density J_{Gen} was optimised using OPAL 2, a freeware optical model for textured silicon [118, 119]. The structure of the simulation was SiN_x-passivated 180-μm-thick random-upright-pyramid textured silicon solar cells, assuming a path length enhancement factor of $Z = 3$, and using the $n(\lambda)$ and $k(\lambda)$ measured from Spectrophotometer. The optimisation is restricted to the range $280 \leq \lambda \leq 1200$ nm when simulating solar cells operating in air, and $366 \leq \lambda \leq 1200$ nm when simulating cells encapsulated by glass/EVA (using $n(\lambda)$ and $k(\lambda)$ from given in [120]), respectively. The thickness of SiN_x was optimised to minimise current loss including ARC absorptance J_{Abs} and module reflectance J_{Refl}, consequently maximising J_{Gen}.

The simulated results are summarised in Table 4.4. The low absorption associated with our 300 °C-deposited SiN_x improves J_{Gen} by more than 0.66 mA/cm^2 at one sun (AM1.5G spectrum) when comparing to Si-rich SiN_x ($n_{632} = 2.5$) when the solar cell operating beneath glass/EVA module. The enhancement of J_{Gen} is greater than 1.40 mA/cm^2 when solar cells operate in air.

Furthermore, as observed in Figure 4.15 and Table 4.4, while the 300-°C-deposited SiN_x provides better surface passivation than the 235-°C-deposited SiN_x, it exhibits slightly higher light absorption and consequently lower J_{Gen}. The result implies that trade-off needs to be considered in the optimisation of optical absorption and surface passivation. We have found that a broad range of refractive indices can be obtained while maintaining a considerably low S_{eff} using process conditions

different to those presented here (see Chapter 5). This suggests a higher flexibility in optimising the optical transmission for various cell and module structures.

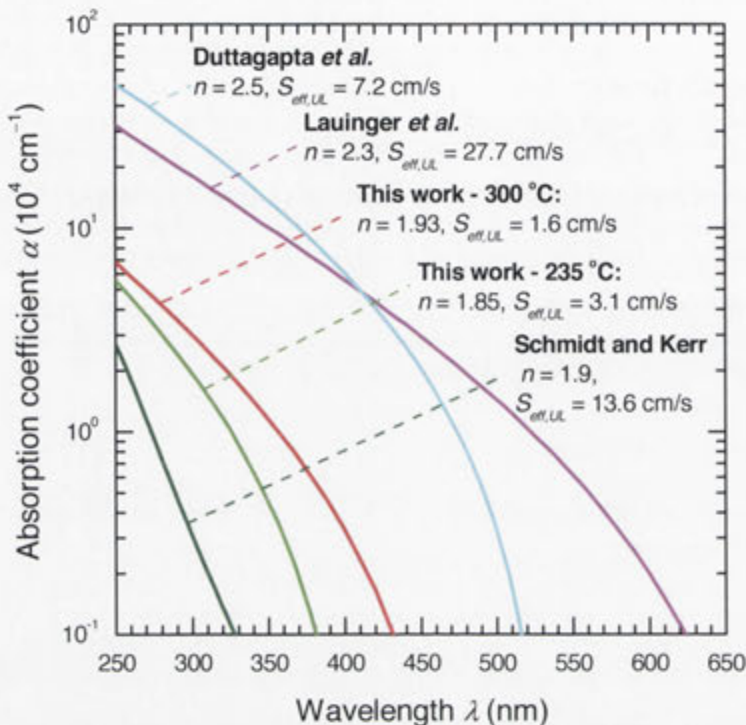

Figure 4.15: Absorption coefficient α of the SiN_x films shown in Figure 4.14. n_{632} and $S_{eff,UL}$ at $\Delta n = 10^{15}$ cm^{-3} on FZ {100} *p*-Si associated with each sample are also indicated.

4.6 Chapter summary

This chapter presented an extensive study into SiN_x prepared by the μW/RF dual-mode PECVD reactor. Section 4.3 presented the experimental results of a CCE. The dependence of SiN_x properties on deposition conditions was systematically investigated, with the deposition pressure, substrate temperature and NH_3:SiH_4 ratio identified as the most sensitive parameters for controlling SiN_x optical and surface passivation properties. By correlating the relationship between SiN_x properties, it was shown that *(i)* S_{eff} does not correlate universally with the bulk structural and optical properties such as chemical bond densities and refractive index; and *(ii)* S_{eff} depends primarily on the defect density at the SiN_x/Si interface rather than the insulator charge. The results in this work introduce the potential to

Table 4.4: Summary of the simulated results including the optimum SiN_x thickness and current generation

			Cell under air					Cell encapsulated beneath glass/EVA				
Ref.	n_{632}	$S_{eff,UL}$ [b]	J_{Inc} [c]	t_{SiNx} [d]	J_{Gen} [c]	J_{Abs} [c]	J_{Refl} [c]	J_{Inc} [c]	t_{SiNx} [d]	J_{Gen} [c]	J_{Abs} [c]	J_{Refl} [c]
[8, 18]	2.3	27.7		54	38.49	1.91	0.87		31	37.22	0.72	0.74
[17, 117]	2.5	7.2		58	38.98	1.45	0.84		40	37.58	0.67	0.42
[77, 107]	1.9	13.6	41.27	78	40.53	0.01	0.73	38.69	87	38.36	0.01	0.32
[a]235 °C	1.85	3.1		80	40.50	0.07	0.70		91	38.31	0.01	0.36
[a]300 °C	1.93	1.6		80	40.38	0.21	0.68		88	38.24	0.11	0.34

[a]The nearly stoichiometric SiN_x presented in this work

[b]Auger-corrected $S_{eff,UL}$ at $\Delta n = 10^{15}$ cm^{-3} in cm/s

[c]J_{Inc}, J_{Gen}, J_{Abs} and J_{Refl} represents equivalent current density of incidence, generation, absorptance in SiN_x and reflectance in module, respectively. All current densities have units of mA/cm^2

[d]Optimised thickness of SiN_x in nm to maximise the equivalent J_{Gen}.

independently control the optical and surface recombination properties.Section 4.4 examined the effect of varying the deposition pressure at optimum temperature. We attained a highly transparent and highly passivating SiN_x film that gives a low $S_{eff,UL}$ = 1.6 cm/s on 0.85-Ω·cm *p*-type and immeasurably low $S_{eff,UL}$ on 0.45-Ω·cm *n*-type silicon substrates.

Section 4.5 presented a brief characterisation of the optimum SiN_x film, where *(i)* C–V measurements revealed that $D_{it} = 3.0 \times 10^{11}$ eV^{-1}cm^{-2} at midgap and $Q_{eff} = 5.6 \times 10^{11}$ cm^{-2}; *(ii)* by comparing the measured injection-dependent $S_{eff,UL}$ to calculated $S_{eff,UL}$ by an extended Shockley-Read-Hall model [75], we concluded that either Defect A or B (or both) observed by Schmidt *et al.* [69] is likely to dominate the surface recombination rate at the SiN_x/Si interface; and *(iii)* compared to Si-rich SiN_x (n_{632} = 2.5) of an equivalent passivation, the optimum SiN_x would enhance the photo-generated current density by more than 0.66 mA/cm^2 or 1.40 mA/cm^2 for solar cells encapsulated in glass/EVA or operating in air, respectively. The SiN_x described here is ideally suited for high-efficiency solar cells, which require good surface passivation and low absorption from their front surface coatings.

Finally, the optimum deposition condition that yields the highly transparent and highly passivating SiN_x is to be applied to examine the surface passivation by SiN_x over a wide range of n_{632} on planar undiffused Si (see Chapter 5), textured undiffused Si (see Chapter 6), phosphorus-diffused Si and IBC *n*-type solar cells (see Chapter 7).

Chapter 5

Influence of NH_3:SiH_4 ratio and NH_3 plasma exposure on SiN_x properties

5.1 Introduction

In PV research related to PECVD SiN_x, the reactant gas ratio, e.g. NH_3:SiH_4, is typically varied to alter SiN_x properties. It has been found that by increasing the NH_3:SiH_4 ratio, a wide range of n_{632} from 1.8 (N-rich) to 3.0 (Si-rich) is obtained [18, 20, 21, 29, 104]. On the other hand, an increase in the NH_3:SiH_4 ratio results in an increase in S_{eff} and a decrease in refractive index and absorption coefficient, leading to suboptimal choices—a trade-off—between surface passivation and optical transmission. This trade-off can be circumvented, however, as shown in Chapter 4, which demonstrated that no universal correlation exists between surface recombination and refractive index for SiN_x, indicating that the optical transmission and surface passivation can be independently maximised. This chapter aims to *(i)* examine the surface recombination properties over a wide range of n_{632} by varying the NH_3:SiH_4 ratio, and *(ii)* understand the cause underlying the increase in S_{eff} with the increase in the NH_3:SiH_4 ratio by NH_3 plasma exposure.

In Section 5.3, we employ the optimum deposition conditions developed in Chapter 4, and vary the NH_3:SiH_4 ratio to examine the surface recombination properties over a wide range of n_{632}. It is found that *(i)* S_{eff} remains low and relatively constant when the NH_3:SiH_4 ratio increases from 0 to 1.9, resulting in a good S_{eff} over a broad range of n_{632} (1.87–4.1) on low-resistivity ($\leq 1.1\ \Omega\cdot$cm) *p*-Si and *n*-Si substrates; and *(ii)* S_{eff} increases strongly as the NH_3:SiH_4 ratio increases from 1.9 to 4.7 (n_{632}

decreases from 1.87 to 1.83), consistent with the results presented in prior works [18, 29, 104].

The physical cause underlying the increase in S_{eff} with the increase in the NH_3:SiH_4 ratio is postulated to be an excessive incorporation of NH_b radicals into SiN_x network. This hypothesis is evaluated by introducing NH_b radicals into the SiN_x–Si and a-Si–Si systems through exposing the samples to an NH_3 plasma. The experimental results are presented in Section 5.4. It is found that the exposure degrades the surface passivation provided by both SiN_x and a-Si films. It is further found that the NH_3 plasma exposure causes *(i)* an increase in the density of $Si{\equiv}N_3$ groups in both SiN_x and a-Si films, *(ii)* a reduction in refractive index and permittivity, *(iii)* an increase in D_{it} at the SiN_x/Si interface, and *(iv)* a reduction in Q_{eff} in the SiN_x. The changes in film properties are likely due to an insertion of NH_b radicals.

Finally, in comparing the effect of the NH_3:SiH_4 ratio and NH_3 plasma exposure on film properties, we observe *(i)* a different influence on the film bond configuration, *(ii)* opposing effects on Q_{eff}, and *(iii)* similar effects on n_{632}, D_{it} and S_{eff}. Despite the aforementioned differences, the experimental results suggest that an excessive incorporation of NH_b radicals, either by increasing the NH_3:SiH_4 ratio or the NH_3 plasma exposure, is detrimental to SiN_x surface passivation. In other words, minimising the incorporation of NH_b radicals during film deposition is of great importance to enable good surface passivation by SiN_x.

5.2 Experimental details

This chapter contains two principle experiments. Experiment 1 varies the NH_3:SiH_4 ratio to examine the surface recombination properties over a wide range of n_{632}, as presented in Section 5.3. Experiment 2 exposes as-passivated samples to an NH_3 plasma to understand the physical cause underlying the increase in S_{eff} with the increase in the NH_3:SiH_4 ratio, as presented in Section 5.4.

The lifetime samples used for Experiment 1 were fabricated from three types of low resistivity FZ {100} Si samples: 0.85 Ω·cm *p*-type, 0.45 Ω·cm *n*-type, and 1.1 Ω·cm

n-type. The thickness of the three substrates were 300 μm, 245 μm and 390 μm, respectively. All wafers received a TMAH silicon etch, RCA clean and HF dip. Next, all wafers were coated with SiN_x on both surfaces by two sequential depositions using the optimised deposition condition presented in Chapter 4. In this experiment, the NH_3:SiH_4 ratio was varied to obtain a broad range of n_{632}, from 1.83 (N-rich) to 4.1 (a-Si). Note that prior to the deposition of the SiN_x films, the PECVD reactor and silicon samples were prepared in accordance with Section 3.4.

The lifetime samples for Experiment 2 were fabricated from *n*-type FZ {100} silicon wafers with a resistivity of 0.45 Ω·cm and a thickness of 245 μm. The wafers were passivated with SiN_x (n_{632} = 1.93) or a-Si on both surfaces by two sequential depositions. The NH_3/SiH_4/Ar gas flow for SiN_x and a-Si was 20/20/20 sccm and 0/40/20 sccm, respectively. The deposition time was varied to achieve a film thickness of 60 ± 5 nm. The symmetrically passivated samples were then exposed to NH_3 plasma at room temperature with NH_3/Ar flow at 20/20 sccm, pressure at 0.2 mbar, μW plasma power at 500 W, and RF bias voltage at 150 V. The plasma exposure time was varied from 5 to 90 minutes. In order to separate the effect of the radiation exposure from the penetration of NH_b radicals, control samples were included in the plasma chamber but protected from the ion penetration by a 1 mm-thick glass plate [121, 122].

The effective lifetime of the samples was measured by photoconductance in the transient mode, and $S_{eff,UL}$ was calculated in accordance with Section 2.5.3. Reflectance, FTIR, and C–V measurements were performed on DSP *n*-type {100} FZ Si with a resistivity of 1.0 Ω·cm and a thickness of 290 μm. The sample preparation, characterisation and analysis of the three measurements were undertaken in accordance with Sections 2.2.3, 2.3.4 and 2.4.3, respectively.

5.3 Experiment 1—varying the NH_3:SiH_4 ratio

Employing the optimum deposition condition developed in Chapter 4, this section examines the surface recombination properties over a wide range of n_{632} by varying the NH_3:SiH_4 ratio, where n_{632} ranges from 1.83 (N-rich) to 4.1 (a-Si).

5.3.1 Background

Previous works found that an increase in the NH_3:SiH_4 ratio causes an increase in S_{eff} and a decrease in n_{632}, suggesting an apparent correlation: S_{eff} increases as n_{632} decreases [18, 20, 21, 29, 104] (see the red line Figure 1.1(b)). The work we use as the benchmark—that is, the most thorough study on the relationship between S_{eff} and n_{632}—is Lauinger *et al.* [18]. S_{eff} in [18] was relatively small and constant for $n_{632} > 2.3$, implying that the optimum S_{eff} is obtained by highly absorbing films. Within an even broader range of n_{632} (N-rich to a-Si), a significantly lower S_{eff} on low resistivity ($\leq 1.1\ \Omega\cdot$cm) *p*- and *n*-Si substrates has not been attained.

5.3.2 Results and discussion

Figure 5.1(a) plots the effect of the NH_3:SiH_4 ratio on SiN_x optical properties (i.e., n_{632} and k_{360}). As NH_3:SiH_4 ratio increases from 0 to 1.0, n_{632} decreases from 4.1 to 1.93. A similar trend is observed for the k_{360}, where it first exhibits a substantial decrease and then negligible absorption ensues when NH_3:$SiH_4 \geq 1.0$.

The effect of NH_3:SiH_4 ratio on $S_{eff,UL}$ for the three types of samples (0.85 $\Omega\cdot$cm *p*-Si, 0.45 $\Omega\cdot$cm *n*-Si, and 1.1 $\Omega\cdot$cm *n*-Si) is plotted in Figure 5.1(b). When the NH_3:SiH_4 ratio is less than 1.9, $S_{eff,UL}$ shows negiligible dependence on the gas ratio. On the other hand, $S_{eff,UL}$ increases strongly as the NH_3:SiH_4 ratio increases from 1.9 to 4.7.

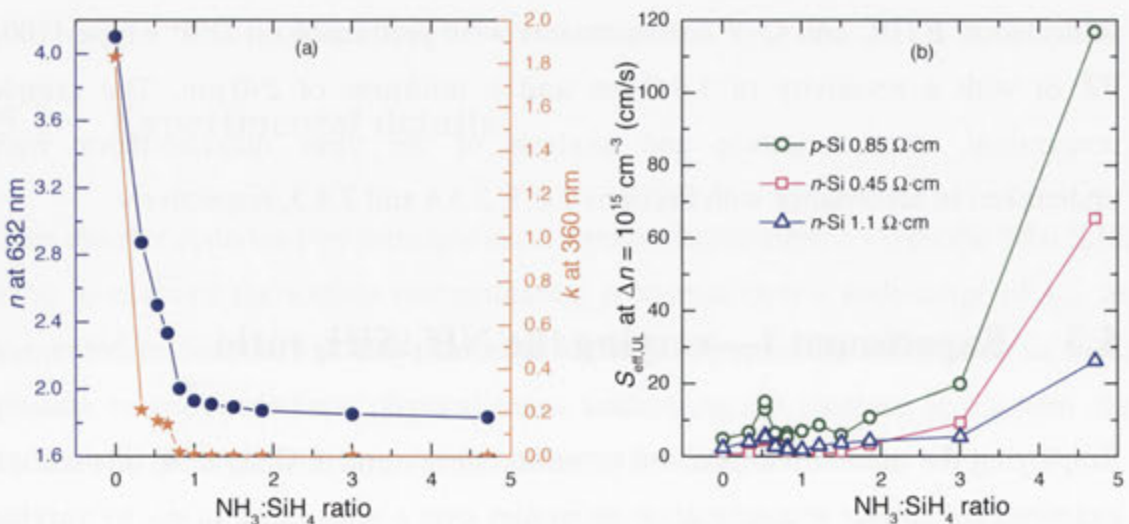

Figure 5.1: The effect of NH_3:SiH_4 ratio on SiN_x **(a)** optical properties (i.e., n_{632} and k_{360}), and **(b)** $S_{eff,UL}$ at $\Delta n = 10^{15}$ cm^{-3}.

Notably, over the range where $S_{eff,UL}$ is small and constant (NH_3:SiH_4 ratio of 0–1.9), there is a very wide range of n_{632} (1.87–4.1). This is made clearer in Figure 5.2, which plots $S_{eff,UL}$ versus n_{632}. $S_{eff,UL}$ first decreases as n_{632} increases and then it saturates over the range n_{632} = 1.87–4.1. This behaviour is evident for all three substrate resistivities. Note that the $S_{eff,UL}$ for 0.45 Ω·cm *n*-Si seems typically lower than the $S_{eff,UL}$ for 1.1 Ω·cm *n*-Si. One possible reason is that the Auger model proposed by Richter *et al.* [1] underestimates the bulk intrinsic lifetime for the 0.45 Ω·cm *n*-Si, leading to a lower $S_{eff,UL}$. Note further that all $S_{eff,UL}$ reported in this section is by the as-deposited SiN_x.

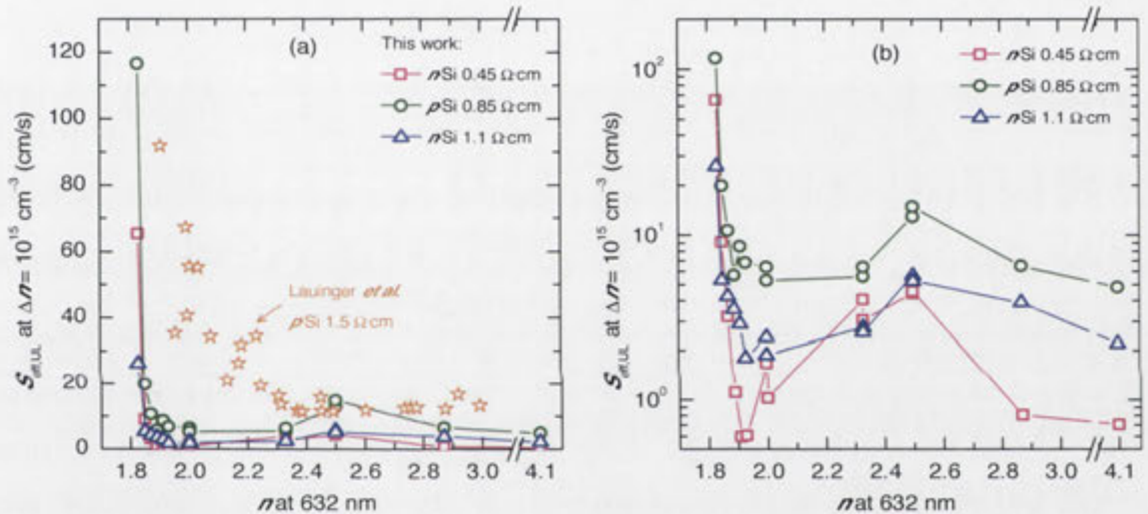

Figure 5.2: Extracted $S_{eff,UL}$ for three types of FZ Si substrates as a function of n_{632} in **(a)** linear scale, and **(b)** logarithmic scale. In this experiment, only the NH_3:SiH_4 ratio was varied to alter the SiN_x properties. Results of Lauinger *et al.* [18] are also included as a representative of previous works.

In comparison to Lauinger *et al.*, we find that *(i)* $S_{eff,UL}$ is significantly smaller at all n_{632}; and *(ii)* $S_{eff,UL}$ saturates at lower n_{632} (1.87 instead of 2.3). The results in Figure 5.2 suggest that an appropriate deposition of SiN_x can circumvent the trade-off between optical transmission and surface passivation, as also illustrated in Chapter 4. In short, solar cells that require high surface passivation need not be compromised by light absorption in the SiN_x.

Despite the superior passivation, our results remain consistent with a general trend observed in prior works [18-21]. As evident in Figures 2.9(a) and 5.2, as the NH_3:SiH_4 ratio increases, S_{eff} increases. Previously, this trend had been explained as being related to the concentration of Si atoms in the film (and therefore the refractive index) [20]. The results of Chapter 4, however, clearly debunk this hypothesis and show that surface recombination does not necessary depend on *(i)* film bond densities (i.e., [Si–N], [Si–H], and [N–H]), and *(ii)* optical properties (i.e., n_{632} and k_{360}). The results in Chapter 4 show further that, irrespective of n_{632}, the increase in S_{eff} was attributed to an increase in D_{it} rather than a reduction in Q_{eff}. We now discuss the possible physical causes for the formation of interface defects due to the high NH_3:SiH_4 ratio.

According to Lucovsky *et al.* [123], the interface defects can be formed via two pathways: *(i)* light-induced rearrangement of structural network between Si–H and Si–Si bonds, and *(ii)* ion-induced penetration of external specices such as N–H related radicals into the bulk of film. The defects at the SiN_x/Si interface due to the high NH_3:SiH_4 ratio could be formed via either pathway.

The light-induced defects at a-Si/Si interface, well-known as the Staebler–Wronski effect [124], has been investigated by several works [125-127], showing that additional interface defects, most likely as Si dangling bonds [126, 128], are generated by light exposure. The SiN_x/Si interface might also suffer from this light-induced damage during plasma deposition.

The ion-induced penetration of NH_b radicals is a critical process in forming SiN_x films (see Section 3.3.2). According to Oever *et al.* [96], an increase in the NH_3 gas flow increases the density of NH_b radicals in the plasma chamber. We therefore speculate that as the NH_3:SiH_4 ratio increases, a greater fraction of NH_b radicals is incorporated into the SiN_x network and onto the SiN_x/Si interface, breaking the existing interfacial Si–H and creating new dangling bonds (i.e., defects).

The next section investigates the two possible degradation mechanisms—light- and ion-induced degradation—by exposing the as-passivated samples to an NH_3 plasma. By comparing the effects of varying the NH_3:SiH_4 ratio to that of NH_3 plasma

exposure, the mechanism for the interface defects formed at the high NH_3:SiH_4 ratio is elucidated.

5.4 Experiment 2—NH_3 plasma exposure

This section examines the effects of NH_3 plasma exposure on the properties of SiN_x and a-Si films with an emphasis on the surface recombination properties.

5.4.1 Background

Ammonia plasmas have been investigated for the nitridation of bare silicon surfaces and dielectric materials. When the bare silicon surface is exposed to the NH_3 plasma before the deposition of a SiN_x gate insulator, Shimoda *et al.* [129] reports that a metal–insulator–semiconductor field effect transistor with SiN_x as gate insulator has a high field-effect mobility. The NH_3 plasma exposure before the SiN_x deposition was also used in several studies to improve the surface passivation by SiN_x [130-133].

NH_3 plasma has also been used for the nitridation of dielectrics such as thin thermal SiO_2, forming an oxynitride layer. Two groups have shown that the exposure of SiO_2-coated Si samples to NH_3 plasma results in a drastic increase in the amount of interface defects [134, 135]. In addition, Jin *et al.* exposed SiO_2-passivated Si with NH_3 plasma at room temperature, resulting in a significant increase in emitter saturation current density [136]. However, to the best of our knowledge, no studies on the exposure of SiN_x and a-Si passivated samples to NH_3 plasma have been published.

5.4.2 Results and discussion

A. Lifetime measurements

Figure 5.3 plots $S_{eff,UL}$ as a function of NH_3 plasma exposure time for SiN_x and a-Si samples. The samples were either exposed directly to plasma or protected from the plasma by a glass plate. The covered samples were therefore exposed to light

(although not at very short wavelengths), but were protected from the ion penetration [121, 122].

The figure shows that for the SiN_x samples, $S_{eff,UL}$ increases dramatically when exposed to the plasma, but remains constant when protected by the glass plate. The results indicate that the degradation of SiN_x passivation upon plasma exposure is induced by ion penetration rather than by light exposure.

For the a-Si samples, $S_{eff,UL}$ increases rapidly during the first 10 minutes with or without the glass plate. As the exposure continues, $S_{eff,UL}$ for the sample exposed to the plasma continues to increase but at a slow rate. By contrast, $S_{eff,UL}$ for the sample protected by the glass plate appears to be constant. The results suggest that the fast increase in $S_{eff,UL}$ is primarily induced by the light exposure, likely the Staebler–Wronski effect, and the slow increase in $S_{eff,UL}$ is caused by the ion penetration.

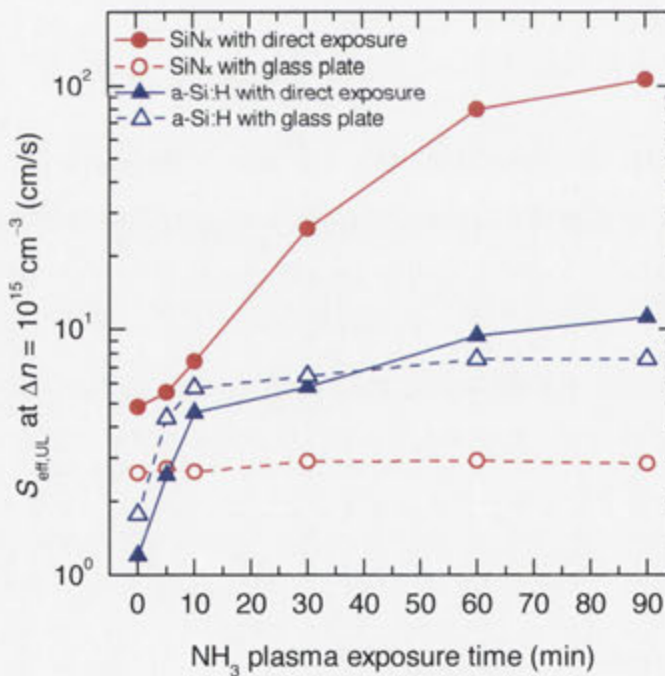

Figure 5.3: $S_{eff,UL}$ as a function of NH_3 plasma exposure time for SiN_x and a-Si samples. The samples were either exposed directly to the plasma or protected from the plasma by a glass plate.

In addition, the figure shows that the NH_3 plasma exposure is more detrimental to the surface passivation by SiN_x than by a-Si. Upon 90-minutes exposure to the plasma, $S_{eff,UL}$ for the SiN_x sample is nearly one order of magnitude higher than the $S_{eff,UL}$ for the a-Si sample.

B. FTIR measurements

FTIR spectra were recorded after each step of the NH_3 plasma exposure to evaluate the influence on film structures. The results are shown in Figure 5.4.

Before any plasma exposure, both SiN_x and a-Si films exhibit typical FTIR spectra. The SiN_x has four distinctive absorption peaks: one associated with Si–N at ~840 cm^{-1} ($N{\equiv}Si_3$ asymmetric stretching), one with Si–H at ~2140 cm^{-1} ($H{-}Si{\equiv}N_3$ stretching) and two with N–H at ~1150 cm^{-1} (bending) and ~3340 cm^{-1} (stretching). The a-Si has three distinctive absorption peaks, all associated with Si–H: ~640 cm^{-1} (wag-rocking), ~2000 cm^{-1} (Si–H stretching), and ~2090 cm^{-1} ($Si{=}H_2$ stretching) [46, 137].

After 5 minutes of plasma exposure, a new shoulder that peaks at ~1055 cm^{-1} appears for both SiN_x and a-Si films. This shoulder was assigned to the Si–N stretching vibrations of $Si{\equiv}N_3$ groups by Sénémaud *et al.* [138]. Furthermore, we note that the density of the $Si{\equiv}N_3$ groups increases significantly as the exposure time increases. By constrast, no obvious change in film structure can be observed for the samples protected by the glass plate. Based on these observations, we conclude that the chemical bond peaked at ~1055 cm^{-1} is introduced by the incorporation of NH_b radicals. It is interesting to note that in Ref. [53], the $Si{\equiv}N_3$ groups were assigned as the bonding configuration of the so-called "K-center". If correct, then the NH_3 plasma exposure increases the density of K-centres, thereby enhancing its capability of trapping charge [139].

Based on the FTIR results and the defect formation model proposed by Lucovsky *et al.* [123], it is interesting to discuss possible reaction pathways for the formation of the $Si{\equiv}N_3$ groups. In the model of Lucovsky *et al.* [123], N–H related radicals are proposed to be the precursors for the formation of defects. We therefore propose that the $Si{\equiv}N_3$ groups are formed by an insertion of N–H related radicals

into SiN_x or a-Si films in the following reaction pathways: *(i)* for SiN_x samples: $Si\equiv N_3 + 8(N\text{–}H) \rightarrow 3(Si\equiv N_3) + 4H_2$; and *(ii)* for a-Si samples: $Si\text{–}H + 3(N\text{–}H) \rightarrow Si\equiv N_3 + 2H_2$.

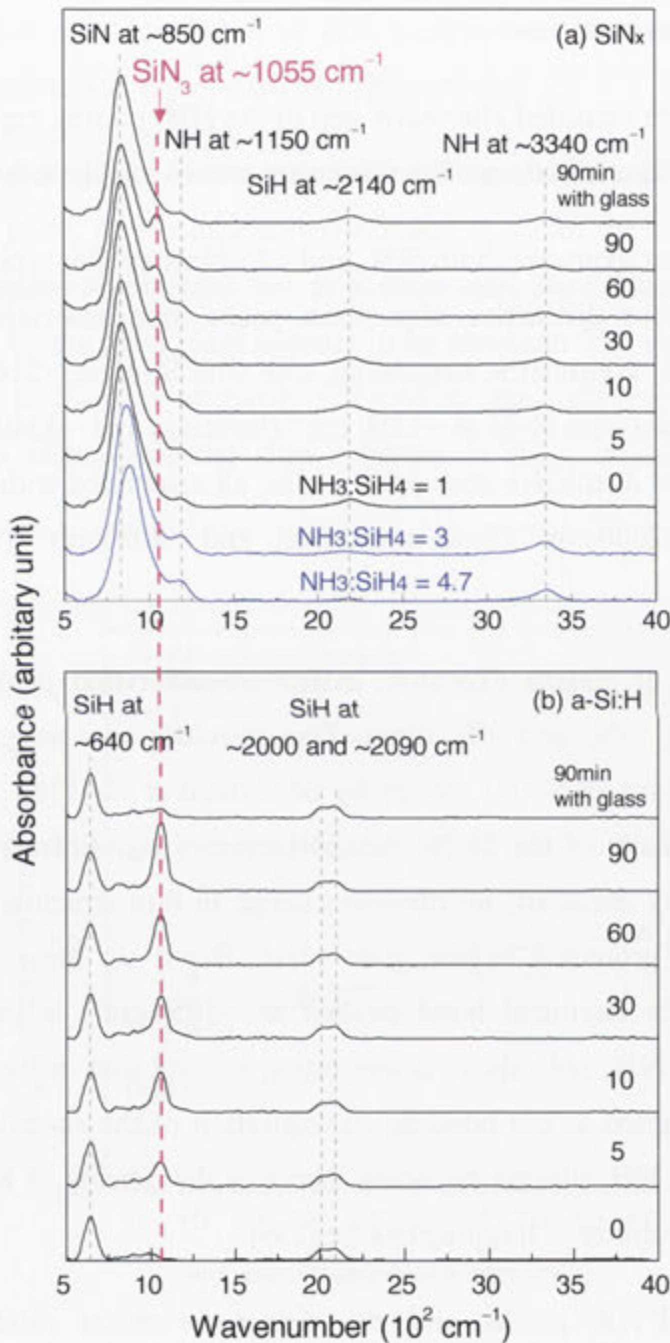

Figure 5.4: The impact of NH_3 plasma exposure on the absorbance measured by FTIR for **(a)** SiN_x, and **(b)** a-Si. FTIR spectra for other two NH_3:SiH_4 ratios are included in (a), as represented by the blue curves.

Finally, Figure 5.4(a) also includes the FTIR spectra of two other NH_3:SiH_4 ratios for SiN_x samples not exposed to the NH_3 plasma, as represented by the blue curves. As the NH_3:SiH_4 ratio increases, besides an expected increase in stretching N–H at ~3340 cm^{-1} and a decrease in stretching Si–H at ~2140 cm^{-1}, no shoulder at 1055 cm^{-1} on the main Si–N band is observed. The FTIR results suggest, therefore, that varying the NH_3:SiH_4 ratio has a different effect on the film bonding configuration, than exposing the samples to NH_3 plasma exposure, even though they cause a similar degradation in SiN_x surface passivation. Remember, however, that the FTIR signal is dominated by the structure in the bulk of the film rather than at its interface.

C. Optical measurements

In addtion to the alteration of the films' structural properties, NH_3 plasma exposure also affects their optical properties. Figure 5.5 plots the relationship between n_{632} and exposure time. It is shown that n_{632} of both SiN_x and a-Si films decreases monotonically with an increase in exposure time. The trends for n_{632} correlate directly to those for the density of Si≡N_3 groups, suggesting that the reduction in n_{632} is most likely attributtable to the incorporation of NH_b radicals into film network upon plasma exposure.

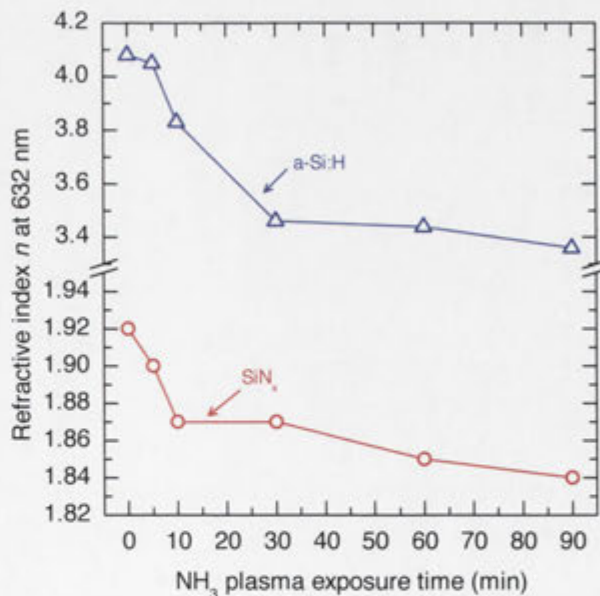

Figure 5.5: Refractive indices of SiN_x and a-Si films as a function of NH_3 plasma exposure time.

D. C–V measurements

C–V measurements reveal how the NH_3 plasma exposure influences D_{it} at midgap, Q_{eff}, and film permittivity (i.e., the dielectric constant κ). Figure 5.6 plots the results and the high-frequency C–V curves are included in the inset. Note that high-frequency C–V curves can only be obtained from SiN_x but not a-Si due to the high leakage current of the a-Si [63]. Note further that the C–V curves in Figure 5.6 are solely for the SiN_x samples exposed to plasma, since no significant change in $S_{eff,UL}$ and film structure was observed for the sample protected by the glass plate.

It can be seen that upon 90 minutes of exposure *(i)* D_{it} increases significantly by approximately one order of magnitude; *(ii)* Q_{eff} decreases significantly from $+ 6.6 \times 10^{11}$ cm^{-2} to $- 4.2 \times 10^{11}$ cm^{-2}; and *(iii)* κ decreases from 7.5 to 3.6. Notably, these trends correlate clearly with a reduction in n_{632}, which is correlated with an increase in the density of Si≡N_3 groups in the SiN_x bulk. We therefore conclude that the changes to Q_{eff} and κ are induced by the incorporation of NH_b radicals into the bulk. We cannot be as conclusive for D_{it}, since it is an interface property, but its rapid increase is most likely caused by the incorporation of NH_b radicals.

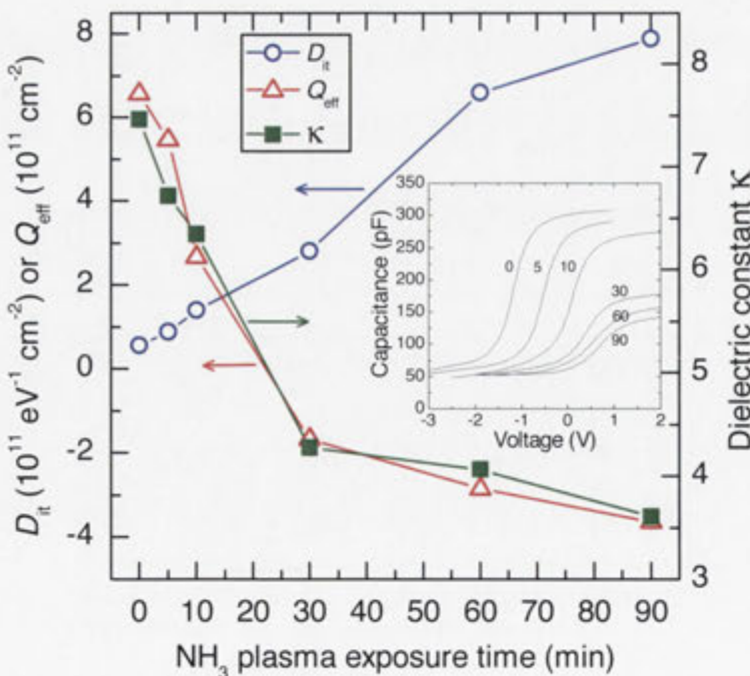

Figure 5.6: C–V measurements on SiN_x samples and the extracted D_{it} at midgap, Q_{eff} and dielectric constant κ.

5.5 Discussion

Summarising the results in Chapter 4 and Section 5.3, we find that as the NH_3:SiH_4 ratio increases *(i)* [N–H] increases and [Si–H] decreases; *(ii)* n_{632} decreases; and *(iii)* S_{eff}, D_{it} and Q_{eff} increase. In comparing the effect of the NH_3:SiH_4 ratio and NH_3 plasma exposure on SiN_x properties, as summarised in Table 5.1, we observe *(i)* a different influence on the bond configuration in the bulk of the film, *(ii)* opposing effects on Q_{eff}, probably relating to the difference in film configuration; and *(iii)* similar effects on the n_{632}, D_{it} and S_{eff}.

Table 5.1: Comparison of the influence on the SiN_x properties by varying the NH_3:SiH_4 ratio and exposing to NH_3 plasma

SiN_x properties		Increase in NH_3:SiH_4 ratio	Increase in NH_3 plasma exposure
Structural	[N–H]	Increase	Negligible
	Density of $Si{\equiv}N_3$ groups at 1055 cm^{-1}	Negligible	Increase
Optical	n_{632}	Decrease	Decrease
Electronic	Q_{eff}	Increase	Decrease
	D_{it}	Increase	Increase
	S_{eff}	Increase	Increase

Despite the different effects on the bulk properties (i.e., the bond configurations and Q_{eff}) there are similar effects on the interface properties (i.e., D_{it} and S_{eff}). Thus, the increase in interface defects might still be created via the same formation pathway. As presented in Section 5.4.2–A, the degradation of SiN_x passivation upon plasma exposure was induced by ion penetration rather than by light exposure. We therefore concluded tentatively that the increase of D_{it} and therefore S_{eff} with an increase in the NH_3:SiH_4 ratio is caused by an incorporation of NH_b radicals rather

than by the light exposure in the plasma. The experimental results in this work suggest that an excessive incorporation of NH_b radicals, either by increasing the NH_3:SiH_4 ratio or exposing to the NH_3 plasma, is detrimental to SiN_x surface passivation. In other words, minimising the incorporation of NH_b radicals during film deposition is of great importance to enable good surface passivation by SiN_x.

5.6 Chapter summary

This chapter examined the influence of the NH_3:SiH_4 ratio and NH_3 plasma exposure on SiN_x properties.

Section 5.3 employed the optimum deposition condition established in Chapter 4 and varied the NH_3:SiH_4 ratio. It was shown that *(i)* S_{eff} stayed constant when the NH_3:SiH_4 ratio increased from 0 to 1.9, leading to a relatively constant and low S_{eff} over a broad range of n_{632} (1.87–4.1) on low-resistivity ($\leq 1.1\ \Omega\cdot$cm) *p*-Si and *n*-Si substrates; and *(ii)* S_{eff} increased strongly as the NH_3:SiH_4 ratio increased from 1.9 to 4.7 (n_{632} decreases from 1.87 to 1.83). The results in this work demonstrated that the perceived trade-off between optical transmission and surface passivation can be circumvented by a judicious deposition of SiN_x.

The physical cause underlying the increase in S_{eff} with the increase in the NH_3:SiH_4 ratio was postulated to be an incorporation of NH_b radicals into the bulk and interface of the SiN_x. Section 5.4 evaluated this hypothesis by introducing NH_b radicals into the SiN_x–Si and a-Si–Si systems via exposing the samples to an NH_3 plasma. It was found that the NH_3 plasma exposure caused *(i)* an increase in S_{eff}, *(ii)* an increase in the density of Si≡N_3 groups, *(iii)* a reduction in refractive index and permittivity, *(iv)* an increase in D_{it} at SiN_x/Si interface, and *(v)* a reduction in Q_{eff} in SiN_x.

By comparing the effect of the NH_3:SiH_4 ratio and NH_3 plasma exposure on SiN_x film properties, we observed *(i)* a different influence on the film bond configuration, *(ii)* opposing effects on Q_{eff}, and *(iii)* similar effects on n_{632}, D_{it} and S_{eff}. The high density of interface defects due to *(i)* the high NH_3:SiH_4 ratio, and *(ii)* NH_3 plasma

exposure, is most likely to be induced by ion penetration rather than by light exposure.

The recombination studies on the influence of NH_3:SiH_4 ratio and NH_3 plasma exposure are extended at textured Si surfaces in the next chapter.

Recombination at SiN_x-passivated undiffused textured silicon

6.1 Introduction

Textured surfaces are incorporated into solar cells because they reduce the front-surface reflectance and enhance light trapping [140]. Textured surfaces that contain random upright pyramids (rantex) [141] and periodically inverted pyramids (intex) [140] can be formed through an immersion of monocrystalline silicon wafers in an alkaline solution. Isotropically textured surfaces that feature bowl-like structures (isotex) can be formed by submitting wafers to an acidic, isotropic etchant [142]. Rantex, intex and isotex, as depicted in Figure 6.1, are typically featured in industrial monocrystalline, record-efficiency monocrystalline [23] and industrial multicrystalline [143] silicon solar cells, respectively. Additionally, an ARC layer such as PECVD SiN_x is usually deposited on the sunward surface to improve optical performance. The recombination at SiN_x-passivated textured surface therefore impacts the performance of virtually all silicon solar cells.

Studies on the recombination at SiN_x-passivated textured surfaces are rare. A critical review of previous works with this focus is undertaken in Section 6.2. It is found that *(i)* the recombination at {100} and {111} planar surfaces is similar, regardless of SiN_x stoichiometry; and *(ii)* additional recombination at pyramid vertices and edges decreases rapidly as n_{632} increases and becomes negligible when $n_{632} \geq 2.3$.

In this chapter, we extend the recombination studies on a variety of Si surface morphologies (i.e., planar {100} and {111}, rantex, intex and isotex), where the

surfaces are passivated by SiN_x films with a wide range of refractive indices. By observing the relationship between S_{eff} and n_{632} for the various surfaces, we are able to elucidate the dependence of S_{eff} on substrate orientation, morphology, and film stoichiometry. The experimental results are presented in Section 6.4 and three key conclusions are drawn: *(i)* over a large range of refractive indices (n_{632} = 1.9–4.1), we achieve a low S_{eff} on rantex samples ($S_{eff,UL}$ < 10 cm/s); *(ii)* as the NH_3:SiH_4 ratio decreases (and n_{632} increases), S_{eff} at textured surfaces (after area-correction) decreases rapidly and approaches the same S_{eff} as the planar surfaces when NH_3:$SiH_4 \leq 0.7$ ($n_{632} \geq 2.3$); and *(iii)* by contrast, irrespective of the NH_3:SiH_4 ratio, and therefore n_{632}, S_{eff} is equivalent on {100} and {111} planar surfaces. The latter two findings are consistent with the results presented in Section 6.2, indicating that the increase in S_{eff} at textured surfaces is related to the presence of vertices and/or edges of the pyramids rather than to the presence of {111}-orientated facets.

The corona-lifetime analyses presented in Section 6.5 reveal that an increase in S_{eff} introduced by *(i)* the higher NH_3:SiH_4 ratio, and *(ii)* the concave and convex features on a textured surface, is primarily due to an increase in D_{it} rather than a decrease in Q_{eff}. An NH_3 plasma exposure experiment presented in Section 6.6 indicates that the increase in D_{it}, and therefore S_{eff}, relates to an excessive incorporation of NH_b radicals, consistent with the hypothesis developed in Chapter 5.

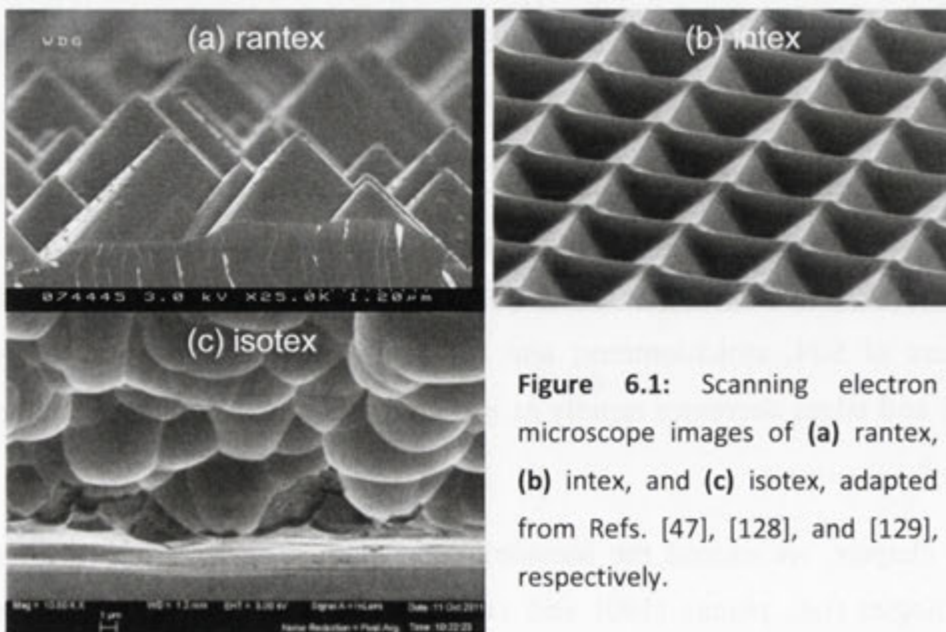

Figure 6.1: Scanning electron microscope images of **(a)** rantex, **(b)** intex, and **(c)** isotex, adapted from Refs. [47], [128], and [129], respectively.

6.2 Literature review

Three factors are generally considered to be responsible for the higher recombination at textured surfaces compared to identically prepared planar {100} equivalents: *(i)* a larger surface area, *(ii)* the presence of {111}-oriented facets, and *(iii)* the presence of vertices and/or edges [144]. Following Baker-Finch [145], we denote the three factors as f_A, f_O and f_V, where the subscripts A, O and V stand for area, orientation and vertices, respectively. A thorough analysis of the literature suggests that the latter two factors (i.e, f_O and f_V) depend significantly on the passivation scheme.

The passivation scheme impacts strongly on f_O. When the surface is passivated by thermal SiO_2, planar {111} surfaces exhibit a significantly higher density of dangling bonds than planar {100} equivalents [146, 147]. For thermally grown and hydrogenated SiO_2, Baker-Finch and McIntosh [148] found that $f_O = 4.0$. On the other hand, f_O tends to be unity when passivated by PECVD SiN_x [148] and a-Si [149].

The passivation scheme also impacts significantly on f_V. A detailed investigation into this aspect is given in [148]. Note that we assume a 1.7-fold increase in surface area for rantex compared to planar surfaces (i.e., an ideal pyramidal texture with a base angle of $\arctan\sqrt{2}$). Whereas $f_V \approx 1.0$ when passivated by thermal SiO_2, f_V for SiN_x was found to be significantly higher at 3.5 [148]. Notably, the SiN_x used in [148] had an n_{632} of 1.85. By contrast, in similar studies but on SiN_x with $n_{632} = 2.3$, both Lauinger *et al.* [8] and Rohatgi *et al.* [150] found the area-corrected S_{eff} ratio of rantex to {100} surfaces to be $f_O f_V \approx 1.0$.

The observations above suggest that f_V for SiN_x passivation relates significantly to n_{632}, and therefore film stoichiometry. This speculation is supported by a re-examination of the results presented by Chen *et al.* [39]. They investigated SiN_x with a range of compositions, or more specifically, a range of [Si–N], on planar {100}, planar {111}, and rantex. These samples were all FZ n-Si with a nominal resistivity of 1.0 Ω·cm. We re-analyse the data in Chen *et al.* by plotting the area-corrected S_{eff}

ratios, f_O and f_V, as a function of n_{632}. The S_{eff} ratio is extracted from their implied open-circuit voltage V_{OC} measured on symmetrically passivated lifetime samples by implementing *(i)* the relationship between implied V_{OC} and excess carrier density Δn [151], and *(ii)* the reciprocal relationship between the S_{eff} ratio and Δn ratio [4]. The value of n_{632} was extracted from the FTIR measurements of Chen *et al.* by implementing *(i)* the linear relationship between Si/N ratio and [Si–H]/[N–H] ratio determined by Claassen *et al.* [25], and *(ii)* the relationship between the N/Si ratio and n_{632} depicted in Eq. 2.1, as proposed by Bustarret *et al.* [28].

The re-examination of the data in [39] is presented in Figure 6.2. It shows that $f_O \approx 1.0$ over the tested range of PECVD SiN_x; that is, the recombination at {100} and {111} planar surfaces is similar, regardless of film stoichiometry. Figure 6.2 also shows that f_V decreases as n_{632} increases, tending toward unity when passivated by Si-rich films ($n_{632} > 2.6$). This is consistent with the observations mentioned above, where f_V is 3.5 when passivated by a N-rich SiN_x (n_{632} = 1.85) [148], and ~1.0 when passivated by a Si-rich film [8, 150]. The data points from Refs. [8, 148, 150] are also plotted in Figure 6.2. We treat these comparative studies with caution because the refractive indices for Ref. [39] were determined indirectly using two empirical equations, whereas the refractive indices for Refs. [8, 148, 150] were given in the original works.

In summary, two clear trends can be established from a re-examination of previous studies:

- f_O is approximately unity regardless of SiN_x stoichiometry, indicating that {100} and {111} orientations are passivated equally;
- f_V varies strongly with film stoichiometry, exhibiting highest values when the film is N-rich (low n_{632}), and reducing to unity when the film becomes Si-rich (high n_{632}).

In this chapter, we first extend the experiment embodied in Figure 6.2 on a variety of Si surface morphologies (i.e., planar {100} and {111}, rantex, intex and isotex). SiN_x films with a wide range of refractive indices are obtained by varying the NH_3:SiH_4 ratio, pressure and temperature. By studying the relationship between S_{eff} and n_{632} for the various silicon surfaces, we are able to elucidate the dependence of

S_{eff} on substrate orientation, morphology, and film stoichiometry. We then deposit corona charge and monitor S_{eff} to provide more insight into the recombination mechanisms associated with SiN_x-passivated Si surfaces. This method determines an effective insulator charge density Q_{eff} and provides qualitative access to the interface defect density D_{it}. Finally, following the recombination studies presented in Chapter 5, SiN_x-passivated samples are exposed to an NH_3 plasma to investigate the impact of NH_b radicals on the recombination at the textured surfaces.

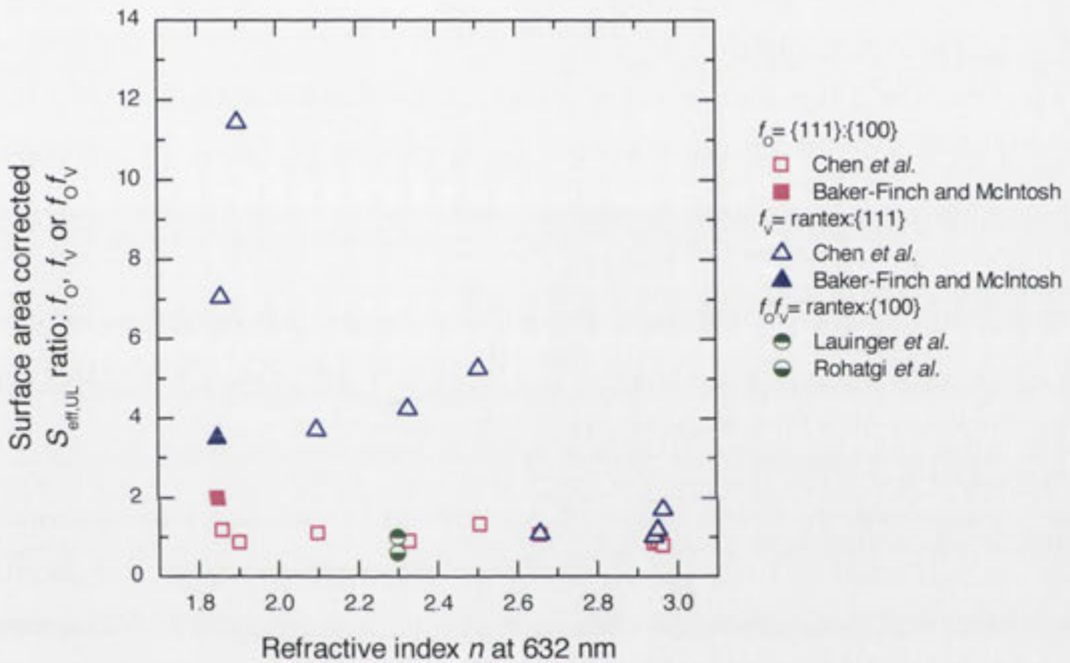

Figure 6.2: Surface area corrected $S_{eff,UL}$ ratio (f_O, f_V or f_Of_V) plotted as a function of n_{632}. Results for Chen *et al.* [39] were re-examined from the measurements of the dependence of implied open circuit voltage on Si–N bond density. Results from several other previous studies [8, 148, 150] are also included for comparison.

6.3 Experimental details

Lifetime samples were fabricated from *n*-type FZ Si wafers of {100} or {111} orientation with a resistivity of 1.1 Ω·cm. The resistivity of the substrates was calculated from their dark conductance as measured with a calibrated WCT-120 inductive coil instrument [152], where the calibration procedure is described in Section 3.3 of [153]. The thickness for {100} and {111} oriented planar samples was 390 μm and 290 μm, respectively. Planar samples (both {100} and {111}

orientations) were prepared by immersing as-cut wafers in tetramethylammonium hydroxide (TMAH, 25 wt%) at ~ 85 °C to remove saw damage. Rantex samples were prepared by submitting as-cut {100} samples into an alkaline solution of TMAH, deionised water, isopropyl alcohol (IPA) and dissolved silicon at a temperature of 85 °C for 60 min [141, 154-157].

Intex and isotex samples used in this work were recycled from the samples used in Refs. [148] and [158]. The intex surfaces with a range of proportions of {111} orientation, P_{111}, were prepared from as-cut planar {100} samples via oxide masking, photolithographic, and etching (25wt% TMAH with no additives at 85 °C) steps. The isotex samples were fabricated from 1.8 Ω·cm Czochralski *p*-type silicon wafers with a thickness of 180 μm. Samples were first textured in a cooled (10 °C) aqueous acid solution containing nitric and hydrofluoric acids using an inline RENA InTex tool. Texturing proceeded to various depths, corresponding to between 1 and 9 μm of saw damage removal. The control planar samples for intex and isotex surfaces were prepared by chemically polishing the existing intex and isotex samples in 1:10 HF:HNO_3 solution.

Next, all samples were cleaned by the RCA procedure, dipped in HF to remove the native oxide, and then coated with SiN_x on both surfaces by two sequential depositions. SiN_x was deposited using the μW/RF dual-mode PECVD system described in Chapter 3. The baseline recipe for SiN_x deposition followed an optimised deposition condition developed in Chapter 4, where the deposition temperature was 300 °C, the pressure was 0.2 mbar, the $NH_3/SiH_4/Ar$ gas flow was 20/20/20 sccm, the μW plasma power was 500 W, and the RF bias voltage was 150 V. The NH_3:SiH_4 ratio, deposition pressure, and substrate temperature were varied in this work to alter the film properties. The deposition time for all conditions was 3 min, and the resultant film thickness ranged from 35 to 90 nm. As presented in [108], for thick (> 20 nm) SiN_x film, the thickness has little impact on surface recombination. The effective lifetime of the samples were then measured by photoconductance in the transient mode, and $S_{eff,UL}$ was calculated in accordance with Section 2.5.3.

Following an initial recombination analysis, corona charge was deposited onto the lifetime samples to alter the surface recombination velocity. After rinsing the samples with IPA to remove any charge existing on the SiN_x surface, the samples were subjected to corona charging using a conventional setup with a metal grid [159]. A +6 kV potential was applied to the steel needle located 11 cm above the sample. Both surfaces of the samples were charged identically for various durations until the *n*-type silicon surfaces entered strong accumulation. The samples were then rinsed with IPA again to remove the positive charges on the SiN_x surfaces. $S_{eff,UL}$ was re-measured and found to be within ± 5% of its starting point before corona charging. Next, a –6 kV potential was applied to cause the *n*-type silicon surfaces to enter depletion and then inversion. The surface charge Q_s was determined from the measured surface potential using a Kelvin probe [159] and the insulator capacitance measured by high frequency (1 MHz) C–V. The samples for the measurement of surface potential and insulator capacitance were the same as those used for reflectance measurements.

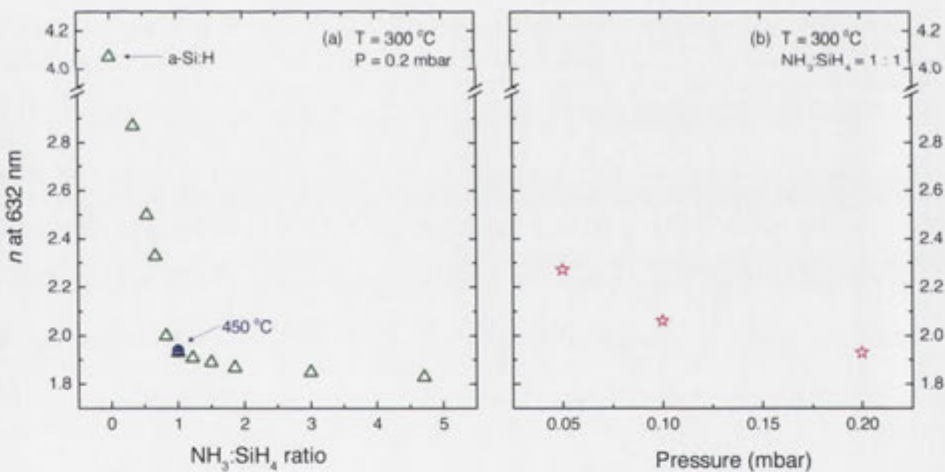

Figure 6.3: A broad range of SiN_x n_{632} are obtained by varying **(a)** the NH_3:SiH_4 ratio at two substrate temperatures, and **(b)** the deposition pressure.

Samples for reflectance measurements were DSP *n*-type {100} FZ Si with a resistivity of 1.1 Ω·cm and a thickness of 290 μm. The film thickness and n_{632} was determined from reflectance measurements in accordance with Section 2.2.3. Figure 6.3 illustrates the impact of various process conditions on n_{632}. As the NH_3:SiH_4 ratio and pressure increase, n_{632} decreases, ranging from 1.83 (N-rich) to

4.1 (a-Si). On the other hand, the increase of deposition temperature hardly affects n_{632}. For the studies of intex and isotex surfaces, we varied the NH_3:SiH_4 ratio and obtained three SiN_x films of n_{632} = 1.85, 2.0 and 2.5 and one a-Si film of n_{632} = 4.1.

6.4 Dependence of S_{eff} on substrate orientation, morphology, and SiN_x stoichiometry

PECVD SiN_x is the standard technique for the ARC and passivation of the front surfaces of both laboratory and commercial silicon solar cells, where the sunward front surfaces are usually textured to reduce front surface reflectance and enhance light trapping. Whilst texturing provides an optical benefit, it also invokes additional surface recombination when compared to its original planar {100} surface. This section aims to examine the recombination at SiN_x-passivated textured surfaces, where three types of texturing are investigated, namely rantex, intex and isotex.

6.4.1 Rantex

Rantex is a relatively simple and inexpensive texturing technique that is ubiquitous in commercial monocrystalline silicon solar cells. In this Section, we first extend the experiment embodied in Figure 6.2 by passivating {100}, {111} and rantex silicon surfaces with SiN_x for a wide range of n_{632}. The surface area-corrected $S_{eff,UL}$ at $\Delta n = 10^{15}$ cm^{-3} is plotted against n_{632}. Figure 6.4 plots the results and contains many points of interest.

We first note that over the range n_{632} = 1.91–2.9, $S_{eff,UL}$ on rantex surfaces is relatively low (< 10 cm/s), consistent with the results on planar surfaces (see Section 5.3). The results open a wide process window to maximise optical transmission and surface passivation. In other words, the trade-off between optical transmission and surface passivation of textured silicon is circumvented. This is a notable result for commercial solar cells, which regularly feature rantex surfaces.

A. Varying the NH_3:SiH_4 ratio

We next observe in Figure 6.4 that as n_{632} increases (by decreasing the NH_3:SiH_4 ratio), $S_{eff,UL}$ initially decreases and then saturates over the range n_{632} = 1.91–2.9. This has been observed in several previous studies [8, 20, 21]. Further, this behaviour is found to persist for all three types of silicon surfaces, as evident in Figure 6.4(a).

Moreover, we find that, regardless of n_{632}, and therefore stoichiometry, $S_{eff,UL}$ on planar {100} and {111} surfaces are comparable, for all SiN_x films prepared in this work. Figure 6.4(b) elucidates this phenomenon by plotting f_O as a function of n_{632}. It shows that f_O ranges from 0.8 to 1.7, consistent with the results of prior works summarised in Section 6.2. We therefore conclude that, for a wide variety of SiN_x films, the {111} orientation does not induce significantly more defects than {100}.

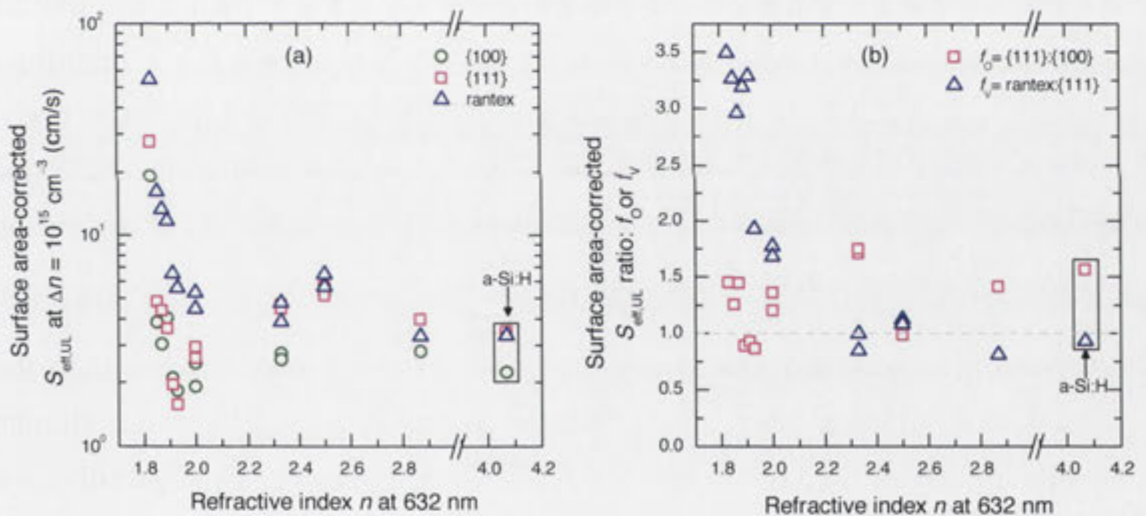

Figure 6.4: Surface area-corrected **(a)** $S_{eff,UL}$ at $\Delta n = 10^{15}$ cm^{-3} and **(b)** $S_{eff,UL}$ ratio (f_O or f_V) as a function of n_{632} for three silicon surfaces. A wide range of SiN_x refractive indices were obtained by varying the NH_3:SiH_4 ratio. Passivation results for a-Si with n_{632} = 4.1 are included.

By contrast, $S_{eff,UL}$ of the rantex is higher than of the planar surfaces when the NH_3:SiH_4 ratio is high (leading to a low n), but decreases rapidly and approaches the same $S_{eff,UL}$ as the planar surfaces when the NH_3:SiH_4 ≤ 0.7 ($n_{632} \geq 2.3$). When passivated with a N-rich SiN_x deposited with NH_3:SiH_4 = 4.7 (n_{632} = 1.83), the vertices and edges of the pyramidal texture drives an f_V = 3.5 times increase in $S_{eff,UL}$.

Again, this is consistent with the results of previous studies summarised in Section 6.2.

In addition to the SiN_x, we examined a-Si (n_{632} = 4.1) by setting the NH_3:SiH_4 ratio to zero. The results are also included in Figure 6.4. They show that the a-Si exhibits similar recombination to the Si-rich SiN_x samples ($n_{632} \geq 2.3$), where the area-corrected $S_{eff,UL}$ for planar {100} surfaces equals 2.2 cm/s, f_O equals 1.6, and f_V equals 0.9.

B. Varying the deposition pressure

As presented in Chapter 4, as the deposition pressure decreases, n_{632} increases and $S_{eff,UL}$ increases markedly. We ascribed the additional recombination at low pressure to an increase in interface defects induced by ion-bombardment. Here, we have rantex as well as planar {100} samples passivated with SiN_x deposited at three different pressures. We denote the area-corrected $S_{eff,UL}$ ratio of rantex to {100} as $f_O f_V$, since planar {111} was not involved in this sub-experiment. The relationships between $S_{eff,UL}$ and $f_O f_V$ are plotted against n_{632} in Figure 6.5(a) and (b), respectively. Note that the lifetime samples for the variation of pressure and temperature (see next subsection) are *n*-type 0.45 Ω·cm FZ silicon with a thickness of 245 μm, owing to an unavailability of 1.1 Ω·cm samples at that time.

As shown in Figure 6.5, the results for rantex exhibit similar behaviour to the planar {100} samples, where $S_{eff,UL}$ increases drastically as n_{632} increases. Despite the divergent trend of $S_{eff,UL}$ to n_{632} for the variation of gas ratio and pressure, we observe a similar relationship between $f_O f_V$ and n_{632}, where $f_O f_V$ decreases as n_{632} increases, and is unity when n_{632} = 2.3. This can be seen in Figure 6.5(b). The data point at n_{632} = 2.3 indicates that the ion bombardment at low pressure does not cause significantly more defects on textured surfaces than it does on planar surfaces.

C. Varying the substrate temperature

All SiN_x films described above were deposited at 300 °C. We also coated the rantex and planar {100} samples with SiN_x deposited at 450 °C. The results are included in Figure 6.5. Consistent with the results presented in Chapter 4, SiN_x deposited at 450 °C provides less passivation than 300 °C-deposited SiN_x, despite a similar n_{632}.

On the other hand, the two SiN_x films have similar $f_O f_V$, implying that an increase in substrate temperature causes a relatively similar increase in recombination on the two morphologies.

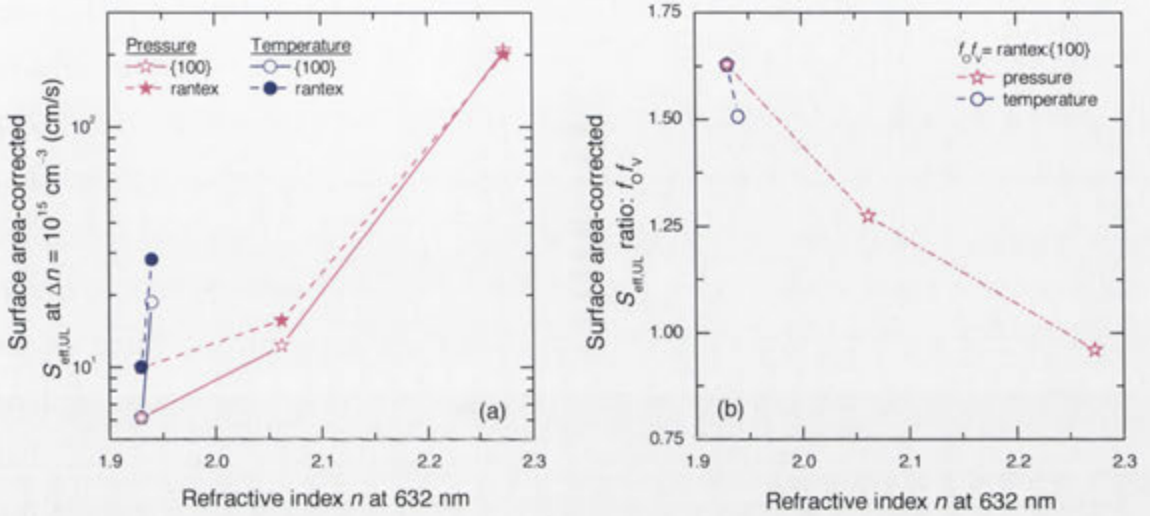

Figure 6.5: Surface area-corrected **(a)** $S_{eff,UL}$ at $\Delta n = 10^{15}$ cm^{-3} and **(b)** $S_{eff,UL}$ ratio ($f_O f_V$) as a function of n_{632} for three silicon surfaces. SiN_x properties were altered by varying the deposition pressure and substrate temperature.

D. Summary

In summary, over a wide range of refractive indices (n_{632} = 1.91–4.1), we obtain a low $S_{eff,UL}$ < 10 cm/s at rantex. Furthermore, S_{eff} is higher for rantex surfaces than it is for planar surfaces when n_{632} is low. For example, $f_V \approx 3.5$ when passivated by a N-rich SiN_x (n_{632} = 1.83). As n_{632} increases, S_{eff} at rantex decreases rapidly and approaches the same $S_{eff,UL}$ as the planar surfaces when $n_{632} \geq 2.3$ (f_V or $f_O f_V \approx 1.0$). In contrast, we find that irrespective of the NH_3:SiH_4 ratio, and therefore n_{632}, S_{eff} is equivalent for {100} and {111} planar surfaces (f_O = 0.8–1.7). The results infer that the increase in S_{eff} at rantex is related to the presence of vertices and/or edges of the pyramids rather than to the presence of {111} orientated facets.

6.4.2 Intex

Intex—a regular array of inverted pyramids—provides favourable light trapping characteristics compared with other morphologies [140, 160], and hence has been used for record efficiency silicon cells [23, 143, 161, 162]. The recombination at intex surfaces was studied in detail by Baker-Finch and McIntosh [148]. Utilising oxide masking and photolithographic pattering, they prepared texturing surfaces featuring a range of inverted pyramids with different proportions of {111} orientation, P_{111}. These textured surfaces were passivated with either hydrogenated thermal SiO_2, atomic layer deposited Al_2O_3 or PECVD SiN_x. They found that, for all three passivation technologies, S_{eff} increases as P_{111} increases. After accounting for surface area enlargement by texturing, the enhancement of S_{eff} related to the pyramids can be attributable to the presence of {111} orientation and/or vertices/edges. Again, we denote these two factors as f_O and f_V. They found that both f_O and f_V depend strongly on the choice of passivation scheme, similar to the behaviour at rantex. When passivated with SiO_2 or Al_2O_3, $f_O \approx 6.0$ and $f_V \approx 1.0$. In contrast, when passivated with SiN_x of $n_{632} = 1.85$, $f_O \approx 1.0$ and $f_V \approx 4.4$.

This section extends the recombination study at the intex surfaces, where the passivating films are three SiN_x films of $n_{632} = 1.85$, 2.0 and 2.5 and one a-Si film of $n_{632} = 4.1$. Figure 6.6(a) plots $S_{eff,UL}$ at $\Delta n = 10^{15}$ cm^{-3} for a variety of surface morphologies. Note that the results in Figure 6.6(a) are separated into two groups. The samples without thermal oxide masking (where the masking facilitated the formation of intex) have a surface of planar {100}, planar {111} and rantex. On the other hand, the samples with thermal oxide masking have intex surfaces with a range of {111} proportion of surface area (i.e., P_{111}). Note further that the $S_{eff,UL}$ reported here is after surface area correction, since surface area increases as P_{111} increases. Figure 6.6(b) presents the area-corrected $S_{eff,UL}$ ratio (i.e., f_O, f_V or f_Of_V) as a function of P_{111}.

We first observe that the recombination results for the samples without thermal oxide masking are consistent with those for rantex surfaces presented in previous section. It is seen that *(i)* irrespective of n_{632}, planar {111} samples generally possess ~1.5 times higher recombination than {100} equivalents (i.e., $f_O \approx 1.5$ and see the

solid symbols in Figure 6.6(b)); and *(ii)* by contrast, f_V varies significantly with n_{632}, decreasing from 2.8 to 1.6 as n_{632} increases from 1.85 to 4.1.

We then note that S_{eff} for samples with thermal oxide masking is generally higher than S_{eff} for the equivalents without thermal oxide masking. In comparing specifically the S_{eff} at planar {100} surfaces, the oxidised sample exhibits approximately four times higher $S_{eff,UL}$ than the non-oxidised sample. Further, this factor is independent of passivating film stoichiometry, implying that the thermal oxide masking employed in this work deteriorates significantly the silicon bulk quality, resulting in an approximately fourfold increase in the extracted $S_{eff,UL}$. We therefore define $f_O f_V$ for intex samples with respect to the planar {100} equivalents that were thermally oxidised and then chemically polished. This ratio is represented by open symbols in Figure 6.6(b).

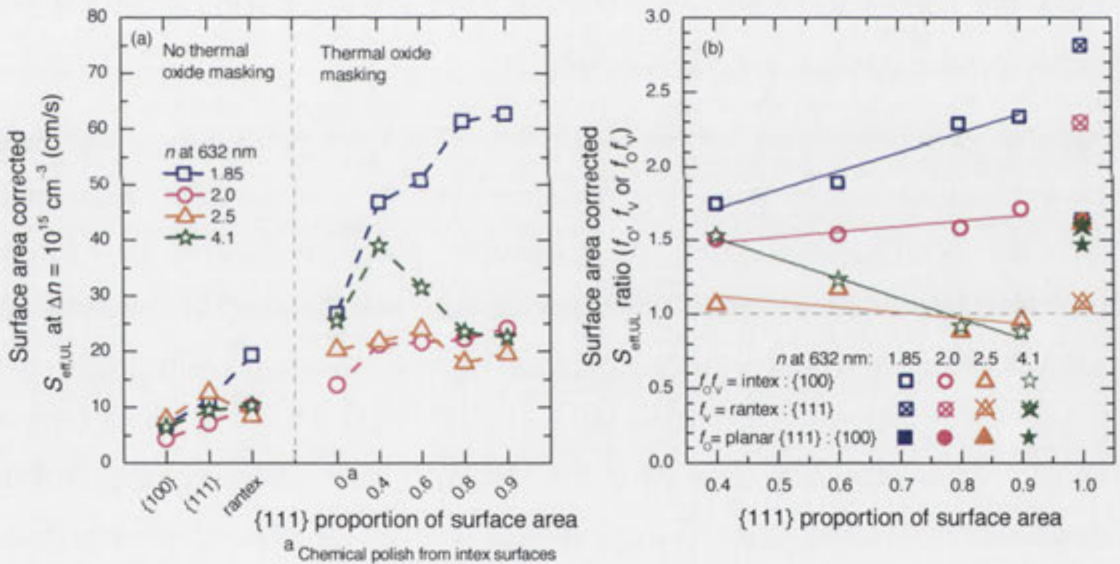

Figure 6.6: Relationship between surface area corrected **(a)** $S_{eff,UL}$, and **(b)** f_O, f_V, or $f_O f_V$ and the proportion of {111}-oriented surface at pyramidally textured silicon surfaces. Note that f_O in (b) represented by solid symbols all fall together at ~1.5. Solid lines in (b) are linear best fits.

Similar to the behaviour of f_V for rantex surfaces, $f_O f_V$ for intex samples also depends significantly on the NH_3:SiH_4 ratio, and therefore n_{632}. When passivated by SiN_x of $n_{632} = 1.85$, $S_{eff,UL}$ increases strongly with an increase in P_{111}. As SiN_x becomes slightly Si-rich at $n_{632} = 2.0$, the dependence of $S_{eff,UL}$ on P_{111} tends to be weaker,

showing a slight increase with P_{111}. When passivated by a very Si-rich film at $n_{632} = 2.5$, $S_{eff,UL}$ is constant with P_{111}, inferring that the vertices and/or edges at pyramidally textured surfaces causes negligibly additional recombination.

Furthermore, when passivated by a-Si, an opposing trend can be observed, showing that $S_{eff,UL}$ decreases as P_{111} increases. The result is inconsistent with the observed $f_V = 1.6$ for rantex equivalent and it is an anomaly, for which it would imply that the presence of pyramids at intex surfaces *enhances* the level of surface passivation. Presumably, the *enhanced* surface passivation can be induced by the presence of {111} orientation, and/or the presence of vertices/edges. Indeed, when passivated with PECVD a-Si, Descoeudres *et al.* [163] attained higher lifetime on planar {111} than identically prepared {100} samples. Also, De Wolf *et al.*[125] found that, after 1 min light soaking, the passivation of the a-Si-passivated {100} surfaces degraded much faster than the {111} counterparts. Interestingly, both phenomena were attributed to a dangling bond density at an unreconstructed {100} surface is twice that existing at the {111} surface [164].

Another possible reason for the lower $S_{eff,UL}$ at intex with higher P_{111} when passivated by a-Si is the existence of an epitaxial layer at the a-Si/c-Si interface. According to Das *et al.* [149], the epitaxial silicon layer induced by hydrogen plasma is more detrimental to the passivation of {100} than {111} surfaces. We speculate that a substantial part of the a-Si in this work was epitaxially grown, since the film was deposited at 300 °C, which is higher than the commonly reported optimum deposition temperature for a-Si (< 200 °C) [165, 166]. We supported this speculation by annealing the {100} samples, showing the passivation deteriorated with increasing annealing time. This observation is consistent with the result given in [165], where the authors confirmed the growth of epitaxial layer in the film deposited at a temperature higher than 205 °C by showing a degradation in passivation upon annealing.

However, both potential causes contradict the behaviour of the identically prepared planar {111} and rantex samples, where both surfaces possess higher recombination than the planar {100} equivalent. The physical cause for the recombination at a-Si passivated intex surfaces needs further investigation.

6.4.3 Isotex

Recombination at isotex surfaces is believed to depend on the depth of saw damage removal (SDR) [167], since surface area, saw damage, and bowl-like curvature decreases as SDR increases. Baker-Finch *et al.* [158] investigated the recombination at isotex surfaces, where the surfaces were etched into a range of depths [158] and passivated with thermal SiO_2 or PECVD SiN_x of $n_{632} = 1.85$. It was found that, after accounting for surface area enlargement by texturing, S_{eff} is identical at isotex and planar {100}, regardless of SDR. The result implies that neither facet orientation nor local curvature caused additional recombination.

In this section, we investigate the recombination at isotex surfaces that are passivated by the same four films employed at intex surfaces. The area-corrected $S_{eff,UL}$ and $S_{eff,UL}$ ratio of isotex to planar surfaces (i.e., $f_Q f_V$) are plotted as a function of SDR in Figure 6.7 (a) and (b) respectively. Note that the surface area is calculated by assuming that features on isotex surfaces have a spherical cap morphology and are tightly packed [168].

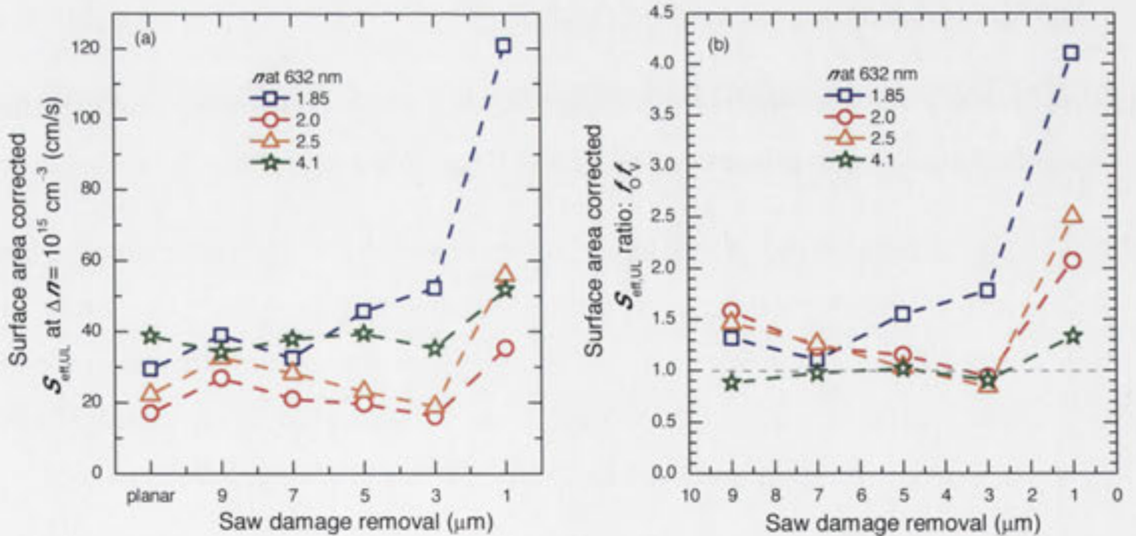

Figure 6.7: Relationship between surface area corrected **(a)** $S_{eff,UL}$, and **(b)** $S_{eff,UL}$ ratio (i.e., $f_Q f_V$) and saw damage removal at isotropically textured silicon surfaces.

We first note that S_{eff} for SDR = 1 μm is generally higher than the identically passivated surface with a higher SDR. This might be a strong indication of saw damage, namely crystal defects located within the near-surface region. In our samples, we suspect that these defects extend more than 1 μm and less than 3 μm into the silicon substrate.

We then focus on the relationship between film stoichiometry and the recombination at isotex surfaces. When passivated by SiN_x of n_{632} = 1.85, S_{eff} increases as SDR decreases, showing that $f_Q f_V$ increases from 1.3 to 4.1 as SDR decreases from 9 μm to 1 μm. The result suggests that for this passivating film, besides the factor of surface area, the recombination is increased by *(i)* the crystal orientations, and/or *(ii)* the local convex and concave features. On the other hand, when isotex surfaces are passivated by the remaining three films (n_{632} = 2.0, 2.5, and 4.1), except at the lowest etch depth (SDR = 1 μm), S_{eff} exhibits a week dependence on SDR. The results indicate that for the three passivating films, besides the surface area, neither the crystal orientations nor the local convex and concave features induce significantly additional recombination at isotex surfaces.

6.4.4 Conclusions

In this section, we investigated the recombination at textured silicon surfaces that were passivated by a wide variety of PECVD films. We found that:

- Over a large range of refractive indices (n_{632} = 1.9–4.1), we achieved a low surface recombination on rantex samples ($S_{eff,UL}$ < 10 cm/s at $\Delta n = 10^{15}$ cm^{-3}). The results demonstrate that we circumvent the trade-off between optical transmission and surface passivation of textured silicon surfaces, as was demonstrated for planar surfaces in Section 5.3.

- S_{eff} was higher for rantex than for planar surfaces when the NH_3:SiH_4 ratio was high (and hence n was low). For example, when passivated by a N-rich SiN_x deposited with NH_3:SiH_4 = 4.7 (n_{632} = 1.83), the vertices and/or edges of rantex drove a 3.5 times increase in S_{eff}. As n_{632} increased, S_{eff} at rantex

decreased rapidly and approached the same S_{eff} as the planar surfaces when $n_{632} \geq 2.3$.

- By contrast, irrespective of the NH_3:SiH_4 ratio, and therefore n, S_{eff} is equivalent on {100} and {111} planar surfaces, indicating that the increase in S_{eff} at rantex was related to the presence of vertices and/or edges of the pyramids rather than to the presence of {111}-orientated facets.

The experimental results for rantex lead clearly to the conclusion that S_{eff} at textured surfaces relates strongly to both the passivating film stoichiometry and the silicon surface morphology. The conclusion was supported by the recombination studies at intex and isotex surfaces, which featured a range of texturing morphologies. It was shown that:

- When passivated by N-rich SiN_x (n_{632} = 1.85), S_{eff} increased significantly as P_{111} at intex increases and as SDR at isotex decreased.

- When passivated by Si-rich SiN_x (n_{632} = 2.0 and 2.5), the dependence of S_{eff} on surface morphologies became weak.

- When passivated by a-Si, the recombination behaved differently at the intex and isotex surfaces. Whereas S_{eff} at intex decreased with an increase in P_{111}, S_{eff} at isotex was constant with SDR.

The results in this section indicate that, although a recombination increase associated with enlarged surface area is unavoidable, increases due to the presence of orientation and local curvatures at textured surfaces can be suppressed by a proper choice of passivating film. These results should prove useful in designing high efficiency solar cells fabricated from textured silicon wafers.

6.5 Probing SiN_x electronic properties at textured surfaces

Typically, C–V analysis is employed to probe electronic properties such as D_{it} and Q_{eff} on planar silicon surfaces. This method however is not suited to the analysis of

textured surfaces, mainly due to high leakage current that occurs on textured morphologies [56]. One alternative to probe interface electronic properties is to deposit corona charge on dielectric passivated samples and monitor the change in S_{eff} [114]. Deposition of corona charge onto a dielectric surface alters the surface carrier concentration at the underlying silicon surface, and consequently alters the surface recombination. This method determines an effective insulator charge density Q_{eff} and provides qualitative access to the interface defect density D_{it}.

By examining the effect of film stoichiometry, substrate orientation and morphology on the SiN_x electronic properties, we can elucidate the fundamental cause for the increase in recombination introduced by *(i)* a higher NH_3:SiH_4 ratio, and *(ii)* the local curvatures of texturing.

6.5.1 Dependence of S_{eff} on surface charge density Q_s

By monitoring the change in S_{eff} along with the varying deposition of corona charge, we observed three types of relationships between $S_{eff,UL}$ and the applied Q_s. Figure 6.8 illustrates the three exemplary relationships on planar {100} *n*-type samples. The samples were passivated with three SiN_x films where the red symbols plot data for n_{632} = 1.83, the blue symbols for n_{632} = 1.93, and the green symbols for n_{632} = 2.5. Prior to applying any corona charge, $S_{eff,UL}$ is denoted as S_0.

The first type of $S_{eff,UL}(Q_s)$ behaviour is represented by the sample passivated with a N-rich SiN_x of n_{632} = 1.83. It exhibits the classic dependence of $S_{eff,UL}$ on Q_s, which is also observed for samples passivated by thermal SiO_2 [113] and plasma-assisted atomic layer deposited Al_2O_3 [169]. The behaviour contains a peak in $S_{eff,UL}$, denoted S_{it}, that occurs when the applied Q_s approximately balances the effective charge Q_{eff} of the SiN_x. Thus, S_{it} is ostensibly not affected by "field-effect passivation" but only the defect states at the SiN_x/Si interface; it can therefore be considered as an indicator of the interface defect density D_{it} [4]. As either positive or negative charge is applied, $S_{eff,UL}$ decreases and then saturates.

The second type of $S_{eff,UL}(Q_s)$ behaviour is represented by blue circles for the sample passivated with a nearly stoichiometric SiN_x of n_{632} = 1.93. As positive charge is applied, $S_{eff,UL}$ decreases and then saturates, similar to the behaviour for the N-rich

SiN_x (n_{632} = 1.83). By contrast, as negative charge is applied, $S_{eff,UL}$ increases and then saturates. The passivation is unaffected by the application of additional negative Q_s. For the samples that follow this behaviour, we define S_{it} to occur where $S_{eff,UL}$ is first within 5% of its saturated level. S_{it} is marked with the solid symbols in Figure 6.8.

The reason why $S_{eff,UL}$ saturates with negative charge is most likely caused by the negative corona charge on the surface of the SiN_x being balanced by the injection of positive carriers from the silicon substrate into the SiN_x [139, 170, 171]. If the injected charge resides near the SiN_x/Si interface, then it does not contribute to the Kelvin-probe voltage [172] but it does prevent the net charge from increasing. In other words, if no charge injection occurs upon depositing corona charge, the extracted S_{it} and Q_{eff} could be higher. Therefore the S_{it} and Q_{eff} presented in this work can be considered a lower limit to the real S_{it} and Q_{eff}.

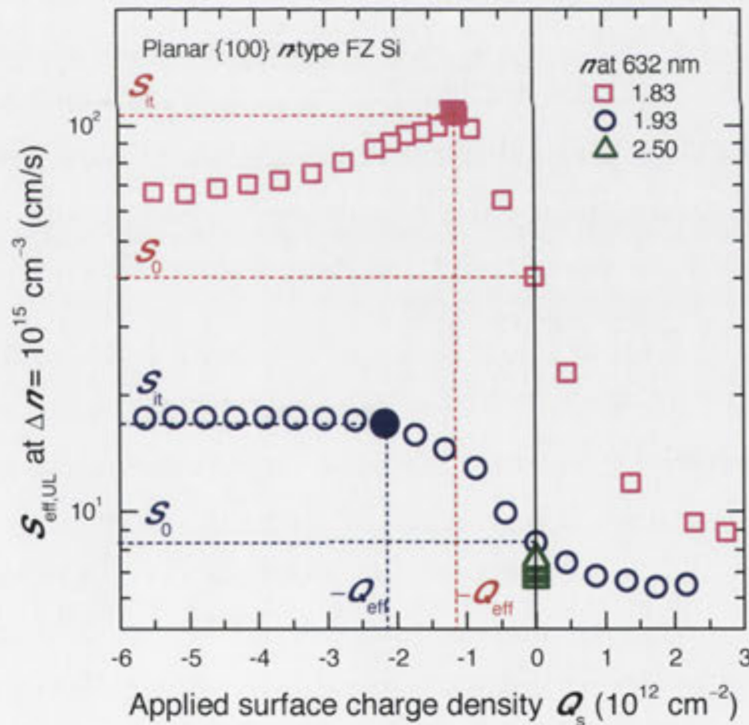

Figure 6.8: Exemplary corona-lifetime measurements of the relationship between $S_{eff,UL}$ and surface charge density Q_s for planar {100} Si surfaces. Samples were passivated by three SiN_x films having an n_{632} of 1.83, 1.93 and 2.5.

The last type of $S_{eff,UL}(Q_s)$ behaviour is represented by green triangles for the sample passivated with a Si-rich SiN_x of n_{632} = 2.5. In this case, within the experimental error, the deposition of either positive or negative corona charge does not affect $S_{eff,UL}$. Kelvin probe measurements indicate that no corona charge remains on the sample surface, that is, that the deposited corona charge leaks through the Si-rich SiN_x, which makes a poor insulator. The samples that exhibited this leaky behaviour had $n_{632} \geq 2.5$; these samples were therefore unable to be included in the analysis that follows.

6.5.2 Depositing corona charge at planar {100}, planar {111} and rantex surfaces

Corona charge was deposited onto the SiN_x-passivated planar {100}, planar {111} and rantex silicon surfaces. As discussed in previous section, the investigated SiN_x n_{632} ranges from 1.83 to 2.3. The extracted values of S_{it} and Q_{eff} are plotted against S_0 in Figure 6.9(a) and (b), respectively. We first observe that for all three silicon surfaces, S_0 tends to increase as S_{it} increases, whereas no universal correlation can be found between S_0 and Q_{eff}. This observation indicates that differences in surface recombination for the samples in this work depends primarily on the interface defect density rather than the insulator charge, consistent with the conclusion deduced from C–V measurements on planar samples (see Section 4.3.2–D).

We then note the insulator charge presented in Figure 6.9(b) is significantly higher than the charge deduced from C–V measurements. In addition to the experimental error, we tentatively attribute the discrepancy to the different energy state for the determination of charge density. While the insulator charge is calculated at flat-band voltage from C–V measurements, the deposition of corona charge causes the silicon surface to deep depletion (i.e., the peak S_{eff}). We therefore suspect that the source of the difference between the charge deduced from C–V and corona is a significant charge trapped at interfacial defects.

Furthermore, comparing the two planar surfaces (red and green symbols), we find that, over the investigated range of n_{632} = 1.83–2.3, the two orientations exhibit a similar S_{it} and Q_{eff}, suggesting that the interface defect density and charge in the

films are independent of crystal orientation. The results further justify a primary conclusion from the Section 6.4, namely that the {100} and {111} surfaces are equivalently passivated by SiN_x.

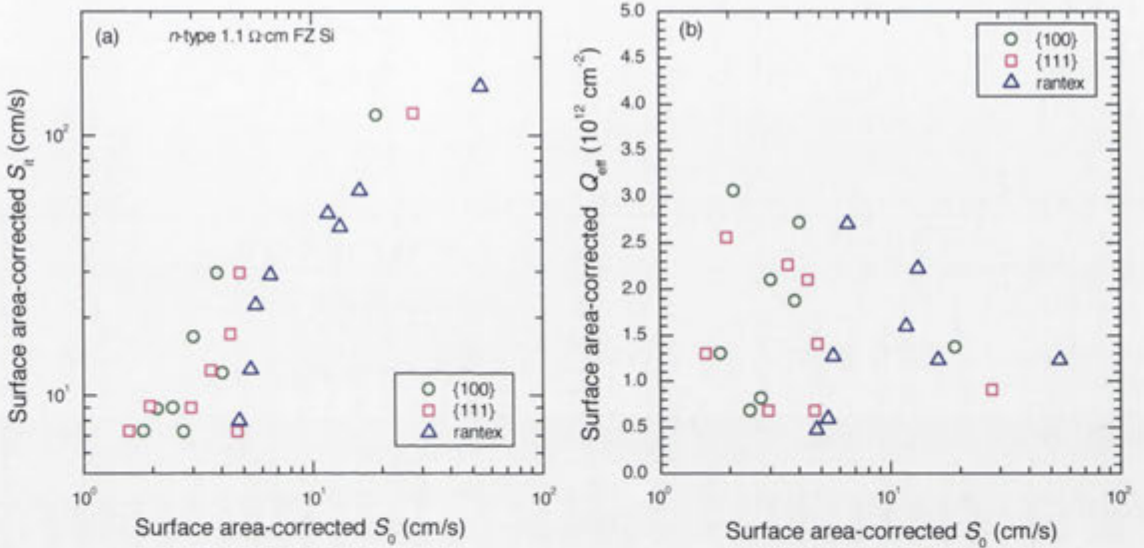

Figure 6.9: The relationship between S_0 and **(a)** S_{it}, and **(b)** Q_{eff} for the three surfaces, as extracted from monitoring $S_{eff,UL}$ upon corona charging.

As presented in Section 6.4.1, when passivated with a N-rich SiN_x ($n_{632} = 1.83$), rantex surfaces exhibit a ~3.5 times higher area-corrected $S_{eff,UL}$ than the planar samples (i.e., $f_V \sim 3.5$). A larger f_V can be caused by *(i)* a lower Q_{eff}, *(ii)* a higher D_{it}, and/or *(iii)* higher capture cross sections associated with the vertices and edges of the pyramids. By examining the relationship of the ratio of rantex to planar {111} for S_0, S_{it} and Q_{eff}, the causes for the enlarged recombination at rantex surfaces can be examined.

Figure 6.10(a) and (b) depicts the results for {111}:{100} and rantex:{111}, respectively. For all SiN_x we find that the ratio of S_0 for {111}:{100} or rantex:{111} samples is equivalent to that for S_{it}, giving a linear relationship close to 1:1. We also find that the associated ratios for Q_{eff} are approximately 1.0. For example, when samples were passivated with a N-rich SiN_x with $f_V \sim 3.5$, the rantex induced an approximately threefold increase in S_{it} but no change in Q_{eff}. These observations

indicate that the large f_V is caused by the increased defect density rather than by a reduction in film charge density associated with the pyramid vertices and edges.

In summary, we conclude that the increase in $S_{eff,UL}$ at rantex due to either *(i)* a higher NH_3:SiH_4, or *(ii)* the presence of vertices and/or edges, is primarily caused by an increase in the interface defect density rather than a reduction in the SiN_x charge density.

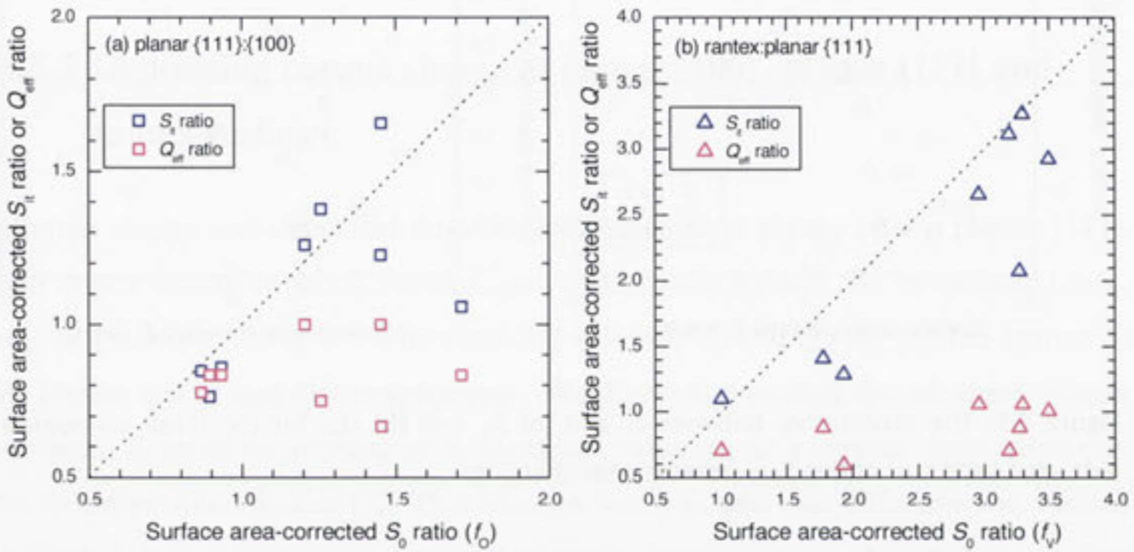

Figure 6.10: The correlation between surface area-corrected S_0 ratio, S_{it} ratio (in blue) and Q_{eff} ratio (in red) of **(a)** planar {111} : {100}, and **(b)** rantex : planar {111}. The 1:1 diagonal relationship is represented by the dash line for reference.

6.5.3 Depositing corona charge at intex surfaces

As presented in Section 6.4.2, when passivated by a N-rich SiN_x (n_{632} = 1.85), S_{eff} increased significantly as P_{111} at intex increases. The enlarged recombination can be attributable to *(i)* higher D_{it}, and/or *(ii)* lower Q_{eff}. By depositing corona charge onto intex surfaces and monitoring the change in $S_{eff,UL}$, we can elucidate the effect of P_{111} on the electronic properties: S_{it} and Q_{eff}.

Figure 6.11(a) depicts the relationship between $S_{eff,UL}$ and applied Q_s for intex samples. Noting that the passivating SiN_x is N-rich (n_{632} =1.85), the samples exhibit the first type of $S_{eff,UL}(Q_s)$ behaviour illustrated in Section 6.5.1. Each curve shows a

peak in $S_{eff,UL}$ that is denoted as S_{it} when the surface charge Q_s balances the effective charge Q_{eff} within SiN_x. Figure 6.11(b) plots the extracted value of S_{it} and Q_{eff} as a function of P_{111}. We first find that S_{it} increases significantly as P_{111} increases. For example, when comparing S_{it} of P_{111} = 0.9 to that of the planar equivalent, S_{it} increases by a factor of 2.9, which correlates well to the $f_Q f_V$ being 2.3 (see Section 6.4.2). We also note that Q_{eff} decreases as P_{111} increases, showing an approximately 50% reduction when comparing the Q_{eff} of P_{111} = 0.9 to that of the planar equivalent. The additional defects induced by the presence of pyramids seem to be the main factor for the increased recombination, although the reduction in Q_{eff} could also make a partial contribution to the increase in recombination.

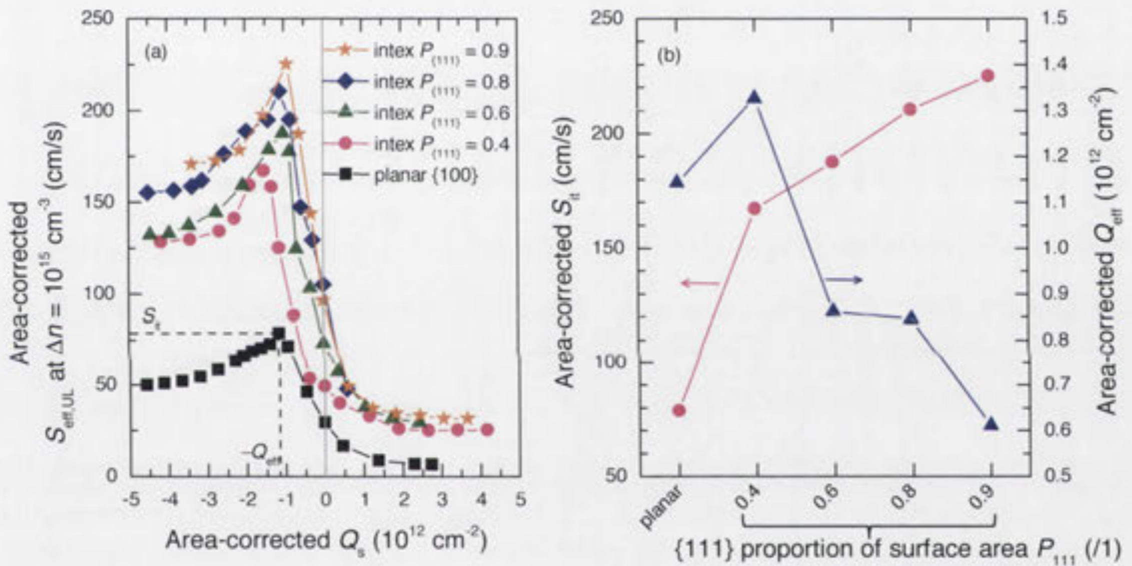

Figure 6.11: (a) Dependence of $S_{eff,UL}$ on corona surface charge density Q_s, and **(b)** the extracted value of S_{it} and Q_{eff} as a function of P_{111} at intex surfaces.

6.5.4 Depositing corona charge at isotex surfaces

Corona charge was deposited onto isotex surfaces with a range of saw damage removals. Figure 6.12(a) depicts the relationship between $S_{eff,UL}$ and applied Q_s and 6.12(b) plots the extracted value of S_{it} and Q_{eff} as a function of SDR. Similar to the case for intex samples, the isotex samples exhibit the first type of $S_{eff,UL}(Q_s)$ behaviour illustrated in Section 6.5.1, as the passivating SiN_x is N-rich (n_{632} =1.85). It is found that, as SDR decreases, S_{it} increases and Q_{eff} decreases. For example, when comparing S_{it} of SDR = 1 μm to that of the planar equivalent, S_{it} increases by

4.3 times, correlating well to the $f_Q f_V$ being 4.1 (see Section 6.4.3). The results lead to a same conclusion to that of intex samples: the increase in recombination is primarily caused by the additional defects induced by the presence of local curvatures at isotex, even though the reduction in Q_{eff} could also contribute partially to the increase in recombination.

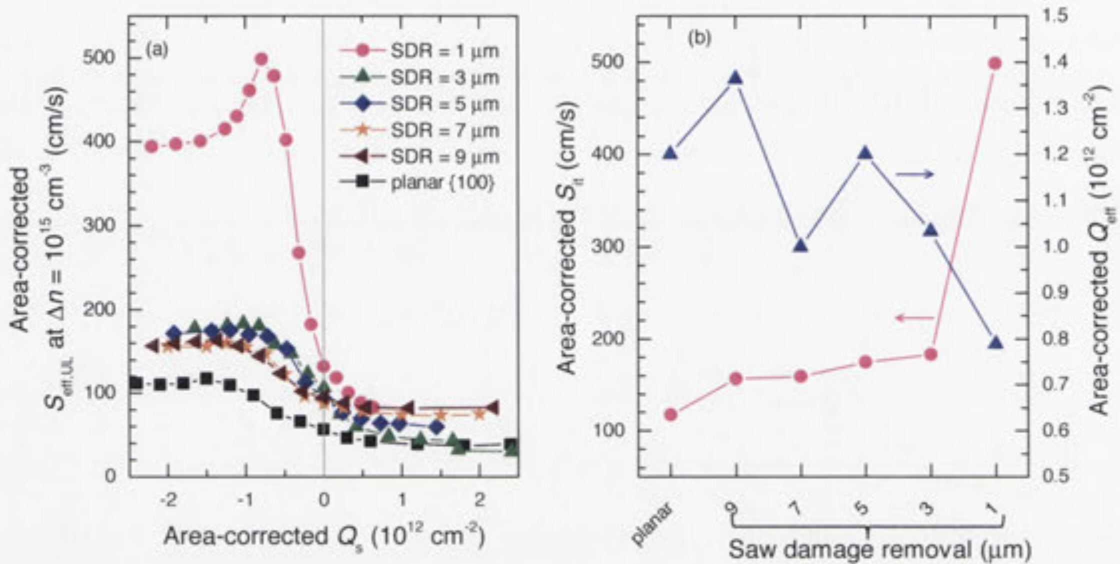

Figure 6.12: (a) Dependence of $S_{eff,UL}$ on corona surface charge density Q_s, and **(b)** the extracted value of S_{it} and Q_{eff} as a function of SDR at isotex surfaces.

Table 6.1: Summary of contributions to the increased recombination at textured surfaces. The $f_Q f_V$ of intex and isotex samples are for P_{111} = 0.9 and SDR=1 µm, respectively. The passivating SiN_x has n_{632} = 1.85.

Contributing factors		S_{eff} ratio	S_{it} ratio	Q_{eff} ratio
f_O	{111}:{100}	1.6	1.3	1.0
f_V	rantex:{111}	2.8	2.7	1.1
$f_Q f_V$	intex:{100}	2.3	2.9	0.6
	isotex:{100}	4.1	4.3	0.7

6.5.5 Conclusions

Varying amounts of corona charge were deposited on a variety of Si surface morphologies. It was deduced that the increase in S_{eff} due to *(i)* a higher NH_3:SiH_4

ratio, and *(ii)* the concave and convex features on a textured surface was primarily caused by an increase in the defect density rather than a reduction in the SiN_x charge density, as summarised in Table 6.1.

6.6 Exposing SiN_x-passivated textured surfaces to NH_3 plasma

It was shown in Section 6.4 that as the NH_3:SiH_4 ratio increases, *(i)* S_{eff} increases at both planar and textured surfaces; and *(ii)* f_V increases, indicating that the increase in recombination was exacerbated by vertices and/or edges. It was shown further in Section 6.5 that the increase in S_{eff} due to *(i)* a higher NH_3:SiH_4 ratio, and *(ii)* the vertices and/or edges of the pyramids was primarily caused by an increase in the defect density rather than a reduction in the SiN_x charge density. In Chapter 5, we proposed that the high S_{eff} at a high NH_3:SiH_4 ratio was attributable to an excessive incorporation of NH_b radicals. This section aims to elucidate the microscopic cause for the increase in defect density and therefore S_{eff} due to *(i)* a higher NH_3:SiH_4 ratio, and *(ii)* the vertices and edges of the pyramids, by exposing as-passivated rantex sample to an NH_3 plasma in a PECVD reactor.

Planar {100} and rantex samples were firstly coated with a SiN_x film having a thickness of 20 nm and n_{632} = 2.5 in accordance with the processing steps described in Section 6.3. The samples were then exposed to an NH_3 plasma at 300 °C by switching off the SiH_4 gas flow and leaving the other parameters the same. The plasma exposure time was varied from 3 to 50 minutes. By observing the relationship between $S_{eff,UL}$ and plasma exposure, we are able to evaluate the impact of defects induced by the incorporation of NH_b radicals on the recombination for planar and textured surfaces.

Figure 6.13 illustrates this relationship by plotting the area-corrected (a) $S_{eff,UL}$, and (b) $S_{eff,UL}$ ratio ($f_Q f_V$) against the NH_3 plasma exposure time. Figure 6.13 also includes the results for control samples that were exposed to the same temperature but within an N_2 ambient in thermal furnace rather than an NH_3 plasma in PECVD reactor.

As seen in Figure 6.13(a), NH_3 plasma exposure increases the recombination at a markedly higher rate than the N_2 ambient exposure. After 50-minutes exposure of the planar samples, the NH_3-plasma exposure induces more than one order of magnitude increase in $S_{eff,UL}$ whereas the N_2 exposure induces a twofold increase. The figure also indicates that the effect of the two processes is even more dramatic on the rantex surfaces, as evidenced in Figure 6.13(b). In terms of the additional recombination due to the vertices and edges, $f_Q f_V$ increases strongly as the plasma exposure time increases, being 2.8 for as-deposited film and 28 after 50-minutes of NH_3 plasma exposure. On the contrary, $f_Q f_V$ decreases as the N_2 exposure time increases, being 2.4 for the as-deposited film and 1.0 after 60-minutes of N_2 exposure.

We can therefore conclude tentatively that it is primarily the NH_b radicals rather than the temperature that degrades the surface passivation of the samples when exposed to the NH_3 plasma at 300 °C. The observations in Figure 6.13 are consistent with the hypothesis proposed in Section 5.4, namely that, the incorporation of NH_b radicals introduces defects at the SiN_x/Si interface and therefore increases S_{eff}. It also suggests that the vertices and/or edges of rantex make the surfaces more prone to the degradation induced by NH_b radical incorporation (assuming similar effects of NH_b radical incorporation on the recombination at planar {100} and {111} surfaces). A possible explanation for this phenomenon relates to the existence of strained bonds in amorphous film. We expect there to be greater density of strained bonds at the convex and concave surfaces associated with the vertices and/or edges of the pyramids, and according to [173], strained bonds are weaker and more susceptible to plasma reactions such as NH_b radical incorporation. Thus we might expect the passivation of SiN_x-coated rantex wafers to degrade more rapidly than that of planar samples when exposed to an NH_3 plasma.

In summary, we propose that the increase in defect density and therefore S_{eff} due to *(i)* a higher NH_3:SiH_4 ratio, and *(ii)* the vertices and edges of the pyramids, was due to a higher proportion of NH_b radicals into the SiN_x network.

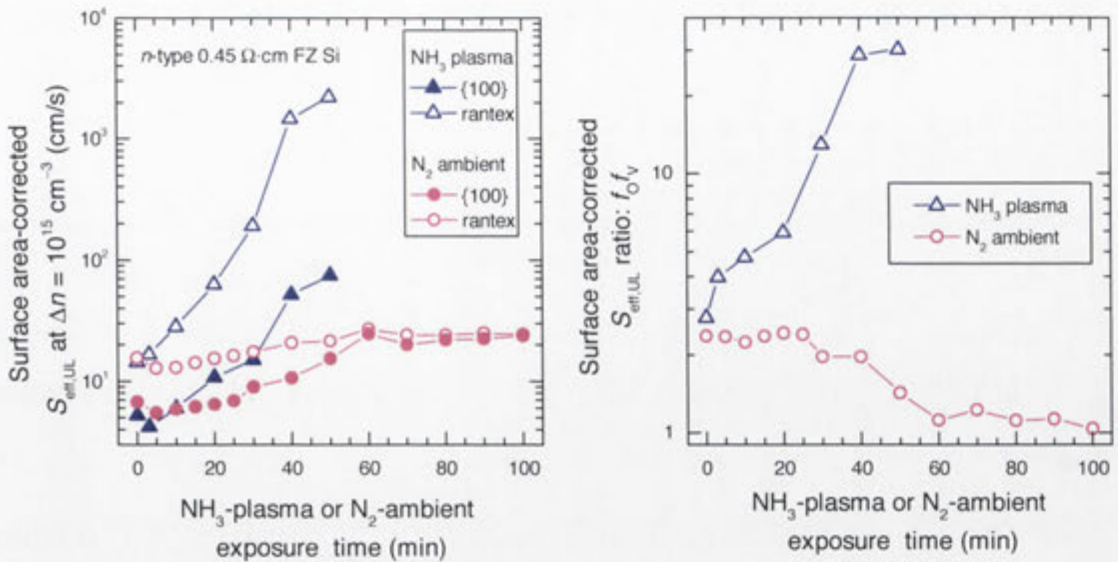

Figure 6.13: The impact of NH_3 plasma in PECVD reactor and N_2 ambient in furnace on the area-corrected **(a)** $S_{eff,UL}$, and **(b)** $S_{eff,UL}$ ratio ($f_O f_V$). The temperature for plasma and ambient exposure is the same as SiN_x deposition temperature, being at 300 °C.

6.7 Chapter summary

In this chapter, we investigated the recombination at Si surfaces that featured several morphologies and were passivated with PECVD SiN_x. A wide variety of SiN_x films were examined by varying the NH_3:SiH_4 ratio, deposition pressure, and substrate temperature. Corona charge deposition and NH_3 exposure were varied to provide more insight into the recombination incurred in the SiN_x–Si system. Several key conclusions were drawn:

- Over a large range of refractive indices (n_{632} = 1.9–4.1), we obtained a significantly low S_{eff} (< 10 cm/s) on rantex samples. The result demonstrated that we can gain more freedom in tuning the optical properties of antireflection as well as passivation layer for the sunward textured surfaces, which is desirable in solar cell design.

- S_{eff} was higher for textured surfaces than for planar surfaces when the NH_3:SiH_4 ratio was high (i.e, when n was low). For example, when passivated by a N-rich SiN_x deposited with NH_3:SiH_4 = 4.7 (n_{632} = 1.83), the vertices and edges of the pyramidal texture drove a 3.5 times increase in S_{eff}.

As the NH_3:SiH_4 ratio decreased, and so n increased, the area-corrected S_{eff} of the textured surfaces decreased rapidly and approached the same S_{eff} as the planar surfaces when $n_{632} \geq 2.3$.

- By contrast, we found that irrespective of the NH_3:SiH_4 ratio, and therefore n, S_{eff} is equivalent on {100} and {111} planar surfaces, indicating that the increase in S_{eff} of the textured surfaces was related to the presence of vertices and edges of the pyramids rather than to the presence of {111}-orientated facets.

- The dependence of S_{eff} on the proportion of {111} orientation (P_{111}) at intex, and on saw damage removal (SDR) at isotex, was found to relate significantly to the NH_3:SiH_4 ratio and hence correlates inversely with n.

  - When passivated by a N-rich SiN_x (n_{632} = 1.85), S_{eff} increased significantly as P_{111} at intex increased and as SDR at isotex decreased.

  - When passivated by Si-rich SiN_x (n_{632} = 2.0 and 2.5), the dependence of S_{eff} on P_{111} at intex and on SDR at isotex became weak.

  - When passivated by a-Si (n_{632} = 4.1), the recombination behaved differently at the intex and isotex surfaces. Whereas S_{eff} at intex surfaces decreased strongly with an increase in P_{111}, S_{eff} at isotex surface was constant with SDR.

- The corona-lifetime analysis deduced that the enlargement in S_{eff} due to *(i)* a higher NH_3:SiH_4 ratio, and *(ii)* the concave and convex features on a textured surface, was primarily caused by an increase in interface defect density rather than a reduction in SiN_x charge density.

- The exposure of SiN_x-passivated rantex samples to NH_3 plasma caused more degradation in the recombination at rantex than that at planar equivalent, probably relating to a higher amount of strained bonds at the SiN_x-passivated textured surface, where strained bonds have been shown to be weaker and more susceptible to plasma reactions such as NH_b radical incorporation.

Importantly, we obtained an $S_{eff,UL}$ as low as 5.6 cm/s at *n*-type 1.1 Ω·cm rantex Si surface, when passivated by a SiN_x with n_{632} = 1.93 and negligible absorption of sunlight ≥ 360 nm. This optimum SiN_x is to be applied as AR coating and passivating layer at the front textured undiffused Si surface of an *n*-type IBC silicon solar cell, as presented in Chapter 7.

Chapter 7

Applicability to phosphorus-diffused surfaces and to silicon solar cells

7.1 Introduction

In silicon solar cells, diffused surfaces are employed to form a p-n junction to collect and separate the photo-generated carriers. An important factor in the design of the diffused surfaces for solar cells is the minimisation of recombination occurring within their volume and at their surfaces. The passivation of diffused surfaces is therefore of primary importance in obtaining high efficiency silicon solar cells. Furthermore, as the majority of solar cells have the diffused surfaces on the sunward side, the passivating layer not only reduces the surface recombination, but also functions simultaneously as an antireflection coating to maximise the photo-generated current within the silicon substrate.

In Chapters 5 and 6, we obtained good passivation of undiffused Si surfaces by SiN_x films over a wide range of refractive indices. In Section 7.2, we undertake similar studies on phosphorus (n^+) diffused surfaces, where the sheet resistance ranges from 16 to 700 Ω/□. It is shown that, over a wide range of n_{632} (1.9–2.9), a low and constant saturation current density J_0 is attained on the n^+-diffused surfaces. Moreover, comparative studies on the recombination of planar and textured surfaces presented in Chapter 6 are extended on n^+-diffused surfaces in this section. It is found that *(i)* at the lightly diffused surfaces, the textured-to-planar J_0 ratio relates strongly to the NH_3:SiH_4 ratio, and hence correlates inversely with n, and *(ii)* at the heavily diffused surfaces, the J_0 ratio is relatively constant, irrespective of SiN_x stoichiometry.

Combining the optical and recombination results, Section 7.3 evaluates the impact of various SiN_x films on Si solar cell performance. SiN_x films with n_{632} in the range of 1.83–2.9 are used in this study. The cell structures used in the simulation are *n*-type IBC cell and *p*-type PERC cell, where the front textured surface is undiffused and n^+-diffused, respectively. The simulations show that, as n_{632} increases, the efficiencies for both cell structures first increase, attributable to a decrease in recombination. As n_{632} is above 1.93, the efficiencies tend to decrease, owing to a significant increase in film absorption. Notably, the optimum SiN_x for both cell structures is at n_{632} = 1.93, which we demonstrated has a negligible absorption and the best surface passivation. Section 7.4 applies the optimum SiN_x at the front textured undiffused surface in an *n*-type IBC cell developed at the ANU, functioning as an AR coating layer as well surface passivation layer. The resulting solar cell has an efficiency of 24.4 ± 0.5%, V_{OC} of 705 mV, *FF* of 82.7% and J_{SC} of 41.9 ± 0.7 mA/cm^2.

7.2 Passivating phosphorus-diffused Si surfaces

Several previous works have examined the recombination at SiN_x-passivated n^+-diffused surfaces, as summarised in Table 7.1. Ruby *et al.* [174] obtained a J_0 = 80 fA/cm^2 on a 100 Ω/□ diffusion using HF direct PECVD SiN_x. Moschner *et al.* [21] also published passivation results for n^+-diffused surfaces with sheet resistance of 100 Ω/□, where they obtained J_0 of 93 and 73 fA/cm^2 when passivated by an inline μW PECVD SiN_x of n_{632} = 2.1 and 2.4, respectively. Kerr *et al.* [175] have performed an extensive investigation on SiN_x-passivated n^+-diffused surfaces with a broad range of sheet resistance. Using a stoichiometric SiN_x (n_{632} = 1.9) deposited by HF direct PECVD, they obtained a low J_0 which is comparable to the values obtained by the-state-of-the-art aluminium annealed (alnealed) thermal SiO_2. Lenkeit *et al.* [26] published J_0 data for 100 Ω/□ diffused surfaces when passivated by SiN_x films prepared using HF direct and remote PECVD reactors. The key result of this experiment is that the J_0 correlates strongly with the refractive indices of SiN_x films, irrespective of the deposition method, showing that, as n_{632} increases, J_0 first decreased sharply and then saturated at

~110 fA/cm^2 when n_{632} > 2.1. Even though they demonstrated a constant J_0 for n_{632} ranges from 2.1 to 2.9, the J_0 is considerably high (~100 fA/cm^2) comparing to that obtained by Kerr *et al.* [175] on equivalently diffused surfaces (i.e., ~40 fA/cm^2). Indeed, within an even broader range of n_{632} (1.9–2.9) associated with SiN_x, a low and constant J_0 has not been achieved on the n^+-diffused surfaces with a wide range of sheet resistance.

This section systematically investigates the trade-off between the optical transmission and surface passivation at the n^+-diffused surfaces with a range of sheet resistance (16–700 Ω/□), where SiN_x properties were altered by varying the NH_3:SiH_4 ratio. Furthermore, comparative studies on the recombination of planar and textured surfaces presented in Chapter 6 are extended on n^+-diffused surfaces in this section.

Table 7.1: Summary of recombination at SiN_x-passivated n^+-diffused surfaces for a range of refractive indices and diffusion profiles.

PECVD reactor	n_{632}	Sheet resistance (Ω/□)	J_0 (fA/cm^2)	Ref.
HF direct	–	100	80	[174]
μW inline	2.1 2.4	100	93 73	[21]
HF direct	1.9	30–430	120–18	[175]
μW remote or HF direct	1.9 >2.1	100	280 110	[26]

7.2.1 Experimental details

The recombination at n^+-diffused surfaces was investigated with symmetrically prepared n^+pn^+ lifetime samples. The n^+pn^+ samples were fabricated on shiny-etched *p*-type FZ Si wafers with a bulk resistivity of 100 Ω·cm, an orientation of {100}, and a thickness of 500 ± 10 μm. Textured samples with random pyramids were prepared by submitting as-cut {100} samples into an alkaline solution of TMAH,

deionised water, isopropyl alcohol (IPA) and dissolved silicon at a temperature of 85 °C for 60 min [141, 154-157].

All lifetime samples were cleaned by the RCA procedure, dipped in HF to remove the native oxide, and then submitted into a tube furnace for phosphorus diffusion. The phosphorus pre-depositions were performed within a temperature range of 760–840 °C using $POCl_3$ as a dopant source. After removing the phosphorus-silica glass, the samples received a drive-in step in pure oxygen within the temperature range of 900–1000 °C for 30–60 min. A total of 7 diffusion profiles were generated, with sheet resistance between 39 ± 2 Ω/□ and 320 ± 15 Ω/□. To obtain an even wider range of sheet resistance, a heavily diffused surface of 16 Ω/□ on planar samples was etched to a variety of sheet resistances with a reasonable uniformity across the sample, using an alkaline solution of TMAH. The sheet resistance on planar and textured samples was determined from dark photoconductance using a calibrated inductive-coil conductance tester from Sinton Instruments [152]. This measurement was conducted at the same location of the diffused samples, where the saturation current density J_0 was measured, and the measurement for planar samples was validated by four point probe measurements.

Prior to the deposition of the passivating SiN_x films, the lifetime samples were cleaned by the RCA procedure and dipped in HF acid to remove the native oxide. SiN_x was deposited using the μW/RF dual-mode PECVD system (Roth & Rau AK-400) described in Chapter 3. The baseline recipe for SiN_x deposition followed an optimised deposition condition developed in Chapter 4, where the deposition temperature was 300 °C, the pressure was 0.2 mbar, the $NH_3/SiH_4/Ar$ gas flow was 20/20/20 sccm, the μW plasma power was 500 W, and the RF bias voltage was 150 V. The $NH_3{:}SiH_4$ ratio was varied in this chapter to alter the SiN_x properties, resulting in n_{632} ranged from 1.83 to 2.9. The recombination at n^+-surfaces was monitored by measuring J_0 in accordance with Section 2.5.3. Note that the PCD measurements were undertaken in the transient mode, which are independent of any variation in the optical factor induced by the SiN_x films with different optical properties on planar and textured surfaces.

7.2.2 Results and discussion

A. J_0 on planar phosphorus-diffused surfaces

Figure 7.1 presents the relationship between J_0 and n_{632} on the planar n^+-diffused surfaces and contains several interesting points. Firstly, we find that the surface passivation properties of the diffused surface are strongly correlated with the NH_3:SiH_4 ratio, and hence inversely related to n. The J_0 first drops drastically as SiN_x films transit from being very N-rich (n_{632} = 1.83) to being nearly stoichiometry (n_{632} = 1.93), and then shows saturation when $n_{632} \geq 1.93$. The trend is consistent with those presented by Lenkeit *et al.* [26], however, with two exceptions. First, by comparing the passivation of 100 Ω/□ diffused surfaces, J_0 provided by our SiN_x films shows generally remarkably lower than those presented by Lenkeit *et al.* [26]. Note that the significance of the comparison can be improved by determining the diffusion profiles of all works included in Figure 7.1. Furthermore, in the goal to attain a constant J_0, we demonstrated a wider range of n_{632} (1.93–2.9), leading to a wider process margin in tuning AR performances. The results demonstrate that the trade-off between the optical transmission and surface recombination at n^+-diffused surfaces is circumvented.

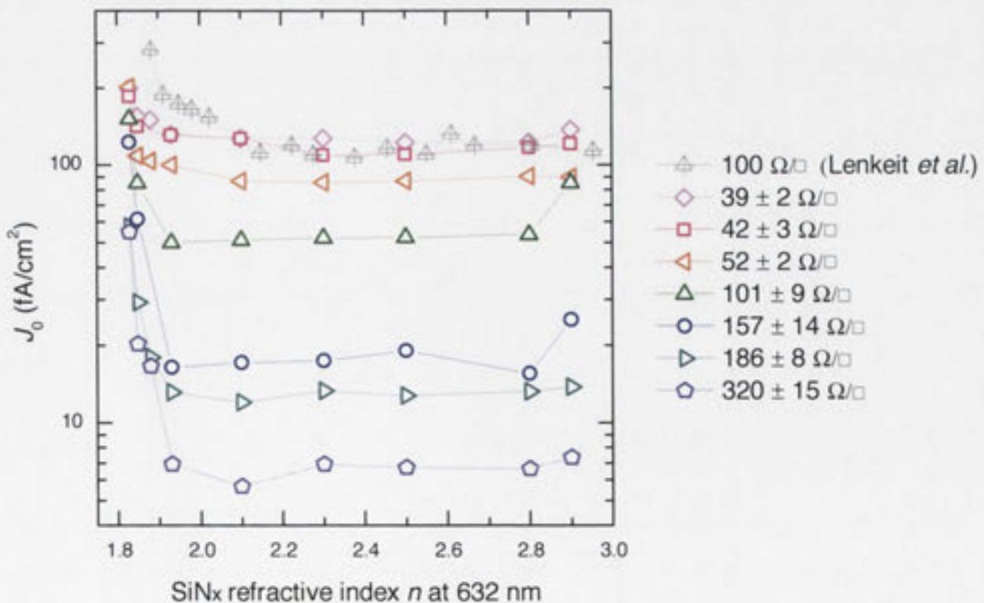

Figure 7.1: The relationship between J_0 and n_{632} of SiN_x on the n^+-diffused planar surfaces with a range of sheet resistance. The results from Lenkeit *et al.* [26] are included for comparison.

We then find that the above mentioned trend applies to all the n^+-diffused surfaces investigated in this work, ranging from 39 ± 2 Ω/□ to 320 ± 15 Ω/□. This is a notable result since the investigated diffused surfaces cover *(i)* the heavily diffused surfaces for industrial screen printed contacts (~40 Ω/□); *(ii)* homogeneous diffused surfaces suitable for evaporated contacts in high efficiency solar cells(~100 Ω/□); and *(iii)* transparent, lightly diffused surfaces as would be used as back surface region or selective emitter (> 150 Ω/□).

Lastly, as expected, the J_0 decreases as the sheet resistance increases. This is made clearer in Figure 7.2. For comparison, we include the results from Kerr *et al.* [175] for the diffused surfaces passivated by both SiN_x and alneaned SiO_2. For the completeness of this work, the experimental results of etching back of the heavily diffused surface (16 Ω/□) are also included (in green crossed circle). All the dopant profiles were passivated with our optimised SiN_x of n_{632} = 1.93. The J_0 of our optimised films compare favourably with those of SiN_x and alneaned SiO_2 in Kerr *et al.* [175], particularly for the lightly diffused surfaces (≥ 150 Ω/□). On the lightly diffused surface with a sheet resistance of 700 Ω/□, a J_0 as low as 4 fA/cm^2 is obtained.

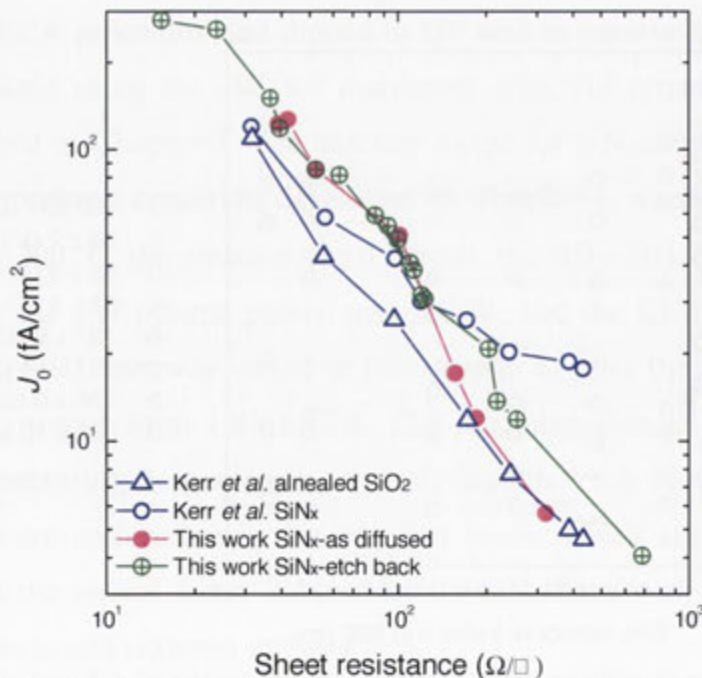

Figure 7.2: Effect of sheet resistance on the J_0 of n^+-diffused planar surfaces. The results from Kerr *et al.* [175] are included for comparison.

B. J_0 on textured phosphorus-diffused surfaces

Figure 7.3 examines the recombination (i.e., J_0) associated with phosphorus-diffused textured and planar surfaces when submitted to the same diffusion and passivation steps. As expected, the same relationships between J_0 and n_{632} as on planar equivalents are observed on textured surfaces, where J_0 first decreases sharply as n_{632} increases and then saturates when n_{632} ≥1.93. Again, this trend applies to all three diffused surfaces. In addition, we note that J_0 at textured surfaces is generally higher than that at planar equivalents, as to be discussed in the next section.

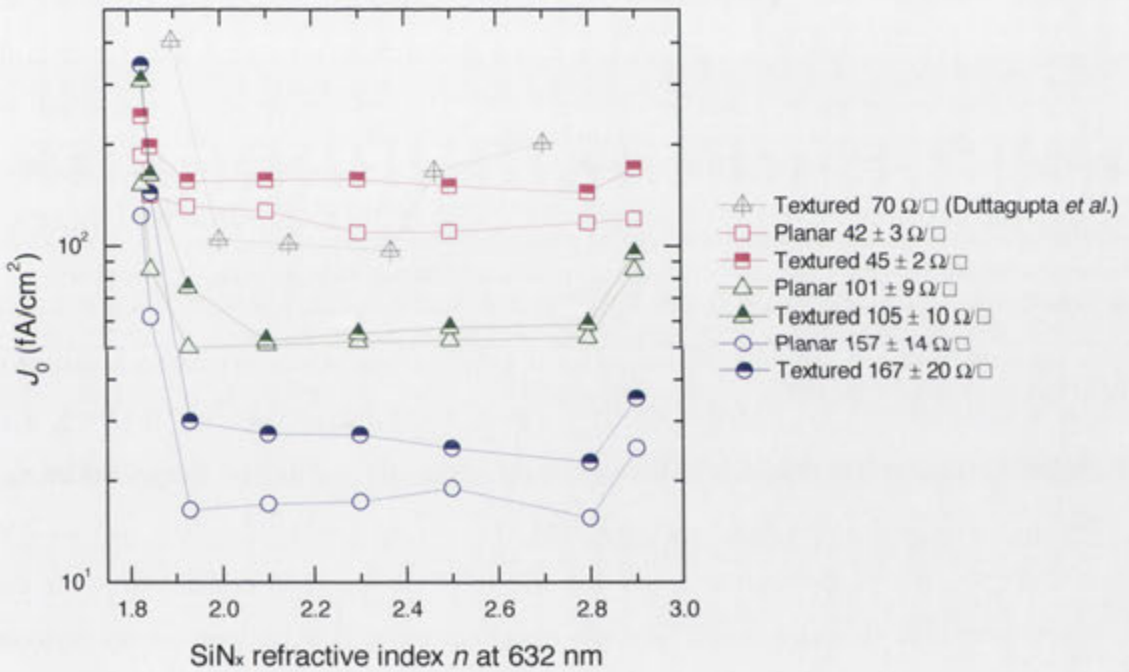

Figure 7.3: The relationship between J_0 and n_{632} on the n^+-diffused textured surfaces with three different sheet resistance (i.e., 45 ± 2, 105 ± 10 and 167 ± 20 Ω/□). The corresponding relationships on planar equivalents are included for reference.

C. Textured-to-planar J_0 ratio at phosphorus-diffused surfaces

Figure 7.4 graphs the textured-to-planar J_0 ratio at the n^+-diffused surfaces with three sheet resistance of 42 ± 3, 101 ± 9 and 157 ± 14 Ω/□, where the sheet resistance corresponds to the measurements on the planar samples.

As discussed in Chapter 6, the increase in recombination at textured surfaces relative to planar surfaces is commonly caused by *(i)* an enlarged surface area of texturing, *(ii)* higher amount of defects at the {111}-oriented facets and *(iii)* the additional recombination induced by the presence of vertices and/or edges of pyramids. For texture comprised of ideal random pyramids, the surface area is increased by a factor of 1.7, independent of the pyramid size, passivating technologies, and diffusion profile.

We first notice in Figure 7.4 that the J_0 ratio is lower than the surface area ratio (see dashed line), suggesting that recombination at planar surfaces is even higher than textured equivalents. This misleading observation, however, can be explained by the fact that the sheet resistance at a textured surface is higher than that at the planar equivalent, which is attributable to larger surface area and lower available dopant dose at textured surface [148, 175]. This effect is also evidenced by measuring the sheet resistance on planar and textured n^+-diffused surfaces, as listed in the legend of Figure 7.3. As a consequence, the textured n^+-diffused surfaces are likely to exhibit lower Auger recombination than that at planar equivalents [56].

We then examine the impact of the NH_3:SiH_4 ratio (and hence n) on the J_0 ratio for each diffusion scenario. For the lightly diffused surfaces (i.e., 157 ± 14 Ω/□), it is found that the J_0 ratio exhibits a strong correlation with n_{632}. It first decreases as n_{632} increases and then saturates at approximately 1.35 as n_{632} ranges from 2.5 to 2.9. Interestingly, we note that the trend for the light diffusion is consistent with the trend observed at the undiffused Si surfaces (see Section 6.4), where the S_{eff} ratio of textured to planar surfaces first decreases as n_{632} increases and then saturates when film becomes Si-rich ($n_{632} \geq 2.3$). In other words, an increase in the NH_3:SiH_4 ratio leads to an increase in recombination on planar wafers, and an even larger increase in recombination on textured wafers. We speculated this behaviour relating to an excessive incorporation of NH_b radicals into SiN_x film network (see Sections 5.4 and 6.6).

A similar relationship between the J_0 ratio and n_{632} is observed for the diffused surfaces with a sheet resistance of 101 ± 9 Ω/□. However, we notice that the J_0 ratio saturates when n_{632} = 2.1, corresponding to a less Si-rich film. As the diffusion

becomes very heavy (i.e., 42 ± 3 Ω/□), J_0 ratio appears constant with n_{632}. The results suggest that, as the diffusion becomes heavier, the additional recombination invoked by the textured surfaces *(i)* decreases and *(ii)* shows less dependence on the properties of passivating SiN_x films.

These observations can be understood by considering the relative contribution of the diffused surface and bulk to the total recombination activity at the diffused surface (i.e., the J_0), as suggested by [56]. As the diffusion becomes heavier, the relative contribution of the surface recombination decreases, making the samples less sensitive to surface passivating technology. We therefore observed *(i)* a strong correlation of the J_0 ratio to n_{632} at the lightly diffused surfaces, and *(ii)* an approximately constant J_0 ratio at the heavily diffused surfaces, regardless of n_{632}.

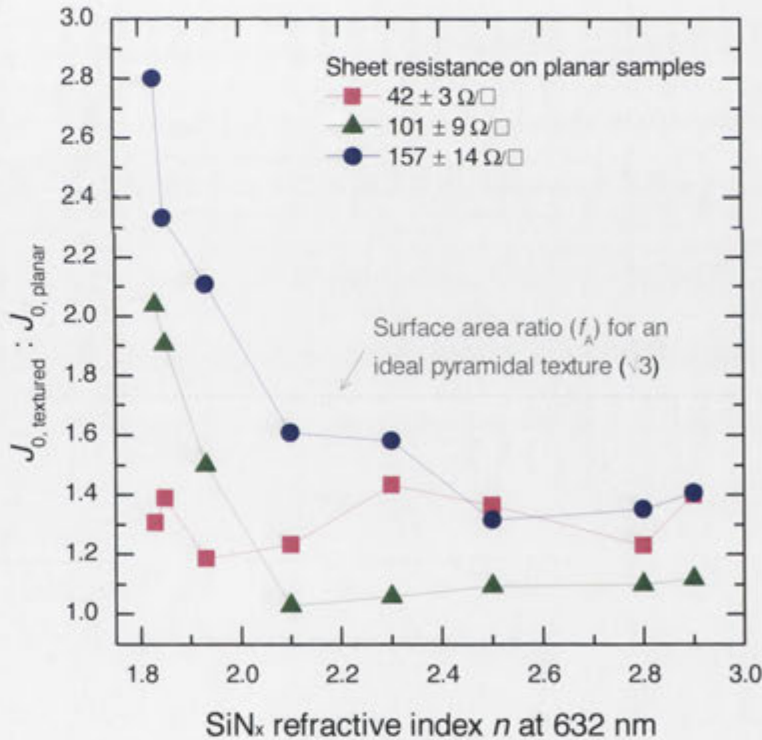

Figure 7.4: Relationship between textured-to-planar J_0 ratio and n_{632}. Note that the J_0 ratio is not area-corrected.

As discussed above, the J_0 ratio depends not only on the NH_3:SiH_4 ratio (and hence *n*), but also on diffusion conditions. We re-examine the data presented in Figure 7.4 by plotting the J_0 ratio as a function of sheet resistance measured on planar samples.

Figure 7.5 plots the results for a range of passivating SiN_x films as listed in the legend. When passivated by SiN_x of n_{632} = 1.83, it is found that the J_0 ratio decreases strongly as diffusion becomes heavier (i.e., sheet resistance decreases and J_0 increases). The trend is consistent with the trend observed by several other authors, as summarised in [56], where the passivating films were either thermal SiO_2 or PECVD SiN_x. As n_{632} increases (i.e., SiN_x film becomes more Si-rich), the dependence of J_0 ratio on diffusion condition becomes weaker. When passivated by SiN_x of $n_{632} \geq 2.1$, the J_0 ratio is relatively constant with the diffusion conditions, implying negligibly additional recombination at the pyramids, consistent with the findings for undiffused Si surfaces (see Section 6.4).

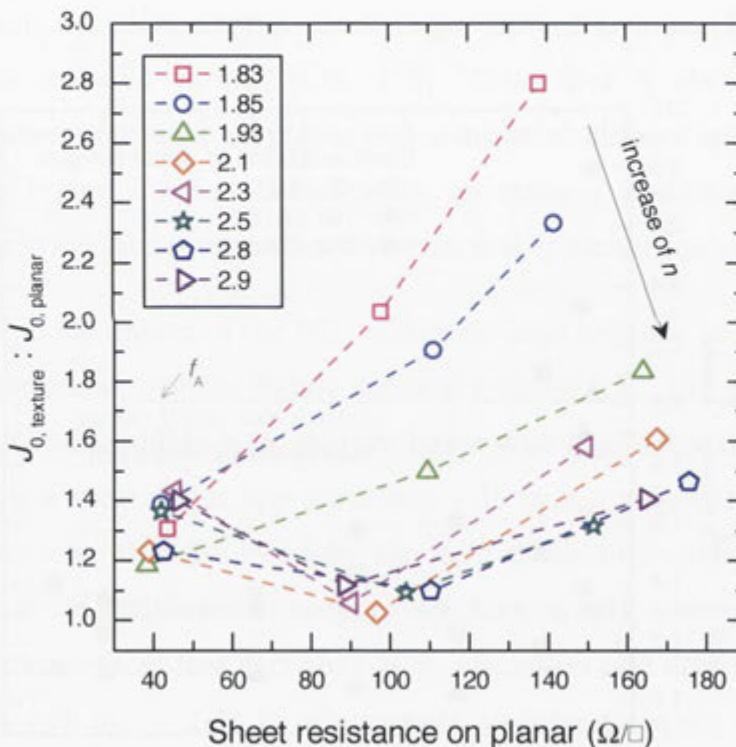

Figure 7.5: The J_0 ratio of textured to planar surfaces passivated by SiN_x with a range of n_{632}, plotted as a function of sheet resistance on planar surfaces.

7.2.3 Conclusions

In this section, we extended the recombination studies to phosphorus (n^+) diffused surfaces. It was found that, across a range of n_{632} (1.9–2.9), a low and relatively

constant J_0 was obtained on the n^+-diffused surfaces with a broad range of sheet resistance (39–320 Ω/□). The results demonstrate that the trade-off between the optical transmission and surface recombination at n^+-diffusion is circumvented. With careful optimisation of SiN_x properties, the optical advantages of SiN_x can be enjoyed without penalty in recombination. In specific, on a light diffusion with sheet resistance of 700 Ω/□, a J_0 as low as 4 fA/cm^2 was obtained using the optimum SiN_x that is highly transparent and highly passivating.

Moreover, comparative studies on the recombination at planar and textured surfaces were extended to n^+-diffused surfaces as well. At the lightly diffused surfaces, the additional recombination at textured surfaces (i.e., the textured-to-planar J_0 ratio) relates strongly to the NH_3:SiH_4 ratio, and consequently correlates inversely with n. In other words, an increase in the NH_3:SiH_4 ratio leads to an increase in recombination on planar wafers, and an even larger increase in recombination on textured wafers. By contrast, at the heavily diffused surfaces, the J_0 ratio is approximately constant, regardless of film stoichiometry, implying a negligible increase in recombination is incurred at textured surfaces. The results in this work indicate that, the additional recombination invoked by the textured surfaces is greater as *(i)* the NH_3:SiH_4 ratio increases, which decreases n, and *(ii)* the phosphorus diffusion is lighter.

In the next section, the measured recombination at textured surfaces (i.e., S_{eff} and J_0 at undiffused and diffused surfaces, respectively) is used to simulate the impact of SiN_x films on the performance of IBC and PERC solar cells.

7.3 Simulating the impact of SiN_x on IBC and PERC cell performance

Combining the experimentally determined optical and recombination results, this section simulates the impact of various SiN_x films on Si solar cells performance. SiN_x films with refractive indices in the range of 1.83–2.9 are used in this study. The cell structures used in the simulation are n-type IBC and p-type PERC cells, where

the front textured surfaces are undiffused and n^+-diffused, respectively. Appendix A gives the details of the simulation.

7.3.1 Antireflection coating of textured Si surfaces

The photogenerated current density J_{Gen} was optimised using OPAL 2, with the measured $n(\lambda)$ and $k(\lambda)$ shown in Figure 7.6. The optimisation is restricted to the range $280 \leq \lambda \leq 1200$ nm when simulating solar cells operating in air, and $366 \leq \lambda \leq 1200$ nm when simulating cells encapsulated by EVA/glass (using $n(\lambda)$ and $k(\lambda)$ given in [120]), respectively. The thickness of SiN_x was optimised to maximise J_{Gen}.

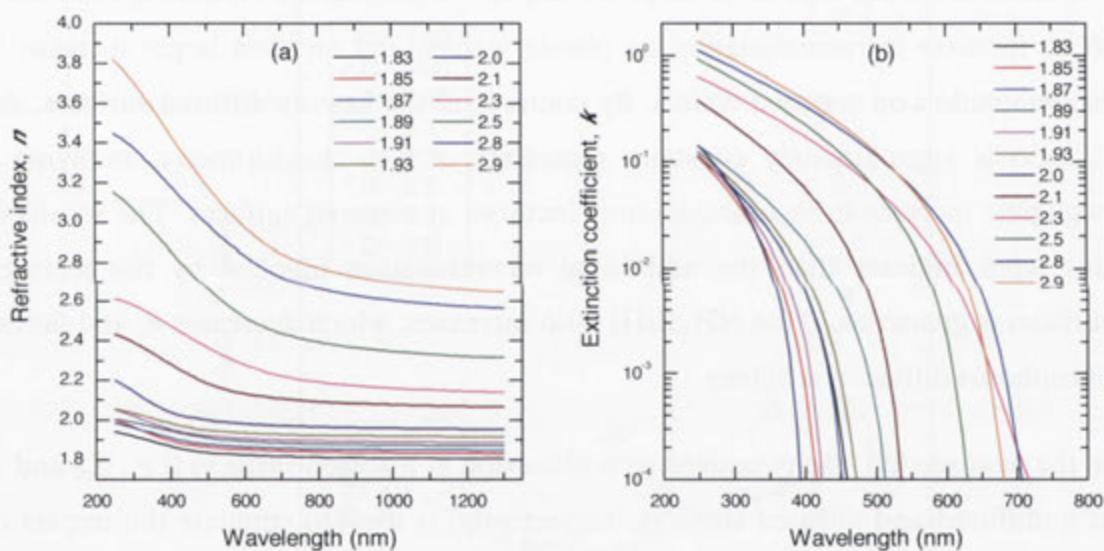

Figure 7.6: The wavelength dependent **(a)** refractive index, and **(b)** extinction coefficient for SiN_x films deposited with a variety of NH_3:SiH_4 ratios.

Figure 7.7 plots the simulated results. It is shown that as n_{632} increases, *(i)* the optimised SiN_x thickness decreases; *(ii)* J_{Abs} increases; *(iii)* J_{Refl} for cell in air increases and J_{Refl} under EVA/glass first decreases slightly and then increases, even though the J_{Refl} under EVA/glass is significantly lower than J_{Refl} in air; and *(iv)* J_{Gen} for cells in air and under EVA/glass stay relatively constant when $n_{632} \leq 2.0$ and then decreases drastically due to a significant increase in J_{Abs}. It is worth mentioning there is a cross-over for optimal layer thickness for cells in air and under EVA/glass. This is due to the fact that the simulations of cell under EVA/glass include the

absorption of short-wavelength light (< 360 nm) in EVA/glass, which makes the reflectance loss more significant than absorption loss, as evident in Figure 7.7(b) and (c).

Overall, the optimum SiN_x region for the AR coating of a textured Si surface is rather similar for cell in air and under EVA/glass, where n_{632} ranges from 1.83 to 2.0. For simplicity, we thus only examine the impact of SiN_x on the cell performance in air, as the conclusions derived from this study rely on trends, rather than the absolute values of the cell efficiency.

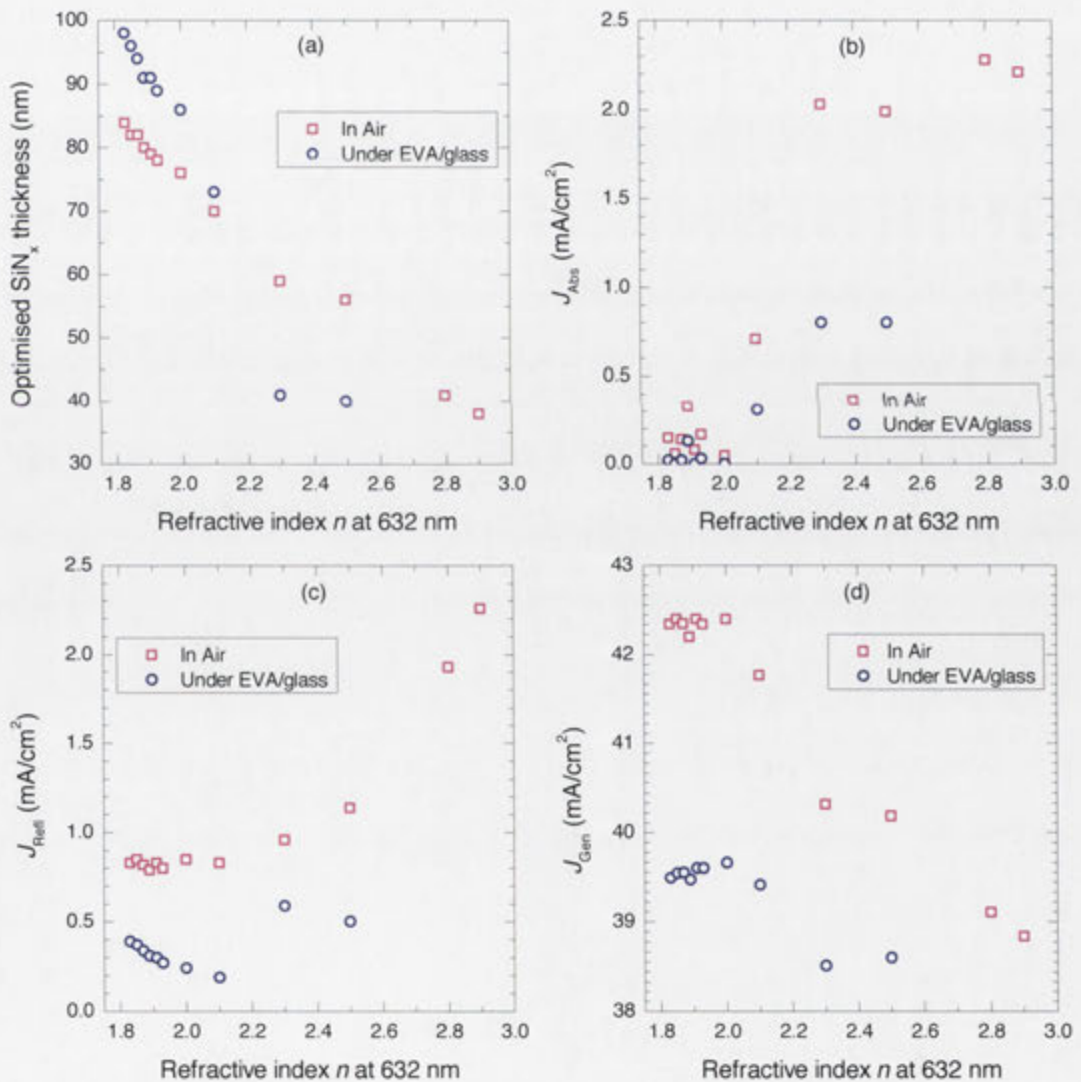

Figure 7.7: The impact of SiN_x films on the ARC performance of textured Si surfaces, including **(a)** optimised SiN_x thickness, **(b)** ARC absorptance J_{Abs}, **(c)** module reflectance J_{Refl}, and **(d)** maximum photogenerated current density J_{Gen}.

7.3.2 Cell performance: V_{OC}, J_{SC}, FF and η

The impact of SiN_x films on cell performance is plotted in Figure 7.8. We first note that V_{OC} and FF for both types of cells behave in a similar fashion to the recombination (see Figures 6.4 and 7.3). Whereas J_{sc} in PERC cell correlates well to J_{Gen}, J_{sc} in IBC cell exhibits a different trend. As n_{632} increases, J_{sc} in IBC cell first increases strongly, attributable to a decreasing recombination at the front surface, and then decreases significantly, owing to a strong increase in film absorption.

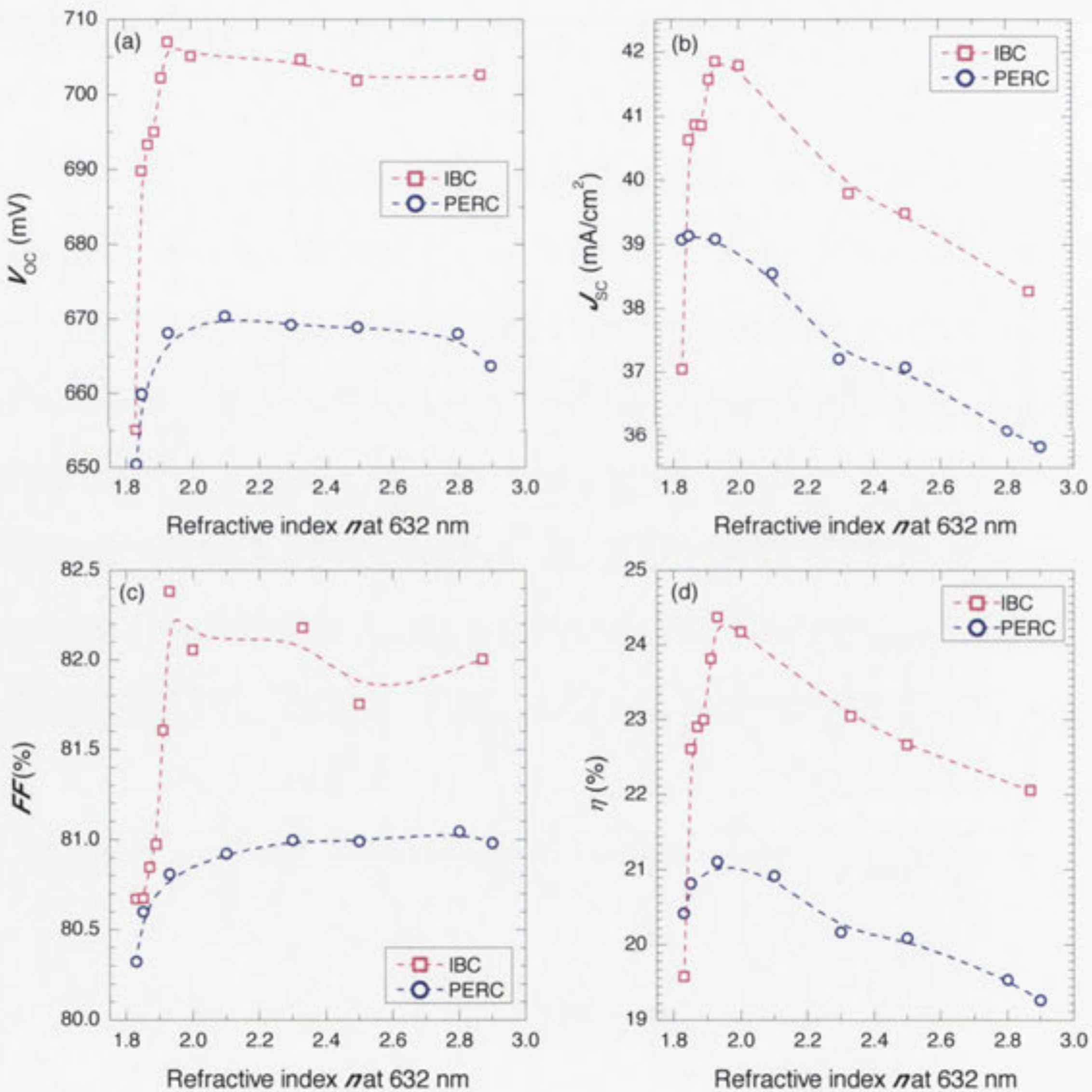

Figure 7.8: The impact of SiN_x films on the performance of IBC and PERC cells, where the front textured surface is undiffused and n^+-diffused, respectively.

These fundamental impacts of SiN_x films are integrated and transferred into the impact on final cell efficiency η. As depicted in Figure 7.8(d), as n_{632} increases, the efficiencies for both cell structures first increase, attributable to a decrease in recombination, which we speculated to be less incorporation of NH_b radicals (see Sections 5.4 and 6.6). When n_{632} is above 1.93, the efficiencies tend to decrease, owing to a significant increase in film absorption induced by increasing incorporation of silicon content. Besides the similar tendency for both cell designs, we note that the impact of SiN_x on the device efficiency is stronger for the IBC cell than for the PERC cell. This is expected since the IBC design places more stringent requirements upon the passivation of its front surface.

Notably, the optimum SiN_x for both cell structures has an n_{632} = 1.93, which was demonstrated to be highly transparent and highly passivating (see Chapters 4, 5, 6 and Section 7.2). The next section applies this optimum SiN_x onto the front textured surface of an IBC solar cell developed at the ANU [15, 16].

7.4 Applying the optimum SiN_x on IBC Si solar cells

IBC cells have the advantage of avoiding shading from the front metal grid, at the cost of transporting electrons and holes to the rear surface. This places stringent requirements upon front surface passivation and bulk lifetime [3]. Figure 7.9 depicts the impact of recombination at the front surface S_{front} of an *n*-type IBC cell developed at the ANU [15, 16], showing that the efficiency decreases drastically from approximately 25% to 20% as S_{front} increases from 1 cm/s to 100 cm/s.

Note that no phosphorus diffusion is featured at the front surface, making the cell highly susceptible to the front surface recombination. The *n*-type IBC cell with no front diffusion therefore is the best candidate to demonstrate the superiorities of our optimum SiN_x at the device level.

In this section, we apply the optimum SiN_x onto the front textured undiffused surface of the IBC solar cell, functioning as an AR coating and surface passivation layer.

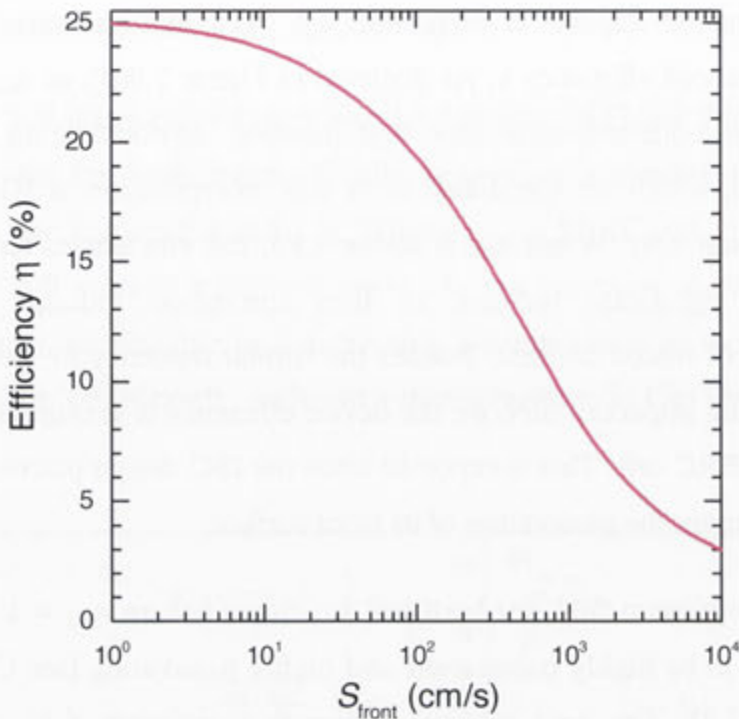

Figure 7.9: The impact of recombination at the front surface S_{front} on cell efficiency of an *n*-type IBC cell developed at ANU [15, 16].

7.4.1 Cell structure and fabrication

The solar cell was fabricated on high lifetime Czochralski phosphorus doped silicon wafers with a diameter of 100 mm, a resistivity of 1.5 Ω·cm and a thickness of 200 μm. Care was taken to maintain a high level of cleanliness during thermal steps in order to preserve high minority carrier lifetimes. The aperture area is 2 × 2 cm^2, where the busbars lie outside the aperture area. Figure 7.10 illustrates the cell structure. The front undiffused surface was textured with random upright pyramids. Antireflection and passivation were achieved through the use of the optimum SiN_x with n_{632} of 1.93 and a thickness of 78 nm.

The rear surface was chemically polished. Approximately two thirds of the rear surface was covered with a boron diffusion, and 2% was covered with a phosphorus contact diffusion comprising a multitude of small circular diffused regions. The balance was undoped. The rear surface was coated with 25 nm of dry thermal SiO_2 and 80 nm of Si_3N_4 prepared by low pressure chemical vapour deposition. This acts as surface passivation, as electrical isolation, and as a component of the rear optical reflector. Contacts to the n^+ and p^+ diffusions on the rear surface comprise an array

of small circular windows in the rear dielectric constituting a total of 0.6% of the rear surface. Most of the rear surface was covered with a 3.6 μm thick layer of aluminium which doubles as electrical conductor for the n^+ and p^+ regions and a back surface reflector. The fabrication flow is given in [15].

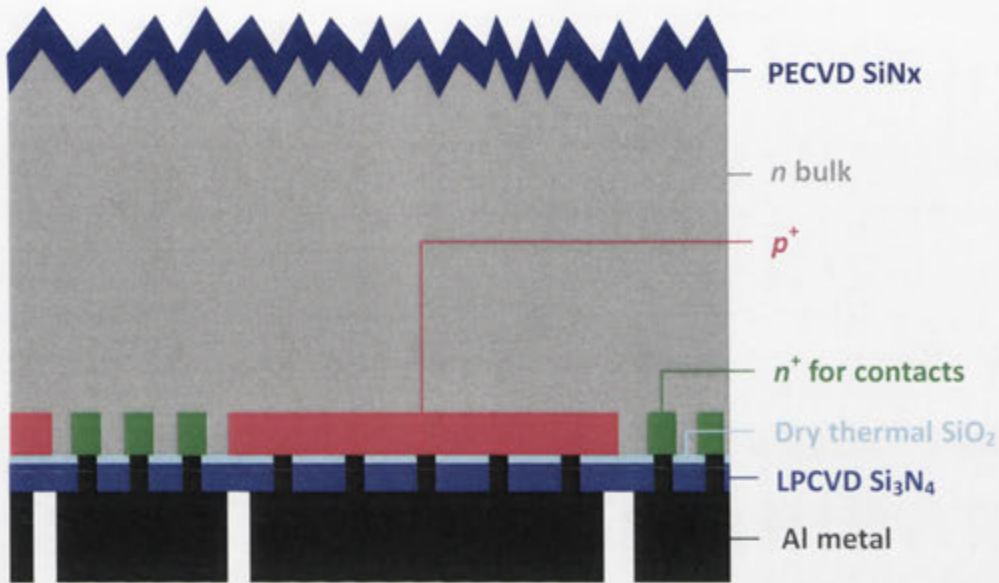

Figure 7.10: Schematic of an IBC solar cell structure on *n*-type silicon. Note that this structure has an undiffused textured front surface.

7.4.2 Cell results & discussion

The best cell to date has an independently confirmed (Fraunhofer ISE CalLab) aperture-area efficiency of 24.4 ± 0.7%, V_{OC} of 703 mV, *FF* of 82.7% and J_{SC} of 41.9 ± 0.7 mA/cm^2. The measured and simulated current-voltage (*J–V*) characteristics are plotted in Figure 7.11 and electrical parameters are summarised in Table 7.2. The results of the best IBC solar cell presently on the market fabricated by SunPower [3] are also included for reference.The V_{OC} is high, indicating that good passivation was attained at all surfaces. The superior V_{OC} attained by SunPower is attributable to the featured "passivating contacts" technology [3]. The J_{SC} is also significantly high, demonstrating excellent AR performance by the optimum SiN_x on the incident surface. The high V_{OC} as well as high J_{SC} indicate that the strengths of both surface passivation and antireflection by our optimum SiN_x were realised simultaneously in the IBC solar cell. In addition, the high *FF* is

indicative of a weak injection dependence of the minority carrier lifetime, as also evident in Figure 4.13(b).

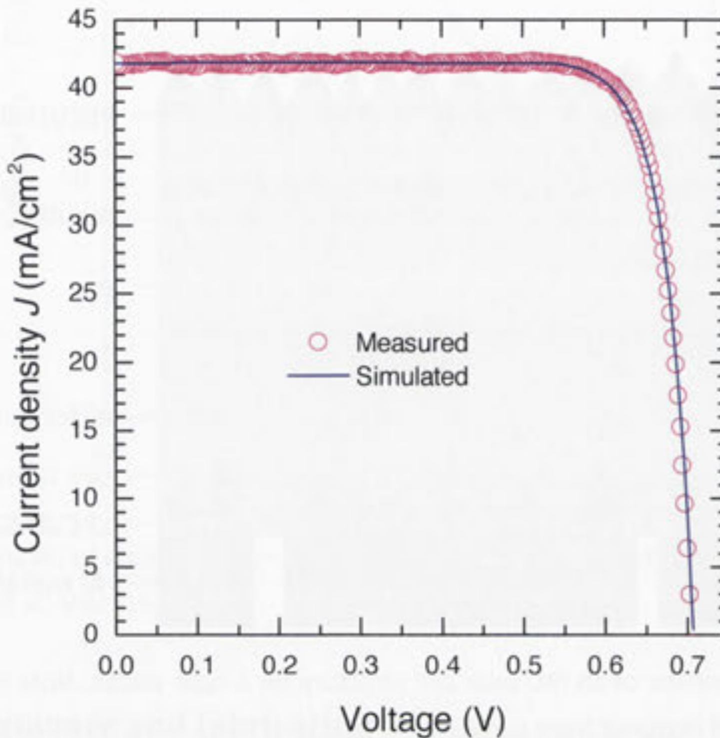

Figure 7.11: The measured and simulated *J–V* curves of the IBC silicon solar cell.

Table 7.2: One-sun electrical parameters of IBC cells measured using 4-cm^2 aperture mask. The results of the best IBC solar cell presently on the market fabricated by SunPower [3] are also included for reference.

	V_{OC} (mV)	J_{SC} (mA/cm^2)	FF (%)	η (%)	Area (cm^2)
Simulated	707	41.9	82.4	24.4	4
Measured	705	41.9 ± 0.7	82.7	24.4 ± 0.5	4
SunPower [3]	721	40.5	82.9	24.2	155

The cell simulation was conducted with the parameters summarised in Appendix A. The simulated efficiency was 24.4%, which is the same as the measured efficiency. However, there are likely to be several competing discrepancy that have

coincidentally provided the close match between simulation and experiment. The most likely contributors to the discrepancy are *(i)* errors in the calibration of spectrophotometer and/or IV testing, *(ii)* errors in the recombination modelling, *(iii)* errors in the internal optics, and *(iv)* differences in the bulk lifetime.

7.4.3 Conclusions

The optimum SiN_x developed in this thesis was applied onto the front surface of an *n*-type IBC silicon solar cell. The best cell to date has an in-house-measured efficiency of 24.4 ± 0.5%, V_{OC} of 705 mV, *FF* of 82.7% and J_{SC} of 41.9 ± 0.7 mA/cm^2. The high V_{OC} as well as high J_{SC} indicate that the strengths of both surface passivation and antireflection by our optimum SiN_x were realised simultaneously in the IBC solar cell. Higher cell efficiencies will require improvements particularly in recombination and optical aspects of the cells, for example, using double-layer AR coatings and passivated-contact technologies.

7.5 Chapter summary

In this chapter, we first investigated the recombination at phosphorus-diffused surfaces, and then demonstrated the applicability of our SiN_x on device level through cell simulation and fabrication.

On the n^+-diffused surfaces with a wide range of sheet resistance (39–320 Ω/□), we obtained a low and relatively constant recombination rate (i.e., J_0) over a range of n_{632} (1.9–2.9), similar to the recombination trends on undiffused surfaces (see Chapters 5 and 6). The results demonstrate that the trade-off between the optical transmission and surface recombination at n^+-diffusion is circumvented.

Moreover, comparative studies on the recombination at planar and textured surfaces were extended to n^+-diffused surfaces as well. At the lightly diffused surfaces, the additional recombination at textured surfaces (i.e., the textured-to-planar J_0 ratio) related strongly to the NH_3:SiH_4 ratio, and consequently correlated inversely with *n*. In other words, an increase in the NH_3:SiH_4 ratio leads to an increase in recombination on planar wafers, and an even larger increase in

recombination on textured wafers. By contrast, at the heavily diffused surfaces, the J_0 ratio is relatively constant, regardless of film properties, implying a negligible increase in recombination is incurred at textured surfaces.

Simulation of cell performances showed that, as n_{632} increased, the efficiencies for both IBC and PERC cells first increased, attributable to a decrease in recombination that was speculated to be less incorporation of NH_b radicals (see Sections 5.4 and 6.6). As n_{632} increased above 1.93, the efficiencies decreased strongly, owing to a significant increase in film absorption. Notably, the optimum SiN_x for both cell structures has an n_{632} of 1.93, which was demonstrated to have high light transmission as well as high surface passivation.

Finally, the optimum SiN_x was applied onto the front textured undiffused surface of an n-type IBC cell, enabling a conversion efficiency of 24.4 ± 0.5%, V_{OC} of 705 mV, FF of 82.7% and J_{SC} of 41.9 ± 0.7 mA/cm^2.

Chapter 8

Conclusions

8.1 Summary

This thesis comprises a thorough investigation into the optimisation and application of PECVD SiN_x for silicon solar cells. SiN_x thin films have a long history of application in the PV industry, owing to a threefold functionality of the material: (*i*) it constitutes the antireflection coating; (*ii*) it provides surface and bulk passivation; and (*iii*) it forms a chemical barrier to protect underlying interfaces from the degrading effects of moisture, humidity and sodium ions. Before the presentation of this thesis, it has generally been perceived that surface recombination decreases as SiN_x becomes Si-rich, leading to a trade-off between optical transmission and surface passivation. With a trend toward lighter front surface diffusion, thinner substrates and higher bulk lifetimes, the importance of front surface passivation increases, making a thorough re-assessment of SiN_x an imperative.

The primary focus of this thesis was to improve the understanding of PECVD SiN_x properties and to develop a film that maximises light transmission and simultaneously minimises surface recombination. Extensive studies into SiN_x prepared by the μW/RF dual-mode PECVD reactor revealed that there is no universal correlation between surface recombination and *(i)* the bulk structural properties such as chemical bond densities, and *(ii)* the bulk optical properties such as refractive index. The finding introduces the potential to independently control the optical and surface recombination properties. This is of great importance for the industrial application of SiN_x films on solar cells, as it allows the front surface transmission to be maximised while still maintaining good surface passivation.

In this study, we have attained a low and relatively constant surface recombination over a wide range of SiN_x refractive indices. Notably, the behaviour is observed on several types of Si surface surfaces—planar, textured, *p*-type, *n*-type, diffused and undiffused—with direct relevance to most of silicon solar cell structures.

In specific, we have attained a highly transparent and highly passivating SiN_x film. The value of this film is best demonstrated on an *n*-type IBC solar cell with no front diffusion, which makes the cell highly susceptible to the quality of the surface passivation. On such a cell, the optimised film developed in this thesis enabled a conversion efficiency of $24.4 \pm 0.5\%$. As depicted in Figure 8.1, comparing to the-state-of-the-art SiN_x, our optimum SiN_x provided an absolute efficiency gain of 2.4%, attributable to *(i)* lower absorption in the film, and *(ii)* lower surface recombination. This thesis demonstrates that, with careful optimisation of SiN_x properties, the SiN_x can be optically optimised without penalty in recombination.

Besides the significant improvement in optical transmission and surface passivation, the results of this thesis also advance the current understanding of recombination at SiN_x-passivated surfaces. It was found that an increase in recombination of the textured surfaces was related to the presence of vertices and/or edges of the pyramids rather than to the presence of {111}-orientated facets. Furthermore, this thesis demonstrated that the increase in recombination introduced by *(i)* a lower pressure, leading to a higher *n*, *(ii)* a higher NH_3:SiH_4 ratio, leading to a lower *n*, and *(iii)* the vertices and edges of the pyramids, was primarily attributable to an increase in interface defect density rather than a decrease in SiN_x charge density. In addition, we hypothesised the increase in D_{it} (and hence S_{eff}) to be caused by ion bombardment of the silicon surface at a lower pressure and an excessive incorporation of NH_b radicals into SiN_x film network at a higher NH_3:SiH_4 ratio, as summarised by Figure 8.2.

In summary, this thesis has advanced significantly *(i)* the optical transmission and surface passivation by SiN_x, and *(ii)* the understanding of recombination at SiN_x-passivated Si surfaces.

In this concluding chapter, key results and their implications are reiterated, and several potential areas for further research are suggested.

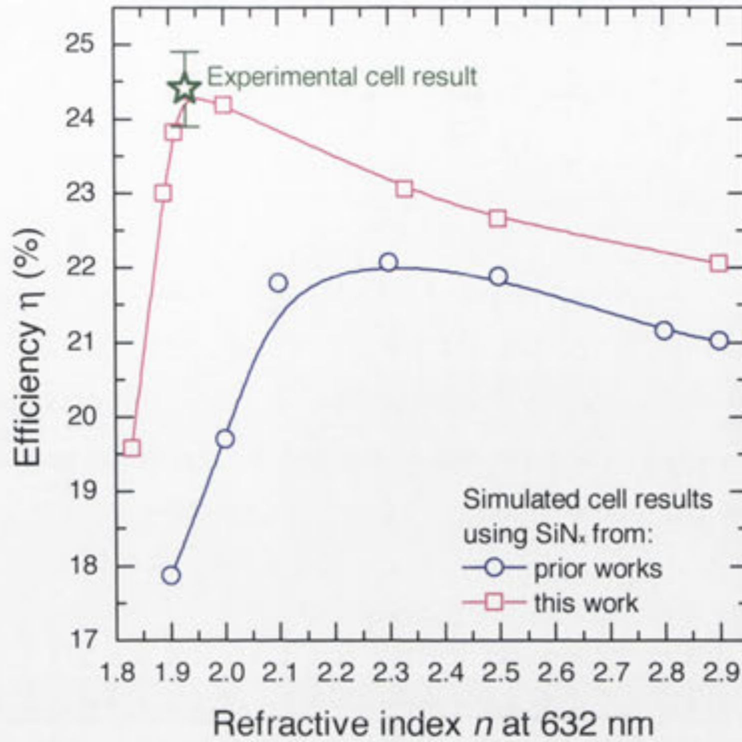

Figure 8.1: The relationship between *n*-type IBC cell efficiency and SiN_x refractive index. The experimentally obtained cell result is included.

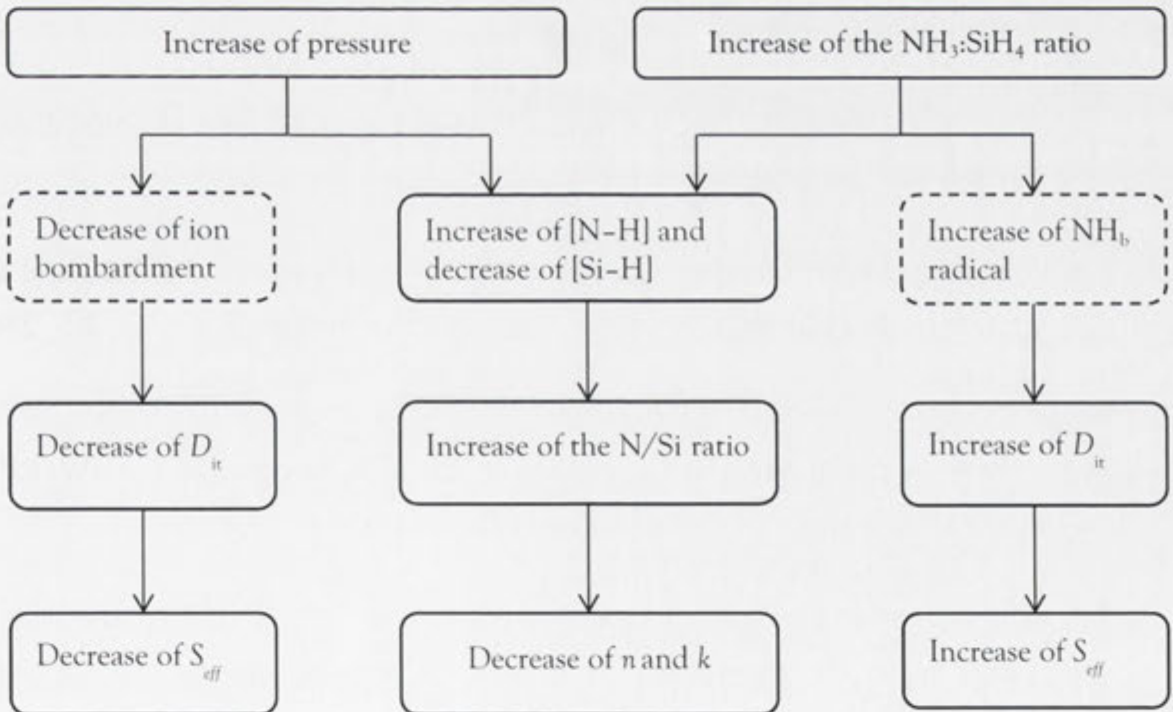

Figure 8.2: The influence of increasing *(i)* the deposition pressure, and *(ii)* the NH_3:SiH_4 ratio, on SiN_x properties. The dash-dot boxes represent the hypotheses proposed in Chapters 4 & 5.

8.2 Specific conclusions by chapter

The specific conclusions of this thesis are now summarised.

In Chapter 2, we reviewed SiN_x film properties and relevant characterisation techniques used in this thesis. It was found that (*i*) irrespective of deposition techniques and conditions, the bulk structural and optical properties are correlated universally to the N/Si atomic ratio; and (*ii*) the electronic properties including insulator charge Q_{eff}, interface defect density D_{it}, and S_{eff}, appear independent of the N/Si ratio.

In Chapter 3, we presented the reactor configurations for laboratory and inline PECVD, followed by their impacts on surface passivation. The chemical reactions that occur during SiN_x deposition were investigated. We then developed three types of procedures in the preparation of PECVD reactor and Si sample in the pursuit of high surface passivation. The improved procedures resulting from the preliminary experiments were:

- The duration at Outgassing Step is 20 minutes.
- The RCA-cleaned Si samples receive a short dip in HF and an immediate loading into chamber.
- The reactor upon cleaning is coated with six layers of passivating SiN_x and a gradient-index film that consists of four refractive indices (n_{632} = 1.9, 2.3, 2.9 and 4.1).

In Chapter 4, we performed an extensive study into SiN_x prepared by the μW/RF dual-mode PECVD reactor. The conclusions of this work are:

- The deposition pressure, substrate temperature and the NH_3:SiH_4 ratio were identified as the most sensitive parameters to SiN_x optical and surface passivation properties.

- By correlating the relationship between SiN_x properties, it was found that *(i)* S_{eff} does not correlate universally with the bulk structural and optical properties; and *(ii)* S_{eff} depends primarily on D_{it} rather than Q_{eff}.

- With the optimised deposition condition, we obtained a highly transparent and highly passivating SiN_x film with a $S_{eff,UL}$ of 1.6 cm/s on 0.85-Ω·cm *p*-type and immeasurably low $S_{eff,UL}$ on 0.45-Ω·cm *n*-type silicon substrates.

- A brief characterisation of the optimum SiN_x was presented, where

  - C–V measurements revealed that the optimum SiN_x has a $D_{it} = 3.0 \times 10^{11}$ eV^{-1}cm^{-2} at midgap and a $Q_{eff} = 5.6 \times 10^{11}$ cm^{-2} at flat-band.

  - By comparing the measured injection-dependent S_{eff} to calculated S_{eff} using an extended Shockley-Read-Hall model, we concluded that either Defect A or B (or both) observed by Schmidt *et al.* likely dominates the surface recombination rate at the SiN_x/Si interface.

  - Compared to Si-rich SiN_x ($n_{632} = 2.5$) of an equivalent passivation, the optimum SiN_x would enhance the photo-generated current density by more than 0.66 mA/cm^2 or 1.40 mA/cm^2 for solar cells encapsulated in glass/EVA or operating in air, respectively.

In Chapter 5, we investigated the influence of NH_3:SiH_4 ratio and NH_3 plasma exposure on SiN_x properties. The conclusions of this work are:

- S_{eff} remained low and relatively constant when the NH_3:SiH_4 ratio was increased from 0 to 1.9 (n_{632} decreased from 4.1 to 1.87), leading to a low S_{eff} over a broad range of n_{632} (1.87–4.1) on low-resistivity (≤ 1.1 Ωcm) *p*-Si and *n*-Si substrates. As the NH_3:SiH_4 ratio increased from 1.9 to 4.7 (n_{632} decreased from 1.87 to 1.83), S_{eff} increased strongly.

- The physical cause underlying the increase in S_{eff} with an increase in the NH_3:SiH_4 ratio was postulated to be an incorporation of NH_b radicals into the bulk and interface of the SiN_x. This hypothesis was evaluated by

introducing NH_b radicals into the SiN_x–Si system via exposing the samples to an NH_3 plasma. It was found that the NH_3 plasma exposure caused *(i)* an increase in S_{eff}, *(ii)* an increase in the density of Si≡N_3 groups, *(iii)* a reduction in refractive index and permittivity, *(iv)* an increase in D_{it} at SiN_x/Si interface, and *(v)* a reduction in Q_{eff} in SiN_x.

- By comparing the effect of the NH_3:SiH_4 ratio and NH_3 plasma exposure on SiN_x properties, we observed *(i)* a different influence on the film bond configuration, *(ii)* opposing effects on Q_{eff}, and *(iii)* similar effects on n_{632}, D_{it} and S_{eff}. The high density of interface defects due to *(i)* the high NH_3:SiH_4 ratio, and *(ii)* NH_3 plasma exposure, was most likely to be induced by ion penetration rather than by light exposure.

In Chapter 6, we investigated the recombination at Si surfaces that featured several morphologies and were passivated with PECVD SiN_x. A wide variety of SiN_x films were examined by varying the NH_3:SiH_4 ratio, deposition pressure, and substrate temperature. Corona charge deposition and NH_3 exposure were varied to provide more insight into the recombination incurred in the SiN_x–Si system. Several key conclusions are drawn:

- Over a large range of refractive indices (n_{632} = 1.9–4.1), we attained a significantly low S_{eff} (< 10 cm/s) on rantex samples. The result demonstrates that we gain more freedom in tuning the optical properties of antireflection as well as passivation layer for the sunward textured surfaces, which is desirable in solar cell design.

- In specific, when the rantex surface was passivated by the optimum SiN_x (n_{632} = 1.93), an $S_{eff,UL}$ as low as 5.6 cm/s was obtained on FZ 1.1 Ω·cm *n*-Si.

- Recombination was higher for textured surfaces than for planar surfaces when the NH_3:SiH_4 ratio was high (i.e, when *n* was low). For example, when passivated by a N-rich SiN_x deposited with NH_3:SiH_4 = 4.7 (n_{632} = 1.83), the vertices and edges of the pyramidal texture drove a 3.5 times increase in S_{eff} (i.e., f_V = 3.5). As the NH_3:SiH_4 ratio decreased, and so

n increased, the S_{eff} of the textured surfaces (after area-correction) decreased rapidly and approached the same S_{eff} as the planar surfaces when $n_{632} \geq 2.3$.

- By contrast, we found that irrespective of the NH_3:SiH_4 ratio, and therefore n, S_{eff} is equivalent on {100} and {111} planar surfaces, indicating that the increase in S_{eff} of the textured surfaces was related to the presence of vertices and edges of the pyramids rather than to the presence of {111}-orientated facets.

- The dependence of recombination on the pyramids density (i.e., P_{111}) at intex surfaces, and on saw damage removal (SDR) at isotex surfaces, was found to relate significantly to the NH_3:SiH_4 ratio and hence correlates inversely with n.

    - When passivated by a N-rich SiN_x (n_{632} = 1.85), S_{eff} increased significantly as P_{111} at intex increased and as SDR at isotex decreased.

    - When passivated by Si-rich SiN_x (n_{632} = 2.0 and 2.5), the dependence of S_{eff} on P_{111} at intex and on SDR at isotex was weak.

    - When passivated by a-Si (n_{632} = 4.1), the recombination behaved differently at the intex and isotex surfaces. Whereas S_{eff} at intex surfaces decreased strongly with an increase in P_{111}, S_{eff} at isotex surface was constant with SDR.

- From the deposition of corona charge, we deduced that the increase in recombination due to *(i)* a higher NH_3:SiH_4 ratio, and *(ii)* the concave and convex features on a textured surface, was primarily caused by an increase in the density of interface defects (i.e., S_{it}—a proxy for D_{it}) rather than a reduction in Q_{eff}.

- The exposure of SiN_x-passivated rantex samples to NH_3 plasma caused more degradation in the recombination at rantex than that at planar equivalent samples, probably relating to a higher amount of strained bonds at the SiN_x-passivated textured surface, where strained bonds have been shown to be

weaker and more susceptible to plasma reactions such as NH_b radical incorporation.

In Chapter 7, we first investigated the recombination at phosphorus (n^+) diffused surfaces, and then demonstrated the applicability of our SiN_x on the device level through cell simulation and fabrication. The conclusions in this work are:

- On the n^+-diffused surfaces with a broad range of sheet resistance (39-320 Ω/□), we obtained a low and relatively constant recombination rate (i.e., J_0) over a range of n_{632} (1.9–2.9), similar to the recombination trends on undiffused surfaces. The results demonstrate that the trade-off between the optical transmission and surface recombination at n^+-diffusion is circumvented.

- Compared to a planar diffused surface, it was shown that, *(i)* additional recombination at a lightly diffused textured surface relates significantly to the NH_3:SiH_4 ratio (and therefore correlates inversely with n), in accordance with the results on undiffused surfaces; and *(ii)* regardless of the NH_3:SiH_4 ratio, a negligible increase in recombination is incurred at a heavily diffused textured surface. The results in this work indicate that, the additional recombination (after area-correction) invoked by the textured surfaces is greater because *(i)* the NH_3:SiH_4 ratio increases, which also increases n, and *(ii)* the phosphorus diffusion is lighter.

- Simulation of cell performance showed that, as n_{632} increased, the efficiencies for both IBC and PERC cell designs first increased, attributable to a decrease in recombination that was speculated to be less incorporation of NH_b radicals. As n_{632} increased above 1.93, the efficiencies decreased strongly, owing to a significant increase in film absorption. Notably, the efficiencies for both cell structures were obtained by our optimum SiN_x (n_{632} = 1.93), which is highly transparent and highly passivating.

- Finally, the optimum SiN_x was applied onto the front textured undiffused surface of an n-type IBC cell, enabling a cell efficiency of 24.4 ± 0.5%, V_{OC} of 705 mV, FF of 82.7% and J_{SC} of 41.9 ± 0.7 mA/cm^2.

8.3 Suggestions for further work

There are several areas of research involving SiN_x that would appear to be promising. Future work on SiN_x might entail:

- Improving the "firing" stability of the optimum SiN_x by altering its film properties or by capping a thermal stable SiN_x on top, as the "firing" process degrades substantially the passivation by the optimum SiN_x.

- Studying the ultraviolet stability of the optimum SiN_x.

- Examining the thin layer that is formed during the plasma ignition step, as the first few nanometres of the layer are of great influence on the surface passivation.

- Developing gradient-index SiN_x layer to reduce front reflectance, while maintaining high light transmission and high surface passivation.

- Extracting and modelling of the fundamental surface recombination velocity of electrons and holes (i.e., S_{n0} and S_{p0}) at SiN_x-passivated Si surfaces, advancing the understanding of the mechanisms underlying *(i)* excellent passivation of p, n, and n^+ surfaces, and *(ii)* poor passivation of p^+ surfaces.

- Investigating the applicability of the optimum SiN_x for rear surface passivation of p-type PERC cells, as Q_{eff} in this SiN_x is relatively low ($\sim 5.6 \times 10^{11}$ cm^{-2}) compared to commonly reported densities ($> 10^{12}$ cm^{-2}).

- Accessing the hypothesis that is the excessive incorporation of NH_b radicals into SiN_x film network causes an increase in surface recombination.

- Understanding the physical mechanism underlying the effect of textured features on film charge (i.e., Q_{eff} increases as the textured feature size decreases and is the highest for planar samples), as presented in Section 6.5.

Appendix A

Cell parameters used in Quokka simulation

In this appendix, Table A.1 and A.2 define the parameters used to model IBC and PERC solar cells, respectively. We use the experimentally determined SiN_x optical and recombination properties to evaluate the impact of SiN_x film properties on cell performances. The simulations were performed with OPAL 2 [118, 119] and Quokka [176].

Table A.1: Summary of the parameters used in Quokka to quantify the impact of SiN_x film properties on the performances of an IBC solar cell, where SiN_x functions as front surface passivation and antireflection coating layer.

Parameters	Definition	Values	Unit
Base material properties			
Thickness		200	μm
Type		*n*-type	
Resistivity		2.5	Ω·cm
Bulk lifetime	Modelled using the parameterisation proposed by Richter *et al.* [82]		
Rear emitter properties [15, 16]			
Type		*p*-type	
Diffusion	Sheet resistance	220	Ω/□
Contact recombination	Saturation current density J_0	1200	fA/cm^2
Non-contact recombination	Saturation current density J_0	22	fA/cm^2
Contact resistivity		10^{-5}	$Ω·cm^2$
Rear local back surface region properties [15, 16]			
Type		*n*-type	
Diffusion	Sheet resistance	30	Ω/□

Contact recombination	Saturation current density J_0	400	fA/cm^2
Non-contact recombination	Saturation current density J_0	120	fA/cm^2
Contact resistivity		10^{-5}	Ω·cm^2
Front surface properties			
Type		*n*-type undiffused	
Recombination	Experimentally measured (see Figure 6.4)		
Settings for the modelled generation profiles using OPAL 2 [119]			
Surface morphology	Random upright pyramid with characteristic angle of 51°		
Z path	Optical enhancement	12	
Incident illumination	Spectrum AM1.5g		
Optical constants of ARC layer	Experimentally determined (see Figure 7.6)		
External circuit settings			
R_{series}	Series resistance	0	Ω·cm^2
R_{shunt}	Shunt resistance	10^7	Ω·cm^2

Table A.2: Summary of the parameters used in Quokka to quantify the impact of SiN_x film properties on the performance of a PERC solar cell, where SiN_x functions as front surface passivation and antireflection coating layer.

Parameters	Definition	Values	Unit
Base material properties			
Thickness		180	μm
Type		*p*-type	
Resistivity		1.0	Ω·cm
Bulk lifetime	Modelled using the parameterisation proposed by Richter *et al.* [82]		
Front emitter properties			
Type		*n*-type	
Diffusion	Sheet resistance	100	Ω/□
Contact recombination	Saturation current density J_0	1000	fA/cm^2
Non-contact recombination	Experimentally measured (see Figure 7.3)		
Contact resistivity		10^{-3}	Ω·cm^2
Rear back surface region properties			
Type		*p*-type	
Diffusion	Sheet resistance	20	Ω/□

Contact recombination	Saturation current density J_0	400	fA/cm^2
Contact resistivity		10^{-3}	$\Omega\cdot cm^2$
Rear undiffused surface properties			
Type		*p*-type	
Recombination	Saturation current density J_0	10	fA/cm^2
***Settings for the modelled generation profiles using OPAL 2* [119]**			
Surface morphology	Random upright pyramid with characteristic angle of 51°		
Z path	Optical enhancement	12	
Incident illumination	Spectrum AM1.5g		
Optical constants of ARC layer	Experimentally determined (see Figure 7.6)		
External circuit settings			
R_{series}	Series resistance	0.4	$\Omega\cdot cm^2$
R_{shunt}	Shunt resistance	10^5	$\Omega\cdot cm^2$

Appendix B

Calibration of silicon substrate temperature in the PECVD reactor

The deposition temperature affects enormously the film properties of SiN_x, as it affects critically the film densification and formation of Si–N (i.e., step III in Section 3.3.2). As presented by Lauinger *et al.* [18], the lifetime on *p*-type 1.5 Ω·cm FZ silicon varies from 7 μs for SiN_x deposited at 250 °C to 1000 μs for SiN_x deposited at 400 °C. Typically, there is an offset between setpoint and actual substrate temperature, owing to thermocouple placement and heat transfer loss. We measure the substrate temperature independently using an external thermocouple and infrared thermometer, to verify the actual substrate temperature for a given setpoint.

B.1 Measurement of silicon wafer temperature using thermocouple

Four sets of thermocouples were installed through hole-flanges to measure the temperature of heating element, graphite substrate and silicon wafers at four different positions. The average of the four readings was calculated and plotted against the temperature setpoint in Figure B.1. Note that all the measurements were performed in vacuum.

We first find the measured temperature on heating element is lower than the setpoint. The difference becomes greater as the temperature setpoint increases. This can be seen clearly in Figure B.1(b). The difference between the measured

temperature and setpoint is more pronounced on graphite substrate. For a setpoint temperature at 500 °C, the measured temperature on heating element is 440 °C, whereas the reading on graphite is 253 °C. The result indicates that a significant heat loss exists during the heat transfer from heating element to graphite substrate. Furthermore, we note that the measured temperature on silicon samples shows approximately equivalent to that on graphite substrate, indicating a reasonably good contact between silicon samples and the graphite substrate.

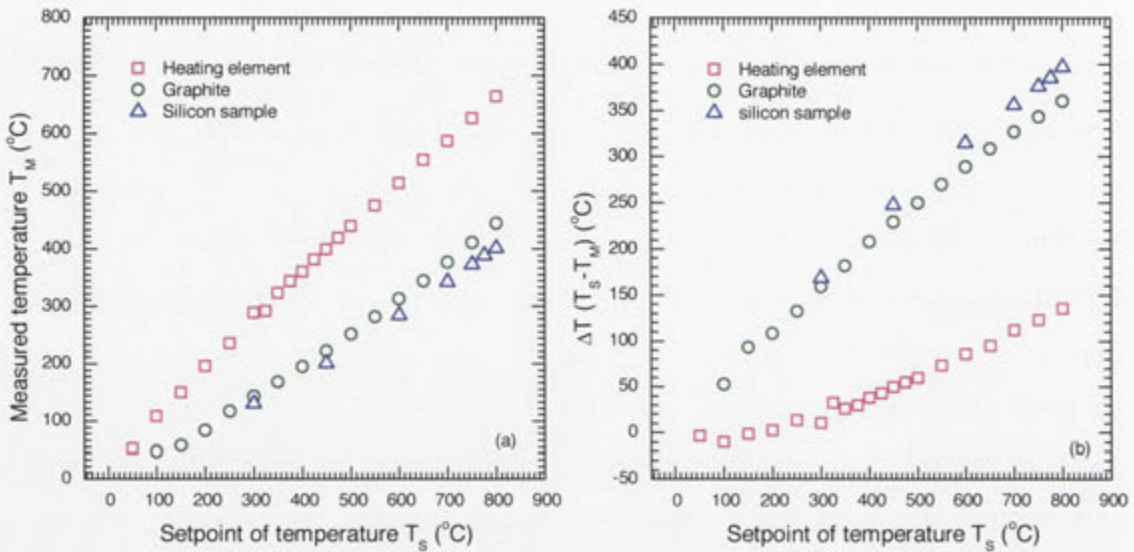

Figure B.1: (a) Measured temperature, and **(b)** the deviation between measured temperature and setpoint, plotted versus the setpoint temperature before service.

A service was performed on the heating element and thermocouple probe to minimise the gap between the setpoint and the measured temperature. The distance between the thermocouple probe and heating element was adjusted. Figure B.2 shows the measured temperatures on graphite substrate before and after service. We clearly see that at the same setpoint of temperature, the measured deviation after service is consistently ~50 °C lower than that before service. For a setpoint temperature at 500 °C, the measured temperature on graphite after service is 300 °C.

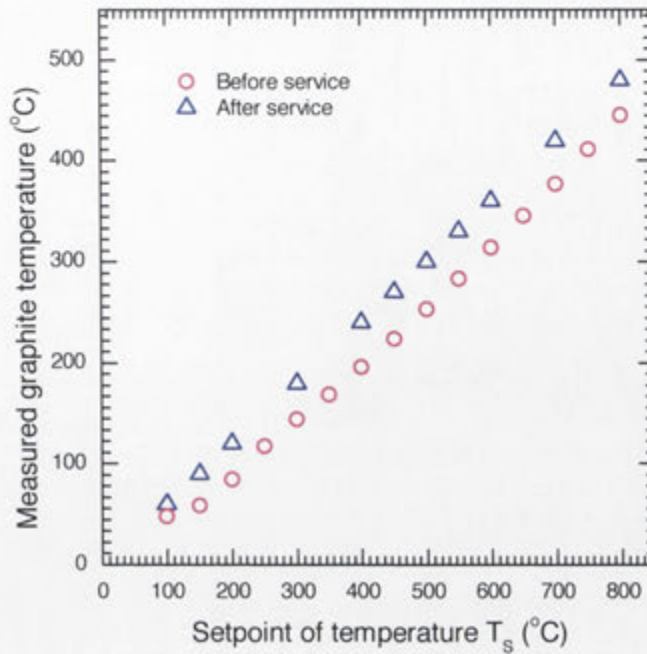

Figure B.2: Measured graphite temperature versus the setpoint temperature after service.

B.2 Installation and calibration of infrared thermometer

The actual wafer temperature varies with time during processing; it is hence interesting to monitor the actual wafer temperature during each deposition. This is realised by installing an in-situ infrared thermometer, namely Optris. Figure B.3(a) shows a picture of Optris. It consists of an external LED monitor for temperature reading and an internal infrared thermo detector.

A calibration between the measured temperature by the external thermocouple and Optris was conducted and the result is shown in Figure B.3(b). It shows that the two measured temperatures match well with each other, confirming the reliability of the calibration procedure.

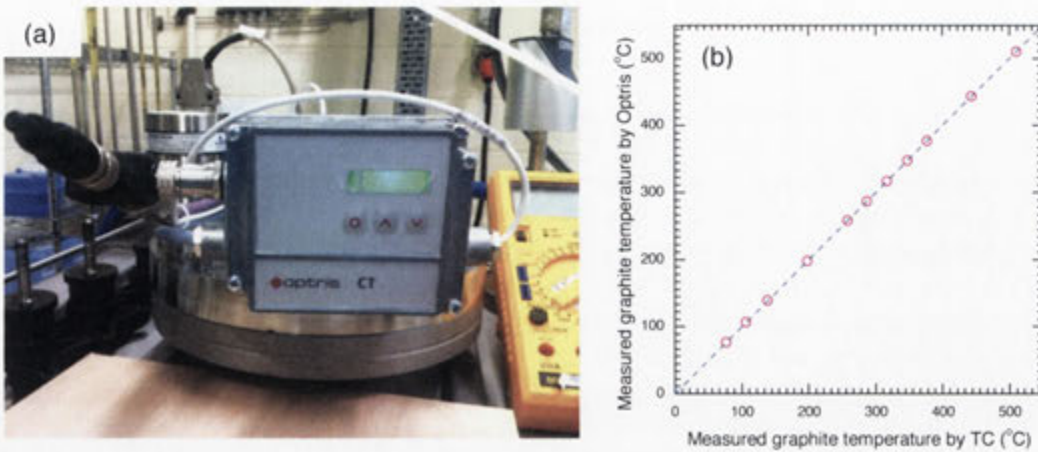

Figure B.3: (a) Infrared thermometer-Optris, and **(b)** measured graphite temperature by Optris versus that by external thermocouple.

B.3 Summary

In summary, we found that the measured temperature on graphite substrate was significantly lower than the setpoint. This gap was reduced by adjusting the distance between thermocouple probe and heating element, resulting in a ~50 °C reduction in the thermal deviation. For a temperature setpoint of 500 °C, the measured temperature on graphite substrate (so as the temperature on silicon wafers) read 300 °C. An in-situ infrared thermometer was in our system to record the actual wafer temperature during every deposition.

Characterisation of stress in SiN_x and its effect on surface passivation

C.1 Introduction

PECVD SiN_x is commonly employed in a variety of electronic devices, such as gate insulators in thin-film transistors, charge storage in memory devices, as well as anti-reflection coating and passivation layers in silicon solar cells. These SiN_x films are typically chosen for their excellent insulating, optical, and electrical properties. However, their mechanical properties are also of primary importance as they might cause potential problems in the integrity of a device. For example, film cracking and blistering induced by excessive film stress can cause device failure. Moreover, high film stress on silicon can generate defects at the SiN_x/Si interface [177].

On a pyramidal-textured silicon surface, which is usually featured in high-efficiency and industrial c-Si solar cells, film stress is often suspected of creating defects at the peaks and troughs of the pyramids, and consequently of increasing the surface recombination when passivated by either silicon dioxide [56, 144, 148] or SiN_x [92, 148]. Thus it is important to investigate the stress properties in SiN_x-passivated Si system in order to understand its impact on the surface passivation.

In this work, we investigate the stress in SiN_x prepared by our dual-mode PECVD and study its correlations to other properties of SiN_x, such as stoichiometry, chemical structure, surface passivation, and density of interface states.

C.2 Experimental details

Stress characterisation was performed on the same sample as those used for reflectance and FTIR measurements (see Section 4.2). An optical profiler (Veeco Wyko NT9100) was used to measure the radius of curvatures before and after SiN_x deposition on DSP silicon substrate using a scanning laser reflection technique [178]. The film stress σ was then calculated from the radius of curvature using the well-known Stoney equation [179]:

$$\sigma = \frac{E_{Si}}{6(1-v_{Si})}\frac{d_{Si}^2}{d_f}\left(\frac{1}{R}-\frac{1}{R_0}\right) \tag{C.1}$$

where E_{Si} is Young's Modulus of silicon, ν_{Si} is Poisson ratio of silicon, d_{Si} is the thickness of substrate, d_f is the thickness of SiN_x film, R and R_0 are the sample's radius of curvature when coated with SiN_x and prior to coating, respectively. For the {100} silicon substrate, the biaxial modulus, $E_{Si}/(1-\nu_{Si})$, is 180.5 GPa [180] [181]. In fact, the stress calculated from Eq. (C.1) is composed of thermal stress due to mismatch in the thermal expansion between the film and silicon substrate, and to intrinsic stress induced by the deposition process of the film [182]. Since we do not experimentally distinguish these two types of stress, from here on, the reported stress is actually the total stress in SiN_x–Si system.

The sample preparation and analysis for the measurement of photoconductance, reflectance, FTIR and C–V are in accordance with Section 4.2.

C.3 Results and discussion

C.3.1 Front and rear radius of curvature measurements

Figure C.1 plots the stress calculated from the radius of curvature measured on the uncoated surface versus stress calculated from radius of curvature measured at SiN_x-coated surface. The data exhibits an approximately linear correlation between the stress determined from each measurement. As evident in Figure C.1, the 1:1 correlation line is within the 95% confidence interval of the linear best fit. We

conclude that a similar stress is determined from measuring the radius of curvature on either side of the wafer. Following the standard procedure for stress measurement and calculation [179], the stress reported in this work is that calculated from the radius of curvature measured at the SiN_x-coated silicon surface.

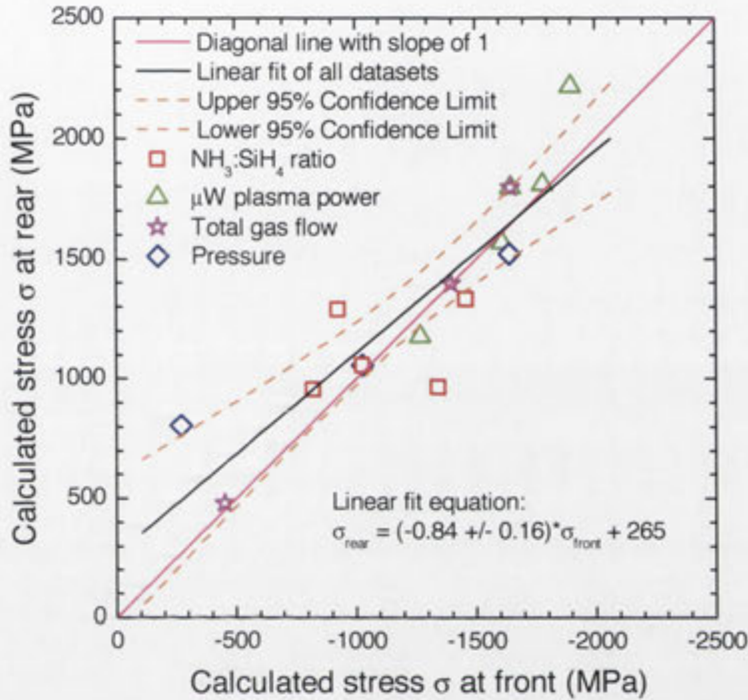

Figure C. 1: Correlation between the calculated stress at front SiN_x-coated and rear uncoated silicon substrate. Four variation experiments indicated by legends were performed to investigate the impact on stress.

C.3.2 Effect of SiN_x stoichiometry and chemical bond density on stress

Figure C.2 plots the stress versus the N/Si atomic ratio for several sets of process conditions. The stress appears to depend on the N/Si ratio and to be independent of the process conditions. Similar behaviour was observed by Sinha *et al.* [183] and Van Erven *et al.* [30]. Both publications found that the tensile stress increases with the N/Si ratio and reaches a maximum at n_{632} ~2.0. It is consistent with the stoichiometry exhibiting the maximum stress in this work, where the peak occurs at the N/Si ratio about 1.2. There is, however, the glaring discrepancy that the stress was tensile in [183] and [30], but compressive in this work. This might be due to

different film growth mechanisms associated with the different deposition techniques [95, 184].

The dependence of the stress on stoichiometry is not fully understood, however, two mechanisms have been proposed as contributing to this relationship. Witczak *et al.* [177] suggested that the dependence might be affected by the mismatch between the lattice constant of silicon and that of the nearest neighbouring atoms in SiN_x. As SiN_x becomes rich in Si and behaves more like the underlying silicon substrate, the lattice mismatch is plausibly less pronounced, resulting in the reduction of stress. Conversely, stress increases with the increase of lattice mismatch between two materials as more nitrogen atoms are incorporated into SiN_x structural network.

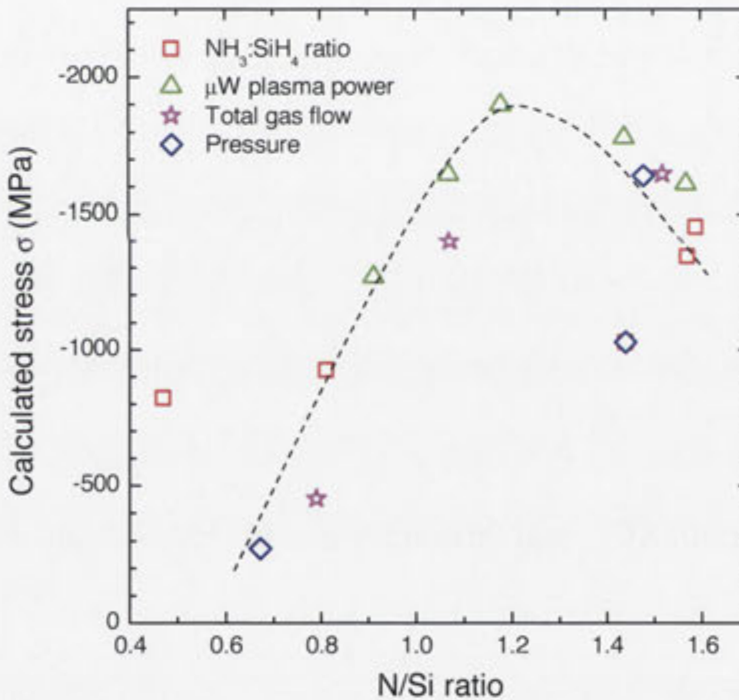

Figure C.2: Calculated stress versus the [N]/[Si] ratio, determined from the n_{632} using an empirical equation from Ref. [28]. The dashed line is a guide for the eye.

The stress in SiN_x–Si system is also believed to be influenced by film mass density. When PECVD SiN_x was deposited by varying the gas flow ratio, NH_3/SiH_4, Sinha *et al.* [183] demonstrated a good correlation between stress and film density. A similar relationship was also found by Van Erven *et al.* [30], showing the increase

of stress is associated with the increase in film mass density and additionally they demonstrated a good correlation between the film mass density and Si–N bond density measured by FTIR.

Both mechanisms can be considered to be the result of the incorporation of nitrogen atoms into SiN_x structural network as SiN_x transforms from Si-rich to N-rich (alternatively the N/Si ratio increases).

The relationship between the calculated stress and the peak wavenumber of the Si–H stretching IR absorption and the total nitrogen related bonds is illustrated in Figure C.3 (a) and (b), respectively. As revealed in Figure C.3(a), compressive stress in our SiN_x–Si system increases as Si–H peak shifts to a higher wavenumber. It is well-known that the Si–H peak can be assigned to different types of N_m–Si–H bonds [46, 50, 137], where m can be 0, 1, 2 or 3. According to the assigned Si–H vibration modes summarised in Refs. [46, 137], we can observe that the stress increases as more N atoms are back-bonded to Si–H sites. Indeed, the Si–H stretching peak position has been reported by Okada *et al.* [185] to increase linearly with an increase of compressive stress.

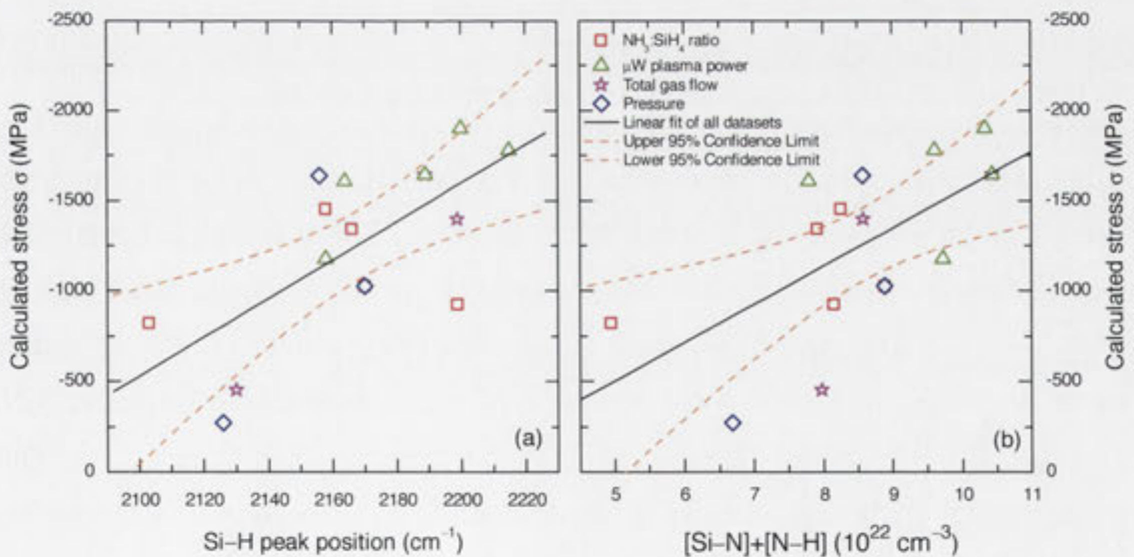

Figure C.3: Calculated stress versus SiN_x structural properties determined from FTIR spectroscopy: **(a)** peak wavenumber of Si–H stretching vibration; and **(b)** total nitrogen-related bond densities that are the sum of Si–N and N–H bond densities. The solid lines are linear fits and the dashed lines are the 95% confidence interval of the fit.

Another indicator of N atoms being incorporated into SiN_x network is the total bond densities of nitrogen-related bonds, which are the sum of the Si–N and N–H bond densities calculated from FTIR measurements. As revealed in Figure C.3(b), an increase in the N-related bond densities correlates to more compressive stress.

We can therefore conclude that film stress depends on film composition, as one would expect, and that this dependence is not strongly influenced by the deposition conditions.

C.3.3 Relationship between surface recombination and stress

The $S_{eff,UL}$ is plotted against stress for each series of process conditions in Figure C.4, including the plotted D_{it} versus stress in the inset. We do not observe a global relationship between either $S_{eff,UL}$ or D_{it} with stress for all process conditions investigated in this work. That is, the interface recombination does not necessarily increase (or decrease) as stress increases.

We do, however, observe correlations for each individual process group. For example, when SiN_x was prepared by varying only the NH_3:SiH_4 ratio (red symbols), a monotonic increase of $S_{eff,UL}$ and D_{it} is observed as stress increases. On the contrary, when SiN_x was prepared solely by varying deposition pressure (brown symbols), $S_{eff,UL}$ and D_{it} is observed to decrease as stress increases.

These results suggest that while film stress in SiN_x passivated Si system might introduce interface defects, it is not the main driver. For example, although SiN_x deposited at low pressure yielded low compressive stress, there still exists high D_{it} and $S_{eff,UL}$ caused by other factors such as ion bombardment at low pressure, leading to an increase of D_{it} and consequently surface recombination. Similarly, SiN_x synthesised at high NH_3:SiH_4 ratio exhibited low stress but high D_{it} and $S_{eff,UL}$. This could be attributed to an excessive incorporation of NH_b radicals into SiN_x network, which probably *(i)* enhances the flexibility of SiN_x network, consequently relaxing the stress, as suggested by Hasegawa *et al.* [182], and *(ii)* introduces additional defects at SiN_x/Si interface, as discussed in Chapter 5.

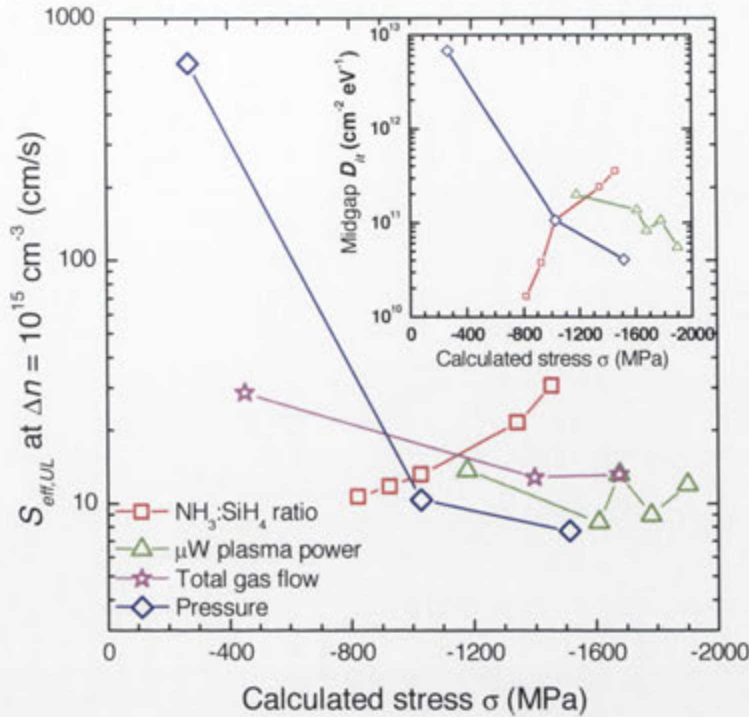

Figure C.4: Extracted $S_{eff,UL}$ at $\Delta n = 10^{15}$ cm^{-3} as a function of the calculated stress for a variety of PECVD process conditions. The inset indicates D_{it} revealed by C–V measurements as a function of measured stress.

C.4 Conclusion

We investigated the stress in SiN_x–Si system. Irrespective of the deposition conditions, the stress depended on the N/Si ratio, showing a maximum at about 1.2. We also presented two sets of approximately linear correlations between chemical bond density and film stress, indicating that stress increases with the increase of N–atoms being incorporated into SiN_x network. Moreover, we found that there is no global relationship between $S_{eff,UL}$ or D_{it} and stress, however, we did demonstrate that, for SiN_x prepared by varying a single deposition parameter such as the NH_3:SiH_4 ratio, there existed correlation between interface electrical properties and stress. These results suggest that the surface recombination is less dependent on stress than they are on other factors, such as ion bombardment or the incorporation of NH_b radicals that can be altered by varying deposition conditions.

List of Publications

Publications arising from the work in this thesis

Refereed journal papers

1. **Y. Wan**, K. R. McIntosh, A. F. Thomson and A. Cuevas, "Influence of post-deposition NH_3-plasma exposure on the surface passivation of C-Si by PECVD silicon nitride and amorphous silicon", in preparation.

2. **Y. Wan** and K. R. McIntosh, "On the Surface Passivation of Textured C-Si by PECVD Silicon Nitride," *Photovoltaics, IEEE Journal of,* vol. PP, pp. 1-7, 2013.

3. **Y. Wan**, K. R. McIntosh and A. F. Thomson, "Characterisation and optimisation of PECVD SiN_x as an antireflection coating and passivation layer for silicon solar cells", AIP ADVANCES, 3, 032113, 2013.

4. **Y. Wan**, K. R. McIntosh, A. F. Thomson, and A. Cuevas, "Low Surface Recombination Velocity by Low-Absorption Silicon Nitride on c-Si," *Photovoltaics, IEEE Journal of,* vol. 3, pp. 554-559, 2013. [*First presented (Oral) in 38th IEEE Photovoltaic Specialists Conference, Texas.*]

Refereed conference papers

5. **Y. Wan**, K. R. McIntosh, D. Yan, and A. Cuevas, "Passivation of phosphorus-diffused surfaces by PECVD SiN_x," Oral presentation in *40th IEEE Photovoltaic Specialists Conference*, Denver, Colorado, USA, 2014.

6. **Y. Wan**, C. Samundsett, T. Kho, J. McKeon, L. Black, D. Macdonald, A. Cuevas, J. Sheng, Y. Sheng, S. Yuan, C. Zhang, Z. Feng, and P. J. Verlinden, "Towards industrial advanced front-junction n-type silicon solar cells," Oral presentation in *40th IEEE Photovoltaic Specialists Conference*, Denver, Colorado, USA, 2014.

7. D. Yan, J. Bullock, **Y. Wan**, and A. Cuevas, "Development of a Self-aligned Etch-Back Process for Selectively Doped Silicon Solar cells," Poster presenation in in *40th IEEE Photovoltaic Specialists Conference*, Denver, Colorado, USA, 2014.

8. K. R. McIntosh, K. C. Fong, T. C. Kho, **Y. Wan**, S. C. Baker-Finch, M. D. Abbott, S. Zin, D. Wang, N. E. Grant, E. C. Wang, M. Stocks, E. Franklin, and A. W. Blakers, "Quantification of optical losses in back-contact solar cells," Oral presentation in *40th IEEE Photovoltaic Specialists Conference*, Denver, Colorado, USA, 2014.

9. E. Franklin, K. Fong, K. McIntosh, A. Blakers, K. Teng, A. Fell, D. Walter, D. Wang, S. Z. Ngwe, M. Stocks, E.-C. Wang, N. Grant, **Y. Wan**, Y. Yang, X. Zhang, Z. Feng, and P. J. Verlinden, "Design, Fabrication and Characterisation of a 24.4% Efficient Interdigitated Back Contact Solar Cell," Oral presentation in *29th European Photovoltaic Solar Energy Conference and Exhibition*, Amsterdam, The Netherlands, 2014. [*Invited submission for Progress in Photovoltaics*]

10. E. Franklin, K. Fong, K. McIntosh, A. Blakers, K. Teng, D. Wang, S. Z. Ngwe, M. Stocks, E.-C. Wang, N. Grant, A. Fell, **Y. Wan**, Y. Yang, X. Zhang, Z. Feng, and P. J. Verlinden, "Fabrication of 24% Efficient IBC Cells," in *8th SNEC PV POWER EXPO*, Shanghai, China, 2014.

11. A. Blakers, K. C. Fong, E. Franklin, T. C. Kho, K. McIntosh, **Y. Wan**, D. Wang, and N. S. Zin, "24.4% efficient back contact cell with oxide - nitride passivation," Oral presentation in *23rd Asian Photovoltaic Solar Energy Conference and Exhibition* Taipei, Taiwan, 2013.

12. N. E. Grant, K. R. McIntosh, J. Tan, F. Rougieux, J. Bullock, **Y. Wan**, and C. Barugkin, "Light Enhanced Hydrofluoric Acid Passivation for Evaluating Silicon Bulk Lifetimes," Oral presentation in *28th European Photovoltaic Solar Energy Conference and Exhibition*, Paris, France, 2013.

13. H. C. Sio, S. P. Phang, **Y. Wan**, W. Liang, T. Trupke, S. Cao, D. Hu, Y. Wan, and D. Macdonald, "The Influence of Crystal Orientation on Surface Passivation in Multi-Crystalline Silicon," Oral presentation in *39th IEEE Photovoltaic Specialists Conference*, Tampa, Florida USA, 2013.

14. **Y. Wan**, S. Baker-Finch, K. R. McIntosh, A. F. Thomson and A. Cuevas, "Surface passivation of pyramidally and isotropically textured c-Si by PECVD SiN_x and a-Si", Oral presentation in *7th SNEC PV POWER EXPO*, Shanghai, China, 2013.

15. **Y. Wan**, K. R. McIntosh and A. F. Thomson, "Characterization of Stress in Amorphous Silicon Nitride and Implications to c-Si Surface Passivation", Poster presentation in *38th IEEE Photovoltaic Specialists Conference*, Texas, USA, 2012.

Other related publications

16. J. Bullock, D. Yan, **Y. Wan**, A. Cuevas, B. Demaurex, A. Hessler-Wyser, and S. D. Wolf, "Amorphous silicon passivated contacts for diffused junction silicon solar cells," *Journal of Applied Physics,* 2014.

17. X. Zhang, S. Hargreaves, **Y. Wan**, and A. Cuevas, "Surface passivation of crystalline silicon by sputter deposited hydrogenated amorphous silicon," *physica status solidi (RRL) – Rapid Research Letters,* 2013.

18. C. Barugkin, **Y. Wan**, D. Macdonald, and K. R. Catchpole, "Evaluating Plasmonic Light Trapping With Photoluminescence," *Photovoltaics, IEEE Journal of,* vol. 3, pp. 1292-1297, 2013.

19. S. C. Baker-Finch, K. R. McIntosh, M. L. Terry, and **Y. Wan**, "Isotextured Silicon Solar Cell Analysis and Modeling 2: Recombination and Device Modeling," *Photovoltaics, IEEE Journal of,* vol. 2, pp. 465-472, 2012.

20. K. R. McIntosh, L. E. Black, S. C. Baker-Finch, T. C. Kho, and **Y. Wan**, "Determination of the Magnitude and Centroid of the Charge in a Thin-film Insulator by CV and Kelvin Probe Measurements," *Energy Procedia,* vol. 15, pp. 162-170, 2012.

Bibliography

[1] C. Winneker, "World's solar photovoltaic capacity passes 100-gigawatt landmark after strong year," E. P. I. Association, Ed., ed. Brussels, 2013.

[2] G. Carr. "Sunny Uplands: Alternative energy will no longer be alternative". *The Economist*. 2012.

[3] P. J. Cousins, D. D. Smith, L. Hsin-Chiao, J. Manning, T. D. Dennis, A. Waldhauer, K. E. Wilson, G. Harley, and W. P. Mulligan, "Generation 3: Improved performance at lower cost," in *Photovoltaic Specialists Conference (PVSC), 2010 35th IEEE*, 2010, pp. 000275-000278.

[4] A. Aberle, *Crystalline Silicon Solar Cells: Advanced Surface Passivation and Analysis*, 1999.

[5] A. G. Aberle, "Surface passivation of crystalline silicon solar cells: a review," *Progress in Photovoltaics: Research and Applications,* vol. 8, pp. 473-487, 2000.

[6] A. G. Aberle, "Overview on SiN surface passivation of crystalline silicon solar cells," *Solar Energy Materials and Solar Cells,* vol. 65, pp. 239-248, 2001.

[7] C. Leguijt, P. Lölgen, J. A. Eikelboom, A. W. Weeber, F. M. Schuurmans, W. C. Sinke, P. F. A. Alkemade, P. M. Sarro, C. H. M. Marée, and L. A. Verhoef, "Low temperature surface passivation for silicon solar cells," *Solar Energy Materials and Solar Cells,* vol. 40, pp. 297-345, 1996.

[8] T. Lauinger, J. Schmidt, A. G. Aberle, and R. Hezel, "Record low surface recombination velocities on 1 Ω·cm p-silicon using remote plasma silicon nitride passivation," *Applied Physics Letters,* vol. 68, pp. 1232-1234, 1996.

[9] R. Hezel and R. Schorner, "Plasma Si nitride—A promising dielectric to achieve high-quality silicon MIS/IL solar cells," *Journal of Applied Physics,* vol. 52, pp. 3076-3079, 1981.

[10] H. F. W. Dekkers, L. Carnel, and G. Beaucarne, "Carrier trap passivation in multicrystalline Si solar cells by hydrogen from SiN_x:H layers," *Applied Physics Letters,* vol. 89, p. 013508, 2006.

[11] X. Dai and K. R. McIntosh, "Protection of Si–SiO_2 interfaces from damp heat by overlying SiNx and Si3N4 coatings," in *Proc. 35th IEEE PVSC*, Proc. 35th IEEE PVSC, 2010, pp. pp. 3205–3209.

[12] B. Gorowitz, T. B. Gorczyca, and R. J. Saia, "Applications of plasma enhanced chemical vapor deposition in VLSI," *Solid State Technology,* vol. 28, pp. 197-203, 1985.

[13] T. E. Burgess, J. C. Baum, F. M. Fowkes, R. Holmstrom, and G. A. Shirn, "Thermal diffusion of sodium in silicon nitride shielded silicon oxide films," *Journal of The Electrochemical Society,* vol. 116, pp. 1005-1008, July 1, 1969 1969.

[14] J. V. Dalton and J. Drobek, "Structure and sodium migration in silicon nitride films," *Journal of The Electrochemical Society,* vol. 115, pp. 865-868, August 1, 1968 1968.

[15] N. Zin, A. Blakers, K. R. McIntosh, E. Franklin, T. Kho, K. Chern, J. Wong, T. Mueller, A. G. Aberle, Y. Yang, X. Zhang, Z. Feng, Q. Huang, and P. J. Verlinden, "Continued development of all-back-contact silicon wafer solar cells at ANU," *Energy Procedia,* vol. 33, pp. 50-63, 2013.

[16] A. Blakers, K. C. Fong, E. Franklin, T. C. Kho, K. McIntosh, Y. Wan, D. Wang, and N. S. Zin, "24.6% efficient back contact cell with oxide - nitride

passivation," in *23rd Asian Photovoltaic Solar Energy Conference and Exhibition* Taipei, Taiwan, 2013.

[17] S. Duttagupta, B. Hoex, F. Lin, T. Mueller, and A. Aberle, "High-quality surface passivation of low-resistivity p-type c-Si by hydrogenated amorphous silicon nitride deposited by industrial-scale microwave PECVD," in *37th IEEE Photovoltaic Specialists Conference (PVSC)*, Seattle, WA, USA, 2011.

[18] T. Lauinger, J. Moschner, A. G. Aberle, and R. Hezel, "Optimization and characterization of remote plasma-enhanced chemical vapor deposition silicon nitride for the passivation of p-type crystalline silicon surfaces," *Journal of Vacuum Science & Technology A: Vacuum, Surfaces, and Films,* vol. 16, pp. 530-543, 1998.

[19] J. F. Lelièvre, E. Fourmond, A. Kaminski, O. Palais, D. Ballutaud, and M. Lemiti, "Study of the composition of hydrogenated silicon nitride SiNx:H for efficient surface and bulk passivation of silicon," *Solar Energy Materials and Solar Cells,* vol. 93, pp. 1281-1289, 2009.

[20] H. Mäckel and R. Lüdemann, "Detailed study of the composition of hydrogenated SiN_x layers for high-quality silicon surface passivation," *Journal of Applied Physics,* vol. 92, pp. 2602-2609, 2002.

[21] J. D. Moschner, J. Henze, J. Schmidt, and R. Hezel, "High-quality surface passivation of silicon solar cells in an industrial-type inline plasma silicon nitride deposition system," vol. 12, pp. 21-31, 2004.

[22] D. D. Smith, P. J. Cousins, A. Masad, A. Waldhauer, S. Westerberg, M. Johnson, T. Xiuwen, T. Dennis, G. Harley, G. Solomon, R. Seung, M. Shepherd, S. Harrington, M. Defensor, A. Leygo, P. Tomada, W. Junbo, T. Pass, L. Ann, L. Smith, N. Bergstrom, C. Nicdao, P. Tipones, and D. Vicente, "Generation III high efficiency lower cost technology: Transition to full scale manufacturing," in *Photovoltaic Specialists Conference (PVSC), 38th IEEE*, Austin, Texas, USA, 2012, pp. 001594-001597.

[23] J. Zhao, A. Wang, and M. A. Green, "24·5% Efficiency silicon PERT cells on MCZ substrates and 24·7% efficiency PERL cells on FZ substrates," 7, Progress in Photovoltaics: Research and Applications, John Wiley & Sons, Ltd., 1999.

[24] V. Verlaan, A. D. Verkerk, W. M. Arnoldbik, C. H. M. van der Werf, R. Bakker, Z. S. Houweling, I. G. Romijn, D. M. Borsa, A. W. Weeber, S. L. Luxembourg, M. Zeman, H. F. W. Dekkers, and R. E. I. Schropp, "The effect of composition on the bond structure and refractive index of silicon nitride deposited by HWCVD and PECVD," *Thin Solid Films,* vol. 517, pp. 3499-3502, 2009.

[25] W. A. P. Claassen, W. G. J. N. Valkenburg, F. H. P. M. Habraken, and Y. Tamminga, "Characterization of plasma silicon nitride layers," *Journal of The Electrochemical Society,* vol. 130, pp. 2419-2423, 1983.

[26] B. Lenkeit, T. Lauinger, A. G. Aberle, and R. Hezel, "Comparison of remote versus direct PECVD silicon nitride passivation of phosphorus-diffused emitters of silicon solar cells," in *2nd World Conference on Photovoltaic Energy Conversion*, 1998, pp. 1434-1437.

[27] T. Makino, "Composition and Structure Control by Source Gas Ratio in LPCVD SiN_x," *Journal of The Electrochemical Society,* vol. 130, pp. 450-455, February 1, 1983 1983.

[28] E. Bustarret, M. Bensouda, M. C. Habrard, Bruy, egrave, J. C. re, S. Poulin, and S. C. Gujrathi, "Configurational statistics in a-$Si_xN_yH_z$ alloys: A quantitative bonding analysis," *Physical Review B,* vol. 38, p. 8171, 1988.

[29] P. Doshi, G. E. Jellison, and A. Rohatgi, "Characterization and optimization of absorbing plasma-enhanced chemical vapor deposited antireflection coatings for silicon photovoltaics," *Appl. Opt.,* vol. 36, pp. 7826-7837, 1997.

[30] A. J. M. van Erven, R. C. M. Bosch, and M. D. Bijker, "Textured silicon surface passivation by high-rate expanding thermal plasma deposited SiN

and thermal SiO_2/SiN stacks for crystalline silicon solar cells," *Progress in Photovoltaics: Research and Applications,* vol. 16, pp. 615-627, 2008.

[31] S. K. O'Leary, S. R. Johnson, and P. K. Lim, "The relationship between the distribution of electronic states and the optical absorption spectrum of an amorphous semiconductor: An empirical analysis," *Journal of Applied Physics,* vol. 82, pp. 3334-3340, 1997.

[32] J. G. E. Jellison and F. A. Modine, "Parameterization of the optical functions of amorphous materials in the interband region," *Applied Physics Letters,* vol. 69, pp. 371-373, 1996.

[33] H. F. W. Dekkers, G. Beaucarne, M. Hiller, H. Charifi, and A. Slaoui, "Molecular hydrogen formation in hydrogenated silicon nitride," *Applied Physics Letters,* vol. 89, p. 211914, 2006.

[34] H. F. W. Dekkers, S. De Wolf, G. Agostinelli, F. Duerinckx, and G. Beaucarne, "Requirements of PECVD SiN_x:H layers for bulk passivation of mc-Si," *Solar Energy Materials and Solar Cells,* vol. 90, pp. 3244-3250, 2006.

[35] J. Hong, W. M. M. Kessels, W. J. Soppe, A. W. Weeber, W. M. Arnoldbik, and M. C. M. v. d. Sanden, "Influence of the high-temperature 'firing' step on high-rate plasma deposited silicon nitride films used as bulk passivating antireflection coatings on silicon solar cells," *Journal of Vacuum Science & Technology B: Microelectronics and Nanometer Structures,* vol. 21, pp. 2123-2132, 2003.

[36] I. Romijn, W. Soppe, H. Rieffe, A. Burgers, and A. Weeber, "Passivating mc-Si solar cells using SiN_x:H: from magic to physics," in *Proceedings of the 20th European Photovoltaic Solar Energy Conference and Exhibition*, 2005.

[37] A. W. Weeber, H. C. Rieffe, M. J. A. A. Goris, J. Hong, W. M. M. Kessels, M. C. M. van de Sanden, and W. J. Soppe, "Improved thermally stable surface and bulk passivation of PECVD SiN_x:H using N_2 and SiH_4," in *Photovoltaic Energy Conversion, 2003. Proceedings of 3rd World Conference on,* 2003, pp. 1131-1134 Vol.2.

[38] A. Cuevas, F. Chen, J. Tan, H. Mackel, S. Winderbaum, and K. Roth, "FTIR analysis of microwave-excited PECVD silicon nitride layers," in *Photovoltaic Energy Conversion, Conference Record of the 2006 IEEE 4th World Conference on*, 2006, pp. 1148-1151.

[39] F. Chen, I. Romijn, A. Weeber, J. Tan, B. Hallam, and J. Cotter, "Relationship between PECVD silicon nitride film composition and surface and edge passivation," in *22nd European Photovoltaic Solar Energy Conference*, Milan, Italy, 2007, pp. 1053–1060.

[40] S. Winderbaum, A. Cuevas, F. Chen, J. Tan, K. Hanton, D. Macdonald, and K. Roth, "Industrial PECVD silicon nitride: surface and bulk passivation of silicon wafers," presented at the European Photovoltaic Solar Energy Conference WIP Munich and ETA-Florence, 2004.

[41] C. Boehme and G. Lucovsky, "H loss mechanism during anneal of silicon nitride: Chemical dissociation," *Journal of Applied Physics*, vol. 88, pp. 6055-6059, 2000.

[42] C. Boehme and G. Lucovsky, "Dissociation reactions of hydrogen in remote plasma-enhanced chemical-vapor-deposition silicon nitride," *Journal of Vacuum Science & Technology A: Vacuum, Surfaces, and Films,* vol. 19, pp. 2622-2628, 2001.

[43] A. W. Weeber, H. C. Rieffe, I. G. Romijn, W. C. Sinke, and W. J. Soppe, "The fundamental properties of SiN_x:H that determine its passivating qualities," in *Photovoltaic Specialists Conference, 2005. Conference Record of the Thirty-first IEEE*, 2005, pp. 1043-1046.

[44] V. Verlaan, R. Bakker, C. H. M. van der Werf, Z. S. Houweling, Y. Mai, J. K. Rath, and R. E. I. Schropp, "High-density silicon nitride deposited at low substrate temperature with high deposition rate using hot wire chemical vapour deposition," *Surface and Coatings Technology,* vol. 201, pp. 9285-9288, 2007.

[45] S. Hasegawa, M. Matsuda, and Y. Kurata, "Si-H and N-H vibrational properties in glow-discharge amorphous SiN_x:H films ($0 < x < 1.55$)," *Applied Physics Letters,* vol. 57, pp. 2211-2213, 1990.

[46] F. Giorgis, F. Giuliani, C. F. Pirri, E. Tresso, C. Summonte, R. Rizzoli, R. Galloni, A. Desalvo, and P. Rava, "Optical, structural and electrical properties of device-quality hydrogenated amorphous silicon-nitrogen films deposited by plasma-enhanced chemical vapour deposition," *Philosophical Magazine Part B,* vol. 77, pp. 925 - 944, 1998.

[47] D. K. Schroder, *Semiconductor material and device characterization*, 3rd ed. Hoboken, New Jersey, USA: John Wiley & Sons Inc., 2006.

[48] M. Cardona, "Vibrational spectra of hydrogen in silicon and germanium," *physica status solidi (b),* vol. 118, pp. 463-481, 1983.

[49] V. Verlaan, C. H. M. van der Werf, W. M. Arnoldbik, H. D. Goldbach, and R. E. I. Schropp, "Unambiguous determination of Fourier-transform infrared spectroscopy proportionality factors: The case of silicon nitride," *Physical Review B,* vol. 73, p. 195333, 2006.

[50] S. Hasegawa, L. He, Y. Amano, and T. Inokuma, "Analysis of SiH and SiN vibrational absorption in amorphous SiN_x:H films in terms of a charge-transfer model," *Physical Review B,* vol. 48, p. 5315, 1993.

[51] W. A. Lanford and M. J. Rand, "The hydrogen content of plasma-deposited silicon nitride," *Journal of Applied Physics,* vol. 49, pp. 2473-2477, 1978.

[52] D. T. Krick, P. M. Lenahan, and J. Kanicki, "Nature of the dominant deep trap in amorphous silicon nitride," *Physical Review B,* vol. 38, pp. 8226-8229, 1988.

[53] P. M. Lenahan and S. E. Curry, "First observation of the Si hyperfine spectra of silicon dangling bond centers in silicon nitride," *Applied Physics Letters,* vol. 56, pp. 157-159, 1990.

[54] J. Schmidt and A. G. Aberle, "Carrier recombination at silicon--silicon nitride interfaces fabricated by plasma-enhanced chemical vapor deposition," *Journal of Applied Physics,* vol. 85, pp. 3626-3633, 1999.

[55] K. J. Park and G. N. Parsons, "Bulk and interface charge in low temperature silicon nitride for thin film transistors on plastic substrates," *Journal of Vacuum Science & Technology A: Vacuum, Surfaces, and Films,* vol. 22, pp. 2256-2260, 2004.

[56] K. R. McIntosh and L. P. Johnson, "Recombination at textured silicon surfaces passivated with silicon dioxide," *Journal of Applied Physics,* vol. 105, p. 124520, 2009.

[57] D. Landheer, K. Rajesh, D. Masson, J. E. Hulse, G. I. Sproule, and T. Quance, "Factors affecting interface-state density and stress of silicon nitride films deposited on Si by electron-cyclotron resonance chemical vapor deposition," *Journal of Vacuum Science & Technology A: Vacuum, Surfaces, and Films,* vol. 16, pp. 2931-2940, 1998.

[58] R. Hezel, K. Blumenstock, and R. Schorner, "Interface States and Fixed Charges in MNOS Structures with APCVD and Plasma Silicon Nitride," *Journal of The Electrochemical Society,* vol. 131, pp. 1679-1683, 1984.

[59] S. D. Wolf, G. Agostinelli, G. Beaucarne, and P. Vitanov, "Influence of stoichiometry of direct plasma-enhanced chemical vapor deposited SiN[sub x] films and silicon substrate surface roughness on surface passivation," *Journal of Applied Physics,* vol. 97, p. 063303, 2005.

[60] P. E. Bagnoli, A. Piccirillo, A. L. Gobbi, and R. Giannetti, "Electrical characteristics of silicon nitride on silicon and InGaAs as a function of the insulator stoichiometry," *Applied Surface Science,* vol. 52, pp. 45-52, 1991.

[61] D. Landheer, G. C. Aers, G. I. Sproule, R. Khatri, P. J. Simpson, and S. C. Gujrathi, "Positron study of plasma-enhanced chemical vapor deposited silicon nitride films," *Journal of Applied Physics,* vol. 78, pp. 2568-2574, 1995.

[62] S. Garcia, I. Martil, G. G. Diaz, E. Castan, S. Duenas, and M. Fernandez, "Deposition of SiN[sub x]:H thin films by the electron cyclotron resonance and its application to Al/SiN[sub x]:H/Si structures," *Journal of Applied Physics,* vol. 83, pp. 332-338, 1998.

[63] S. Dauwe, "Low temperature surface passivation of crystalline silicon and its application to the rear side of solar cells," Phd Phd thesis, Hannover Universitat,Germany, Hannover, 2004.

[64] M. W. P. E. Lamers, K. T. Butler, J. H. Harding, and A. Weeber, "Interface properties of a-SiNx:H/Si to improve surface passivation," *Solar Energy Materials and Solar Cells,* vol. 106, pp. 17-21, 2012.

[65] S. Fujita and A. Sasaki, "Dangling Bonds in Memory-Quality Silicon Nitride Films," *Journal of The Electrochemical Society,* vol. 132, pp. 398-402, 1985.

[66] A. Stesmans, "The .Si identical to Si_3 defect at various (111)Si/SiO_2 and (111)Si/Si_3N_4 interfaces," *Semiconductor Science and Technology,* vol. 4, p. 1000, 1989.

[67] A. Stesmans and G. Van Gorp, "-Si $\equiv$ Si3 defect at thermally grown (111)Si/Si_3N_4 interfaces," *Physical Review B,* vol. 52, p. 8904, 1995.

[68] D. Jousse, J. Kanicki, and J. H. Stathis, "Observation of multiple silicon dangling bond configurations in silicon nitride," *Applied Physics Letters,* vol. 54, pp. 1043-1045, 1989.

[69] J. Schmidt, F. M. Schuurmans, W. C. Sinke, S. W. Glunz, and A. G. Aberle, "Observation of multiple defect states at silicon-silicon nitride interfaces fabricated by low-frequency plasma-enhanced chemical vapor deposition," *Applied Physics Letters,* vol. 71, pp. 252-254, 1997.

[70] E.H.Nicollian and J.R.Brews, *MOS (Metal Oxide Semiconductor) Physics and Technology*: (Wiley, New Jersey, 2003), Chap. 3.

[71] R. Castagné and A. Vapaille, "Description of the SiO_2-Si interface properties by means of very low frequency MOS capacitance measurements," *Surface Science,* vol. 28, pp. 157-193, 1971.

[72] L. M. Terman, "An investigation of surface states at a silicon/silicon oxide interface employing metal-oxide-silicon diodes," *Solid-State Electronics,* vol. 5, pp. 285-299, 1962.

[73] W. D. Eades and R. M. Swanson, "Calculation of surface generation and recombination velocities at the Si-SiO_2 interface," *Journal of Applied Physics,* vol. 58, pp. 4267-4276, 1985.

[74] A. S. Grove, O. Leistiko, Jr., and W. W. Hooper, "Effect of surface fields on the breakdown voltage of planar silicon p-n junctions," *Electron Devices, IEEE Transactions on,* vol. 14, pp. 157-162, 1967.

[75] R. B. M. Girisch, R. P. Mertens, and R. F. De Keersmaecker, "Determination of Si-SiO_2 interface recombination parameters using a gate-controlled point-junction diode under illumination," *Electron Devices, IEEE Transactions on,* vol. 35, pp. 203-222, 1988.

[76] A. G. Aberle, S. Glunz, and W. Warta, "Impact of illumination level and oxide parameters on Shockley--Read--Hall recombination at the Si-SiO[sub 2] interface," *Journal of Applied Physics,* vol. 71, pp. 4422-4431, 1992.

[77] J. Schmidt and M. Kerr, "Highest-quality surface passivation of low-resistivity p-type silicon using stoichiometric PECVD silicon nitride," *Solar Energy Materials and Solar Cells,* vol. 65, pp. 585-591, 2001.

[78] M. Kerr, "Surface, emitter and bulk recombination in silicon and development of silicon nitride passivated solar cells," Ph.D Ph.D. thesis, Australian National University, Canberra, 2002.

[79] S. W. Glunz, A. B. Sproul, W. Warta, and W. Wettling, "Injection-level-dependent recombination velocities at the Si-SiO_2 interface for various

dopant concentrations," *Journal of Applied Physics,* vol. 75, pp. 1611-1615, 1994.

[80] M. J. Kerr and A. Cuevas, "General parameterization of Auger recombination in crystalline silicon," *Journal of Applied Physics,* vol. 91, pp. 2473-2480, 2002.

[81] P. P. Altermatt, J. Schmidt, G. Heiser, and A. G. Aberle, "Assessment and parameterisation of Coulomb-enhanced Auger recombination coefficients in lowly injected crystalline silicon," *Journal of Applied Physics,* vol. 82, pp. 4938-4944, 1997.

[82] A. Richter, S. W. Glunz, F. Werner, J. Schmidt, and A. Cuevas, "Improved quantitative description of Auger recombination in crystalline silicon," *Physical Review B,* vol. 86, p. 165202, 2012.

[83] D. Kane and R. M. Swanson, "Measurement of the emitter saturation current by a contactless photoconductivity decay method," in *18th IEEE Photovoltaic Specialists Conference*, Las Vegas, USA, 1985, pp. 578 -583

[84] W. L. F. Chen, "PECVD silicon nitride for n-type silicon solar cells," Doctor of Philosophy, School of Photovoltaic and Renewable Energy Engineering, University of New South Wales, Sydney, 2008.

[85] H. F. Sterling and R. C. G. Swann, "Chemical vapour deposition promoted by r.f. discharge," *Solid-State Electronics,* vol. 8, pp. 653-654, 1965.

[86] G. Lucovsky and D. V. Tsu, "Plasma enhanced chemical vapor deposition: Differences between direct and remote plasma excitation," *Journal of Vacuum Science & Technology A: Vacuum, Surfaces, and Films,* vol. 5, pp. 2231-2238, 1987.

[87] *http://www.oxfordplasma.de/systems/100ll.htm*.

[88] K. Kimura, in *Tech. Digest First International Photovoltaic Science and Engineering Conference*, Kobe, 1984, p. 37.

[89] T. Lauinger, A. G. Aberle, and R. Hezel, "Comparision of direct and remote PECVD silicon nitride films for low-temperature surface passivation of p-type crystalline silicon," in *14th European Photovoltaic Solar Energy Conference*, 1997, pp. 853-856.

[90] M. Moisan, C. Barbeau, R. Claude, C. M. Ferreira, J. Margot, J. Paraszczak, A. B. Sa, G. Sauve, and M. R. Wertheimer, "Radio frequency or microwave plasma reactors? Factors determining the optimum frequency of operation," *Journal of Vacuum Science & Technology B: Microelectronics and Nanometer Structures,* vol. 9, pp. 8-25, 1991.

[91] W. Soppe, H. Rieffe, and A. Weeber, "Bulk and surface passivation of silicon solar cells accomplished by silicon nitride deposited on industrial scale by microwave PECVD," *Progress in Photovoltaics: Research and Applications,* vol. 13, pp. 551-569, 2005.

[92] F. W. Chen, T. T. A. Li, and J. E. Cotter, "PECVD silicon nitride surface passivation for high-efficiency N-type silicon solar cells," in *Proceedings of the Fourth World Conference on Photovoltaic Energy Conversion*, Waikaloa, IEEE, New York, 2006, p. 1071.

[93] W. A. P. Claassen, W. G. J. N. Valkenburg, M. F. C. Willemsen, and W. M. v. d. Wijgert, "Influence of deposition temperature, gas pressure, gas phase composition, and RF frequency on composition and mechanical stress of plasma silicon nitride layers," *Journal of The Electrochemical Society,* vol. 132, pp. 893-898, April 1, 1985 1985.

[94] D. L. Smith, A. S. Alimonda, and F. J. v. Preissig, "Mechanism of SiN_xH_y deposition from N_2-SiH_4 plasma," *Journal of Vacuum Science & Technology B: Microelectronics and Nanometer Structures,* vol. 8, pp. 551-557, 1990.

[95] W. M. M. Kessels, F. J. H. v. Assche, J. Hong, D. C. Schram, and M. C. M. v. d. Sanden, "Plasma diagnostic study of silicon nitride film growth in a remote Ar-H_2-N_2-SiH_4 plasma: Role of N and SiH_n radicals," *Journal of Vacuum Science & Technology A: Vacuum, Surfaces, and Films,* vol. 22, pp. 96-106, 2004.

[96] P. J. v. d. Oever, J. H. v. Helden, J. L. v. Hemmen, R. Engeln, D. C. Schram, M. C. M. v. d. Sanden, and W. M. M. Kessels, "N, NH, and NH_2 radical densities in a remote Ar-NH_3-SiH_4 plasma and their role in silicon nitride deposition," *Journal of Applied Physics,* vol. 100, p. 093303, 2006.

[97] S. P. Phang and D. Macdonald, "Direct comparison of boron, phosphorus, and aluminum gettering of iron in crystalline silicon," *Journal of Applied Physics,* vol. 109, p. 073521, 2011.

[98] W. Kern and D. A. Puotinen, "Cleaning solutions based on hydrogen peroxide for use in silicon semiconductor technology," *RCA Rev.,* vol. 31, pp. 187-206, 1970.

[99] H. Angermann, J. Rappich, L. Korte, I. Sieber, E. Conrad, M. Schmidt, K. Hübener, J. Polte, and J. Hauschild, "Wet-chemical passivation of atomically flat and structured silicon substrates for solar cell application," *Applied Surface Science,* vol. 254, pp. 3615-3625, 2008.

[100] H. Angermann, F. Wünsch, M. Kunst, A. Laades, U. Stürzebecher, E. Conrad, L. Korte, and M. Schmidt, "Effect of wet-chemical substrate pretreatment on electronic interface properties and recombination losses of a -Si:H/c -Si and a -SiNx:H/c -Si hetero-interfaces," *physica status solidi (c),* vol. 8, pp. 879-882, 2011.

[101] V. D. Mihailetchi, Y. Komatsu, and L. J. Geerligs, "Nitric acid pretreatment for the passivation of boron emitters for n-type base silicon solar cells," *Applied Physics Letters,* vol. 92, p. 063510, 2008.

[102] R. M. William, "Response surface methodology," in *Encyclopedia of Biopharmaceutical Statistics, Second Edition*. vol. null, ed: Taylor & Francis, 2013, pp. 858-869.

[103] D. Macdonald and L. J. Geerligs, "Recombination activity of interstitial iron and other transition metal point defects in p- and n-type crystalline silicon," *Applied Physics Letters,* vol. 85, pp. 4061-4063, 2004.

[104] S. Duttagupta, F. Ma, B. Hoex, T. Mueller, and A. G. Aberle, "Optimised Antireflection Coatings using Silicon Nitride on Textured Silicon Surfaces based on Measurements and Multidimensional Modelling," *Energy Procedia,* vol. 15, pp. 78-83, 2012.

[105] M. H. Kang, K. Ryu, A. Upadhyaya, and A. Rohatgi, "Optimization of SiN AR coating for Si solar cells and modules through quantitative assessment of optical and efficiency loss mechanism," ed: John Wiley & Sons, Ltd.

[106] A. G. Aberle, T. Lauinger, J. Schmidt, and R. Hezel, "Injection-level dependent surface recombination velocities at the silicon-plasma silicon nitride interface," *Applied Physics Letters,* vol. 66, pp. 2828-2830, 1995.

[107] M. J. Kerr and A. Cuevas, "Recombination at the interface between silicon and stoichiometric plasma silicon nitride," *Semiconductor Science and Technology,* vol. 17, p. 166, 2002.

[108] J. R. Elmiger and M. Kunst, "Investigation of charge carrier injection in silicon nitride/silicon junctions," *Applied Physics Letters,* vol. 69, pp. 517-519, 1996.

[109] G. Turban, Y. Catherine, and B. Grolleau, "Mass spectrometry of a silane glow discharge during plasma deposition of a-Si: H films," *Thin Solid Films,* vol. 67, pp. 309-320, 1980.

[110] L. Martinu and D. Poitras, "Plasma deposition of optical films and coatings: A review," *Journal of Vacuum Science & Technology A: Vacuum, Surfaces, and Films,* vol. 18, pp. 2619-2645, 2000.

[111] J. Robertson, "Electronic structure of silicon nitride," *Philosophical Magazine Part B,* vol. 63, pp. 47-77, 1991/01/01 1991.

[112] J. Schmidt and et al., "Surface passivation of silicon solar cells using plasma-enhanced chemical-vapour-deposited SiN films and thin thermal SiO_2 /plasma SiN stacks," *Semiconductor Science and Technology,* vol. 16, p. 164, 2001.

[113] S. W. Glunz, D. Biro, S. Rein, and W. Warta, "Field-effect passivation of the SiO_2-Si interface," *Journal of Applied Physics,* vol. 86, pp. 683-691, 1999.

[114] S. Dauwe, J. Schmidt, A. Metz, and R. Hezel, "Fixed charge density in silicon nitride films on crystalline silicon surfaces under illumination," in *Photovoltaic Specialists Conference, 2002. Conference Record of the Twenty-Ninth IEEE*, 2002, pp. 162-165.

[115] S. Steingrube, P. P. Altermatt, D. S. Steingrube, J. Schmidt, and R. Brendel, "Interpretation of recombination at c-Si/SiN_x interfaces by surface damage," *Journal of Applied Physics,* vol. 108, p. 014506, 2010.

[116] B. Veith, T. Ohrdes, F. Werner, R. Brendel, P. P. Altermatt, N.-P. Harder, and J. Schmidt, "Injection dependence of the effective lifetime of n-type Si passivated by Al_2O_3: An edge effect?," *Solar Energy Materials and Solar Cells,* 2013.

[117] S. Duttagupta, M. F, B. Hoex, T. Mueller, and A. Aberle, "Optimised antireflection coatings using silicon nitride on textured silicon surfaces based on measurements and multidimensional modeling," in *ICMAT*, Singapore, 2011.

[118] S. C. Baker-Finch and K. R. McIntosh, "A freeware program for precise optical analysis of the front surface of a solar cell," in *Photovoltaic Specialists Conference (PVSC), 35th IEEE*, 2010, pp. 002184-002187.

[119] K. R. McIntosh and S. C. Baker-Finch, "OPAL 2: Rapid optical simulation of silicon solar cells," in *Photovoltaic Specialists Conference (PVSC), 38th IEEE*, 2012, pp. 000265-000271.

[120] K. R. McIntosh, J. N. Cotsell, J. S. Cumpston, A. W. Norris, N. E. Powell, and B. M. Ketola, "An optical comparison of silicone and EVA encapsulants for conventional silicon PV modules: a ray-tracing study," in *Proceedings of the 34th IEEE PVSC*, Philadelphia, 2009, pp. 544–549.

[121] A. Illiberi, P. Kudlacek, A. H. M. Smets, M. Creatore, and M. C. M. v. d. Sanden, "Effect of ion bombardment on the a-Si:H based surface passivation of c-Si surfaces," *Applied Physics Letters,* vol. 98, p. 242115, 2011.

[122] B. Demaurex, S. D. Wolf, A. Descoeudres, Z. C. Holman, and C. Ballif, "Damage at hydrogenated amorphous/crystalline silicon interfaces by indium tin oxide overlayer sputtering," *Applied Physics Letters,* vol. 101, p. 171604, 2012.

[123] G. Lucovsky, H. Y. Yang, Z. Jing, and J. L. Whitten, "The Role of Hydrogen Atoms (H) in Metastable Defect Formation at Si–SiO_2 Interfaces and in Hydrogenated Amorphous Si (a-Si:H)," vol. 159, ed: WILEY-VCH Verlag, 1997, pp. 5-15.

[124] D. L. Staebler and C. R. Wronski, "Reversible conductivity changes in discharge-produced amorphous Si," *Applied Physics Letters,* vol. 31, pp. 292-294, 1977.

[125] S. De Wolf, B. Demaurex, A. Descoeudres, and C. Ballif, "Very fast light-induced degradation of a-Si:H/c-Si(100) interfaces," *Physical Review B,* vol. 83, p. 233301, 2011.

[126] H. Plagwitz, B. Terheiden, and R. Brendel, "Staebler-Wronski-like formation of defects at the amorphous-silicon-crystalline silicon interface during illumination," *Journal of Applied Physics,* vol. 103, p. 094506, 2008.

[127] M. Stutzmann, W. B. Jackson, and C. C. Tsai, "Light-induced metastable defects in hydrogenated amorphous silicon: A systematic study," *Physical Review B,* vol. 32, pp. 23-47, 1985.

[128] H. Dersch, J. Stuke, and J. Beichler, "Light-induced dangling bonds in hydrogenated amorphous silicon," *Applied Physics Letters,* vol. 38, pp. 456-458, 1981.

[129] S. Shimoda, I. Shimizu, and M. Migitaka, "Chemical vapor deposition of a silicon nitride layer with an excellent interface by NH_3 plasma treatment," *Applied Physics Letters,* vol. 52, pp. 1068-1070, 1988.

[130] C. Gong and et al., "Study of silicon-silicon nitride interface properties on planar (1 0 0), planar (1 1 1) and textured surfaces using deep-level transient spectroscopy," *Journal of Physics D: Applied Physics,* vol. 43, p. 485301, 2010.

[131] C. Gong, E. Simoen, N. Posthuma, E. V. Kerschaver, J. Poortmans, and R. Mertens, "A deep-level transient spectroscopy study of silicon interface states using different silicon nitride surface passivation schemes," *Applied Physics Letters,* vol. 96, p. 103507, 2010.

[132] T. Takakura, R. Imai, Y. Okamoto, and H. Taniguchi, "Effect of plasma pretreatment on fixed charge at the silicon nitride/silicon interface," *Japanese Journal of Applied Physics,* vol. 49, 2010.

[133] Y. Takahashi, J. Nigo, A. Ogane, Y. Uraoka, and T. Fuyuki, "NH_3 plasma interface modification for silicon surface passivation at very low temperature," *Japanese Journal of Applied Physics,* vol. 47, pp. 5320–5323, 2008.

[134] E. Atanassova, J. Kassabov, and E. Goranova, "Low temperature plasma nitridation of thin thermal SiO_2 and a silicon surface with native oxide," *Microelectronics Journal,* vol. 21, pp. 5-21, 1990.

[135] T. Dimitrova, E. Atanassova, G. Beshkov, and J. Pazov, "Thin thermal SiO_2 after NH_3 or N_2O plasma action under plasma-enhanced chemical vapor deposition conditions," *Thin Solid Films,* vol. 252, pp. 89-97, 1994.

[136] H. Jin, K. J. Weber, and P. J. Smith, "Characterization of the Si–SiO_2 interface following room temperature ammonia plasma exposure," *Journal of The Electrochemical Society,* vol. 154, pp. H417-H421, January 1, 2007 2007.

[137] F. Giorgis, C. F. Pirri, and E. Tresso, "Structural properties of a-$Si_{1-x}N_x$:H films grown by plasma enhanced chemical vapour deposition by SiH_4 + NH_3 + H_2 gas mixtures," *Thin Solid Films,* vol. 307, pp. 298-305, 1997.

[138] C. Sénémaud, A. Gheorghiu, L. Amoura, R. Etemadi, H. Shirai, C. Godet, M. Fang, and S. Gujrathi, "Local order and H-bonding in N-rich amorphous

silicon nitride," *Journal of Non-Crystalline Solids,* vol. 164–166, Part 2, pp. 1073-1076, 1993.

[139] Y. Ren, K. J. Weber, N. M. Nursam, and D. Wang, "Effect of deposition conditions and thermal annealing on the charge trapping properties of SiN_x films," *Applied Physics Letters,* vol. 97, p. 202907, 2010.

[140] P. Campbell and M. A. Green, "Light trapping properties of pyramidally textured surfaces," *Journal of Applied Physics,* vol. 62, pp. 243-249, 1987.

[141] L. M. Landsberger, S. Naseh, M. Kahrizi, and M. Paranjape, "On hillocks generated during anisotropic etching of Si in TMAH," *Microelectromechanical Systems, Journal of,* vol. 5, pp. 106-116, 1996.

[142] Y. Nishimoto, T. Ishihara, and K. Namba, "Investigation of acidic texturization for multicrystalline silicon solar cells," *Journal of The Electrochemical Society,* vol. 146, pp. 457-461, 1999.

[143] J. Zhao, A. Wang, M. A. Green, and F. Ferrazza, "19.8% efficient 'honeycomb' textured multicrystalline and 24.4% monocrystalline silicon solar cells," *Applied Physics Letters,* vol. 73, pp. 1991-1993, 1998.

[144] P. J. Cousins and J. E. Cotter, "Minimizing lifetime degradation associated with thermal oxidation of upright randomly textured silicon surfaces," *Solar Energy Materials and Solar Cells,* vol. 90, pp. 228-240, 2006.

[145] S. C. Baker-Finch, "Rules and Tools for Understanding, Modelling and Designing Textured Silicon Solar Cells," Doctor of Philosophy, The Australian National University, Canberra, 2012.

[146] A. Stesmans and V. V. Afanas'ev, "Thermally induced interface degradation in (100) and (111) Si/SiO_2 analyzed by electron spin resonance," *Journal of Vacuum Science & Technology B: Microelectronics and Nanometer Structures,* vol. 16, pp. 3108-3111, 1998.

[147] E. H. Poindexter, P. J. Caplan, B. E. Deal, and R. R. Razouk, "Interface states and electron spin resonance centers in thermally oxidized (111) and (100) silicon wafers," *Journal of Applied Physics,* vol. 52, pp. 879-884, 1981.

[148] S. C. Baker-Finch and K. R. McIntosh, "The contribution of planes, vertices, and edges to recombination at pyramidally textured surfaces," *IEEE Journal of Photovoltaics,* vol. 1, pp. 59-65, 2011.

[149] U. K. Das, M. Z. Burrows, M. Lu, S. Bowden, and R. W. Birkmire, "Surface passivation and heterojunction cells on Si (100) and (111) wafers using dc and rf plasma deposited Si:H thin films," *Applied Physics Letters,* vol. 92, p. 063504, 2008.

[150] A. Rohatgi, P. Doshi, J. Moschner, T. Lauinger, A. G. Aberle, and D. S. Ruby, "Comprehensive study of rapid, low-cost silicon surface passivation technologies," *Electron Devices, IEEE Transactions on,* vol. 47, pp. 987-993, 2000.

[151] R. A. Sinton, A. Cuevas, and M. Stuckings, "Quasi-steady-state photoconductance, a new method for solar cell material and device characterization," in *Photovoltaic Specialists Conference, 1996., Conference Record of the Twenty Fifth IEEE,* 1996, pp. 457-460.

[152] R. A. Sinton and A. Cuevas, "Contactless determination of current--voltage characteristics and minority-carrier lifetimes in semiconductors from quasi-steady-state photoconductance data," *Applied Physics Letters,* vol. 69, pp. 2510-2512, 1996.

[153] J. Tan, D. Macdonald, F. Rougieux, and A. Cuevas, "Accurate measurement of the formation rate of iron–boron pairs in silicon," *Semiconductor Science and Technology,* vol. 26, p. 055019, 2011.

[154] M. G. C. W. L. Bailey, C. B. Harris, and I. A. Lesk, "United States Patent: 4137123 - Texture etching of silicon: method," U.S. Patent 4137123, Jan. 30, 1979.

[155] O. Tabata, R. Asahi, H. Funabashi, K. Shimaoka, and S. Sugiyama, "Anisotropic etching of silicon in TMAH solutions," *Sensors and Actuators A: Physical,* vol. 34, pp. 51-57, 1992.

[156] J. S. You, D. Kim, J. Y. Huh, H. J. Park, J. J. Pak, and C. S. Kang, "Experiments on anisotropic etching of Si in TMAH," *Solar Energy Materials and Solar Cells,* vol. 66, pp. 37-44, 2001.

[157] P. Papet, O. Nichiporuk, A. Kaminski, Y. Rozier, J. Kraiem, J. F. Lelievre, A. Chaumartin, A. Fave, and M. Lemiti, "Pyramidal texturing of silicon solar cell with TMAH chemical anisotropic etching," *Solar Energy Materials and Solar Cells,* vol. 90, pp. 2319-2328, 2006.

[158] S. C. Baker-Finch, K. R. McIntosh, M. L. Terry, and Y. Wan, "Isotextured silicon solar cell analysis and modeling 2: recombination and device modeling," *Photovoltaics, IEEE Journal of,* vol. 2, pp. 465-472, 2012.

[159] Z. A. Weinberg, W. C. Johnson, and M. A. Lampert, "High-field transport in SiO_2 on silicon induced by corona charging of the unmetallized surface," *Journal of Applied Physics,* vol. 47, pp. 248-255, 1976.

[160] P. Campbell and M. A. Green, "High performance light trapping textures for monocrystalline silicon solar cells," *Solar Energy Materials and Solar Cells,* vol. 65, pp. 369-375, 2001.

[161] J. Zhao, A. Wang, P. Altermatt, and M. A. Green, "Twenty-four percent efficient silicon solar cells with double layer antireflection coatings and reduced resistance loss," *Applied Physics Letters,* vol. 66, pp. 3636-3638, 1995.

[162] J. Benick, B. Hoex, M. C. M. v. d. Sanden, W. M. M. Kessels, O. Schultz, and S. W. Glunz, "High efficiency n-type Si solar cells on Al_2O_3-passivated boron emitters," *Applied Physics Letters,* vol. 92, p. 253504, 2008.

[163] A. Descoeudres, L. Barraud, S. De Wolf, B. Strahm, D. Lachenal, C. Guerin, Z. C. Holman, F. Zicarelli, B. Demaurex, J. Seif, J. Holovsky, and C. Ballif, "Improved amorphous/crystalline silicon interface passivation by

hydrogen plasma treatment," *Applied Physics Letters,* vol. 99, pp. 123506-3, 2011.

[164] T. Sakurai and H. D. Hagstrum, "Interplay of the monohydride phase and a newly discovered dihydride phase in chemisorption of H on Si(100)2 × 1," *Physical Review B,* vol. 14, pp. 1593-1596, 1976.

[165] S. D. Wolf and M. Kondo, "Abruptness of a-Si:H/c-Si interface revealed by carrier lifetime measurements," *Applied Physics Letters,* vol. 90, p. 042111, 2007.

[166] S. D. Wolf, S. Olibet, and C. Ballif, "Stretched-exponential a-Si:H/c-Si interface recombination decay," *Applied Physics Letters,* vol. 93, p. 032101, 2008.

[167] M. L. Terry, A. Meisel, E. Rosenfeld, S. Shah, E. Tai, X. Chen, and T. Du, "All screen-printed 18% homogeneous emitter solar cells using high volume manufacturing equipment," in *Photovoltaic Specialists Conference (PVSC), 35th IEEE,* 2010, pp. 003618-003622.

[168] S. C. Baker-Finch, K. R. McIntosh, and M. L. Terry, "Isotextured silicon solar cell analysis and modeling 1: optics," *Photovoltaics, IEEE Journal of,* vol. 2, pp. 457-464, 2012.

[169] B. Hoex, J. J. H. Gielis, M. C. M. v. d. Sanden, and W. M. M. Kessels, "On the c-Si surface passivation mechanism by the negative-charge-dielectric Al_2O_3," *Journal of Applied Physics,* vol. 104, p. 113703, 2008.

[170] W. S. Lau, "The preparation and characterization of nearly hysteresis-free metal-nitride-silicon capacitors on both p- and n-type silicon substrates," *Journal of Applied Physics,* vol. 71, pp. 489-493, 1992.

[171] K. J. Weber and H. Jin, "Improved silicon surface passivation achieved by negatively charged silicon nitride films," *Applied Physics Letters,* vol. 94, pp. 063509-3, 2009.

[172] K. R. McIntosh, L. E. Black, S. C. Baker-Finch, T. C. Kho, and Y. Wan, "Determination of the magnitude and centroid of the charge in a thin-film insulator by cv and kelvin probe measurements," *Energy Procedia,* vol. 15, pp. 162-170, 2012.

[173] J. J. Boland and G. N. Parsons, "Bond selectivity in silicon film growth," *Science,* vol. 256, pp. 1304-1306, 1992.

[174] D. S. Ruby, W. L. Wilbanks, and C. B. Fleddermann, "A statistical analysis of the effect of PECVD deposition parameters on surface and bulk recombination in silicon solar cells," in *1st World Conference on Photovoltaic Energy Conversion,*, Waikoloa, Hawaii, 1994, pp. 1335–1338.

[175] M. J. Kerr, J. Schmidt, A. Cuevas, and J. H. Bultman, "Surface recombination velocity of phosphorus-diffused silicon solar cell emitters passivated with plasma enhanced chemical vapor deposited silicon nitride and thermal silicon oxide," *Journal of Applied Physics,* vol. 89, pp. 3821-3826, 2001.

[176] A. Fell, "A free and fast three-dimensional/two-dimensional solar cell simulator featuring conductive boundary and quasi-neutrality approximations," *Electron Devices, IEEE Transactions on,* vol. 60, pp. 733-738, 2013.

[177] S. C. Witczak, M. Gaitan, J. S. Suehle, M. C. Peckerar, and D. I. Ma, "The interaction of stoichiometry, mechanical stress, and interface trap density in LPCVD Si-rich SiN_x-Si structures," *Solid-State Electronics,* vol. 37, pp. 1695-1704, 1994.

[178] http://www.veeco.com/.

[179] G. G. Stoney, "The tension of metallic films deposited by electrolysis," *Proceedings of the Royal Society of London. Series A,* vol. 82, pp. 172-175, May 6, 1909 1909.

[180] W. A. Brantley, "Calculated elastic constants for stress problems associated with semiconductor devices," *Journal of Applied Physics,* vol. 44, pp. 534-535, 1973.

[181] M. P. Hughey and R. F. Cook, "Stress development kinetics in plasma-enhanced chemical-vapor-deposited silicon nitride films," *Journal of Applied Physics,* vol. 97, p. 114914, 2005.

[182] S. Hasegawa, Y. Amano, T. Inokuma, and Y. Kurata, "Relationship between the stress and bonding properties of amorphous SiN_x:H films," *Journal of Applied Physics,* vol. 72, pp. 5676-5681, 1992.

[183] A. K. Sinha, H. J. Levinstein, T. E. Smith, G. Quintana, and S. E. Haszko, "Reactive plasma deposited Si-N films for MOS-LSI passivation," *Journal of The Electrochemical Society,* vol. 125, pp. 601-608, 1978.

[184] D. L. Smith, A. S. Alimonda, C.-C. Chen, S. E. Ready, and B. Wacker, "Mechanism of SiN_xH_y deposition from nh3-sih4 plasma," *Journal of The Electrochemical Society,* vol. 137, pp. 614-623, 1990.

[185] Y. Okada and S.-i. Nakajima, "Measurement of local stress in silicon nitride films grown by plasma-enhanced chemical vapor deposition using micro-Raman spectroscopy," *Applied Physics Letters,* vol. 59, pp. 1066-1068, 1991.